Small molecules for applications in solar cells

Deng, Wentao

Award date:
2017

Awarding institution:
University of Bath

Small Molecules for Applications in Solar Cells

By

Wentao Deng

A thesis submitted for the degree of Doctor of Philosophy

University of Bath

Department of Chemistry

September 2017

Abstract

This thesis studies the application of small molecules such as benzoic acids and perylene diimides as interlayers and charge transporting layers in perovskite solar cells. As promising new generation photovoltaics, perovskite solar cells have drawn much attention from scientists around the world due to the high power conversion efficiencies and relatively low energy consumption required during the fabrication process. However, many problems still need to be addressed such as improving stability, reducing hysteresis and removing the expensive charge transporting layers (e.g. spiro-OMeTAD is £850/5g). All of these problems are slowing commercialization of perovskite cells.

Work in this thesis starts with the optimization of the baseline perovskite solar cells, including optimizing the methods of thin film semiconductor preparation, the device architecture and device pattern. By the end of the project average PCE that were consistently above 11% (prepared either in a dry box or in ambient environment) with a narrow distribution were achieved. Further studies into hysteresis and device characterization were also carried out in this part.

Interface engineering was investigated by using perylene diimides (PDIH and PDIV) and benzoic acids (4-aminobenzoic acid, 4-(aminomethyl benzoic acid and 4-(methylamino) benzoic acid) as interlayers to modify the compact TiO_2 layer. Methods to prepare the thin interlayers were optimized and the impacts of the interlayers on the film crystallization, device PCE, stability and hysteresis were also studied. Interlayers were found to significantly change the morphology of the perovskite layer (all molecules), enhance the short circuit current (benzoic acids), and improve the PCE (PDIH) and stability (PDIH). Finally PDIH was studied as the electron transporting layer to replace the TiO_2 film as it can be processed at low temperature (compared with TiO_2). The parameters to fabricate the PDIH layer were optimized and devices with a PCE of 5.7% on average and enhanced stability were achieved.

Declaration of work done in conjunction with others

The collaborative work done for this thesis has been listed in each chapter in the acknowledgements sections.

Acknowledgements

I would like to thank my supervisors Dr. Petra Cameron for supervising me academically and giving support mentally and Prof Laurie Peter for revising my thesis. I would to thank everyone in the PJC group, Kathryn has been kind to me since I started in the group; Shane, Adam, Ralf, Xinxing, Peter, Dom, Sam, Isabella, Rob and Anna the first project student I worked with. It has been great to work with all these people. I received lots of support from inside and outside the university. I would to thank Professor David Adams and Dr Emily Draper in the University of Liverpool (now University of Glasgow), Professor David Lidzey, Ben and Michael at the University of Sheffield; Dr Dan Pantos, Dr Qirong Zhu and Yaoming for their help in providing me the materials and the characterization equipments. I am also very thankful to the support from my friends Daping, Dan, Xiaomei, Qianlong, Xiaolong, Haobo, Meng, Boyang, Yuanyang, Nick, Ruoxi and Andi. I also want to thank the University of Bath for giving me the funding to start my Ph.D.

To get Ph.D. is never easy, and I am proud of myself for all the work I have done though it is not perfect and for the growing confidence I have felt during the last four years. I am a better me! My most cherished thanks are for Xinxing, my parents and my brother, without their strong support I would not be here.

*“学不可以已”*在已迈过的岁月里从萌芽到深刻，每每激励，时有体会。仍以此伴我前行路。

Abbreviations

AM1.5: air mass 1.5

AFM: atomic force microscopy

CV: cyclic voltammetry

CE: counter electrode

DSSC: dye sensitized solar cell

EQE: external quantum efficiency

ETL: electron transporting layer

ETM: electron transporting material

E_F: Fermi energy level

E_{vac}: vacuum energy level

$E_{v:}$: valence band

E_c: conduction band

E_g: band gap

E_g^{opt}: optical band gap

$E_{p/2}$: half peak current potential

$E_{p,a}$: anode peak current potential

$E_{p,c}$:cathode peak current potential

FF: fill factor

FTO: fluorine doped tin oxide

HOMO: highest occupied molecular orbital

J-V: current density-voltage

J_{sc}: short circuit current

LUMO: lowest unoccupied molecular orbital

OPV: organic photovoltaic

PCE: power conversion efficiency

P_{max}: max power point

PL: photoluminescence

PDI: perylene diimide

R_s: series resistance

R_{shunt}: shunt resistance

RH: relative humidity

R_{rec}: recombination resistance

RE: reference electrode

SSPL: steady state photoluminescence

TCO: transparent conductive oxide

TGA: thermal gravimetric analysis

TRPL: transient photoluminescence

HTL: hole transporting layer

HTM: hole transporting material

ITO: indium tin oxide

UV-Vis: ultraviolet-visible light

V_{oc}: open circuit voltage

V_{bi}: built-in voltage

VBM: valence band maximum

WE: working electrode

XRD: x-ray diffraction

XPS: x-ray photoelectron spectroscopy

KPFM: Kelvin probe force microscopy

FWHM: full width half maximum

Publications

1. Deng, W.; Liang, X.; Kubiak, P., Cameron, P.J., Molecular Interlayers in Hybrid Perovskite Solar Cells. Advanced Energy Materials. 2017. DOI: 10.1002/aenm.201701544

2. Pering, S., Deng, W., Cameron, P.J., et.al., Azetidinium lead iodide for Perovskite Solar Cells. Journal of Materials Chemistry A. 2017 DOI:10.1039/C7TA07545F

3. Kubiak, P.; Awhida S.; Hotchen, C.; Deng, W.; et.al. Polymerization of low molecular weight hydrogelators to form electrochromic polymers. Chemical Communications, 2015, 51, 10427-10430.

Table of content

Chapter 1 Literature review

Contents

1.1 Perovskite solar cells and interface engineering

From first generation single crystal silicon solar cells[1] to emerging third generation solar cells, such as dye sensitized solar cells (DSSC),[2, 3] quantum dot solar cells[4, 5], organic solar cells(OPV)[6, 7, 8] and organic-inorganic hybrid perovskite solar cells (PSC),[9, 10, 11, 12] researchers have kept looking for devices that have high power conversion efficiencies (PCEs), are cheap to produce and can be manufactured and disposed of with minimal negative environmental impact. Among all these different types of solar cells, PSC attract tremendous attention as they have the potential to be highly scalable and to be manufactured by low energy routes[13, 14, 15].

Organic-inorganic hybrid perovskite solar cells were first studied in 2009. [16, 17, 18] They developed in an extremely fast speed and the recording power conversion efficiencies reaches 22.1% recently[19]. In addition they can be fabricated with lower energy consumption than many more established technologies in principle[13]. Perovskite solar cells are named after the key material 'perovskite' which is the absorber in the device. It has a ABX_3 structure as shown in **Figure 1-1**, where A is cations such as $CH_3NH_3^+$, $HC\text{-}(NH_2)_2^+$ and Cs^+, B is Pb^{2+} or Sn^{2+} and X is halide such as Cl^-, Br^- and I^-[11, 20, 21, 22]

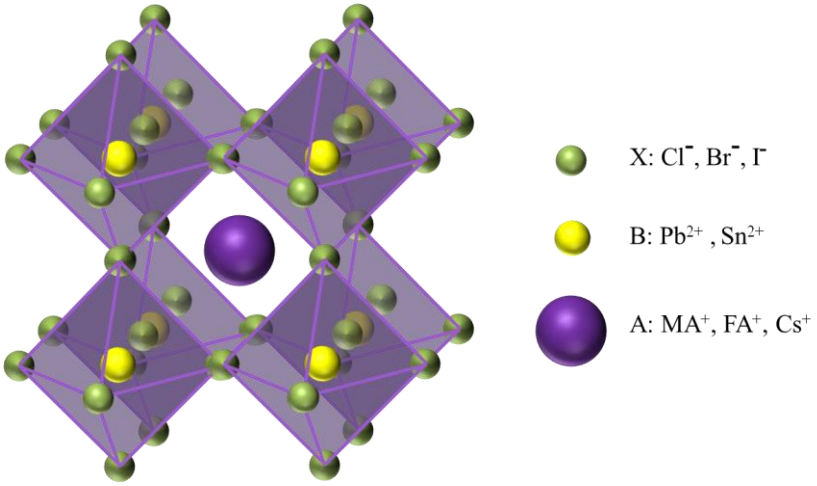

Figure 1-1 Structure of perovskite.

Though showing many outstanding advantages, perovskite solar cells are still suffering some disadvantages that retard the commercialization such as the sustainability and long-term stability problem. Currently there are two main pathways being investigated to improve the efficiency and sustainability of PSC (as shown in **Scheme 1-1**). Firstly, there is a lot of research focusing on the search for better active materials. A range of

(organo-) metal halide perovskites are being investigated for different applications (e.g. $CH_3NH_3PbI_3$, $CH_3NH_3PbI_{3-x}Cl_x$, $CsPbI_3$, HC-$(NH_2)_2PbI_{3-x}Cl_x$) and there is increasing interest in lead free absorber layers[23, 24, 25]. The second approach is to work with existing materials to improve the architecture of the solar cells[16, 17, 26]. The architecture of the device is extremely important as the morphology of the different layers, as well as the nature of the interfaces between them, are critical to ensuring an efficient PCE[16, 27, 28]. In recent years, there has been a focus on interface engineering using small molecules as it is a relatively simple way to improve the performance of PSC[29, 30]. The used interlayers are thin layers or monolayers of organic molecules that modify a specific interface in the solar cell. Here the latest progress in the use of interlayers to optimize the performance of PSC is reviewed. Where appropriate interesting examples from the field of organic photovoltaics are also presented as there are many similarities in the types of interlayers that are used in PSC and OPV.

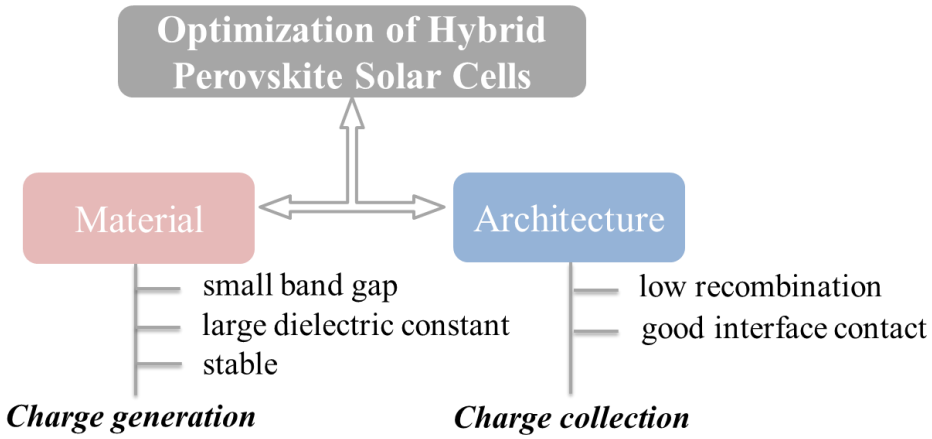

Scheme 1-1 Approaches to improve the PCE of hybrid perovskite and organic solar cells.

Interface engineering can significantly enhance the performance of solar cells in a number of ways. It can be used to modify band energy offsets at an interface and decrease interfacial loss processes caused by surface recombination[31]. Interface engineering can also improve the morphology of the active absorber layer[32], the work function of contact layers[33], the intimacy of the contact at the interface[34] and the long term stability of the devices[35, 36]. In PSC, which typically have a "n-i-p" (or"p-i-n") structure, there are four locations where interlayers have been investigated (**Scheme 1-2**)[37].

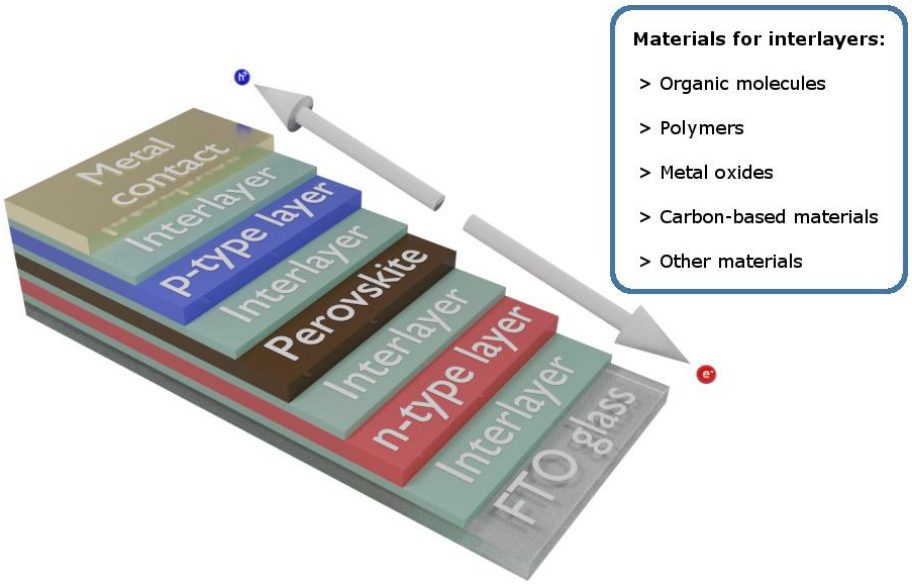

Scheme 1-2. Possible positions of interlayers in hybrid perovskite solar cells.

Many different materials have been investigated as interlayers, including organic molecules[38, 39, 40], metal oxides[41, 42], polymers[43, 44, 45] and carbon based materials.[46, 47, 48] In particular, small organic molecules have attracted interest for their easy synthesis, purification and reproducible properties[49]. Small chemical modifications of the organic molecules' structure allows for further fine-tuning of the interfacial properties according to the research requirements. Additionally, organic molecule interlayers can be deposited by solution-processing at low temperature, making interface engineering a low-energy and scalable technique.[50, 51]

1.2 The role of organic molecule interlayers in solar cells

A broad range of small molecules have been used as interlayers, including benzoic acid derivatives[52, 53], perylene diimide derivatives[49], silanes[54] and several families of amino-functionalized molecules[55]. Interlayer materials need to be carefully selected to ensure an improvement in device performance. For example, an organic molecule with a dipole can be used as an interlayer to improve the V_{oc}. However the ordering of the molecule at the surface, and hence the direction of the dipole, needs to be controlled or it could cause a decrease in V_{oc}[33]. The use of a molecule with good conductivity can significantly improve the contact at the interface and decrease the series resistance(R_s)[34].

1.2.1 Tuning the Morphology of the Absorber Layer

Morphological control of the perovskite absorber layer, e.g. by controlling the crystallinity, thickness and roughness of the film, is critical in the production of high efficiency PSC. A homogeneous perovskite layer with few defects and pin holes can significantly reduce recombination[56] and "shunting pathways" [57]. The morphology of the perovskite films has been controlled by tuning the composition of the precursor solution[58], the annealling temperature[59], solvent engineering[60] and interface engineering[33]. In particular, interface engineering of the substrate on which the active layer is deposited is an easy and effective way to control the active layer morphology. The simplest interlayers influence active layer morphology by controlling the surface energy and the wetting properties of the substrate. [32] An interesting study into surface energy control of ZnO for organic solar cells was presented by Bulliard and co-authors[32]. They used silane molecules with different terminal functional groups to modify the ZnO coated substrate in order to tune the surface energy (30~70mN/m) without changing the work function. The surface energy was effectively adjusted when different ratios of mixed molecules with hydrophilic ($-NH_2$) and hydrophobic terminal grounps ($-CH_3$) were used. Accordingly, as shown in Figure 1 (a) and (b), the morphology of the active P_3HT: PCBM blend varied with the substrate surface energy, leading to a variation in the cell performance. Zuo *et.al*[61] studied the effects of 3-aminopropanoic acid self-assembled monolayers (C3-SAM) as interlayers between $CH_3NH_3PbI_3$ perovskite layers and a ZnO electron selective contact. It was revealed (**Figure 1-2** (c) and (d)) that extended plate-like perovskite grains grew on top of the C3-SAM and better coverage of the substrate (fewer "pin holes") was achieved. As a result, the as-prepared cell showed a 31% enhancement in PCE from 9.8% to 14.2%. The research also found that the amino terminal of the molecule was involved in the crystallization of the perovskite and improved the morphology of the film. Yang *et.al.* used 3-aminopropyltriethoxysilane to treat an SnO_2 electron extracting layer in planar perovskite solar cells, and they also found that the subsequent $CH_3NH_3PbI_3$ layer showed increased grain size and uniformity. The PCE of devices was improved from 14.7% to 17.0%.[62]

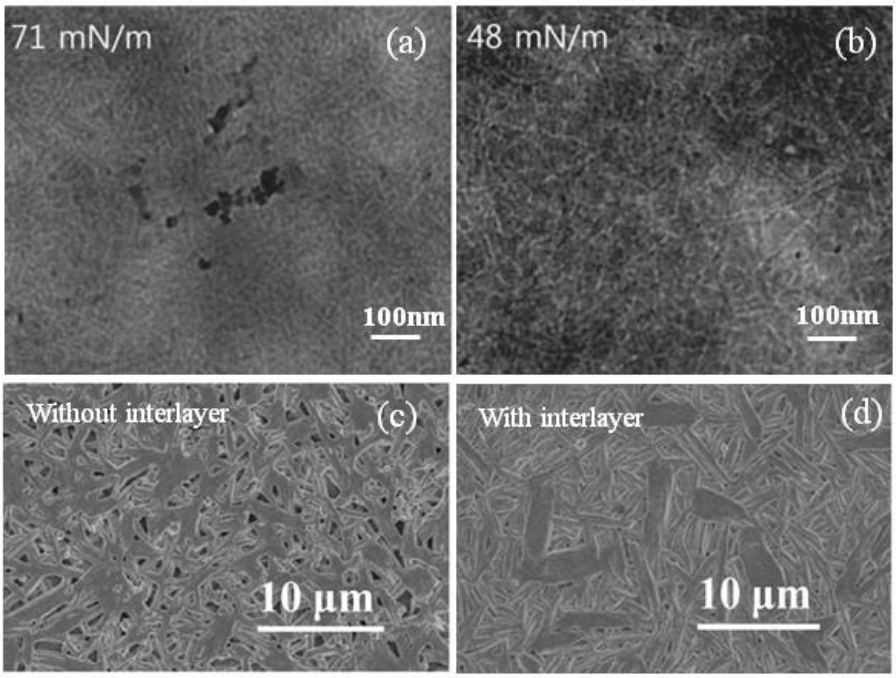

Figure 1-2 SEM images showing morphology changes introduced by interface engineering.[32, 61] (a) and (b) are images of a P3HT: PCBM heterojunction on substrates with different surface energies; (c) and (d) are images of $CH_3NH_3PbI_3$ perovskite layers deposited on substrates with and without 3-aminopropanoic acid interlayers. Reproduced with permission.[32, 61]

1.2.2 Work Function Adjustment

In addition to influencing the morphology, molecules with permanent dipole moments can change the work function at the surface of a given layer. Such molecules can be beneficial to charge collection when used to modify the charge transporting layer, the transparent conducting oxide or the metal electrodes (shown in **Scheme 1-3**) and can expand the choices of metal contacts that can be employed in solar cells[34, 63]. When used to modify the cathode of the device, molecules with a dipole moment that points away from the electrode bends the vacuum level and causes a reduction in the work function (see **Scheme 1-3**(a)). An Ohmic contact is then expected to form between the electrode and the active layer and better electron extraction can be obtained. In contrast, molecules with permanent dipole moments that point toward the cathode are expected to increase the energy barrier for charge extraction and are often used to modify the anode, where they can decrease the energy barrier for hole collection (**Scheme 1-3** (b))[34, 53]. It is worth mentioning that in some situations, the molecules are employed in combination with metal oxides to give a "synergistic effect" for electron or hole extraction[32, 61, 64]. For example, in a polymer solar cell, a layer of metal oxide is used as

an electron blocking layer for its low-lying HOMO level, and a small molecule is used at the same time to decrease the work function.[32]

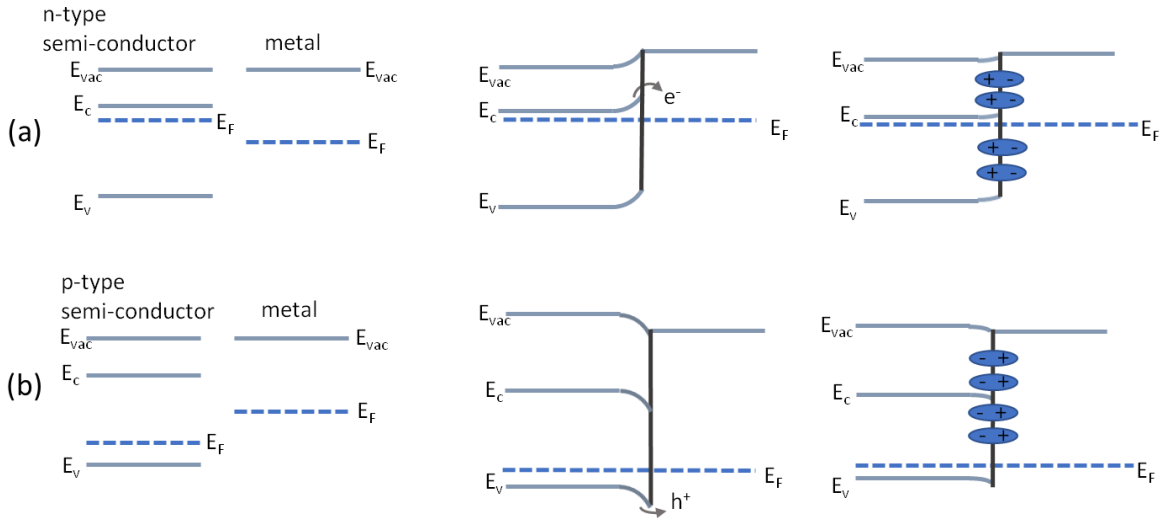

Scheme 1-3. charge collection without (left) and with (right) molecular dipoles as interlayers in solar cells. (a) electron collection, (b) hole collection.

Zhang *et al.* used two perylene diimide derivatives with good conductivity to tune the work function of the electrodes in polymer solar cells [63]. Perylene diimide interlayers can effectively reduce the work function of metal electrodes as can be seen in **Table 1-1**. Devices with PDINO (amino N-oxide functionalised perylene diimide) showed an efficiency of 8.24% which was higher than observed for devices without the interlayer (4.43%). PDINO has also been used in perovsksite solar cells. Min et al. [65] showed that when PDINO was used as an interlayer, the perovskite solar cell showed a decreased series resistance and an increase in efficiency from 10.0% to 14.0%.

Table 1-1. Selected examples of tuning work function by molecular interface engineering.

Substrate	Interlayer	WF before modification/eV	WF after modification/eV
Al[63]	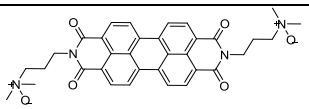	4.3	3.5
Ag[63]	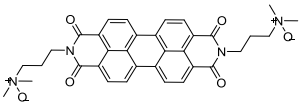	4.3	3.6
ZnO/ITO[61]	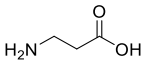	4.2	3.5
TiO_2[37]	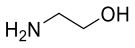	4.0	3.7
P3HT:PCBM[66]	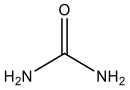	4.5	4.4

Generally, a molecule with dipole moment not only changes the work function but it also changes the surface energy of the substrate. In some cases work function modifications come at the expense of morphological control which is highly dependent on the surface energy[62].

1.2.3 Passivation of the Surface (reduction of trap states)

In PSC and OPV organic molecules can be used to passivate surfaces in order to reduce trap states/defects (especially deep trap states) at the interface. [67, 68, 69, 70, 71] As displayed in **Figure 1-3**, imperfections in the crystal structure or chemical impurities can cause trap states which increase Shockley-Read-Hall (SRH, non-radiative) recombination[72, 73].

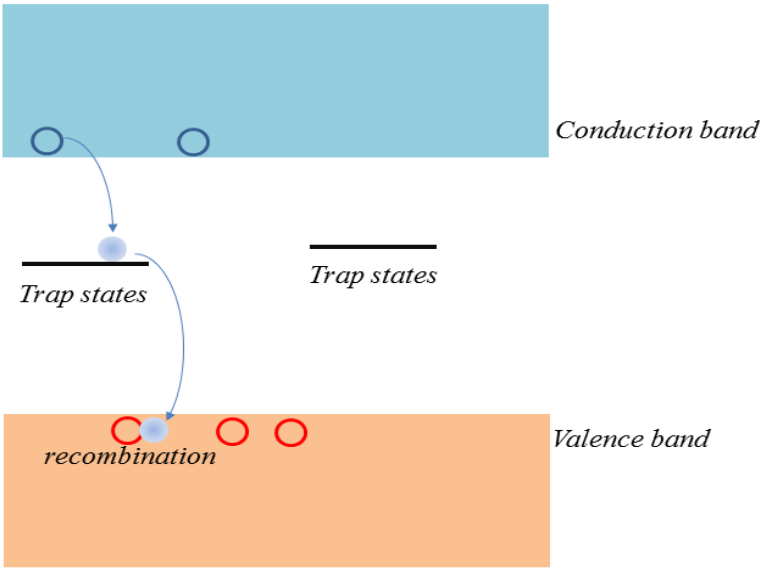

Figure 1-3. Recombination caused by trapping.

To reduce the effect of trap states, small molecules are used that can chemically react with surface non-bonded atoms or surface dangling bonds to reduce the number of surface defects.[69, 71, 74, 75] The passivating interlayer is usually sandwiched between the metal oxide electron extracting layer (e.g. TiO_2, ZnO) and the photoactive layer. For example, molecules that can self-assemble such as thiols, C_{60}-SAMs and some benzoic acid derivatives are widely used to modify the metal oxide layers.[71, 76] They can form monolayers on metal oxides through self-assembly and change the surface energy at the same time. Consequently, the performance of the cells can be improved due to a reduction in surface recombination and an improvement in morphology.

In perovskite solar cells under-coordinated halogen (e.g. I^-) and Pb^{2+} sites on the crystallite surface are believed to form trap states which can act as recombination centers.[67, 77] It has been suggested that the halogen anions act as hole traps and the lead cations as electron traps. It has been shown that Lewis acids can be employed to bond halogen anions and passivate the surface defects. In the same way Lewis bases can be used to passivate non-bonded Pb^{2+} sites. For example, iodopentafluorobenzene (IPFB) shown in **Figure 1-4**(1), is a Lewis acid that was used to reduce surface defects by co-ordinating to under coordinated iodide[77]. The IPFB treated cells reached an efficiency of over 15%, while the cells without IPFB treatment showed an efficiency of 13%. As typical Lewis bases, thiophenes (displayed in **Figure 1-4**(2)) and pyridines are good candidates to passivate surface lead cations.[67] In Noel's work, non-radiative

recombination was significantly reduced, and photoluminescence lifetimes were increased by an order of magnitude. The efficiencies were consequently improved from 13% to 15.3% and 16.5% when the perovskite layer was treated by thiophene and pyridine.

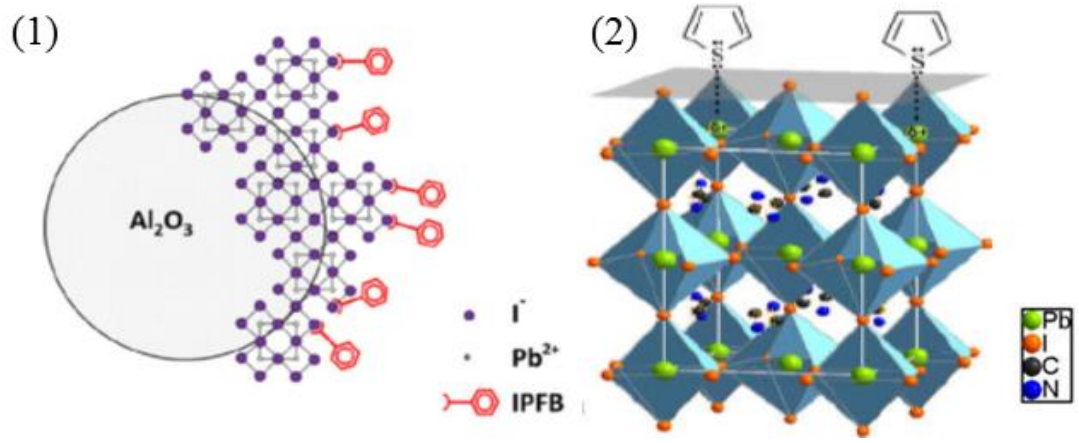

Figure 1-4. Surface passivation of perovskite layer through small molecules. (1) non-bonded I^- was passivated by Lewis acid[77]. (2) non-bonded Pb^{2+} was passivated by Lewis base[67]. Reproduced with permission.[67, 77]

1.2.4 Improvements in Long-Term Stability

Device stability during long term operation is still a major challenge for hybrid perovskite solar cells[78, 79, 80]. Cells can achieve high energy conversion efficiencies but suffer from relatively low stability when they are subjected to high temperature, a humid atmosphere, UV light or even when a current is drawn.[81, 82, 83] It has also been shown that in some cases the inorganic ZnO or SnO_2 electron extracting layer can decompose the perovskite.[84] The high sensitivity of perovskite solar cells to humidity in particular, has complicated commercialization of the technology. As reported by Leijtens et al. [81], without additional protecting strategies, perovskite solar cells with a range of hole transporting materials degrade in hours at 80 ℃ in air. The loss of MAI made the dark-brown films turn yellow which indicated the formation of PbI_2.

Mixed-cation perovskites[85, 86] have been shown to be more stable than single cation perovskites. Recently it has been shown that hybrid 2D-3D perovskite absorber layers can be used to dramatically increase the lifetime of the cells.[87, 88, 89] Other strategies have looked at encapsulation or the use of barrier layers[90]. Finally, there have been a number of studies investigating organic and inorganic interlayers to improve long term

stability under ambient conditions [91, 92, 93]. One approach employs a hydrophobic hole transporting layer or a thin hydrophobic interlayer to protect the perovskite and reduce degradation due to moisture ingress [80, 94, 95]. When a hydrophobic hole conductor (DR3TBDTT) was used to replace the conventional spiro-OMeTAD hole transporting layer in a PSC, the device showed clear improvements in stability.[95] In practice, however, introducing a hydrophobic interlayer is often an easier way to achieve a similar effect. The hydrophobic layers are generally made from small molecules with alkyl groups and have been located both underneath and above the perovskite layer and the hole transporting layer. As shown in **Figure 1-5**, the organic interlayer dodecyl-trimethoxysilane was deposited on a perovskite film ($CH_3NH_3PbI_3$) in a mesoporous perovskite solar cell and greatly improved the device stability as well as the PCE. The PCE of the device was monitored unsealed in ambient environment (humidity < 45%), and 85% of the initial PCE remained after 600h.[54] In Yang's study, a range of alkyl ammonium salts with different functional groups were deposited on perovskite films as hydrophobic interlayers.[80] The substrate wetting properties were observed to change when the perovskite precursor solution was applied and tetra-ethyl ammonium iodide significantly improved the stability of the PSC. The device could be stored for over 30 days at around RH 90%. As mentioned above hydrophobic interlayers have been investigated in all four interlayer positions indicated in Scheme 2, including immediately adjacent to the metal cathode [96, 97, 98]. For instance, Ciro et al. used Rhodamine 101 as a cathode interlayer to optimize the Ag/PCBM interface in a p-i-n structured perovskite solar cell[96]. They showed that device stability was significantly improved as the Rhodamine molecular interlayer appeared to act as a permeation barrier to slow the ingress of moisture from the atmosphere.

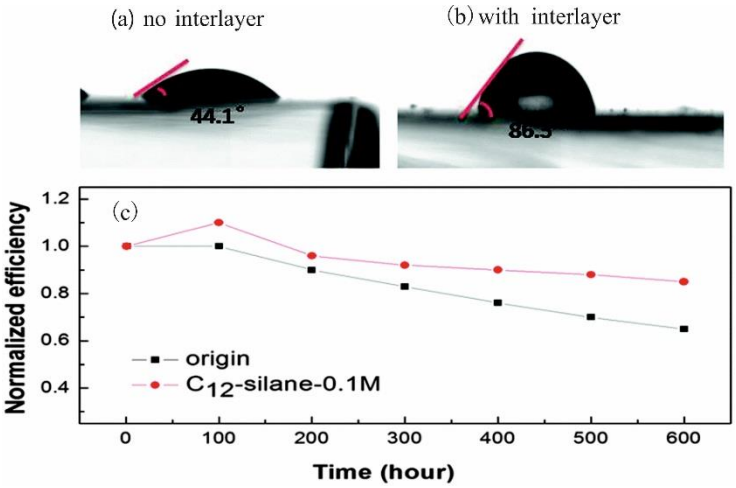

Figure 1-5. long-term stability of solar cells with and without hydrophobic interlayers [54].Figures (a) and (b) show the contact angle before and after the interlayer is added. Figure (c) shows the change of normalized efficiency with time.

1.2.5 Other Roles

Interlayers can also serve many other roles such as blocking charge[99, 100] and improving the intimacy of the contact between two layers[66, 101]. For example, small molecules with low lying HOMO can be used to modify the electron extracting layer. The interlayer prevents the hole from moving to the contact, as shown in **Figure 1-6.** Increasing the selectivity for one charge carrier can result in less recombination and an increase in the efficiency of charge collection.

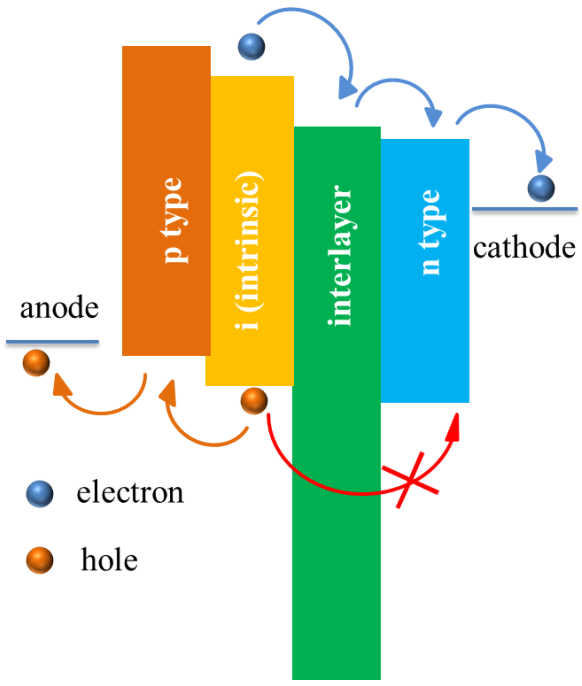

Figure 1-6. Hole transportation blocked by low-lying HOMO of an interlayer.

Organic molecule interlayers are also frequently used to increase the intimacy of the contact between different layers in the solar cells. In some cases the small molecules act to ‚bind' the two layers together, thereby reducing the series resistance as well[66, 102]. For example, when urea was used as the interlayer in polymer solar cells with PCBM and P3HT in the active layer[66], the lone-pair electrons of the $–NH_2$ group were able to coordinate to the Al cathode, causing a 'closer contact' at the interface as well as tuning the work function. In perovskite solar cells, links between perovskite layer and contact layer are improved when the the interlayer moleules have terminal amino groups[52, 103]. For instance, a group of moleucles with generic structure HOOC-R-NH_3I has been used to modify TiO_2 surfaces[102]. These molecules bind the TiO_2 surface through the carboxyl groups and participate in the crystallization process of the perovskite via the $-NH_3^-$ terminus. The resulting peroskite device showed an improvement in PCE from around 7% to around 12%.

1.3 Classes of Small Molecules Used in Interlayers

There are a wide range of organic molecules that can be used as interlayers. Those most frequently used include perylene and its derivatives[51, 63, 65, 104, 105], benzoic acid and its derivatives,[52, 106] amino-functionalized small molecules[55, 107], silanes[54], dyes[108] and fullerene derivatives[109, 110]. As listed in Table 1-2, different molecules are employed depending on the aim of the research. For instance, to reduce the work function, a molecule with permanent dipole moment is required. In order to change the morphology of the active layer, a molecule with hydrophobic or hydrophilic functional groups is important. If the interlayer is deposited on metal oxides, such as indium tin oxide (ITO), fluorine doped tin oxide (FTO), TiO_2 or ZnO, small molecules with a 'surface-active-head-groups' (anchoring group) can be considered, as they can be deposited by a simple immersion process to prepare a self-assembled interlayer (displayed in **Figure 1-7(a)**).

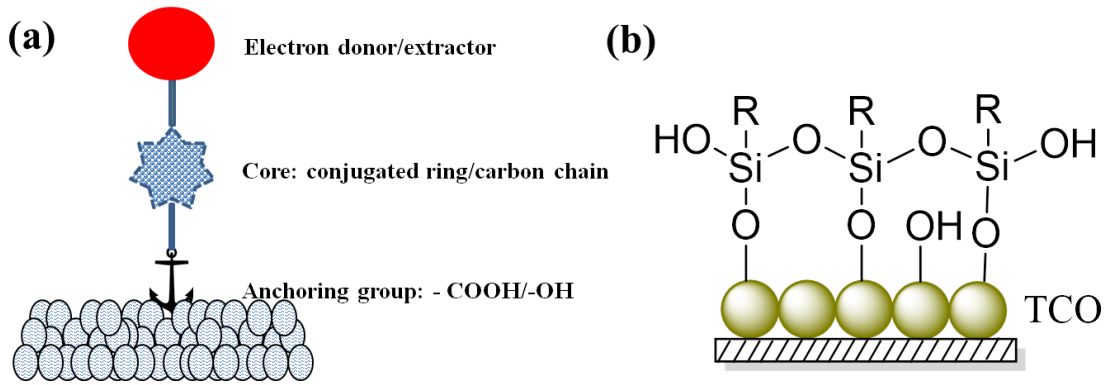

Figure 1-7. (a) Organic molecule with dipole moment and anchoring group. (b) Silane self-assembled on a transparent conductive oxide (TCO) surface.

Table 1-2. Relevant organic molecule interlayers that have been used in perovskite solar cells. Interesting examples of interlayers used in organic solar cells have also been included.

Solar Cell architecture	**Small molecule**	**Role of small molecule**	**PCE Modified cell *vs.* not modified cell***
ITO/PEDOT:PSS/$CH_3NH_3PBI_xCl_{1-x}$/PCBM/ZnO/**PDINO**/Ag[65]	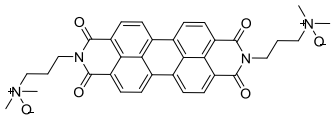	Reduce R_s	14.0% *vs.*11.3% (average)
ITO/PEDOT:PSS/PTB7:PCBM/**PDINO**/metal[63]	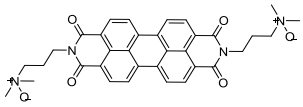	Reduce work function and R_s	7.7% *vs.*4.4%
FTO/c-TiO2/m-TiO2/**benzoic acid derivatives**/$FA_xMA_{1-x}PbI_{3-y}Br_y$/spiro-OMeTAD/Au[103]	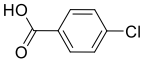	Enhance charge extraction speed	18.4% *vs.* 17.5
FTO/c-TiO2/m-TiO2/**benzoic acid derivatives** / $CH_3NH_3PbBI_3$/spiro-OMeTAD/Au[52]	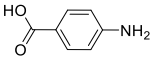	Reduce surface defects	10.5% *vs.* 7.5%
ITO/PEDOT:PSS/P3HT:PCBM/ZnO/**benzoic acid derivatives** /metal[64]	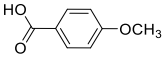	Reduce work function	3.2% *vs.* 0.7%

ITO/**benzoic acid derivatives/**PTB7:PCBM/Al[53]	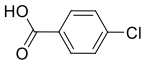	Increase work function/morphological control	8.2 *vs.*5.1%
FTO/TiO_2/**silanes**/$CH_3NH_3PbI_3$@ZrO_2/C[38]	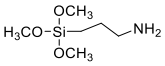	Morphological control	12.8% *vs.* 9.7%
ITO/ZnO/**mixed small molecules**/P3HT:PCBM/MoO_3/Ag[32]	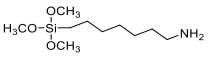 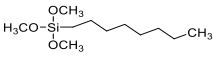	Surface energy/morphological control	3.7% *vs.*3.3% (average)
ITO/ZnO/**3-aminopropanoic acid**/ $CH_3NH_3PbI_3$ /spiro-oMeTAD/MoO_3/Ag[61]	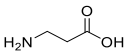	Morphological control and reduce work function	15.7% *vs.*11.9%
FTO/TiO_2/**amino acids**/$CH_3NH_3PbI_3$/spiro-OMeTAD/Au[111]		Enhance charge extraction speed	14.2% *vs.* 10.8%
ITO/PEDOT:PSS/**NH_3**/$CH_3NH_3PbI_{3-x}Cl_x$ /C60/BcP/Ag[112]	NH_3	Morphological control	15.2% *vs.* 14.3%
FTO/c-TiO_2/**EA**/$CH_3NH_3PbI_{3-x}Cl_x$ /spiro-OMeTAD/Au[37]	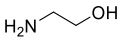	Reduce work function	16.3% *vs.*12.8%
ITO/PEDOT:PSS/P3HT:PCBM/**urea**/Al[66]		Reduce work function and Rs	4.4% *vs.*3.4%
ITO/PEDOT:PSS/**DMSO**/ P3HT:PCBM/BCP/Al[113]		Reduce Rs	2.7% *vs.*0.1%
ITO/**EDTA-N**/PTB7:PCBM/MoO3/Al[114]	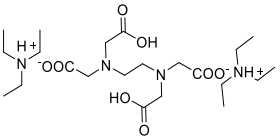	Reduce work function and Rs	6.2% *vs.* 0.7%
FTO/c-TiO_2/mp-TiO_2/**butylphosphonic acid 4-ammonium chloride**/perovskite/spiro-OMeTAD/Au[78]	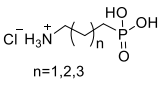	Stability improvement	16.7% *vs.* 8.8%
FTO/c-TiO_2/**PCBA/**perovskite/spiro-OMeTAD/Au[115]	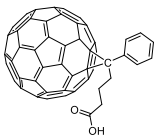	Reduce hysteresis	13.1% *vs.* 10.1%

i) all the PCE data shown here are from the best performing cell and calculated from J-V scans except where otherwise mentioned

1.3.1 Benzoic Acid Derivatives

Benzoic acid derivatives are generally used in organic solar cells and perovskite solar cells to modify metal oxide layers like TiO_2, ZnO or SnO_2[52, 64, 69, 116]. The carboxyl group binds strongly to the oxide making them robust interlayers and the wide range of dipole moments accessible through functional group modification can provide favourable conditions for charge extraction at a variety of interfaces. With an appropriate dipole moment, a benzoic acid derivative can be used to improve the V_{oc}, either as a cathode interlayer or an anode interlayer. **Table 1-3** displays the dipole moment of a range of benzoic acid derivatives that have been used in PSC and OPV.[103, 117, 118]

Table 1-3. Dipole moments of some common benzoic acids.

Molecule	Dipole moment(Debye)
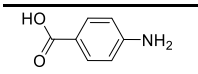	-4.5
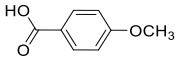	-3.9
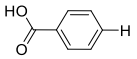	-2.1
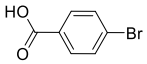	1.4
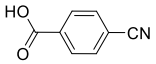	3.4
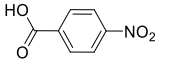	3.8
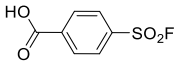	4.5

1.3.2 Amino-functionalized Molecules

The most commonly used amino-functionalized molecules can be classified into two groups: organic ammonium salts and neutral amino-functionalized molecules[119, 120, 121, 122]. Generally, ammonium salts are alcohol soluble and useful for tuning the work function of a surface,[120] Neutral amino-molecules are typically hydrophobic and can be used to tune the morphology of layers deposited on them. Some examples are listed in Table 1-4**.** Wang et al.[120] synthesized several molecules functionalized with different amino groups as cathode interlayers for OPV. Depending on the amino-functional groups chosen, the work function of the modified electrode could be varied allowing the

formation of an Ohmic contact between the charge generating layer and the charge collecting layer.

Table 1-4. Amino-functionalized small molecules as interlayers. Relevant interlayers used in organic solar cells have also been included.

Amino-functionalized small molecules	**Solar cell architecture**	**Molecule structure**	**Ref**
ammonium salts	ITO/ PEDOT:PSS/ PTB7:PC71BM/**ammonium salt**/Al	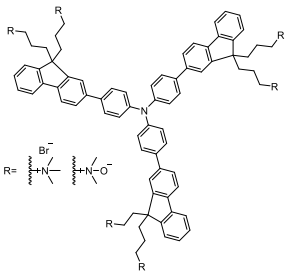	120
	FTO/c-TiO_2/m-TiO_2/**glycine**/$CH_3NH_3PbI_3$/spiro-OMeTAD/Au	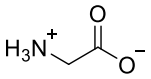	121
	ITO/ZnO/**3-aminopropanoic acid**/ $CH_3NH_3PbI_3$ /spiro-OMeTAD/MoO_3/Ag	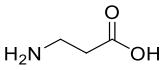	61
	FTO/TiO_2/**amino acids**/$CH_3NH_3PbI_3$/spiro-OMeTAD/Au	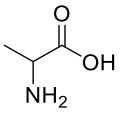	111
	FTO/TiO_2/$CH_3NH_3PbI_3$/**ammonium salt**/spiro-OMeTAD/Au	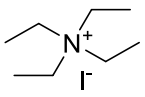	80
	ITO/ammonium salt/ PTB7:PC71BM/MoO_3/Al	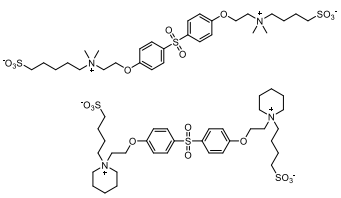	119

	ITO/PEDOT:PSS/PTB7:PC71BM/**TBATPB**/Al	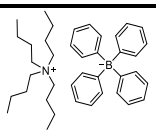	123
Neutral amines	ITO/triarylamine/$CH_3NH_3PbI_3$/PCBM/LiF/Ag	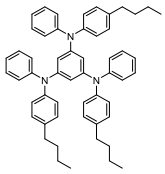	29
	ITO/ammonium interlayer/ PTB7:PC71BM/MoO_3/Al	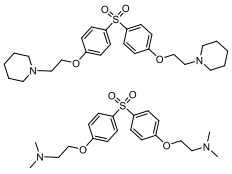	119

1.3.3 Silanes

Silanes can form self-assembled monolayers (SAMs) on a range of substrates. The self-assembly mechanism is shown in Figure 1-7 **(b)**). Their interaction with surface –OH groups is relatively straightforward. They react with transparent conductive oxides (TCO) to form a thin surface layer, while the non-reacting side functional groups are critical for the formation of surface dipoles[124, 125]. They have been used to change the work function, surface wetting properties and the stability of layers in solar cells. **Table 1-5** shows some examples of different silanes used in hybrid perovskite and organic solar cells. Song *et.al.* synthesised a series of silanes with fluorinated head groups as interlayers and systematically studied the effects of different molecular dipoles and packing densities of layers on ITO [126]. After optimization of the structure and composition, the polymer solar cells with silanes exhibited a 54% increase of PCE and a 35% improvement of V_{oc}. A silane with a long alkyl chain (C12) was used in Zhang's work as an insulating layer for perovskite solar cells.[54] It was presumed that it acted as a spatial separator of electrons in the perovskite layer and holes in the HTM layer. As a result the shunt resistance (R_{shunt}) increased and the series resistance R_s decreased. The PCE was enhanced by 40% from 9.8% to 13.7%, and device stability was also improved.

Table 1-5. Silanes in perovskite solar cells. Relevant interlayers used in organic solar cells have also been included.

Solar cell architecture	Silane structure	References
FTO/c-TiO_2/m-TiO_2/ $CH_3NH_3PbI_3$/**silanes**/spiro-MeOTAD/Ag	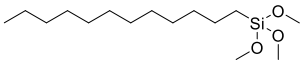	54
FTO/TiO_2/**silane**/$CH_3NH_3PbI_3$@ZrO_2/C[38]	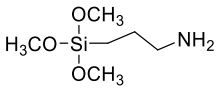	38
ITO/PEDOT:PSS/ $CH_3NH_3PbI_{3-x}Cl_x$ /**silanes**/PCBM/Ca/Al	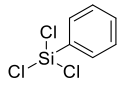 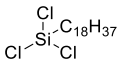	127
ITO/PTAA/ $CH_3NH_3PbI_3$/C60-SAM/**silanes**/BCP/Cu	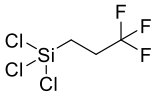	128
FTO/SnO2/**silanes**/$CH_3NH_3PbI_3$/spiro-OMeTAD/Au	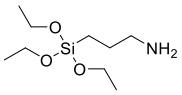	62
ITO/ZnO/**mixed silanes**/P3HT:PCBM/MoO_3/Ag[32]	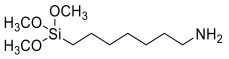 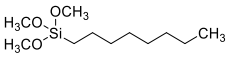	32
ITO/**silanes**/P_3HT:PCBM/metal	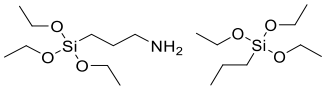 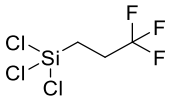	34
ITO/ P3HT:PCBM/**silanes**/Au	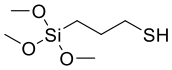	129
ITO/**silanes**/PTB7:PCBM/LiF/Al	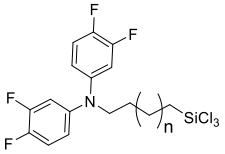	126

1.3.4 Perylene and its Derivatives

Perylene and its derivatives (e.g. perylene diimides (PDIs) or perylene bisimides(PBIs)) are very typical n-type interlayers used in solar cells. The perylene core ensures good

conductivity, and in addition their energy levels and solubility can easily be modified by changing the side functional groups or substitution in the bay positions of the conjugated core. As displayed in **Table 1-6**, several different perylenes (most of them are perylene diimides) have been investigated[130]. As briefly discussed above, a solution prosessable perylene diimide, PDINO was used as cathode modifier in inverted structure perovskite solar cells. It improved the contact between the ZnO and the Ag metal contact, significantly reducing R_s and increasing R_{sh}, the PCE of the device was enhanced from 11.3% to 14%.[65] Due to its good electric and electronic properties, PDINO has also been used in organic solar cells (as shown in **Table 1-6**)[63], and the device showed improved efficiency from 4.8% to 8.2%. To date there are limited examples of perylene derivatives used in perovskite solar cells, however, the sucess in OPV[131, 132](see **Table 1-6**) in organic solar cells suggests that this is an underexplored area in PSC.

Table 1-6. Perylene and its derivatives used in perovskite and organic solar cells.

Solar cell architecture	Perylene and derivatives structure	References
ITO/PEDOT:PSS/**perylene**/ $CH_3NH_3PbI_{3-x}Cl_x$/ PCBM/Bphen/Al	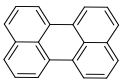	105
ITO/PEDOT:PSS/$CH_3NH_3PbI_xCl_{3-x}$/PCBM/ZnO/**PDINO**/Ag	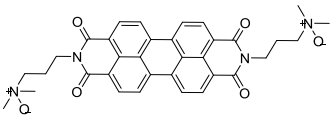	65
ITO/PEDOT:PSS/PTB7:PCBM/**PDINO**/metal	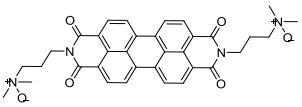	63
ITO/**PDIs**/P_3HT:PCBM/V_2O_5/Al	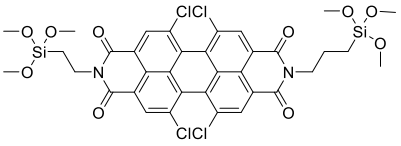	131
ITO/**ZnO:PDIs**/PTB_7Th:PCBM/MoO_3/Al	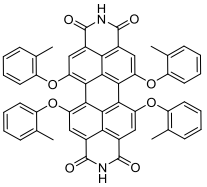	130

ITO/**PDIs**/PTB_7:PCBM/MoO_3/Al	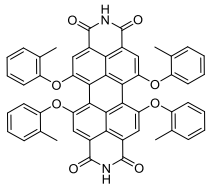	133
ITO/PCDTBT:EP-PDI/**PDIs**/Al	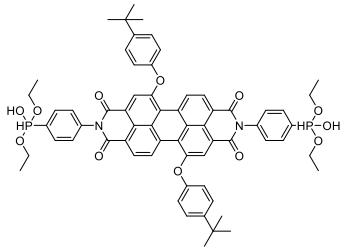	51

It is worth noting that the orientation in which PDIs pack or stack plays an important role in determining the electronic properties of the interlayer.[49, 134, 135] **Figure 1-8** displays two different aggregation orientations of PDIs. It is reported that with different preparation methods, for example dipping or spin coating, the tilt angles of the molecular cores are different[49]. A phosphonic acid functionalized PDI film prepared using a dipping method showed a smaller tilt angle than the one made by spin coating[49] (**Figure 1-8** (a)). Zhang *et.al* investigated how the charge transfer process changed with variation in orientation at the interface[135]. The authors used different solvents to control intermolecular hydrogen bond formation which modified the PDI film morphology **(Figure 1-9).** UPS analysis was used to show that the solar cells with PBI-1 (5,6,12,13-tetrakis(o-tolyloxy)anthra[2,1,9-def:6,5,10-d'e'f']diisoquinoline-1,3,8,10(2H,9H)-tetraone) nanoparticles showed better charge transfer than those with PBI-1 nanofibers at the interface.

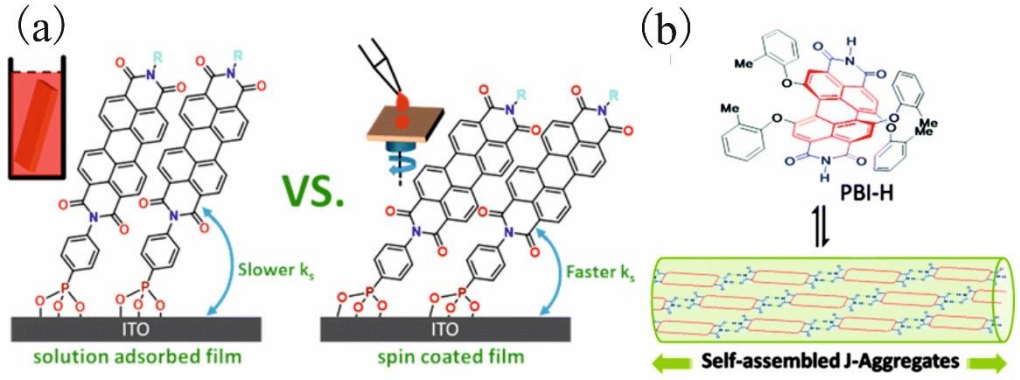

Figure 1-8 PDIs aggregating in different orientations. (a) PDIs aggregates have different tilt angles depending on the preparation methods used.

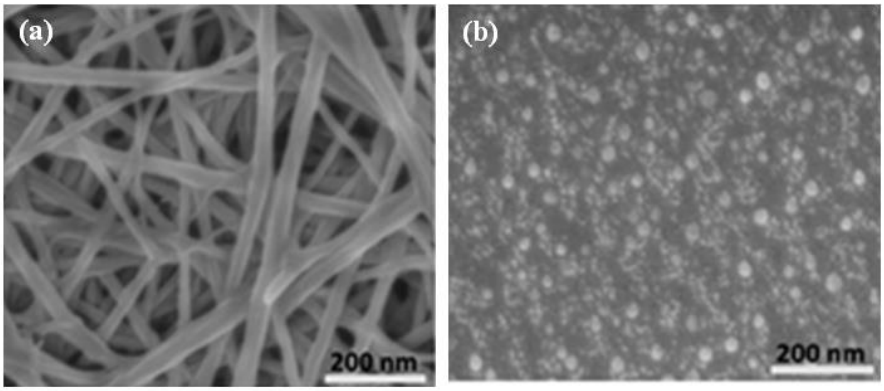

Figure 1-9. PDIs film morphology changes with different solvents (both films obtained by spin coating).[135] (a) $CHCl_3$ as solvent; (b) THF as solvent.

1.3.5 Other Molecules

Other molecules including dyes [104, 136, 137], phosphonic acids[138, 139], metal organo compounds[107, 140] , alcohols[141] and thiols[142, 143, 144] have also been used as interlayers, as shown in **Table 1-7**. Rodamine 101 was found to increase the fill factor effectively when used as an interlayer between PCBM and the Ag contact in perovskite solar cells due to better aligned energy levels.[108] It was suggested that its introduction in the solar cell created an Ohmic contact at the interface, which resulted in an increase of PCE from 12.0% to 14.8%. Interestingly, molecular interlayers can also help build ITO free device architectures in perovskite solar cells.[143] Chang *et.al.* used two types of thiols and Ag was sandwiched between the two interlayers to form an ITO free electron collecting electrode.[143] Thiol interlayers adjusted the work function of the Ag and improved the stability of devices. Due to the low sheet resistance of the modified Ag electrode, it also partially overcame the problem of high sheet resistance introduced by

TCOs in large area devices. The average PCE for devices with an active area of 0.12cm^2 was 15% and 5cm^2 active area devices showed an efficiency of 11.8%.

Table 1-7. Other organic molecule interlayer examples in perovskite solar cells. Relevant interlayers used in organic solar cells have also been included.

Solar cell architecture	Molecule structure	REF	Classification
ITO/PEDOT:PSS/$CH_3NH_3PbI_{3-x}Cl_x$/PCBM/**rodamine101**/Ag	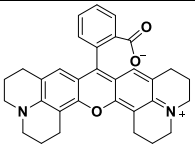	108	dye
ITO/ PEDOT:PSS/**porphyrin**/ $CH_3NH_3PbI_3$/PCBM/BCP/Al	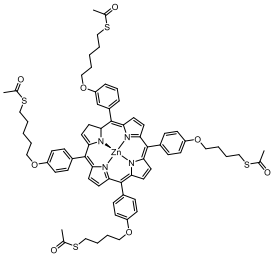	100	dye
FTO/c-TiO_2/m-TiO_2/**thiols**/$CH_3NH_3PbI_3$/**thiols**/spiro-OMeTAD/Au	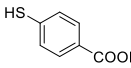 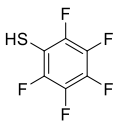	142	thiol
Glass/**thiols**/Ag/**thiols**/PCBM/$CH_3NH_3PbI_3$/PTAA/Ag	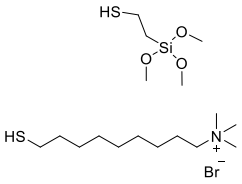	143	thiol
ITO/NiO_x/ $CH_3NH_3PbI_{3-x}Cl_x$/PCBM/**metal organo compound**/Ag	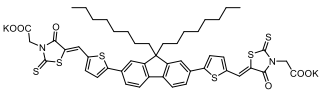	140	metal organo compound
ITO/PEDOT:PSS/ PCDTBT:PC71BM/ **metallophthalocyanine**/Al	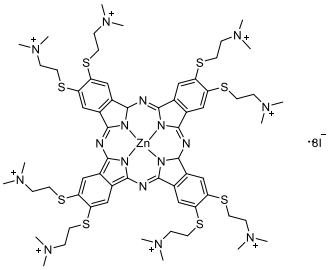	136	dye
ITO/**phosphonic acids**/P3HT:PCBM/Al		139	Phosphonic acid

ITO/**glycol**/PTB_7:$PC_{71}BM$/Al	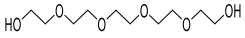	141	glycol

1.4 Methods Used to Prepare Organic Molecular Interlayers

Due to the insulating nature of most small organic molecules, the interlayer in a device is generally less than 10 nanometers thick [63, 66, 145]. Interlayers are also required to be thin in order to avoid unwanted absorption of light before it can reach the active layer,[131] although there are a few exceptions, especially when the molecule has good conductivity. As reported by Wang et al., a perylene diimide based interlayer (conductivity ~ 10^{-5} S cm^{-1}) gave a very good performance with thicknesses ranging from 6 to 25nm.[63]

Several approaches can be employed to prepare thin interlayers. They can be made by solution processing or by vapor deposition. The method chosen depends on the properties of the material being deposited and the surface it is being deposited on. **Scheme 1-4** illustrates the three most common methods used to prepare thin layers, i.e. dip coating, spin coating and thermal evaporation. Notably, when using solution-processed approaches it is extremely important to account for the effects of the solvent on interlayer morphology. The stability of the interlayer in the presence of the solvent used to deposit subsequent layers is also important.

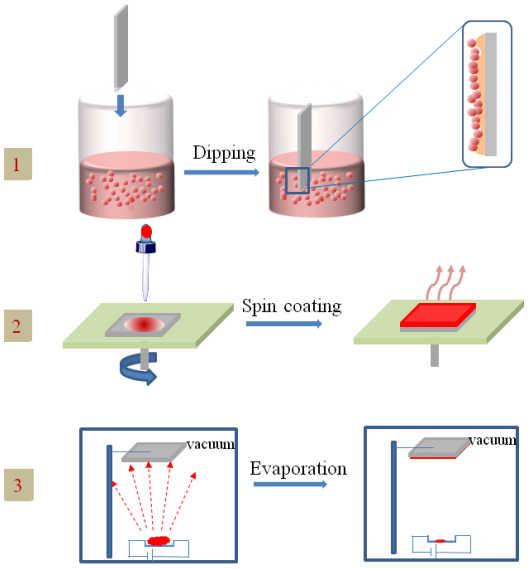

Scheme 1-4. Thin interlayer preparation methods. (1) dipping method, (2) spin coating method, (3) thermal evaporation.

1.4.1 Dip Coating/Immersion

Dip coating is a simple and low energy route to obtaining uniform thin films through molecular self-assembly. Small molecules deposited by dip coating usually have surface-active groups to anchor and self-assemble spontaneously on the solid surface. They can easily rearrange and form well-ordered and highly oriented ultrathin films through specific interactions such as formal chemical bonds, hydrogen bonds or π-π stacking[146]. The molecules should be carefully chosen to match the surface properties of the substrates[147] in order to get uniform layers. As has already been mentioned, molecules with R-O-R', R-OH or R-COOH structures can form chemical bonds with TCO substrate surfaces. Other examples include thiols (R-SH) or dithiols which can self-assemble on metal surfaces[148, 149, 150, 151] (e.g. Au, Ag, Cu, Pd, Pt, Ni, Fe etc.) and phosphonic acids which can also form self-assembled monolayers on oxides such as silicon dioxide and aluminum oxide[152].

Table 1-8 lists the parameters that are important to achieve good dip coated film quality; e.g. the number of surface dangling functional groups (such as –OH on metal oxides) could significantly affect chemical adsorption on the surface. The temperature of the solution will influence the adsorption speed and the dipping time will have impact on the coverage. To make a thin layer that is more strongly bound to the substrate a post annealing process after dipping can help convert physisorption into chemisorption. There are some studies mentioning that the high relative humidity (RH) of the environment needs to be controlled as it can prevent molecules from forming chemical bonds with the substrates[152].

Table 1-8. Dip coating process parameters for making molecular interlayers.

Substrates	Material	Solvent	Concentration	Dipping time	Dipping temperature	REF
SiO_2	ODPA	THF	1mM	3h	60°	[152]
TiO_2	Benzoic acid derivatives	THF: EtOH(1:1)	0.1mM	overnight	-	[69]
TiO_2	Benzoic acid derivatives	MeCN	1mM	2~h	-	[117]

TiO_2	Carboxylic /phosphonic acids	EtOH	0.5mM	18h	-	[153]
TiO_2	glycine	H_2O	1mM	overnight	-	[121]
ITO	Perylene diimide derivatives	DMF/$CHCl_3$	20 µM	1h	Room Temperature	[49]

Where a value has not been entered it was not mentioned in the reference.

Rather than getting a thin layer (monolayer or multilayer) through a self-assembly process, an exact monolayer can be obtained using the Langmuir-Blodgett technique (shown in **Scheme 1-5**). This technique relies on amphiphilic molecules forming a monolayer at the liquid/air interface. By slowly withdrawing a substrate from the liquid, a uniform monolayer can be obtained.[154, 155]

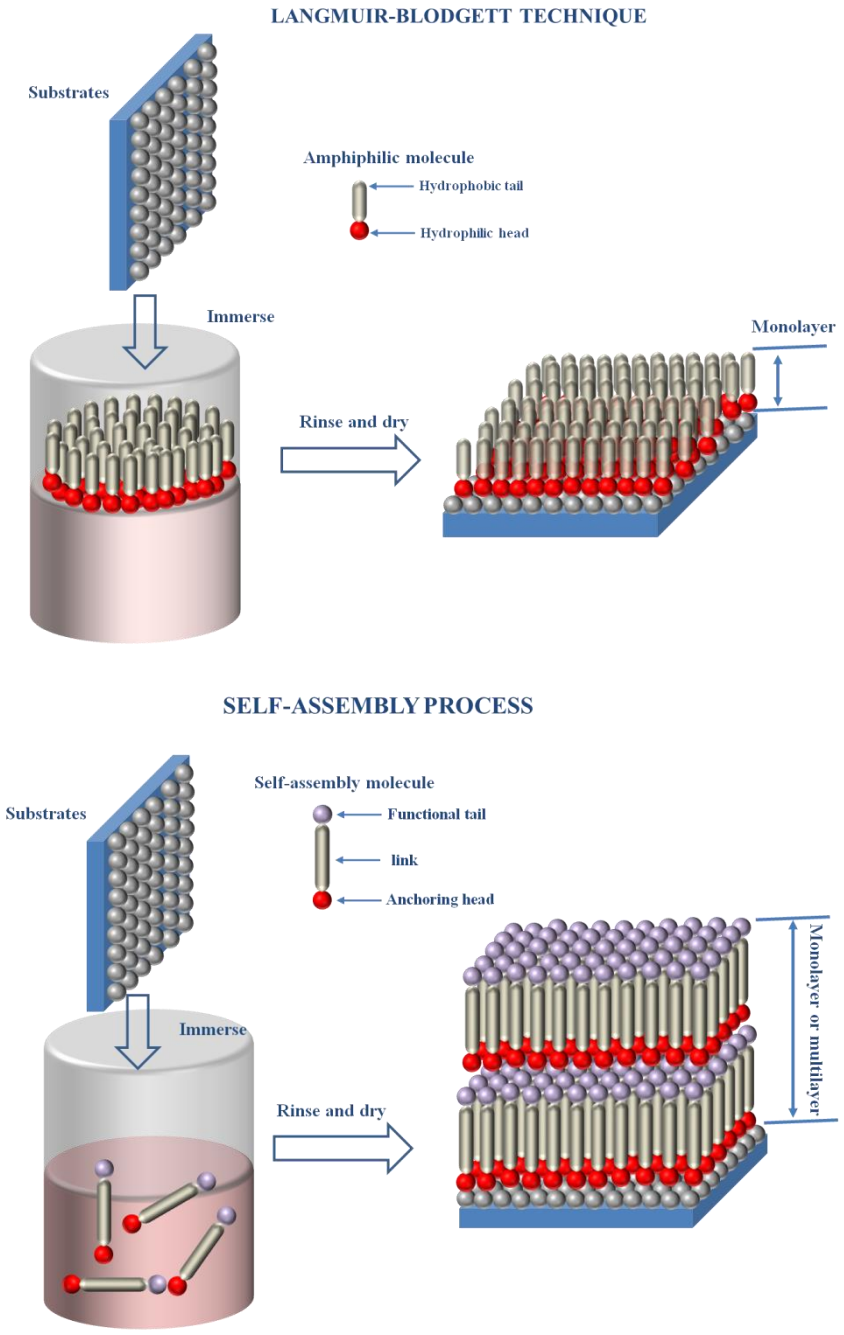

Scheme 1-5. Self-assembly process and Langmuir-Blodgett technique.

1.4.2 Spin Coating

Spin coating is a highly controllable method for depositing thin films. It is very practical for small area substrates as long as the desired material is soluble or well dispersed in the selected solvent. Unlike dip coating, spin coating is a quicker process and has fewer substrates requirements. It typically only takes a few seconds to coat the film and usually a few minutes to anneal it. Spin coating can be used to deposit molecules that can physisorb or chemisorb onto the surface.

The thickness and the quality of spin coated films can be optimized by varying the spin speed, coating time or concentration of the precursor solution. In **Table 1-9**, a few parameters for commonly used spin coating processes are listed. To get good quality thin films, the solvent type, concentration of the solution, pH of the solution, spin coating parameters and annealing procedures are all important factors that need to be considered[131, 135]. As mentioned above Zhang *et.al.*[135] used $CHCl_3$ and THF as two different solvents to control the morphology of perylene diimide cathode interlayers by changing the intermolecular hydrogen bonding. In addition, the authors introduced acetic acid as an aggregation inhibitor to control the structure and dimensionality of the film.

Table 1-9. Spin coating process parameters for making molecular interlayers.

Underlayer	Molecule	Solvent	concentration	Spin coating speed	REF
PCBM	PDINO	MeOH	1mg/mL	1krpm	[65]
TiO_2	Ethanolamine	2-methoxyethanol	0.35wt.%	3krpm	[37]
PCBM:P3HT Heterojunction	Urea	Methanol	1mg/mL	3krpm	[66]
ITO	Perylene diimide derivatives	$CHCl_3$	0.5mM	1krpm	[49]
F-DTS:R-PDI Heterojunction	Perylene diimide derivatives	Methanol with 0.2% acetic acid	1.5mg/mL	3krpm	[134]

1.4.3 Thermal Evaporation

Thermal evaporation is a simple physical vapor deposition process which is suitable for both inorganic and organic materials. The desired material is placed in a boat under vacuum and then heated to form vapor which will condense on nearby substrates. This is an effective approach to deposit multilayer films especially when the desired material has low solubility in common solvents. This method allows precise control of the film thickness (0.1nm precision) and an easily controllable deposition rate. Despite the drawback that some organic materials easily decompose at high temperatures, it is a very popular method to deposit organic compounds for optoelectronic devices[156, 157].

Huang *et.al*. prepared a FPDI (fluorinated perylene diimide derivative) electron transporting layer using the vapor deposition method[158] for $CH_3NH_3PbI_3$ perovskite solar cells. The thickness was precisely controlled from 25nm to 75nm, and the solar cell efficiency was effectively improved with the optimization of FPDI thickness.

1.4.4 Other Methods

There are some other solution based methods to deposit thin films, such as drop-casting, solution printing techniques and solvothermal methods.[159]. For instance, Qu et al.[159] used a solvothermal method to prepare a thin carboxylic acid layer on a TiO_2 surface. The process was carried out in an autoclave at 100 °C for 24h. The higher temperature and pressure conditions make the molecules chemically adsorb onto the TiO_2 surface (bidentate chelation). The coverage was optimized by changing the ratio of TiO_2 to the small molecules.

1.5 References

1. Green MA. *Solar cells: operating principles, technology, and system applications*, 1982.

2. Grätzel M. Dye-Sensitized Solid-State Heterojunction Solar Cells. *MRS Bull* 2005, **30**(01)**:** 23-27.

3. Stergiopoulos T, Kontos AG, Jiang N, Milliken D, Desilvestro H, Likodimos V*, et al.* High boiling point solvent-based dye solar cells pass a harsh thermal ageing test. *Sol Energy Mater Sol Cells* 2016, **144:** 457-466.

4. Kramer IJ, Minor JC, Moreno-Bautista G, Rollny L, Kanjanaboos P, Kopilovic D*, et al.* Efficient Spray-Coated Colloidal Quantum Dot Solar Cells. *Adv Mater* 2015, **27**(1)**:** 116-121.

5. Carey GH, Abdelhady AL, Ning Z, Thon SM, Bakr OM, Sargent EH. Colloidal Quantum Dot Solar Cells. *Chem Rev* 2015, **115**(23)**:** 12732-12763.

6. Kwon OK, Park J-H, Kim DW, Park SK, Park SY. An All-Small-Molecule Organic Solar Cell with High Efficiency Nonfullerene Acceptor. *Adv Mater* 2015, **27**(11)**:** 1951-1956.

7. van Franeker JJ, Turbiez M, Li W, Wienk MM, Janssen RAJ. A real-time study of the benefits of co-solvents in polymer solar cell processing. *Nat Commun* 2015, **6**.

8. Li Y. Molecular Design of Photovoltaic Materials for Polymer Solar Cells: Toward Suitable Electronic Energy Levels and Broad Absorption. *Acc Chem Res* 2012, **45**(5)**:** 723-733.

9. Zhang W, Saliba M, Moore DT, Pathak SK, Hörantner MT, Stergiopoulos T*, et al.* Ultrasmooth organic–inorganic perovskite thin-film formation and crystallization for efficient planar heterojunction solar cells. *Nat Commun* 2015, **6:** 1- 10.

10. Stranks SD, Eperon GE, Grancini G, Menelaou C, Alcocer MJP, Leijtens T*, et al.* Electron-Hole Diffusion Lengths Exceeding 1 Micrometer in an Organometal Trihalide Perovskite Absorber. *Science* 2013, **342**(6156)**:** 341-344.

11. Burschka J, Pellet N, Moon S-J, Humphry-Baker R, Gao P, Nazeeruddin MK*, et al.* Sequential deposition as a route to high-performance perovskite-sensitized solar cells. *Nature* 2013, **499**(7458)**:** 316-319.

12. Gratzel M. The light and shade of perovskite solar cells. *Nat Mater* 2014, **13**(9)**:** 838-842.

13. Gong J, Darling SB, You F. Perovskite photovoltaics: life-cycle assessment of energy and environmental impacts. *Energy Environ Sci* 2015, **8**(7)**:** 1953-1968.

14. Ibn-Mohammed T, Koh SCL, Reaney IM, Acquaye A, Wang D, Taylor S*, et al.* Integrated hybrid life cycle assessment and supply chain environmental profile evaluations of lead-based (lead zirconate titanate) versus lead-free (potassium sodium niobate) piezoelectric ceramics. *Energy Environ Sci* 2016, **9**(11)**:** 3495-3520.

15. Hauck M, Ligthart T, Schaap M, Boukris E, Brouwer D. Environmental benefits of reduced electricity use exceed impacts from lead use for perovskite based tandem solar cell. *Renewable Energy* 2017, **111:** 906-913.

16. Tan H, Jain A, Voznyy O, Lan X, García de Arquer FP, Fan JZ*, et al.* Efficient and stable solution-processed planar perovskite solar cells via contact passivation. *Science* 2017, **355**(6326)**:** 722-726.

17. Bella F, Griffini G, Correa-Baena J-P, Saracco G, Grätzel M, Hagfeldt A*, et al.* Improving efficiency and stability of perovskite solar cells with photocurable fluoropolymers. *Science* 2016, **354**(6309)**:** 203-206.

18. Kojima A, Teshima K, Shirai Y, Miyasaka T. Organometal halide perovskites as visible-light sensitizers for photovoltaic cells. *J Am Chem Soc* 2009, **131**(17)**:** 6050-6051.

19. NREL. Best Research-Cell Efficiencies. *https://wwwnrelgov/pv/assets/images/efficiency-chartpng*.

20. Hutter EM, Gelvez-Rueda MC, Osherov A, Bulovic V, Grozema FC, Stranks SD*, et al.* Direct-indirect character of the bandgap in methylammonium lead iodide perovskite. *Nat Mater* 2017, **16**(1)**:** 115-120.

21. Long M, Zhang T, Xu W, Zeng X, Xie F, Li Q*, et al.* Perovskite Solar Cells: Large-Grain Formamidinium PbI3–xBrx for High-Performance Perovskite

Solar Cells via Intermediate Halide Exchange (Adv. Energy Mater. 12/2017). *Adv Energy Mater* 2017, **7**(12).

22. Liu M, Johnston MB, Snaith HJ. Efficient planar heterojunction perovskite solar cells by vapour deposition. *Nature* 2013, **501**(7467)**:** 395-398.

23. Hao F, Stoumpos CC, Cao DH, Chang RPH, Kanatzidis MG. Lead-free solid-state organic-inorganic halide perovskite solar cells. *Nat Photon* 2014, **8**(6)**:** 489-494.

24. Xi J, Wu Z, Jiao B, Dong H, Ran C, Piao C*, et al.* Multichannel Interdiffusion Driven FASnI3 Film Formation Using Aqueous Hybrid Salt/Polymer Solutions toward Flexible Lead-Free Perovskite Solar Cells. *Adv Mater* 2017**:** 1606964-n/a.

25. Song T-B, Yokoyama T, Aramaki S, Kanatzidis MG. Performance Enhancement of Lead-Free Tin-Based Perovskite Solar Cells with Reducing Atmosphere-Assisted Dispersible Additive. *ACS Energy Letters* 2017, **2**(4)**:** 897-903.

26. Zhao J, Brinkmann KO, Hu T, Pourdavoud N, Becker T, Gahlmann T*, et al.* Self-Encapsulating Thermostable and Air-Resilient Semitransparent Perovskite Solar Cells. *Adv Energy Mater* 2017**:** 1602599.

27. Cho KT, Paek S, Grancini G, Roldan-Carmona C, Gao P, Lee Y*, et al.* Highly efficient perovskite solar cells with a compositionally engineered perovskite/hole transporting material interface. *Energy Environ Sci* 2017, **10**(2)**:** 621-627.

28. Mejía Escobar MA, Pathak S, Liu J, Snaith HJ, Jaramillo F. ZrO2/TiO2 Electron Collection Layer for Efficient Meso-Superstructured Hybrid Perovskite Solar Cells. *ACS Appl Mater Inter* 2017, **9**(3)**:** 2342-2349.

29. Lin Q, Jiang W, Zhang S, Nagiri RCR, Jin H, Burn PL*, et al.* A Triarylamine-Based Anode Modifier for Efficient Organohalide Perovskite Solar Cells. *ACS Appl Mater Inter* 2017, **9**(10)**:** 9096-9101.

30. Marin-Beloqui JM, Lanzetta L, Palomares E. Decreasing Charge Losses in Perovskite Solar Cells Through mp-TiO2/MAPI Interface Engineering. *Chem Mater* 2016, **28**(1)**:** 207-213.

31. Bao X, Wang J, Li Y, Zhu D, Wu Y, Guo P, *et al.* Interface Engineering of a Compatible PEDOT Derivative Bilayer for High-Performance Inverted Perovskite Solar Cells. *Adv Mater Interfaces* 2017**:** 1600948-n/a.

32. Bulliard X, Ihn S-G, Yun S, Kim Y, Choi D, Choi J-Y*, et al.* Enhanced Performance in Polymer Solar Cells by Surface Energy Control. *Adv Funct Mater* 2010, **20**(24)**:** 4381-4387.

33. Zhou H, Chen Q, Li G, Luo S, Song T-b, Duan H-S*, et al.* Interface engineering of highly efficient perovskite solar cells. *Science* 2014, **345**(6196)**:** 542-546.

34. Kim JS, Park JH, Lee JH, Jo J, Kim D-Y, Cho K. Control of the electrode work function and active layer morphology via surface modification of indium tin oxide for high efficiency organic photovoltaics. *Appl Phys Lett* 2007, **91**(11)**:** 112111.

35. Su P-Y, Huang L-B, Liu J-M, Chen Y-F, Xiao L-M, Kuang D-B*, et al.* A multifunctional poly-N-vinylcarbazole interlayer in perovskite solar cells for high stability and efficiency: a test with new triazatruxene-based hole transporting materials. *J Mater Chem A* 2017, **5**(5)**:** 1913-1918.

36. Miyasaka T, Chaudhary B, Kulkarni A, Jena AK, Ikegami M, Udagawa Y*, et al.* Poly(4-vinylpyridine)-based Interfacial Passivation to Enhance Voltage and

Moisture Stability of Lead Halide Perovskite Solar Cells. *ChemSusChem* 2017**:** n/a-n/a.

37. Yu JC, Kim DB, Baek G, Lee BR, Jung ED, Lee S*, et al.* High-Performance Planar Perovskite Optoelectronic Devices: A Morphological and Interfacial Control by Polar Solvent Treatment. *Adv Mater* 2015, **27**(23)**:** 3492-3500.

38. Liu L, Mei A, Liu T, Jiang P, Sheng Y, Zhang L*, et al.* Fully Printable Mesoscopic Perovskite Solar Cells with Organic Silane Self-Assembled Monolayer. *J Am Chem Soc* 2015, **137**(5)**:** 1790-1793.

39. Sun K, Zhao B, Murugesan V, Kumar A, Zeng K, Subbiah J*, et al.* High-performance polymer solar cells with a conjugated zwitterion by solution processing or thermal deposition as the electron-collection interlayer. *J Mater Chem* 2012, **22**(45)**:** 24155-24165.

40. Kim B-S, Kim T-M, Choi M-S, Shim H-S, Kim J-J. Fully vacuum–processed perovskite solar cells with high open circuit voltage using MoO3/NPB as hole extraction layers. *Org Electron* 2015, **17:** 102-106.

41. Jeng J-Y, Chen K-C, Chiang T-Y, Lin P-Y, Tsai T-D, Chang Y-C*, et al.* Nickel Oxide Electrode Interlayer in CH3NH3PbI3 Perovskite/PCBM Planar-Heterojunction Hybrid Solar Cells. *Adv Mater* 2014, **26**(24)**:** 4107-4113.

42. Peng H, Sun W, Li Y, Ye S, Rao H, Yan W*, et al.* Solution processed inorganic V2O x as interfacial function materials for inverted planar-heterojunction perovskite solar cells with enhanced efficiency. *Nano Res* 2016, **9**(10)**:** 1-12.

43. Docampo P, Ball JM, Darwich M, Eperon GE, Snaith HJ. Efficient organometal trihalide perovskite planar-heterojunction solar cells on flexible polymer substrates. *Nat Commun* 2013, **4**.

44. Xue Q, Hu Z, Liu J, Lin J, Sun C, Chen Z*, et al.* Highly efficient fullerene/perovskite planar heterojunction solar cells via cathode modification with an amino-functionalized polymer interlayer. *J Mater Chem A* 2014, **2**(46)**:** 19598-19603.

45. Liu Y, Page ZA, Russell TP, Emrick T. Finely Tuned Polymer Interlayers Enhance Solar Cell Efficiency. *Angew Chem Int Ed* 2015, **54**(39)**:** 11485–11489.

46. Murray IP, Lou SJ, Cote LJ, Loser S, Kadleck CJ, Xu T*, et al.* Graphene Oxide Interlayers for Robust, High-Efficiency Organic Photovoltaics. *J Phys Chem Lett* 2011, **2**(24)**:** 3006-3012.

47. Yeo J-S, Kang R, Lee S, Jeon Y-J, Myoung N, Lee C-L*, et al.* Highly efficient and stable planar perovskite solar cells with reduced graphene oxide nanosheets as electrode interlayer. *Nano Energy* 2015, **12:** 96-104.

48. Wang JT-W, Ball JM, Barea EM, Abate A, Alexander-Webber JA, Huang J*, et al.* Low-Temperature Processed Electron Collection Layers of Graphene/TiO2 Nanocomposites in Thin Film Perovskite Solar Cells. *Nano Lett* 2014, **14**(2)**:** 724-730.

49. Zheng Y, Giordano AJ, Shallcross RC, Fleming SR, Barlow S, Armstrong NR*, et al.* Surface Modification of Indium–Tin Oxide with Functionalized Perylene Diimides: Characterization of Orientation, Electron-Transfer Kinetics and Electronic Structure. *J Phys Chem C* 2016, **120**(36)**:** 20040-20048.

50. Zhang H, xue l, han j, Fu YQ, Shen Y, Zhang Z-G*, et al.* New Generation Perovskite Solar Cells with Solution-Processed Amino-substituted Perylene Diimide Derivative as Electron-Transport Layer. *J Mater Chem A* 2016, **4**(22)**:** 8724-8733.

51. Li M, Lv J, Wang L, Liu J, Yu X, Xing R, *et al.* An alcohol-soluble perylene diimide derivative as cathode interfacial layer for PDI-based nonfullerene organic solar cells. *Colloids Surf Physicochem Eng Aspects* 2015, **469:** 326-332.

52. Li B, Chen Y, Liang Z, Gao D, Huang W. Interfacial engineering by using self-assembled monolayer in mesoporous perovskite solar cell. *RSC adv* 2015, **5**(114)**:** 94290-94295.

53. Choi H, Kim H-B, Ko S-J, Kim JY, Heeger AJ. An Organic Surface Modifier to Produce a High Work Function Transparent Electrode for High Performance Polymer Solar Cells. *Adv Mater* 2015, **27**(5)**:** 892-896.

54. Zhang J, Hu Z, Huang L, Yue G, Liu J, Lu X, *et al.* Bifunctional alkyl chain barriers for efficient perovskite solar cells. *Chem Commun* 2015, **51**(32)**:** 7047-7050.

55. Liu Y, Zhang W, Xie G, Zeng X, Fang J, Yang C. Triazine-core-containing star-shaped compounds as cathode interlayers for efficient inverted polymer solar cells. *J Mater Chem C* 2016, **4**(47)**:** 11278-11283.

56. Yin W-J, Shi T, Yan Y. Unusual defect physics in CH3NH3PbI3 perovskite solar cell absorber. *Appl Phys Lett* 2014, **104**(6)**:** 063903.

57. Ball JM, Lee MM, Hey A, Snaith HJ. Low-temperature processed meso-superstructured to thin-film perovskite solar cells. *Energy Environ Sci* 2013, **6**(6)**:** 1739-1743.

58. Colella S, Mosconi E, Fedeli P, Listorti A, Gazza F, Orlandi F, *et al.* MAPbI3-xClx Mixed Halide Perovskite for Hybrid Solar Cells: The Role of Chloride as Dopant on the Transport and Structural Properties. *Chem Mater* 2013, **25**(22)**:** 4613-4618.

59. Eperon GE, Burlakov VM, Docampo P, Goriely A, Snaith HJ. Morphological Control for High Performance, Solution-Processed Planar Heterojunction Perovskite Solar Cells. *Adv Funct Mater* 2014, **24**(1)**:** 151-157.

60. Jeon NJ, Noh JH, Kim YC, Yang WS, Ryu S, Seok SI. Solvent engineering for high-performance inorganic–organic hybrid perovskite solar cells. *Nat Mater* 2014, **13**(9)**:** 897-903.

61. Zuo L, Gu Z, Ye T, Fu W, Wu G, Li H*, et al.* Enhanced photovoltaic performance of CH3NH3PbI3 perovskite solar cells through interfacial engineering using self-assembling monolayer. *J Am Chem Soc* 2015, **137** (7)**:** 2674–2679.

62. Yang G, Wang C, Lei H, Zheng X, Qin P, Xiong L*, et al.* Interface engineering in planar perovskite solar cells: energy level alignment, perovskite morphology control and high performance achievement. *J Mater Chem A* 2017, **5**(4)**:** 1658-1666.

63. Zhang Z-G, Qi B, Jin Z, Chi D, Qi Z, Li Y*, et al.* Perylene diimides: a thickness-insensitive cathode interlayer for high performance polymer solar cells. *Energy Environ Sci* 2014, **7**(6)**:** 1966-1973.

64. Yip H-L, Hau SK, Baek NS, Ma H, Jen AKY. Polymer Solar Cells That Use Self-Assembled-Monolayer- Modified ZnO/Metals as Cathodes. *Adv Mater* 2008, **20**(12)**:** 2376-2382.

65. Min J, Zhang Z-G, Hou Y, Ramirez Quiroz CO, Przybilla T, Bronnbauer C*, et al.* Interface Engineering of Perovskite Hybrid Solar Cells with Solution-Processed Perylene–Diimide Heterojunctions toward High Performance. *Chem Mater* 2014, **27**(1)**:** 227-234.

66. Zhao X, Xu C, Wang H, Chen F, Zhang W, Zhao Z*, et al.* Application of Biuret, Dicyandiamide, or Urea as a Cathode Buffer Layer toward the Efficiency Enhancement of Polymer Solar Cells. *ACS Appl Mater Inter* 2014, **6**(6)**:** 4329-4337.

67. Noel NK, Abate A, Stranks SD, Parrott ES, Burlakov VM, Goriely A*, et al.* Enhanced Photoluminescence and Solar Cell Performance via Lewis Base Passivation of Organic–Inorganic Lead Halide Perovskites. *ACS Nano* 2014, **8**(10)**:** 9815-9821.

68. Shao Y, Xiao Z, Bi C, Yuan Y, Huang J. Origin and elimination of photocurrent hysteresis by fullerene passivation in CH3NH3PbI3 planar heterojunction solar cells. *Nat Commun* 2014, **5:** 1- 7.

69. Hau SK, Yip H-L, Acton O, Baek NS, Ma H, Jen AKY. Interfacial modification to improve inverted polymer solar cells. *J Mater Chem* 2008, **18**(42)**:** 5113-5119.

70. Venkatesan S, Ngo E, Khatiwada D, Zhang C, Qiao Q. Enhanced Lifetime of Polymer Solar Cells by Surface Passivation of Metal Oxide Buffer Layers. *ACS Appl Mater Inter* 2015, **7**(29)**:** 16093-16100.

71. Hsieh H-H, Sung Y-M, Hsu F-C, Hsiao K-J, Lee Y-J, Chen Y-F. Giant enhancement of inverted polymer solar cells efficiency by manipulating dual interlayers with integrated approaches. *RSC adv* 2015, **5**(2)**:** 1549-1556.

72. Xie FX, Su H, Mao J, Wong KS, Choy WCH. Evolution of Diffusion Length and Trap State Induced by Chloride in Perovskite Solar Cell. *J Phys Chem C* 2016, **120**(38)**:** 21248-21253.

73. Leijtens T, Eperon GE, Barker AJ, Grancini G, Zhang W, Ball JM*, et al.* Carrier trapping and recombination: the role of defect physics in enhancing the open circuit voltage of metal halide perovskite solar cells. *Energy Environ Sci* 2016, **9**(11)**:** 3472-3481.

74. Polydorou E, Zeniou A, Tsikritzis D, Soultati A, Sakellis I, Gardelis S*, et al.* Surface passivation effect by fluorine plasma treatment on ZnO for efficiency and lifetime improvement of inverted polymer solar cells. *J Mater Chem A* 2016, **4**(30)**:** 11844-11858.

75. Lin Y, Shen L, Dai J, Deng Y, Wu Y, Bai Y*, et al.* π-Conjugated Lewis Base: Efficient Trap-Passivation and Charge-Extraction for Hybrid Perovskite Solar Cells. *Adv Mater* 2017, **29**(7)**:** 1604545-n/a.

76. Chiu J-M, Chu C-C, Zena DM, Tai Y. Simultaneous enhancement of photocurrent and open circuit voltage in a ZnO based organic solar cell by mixed self-assembled monolayers. *Applied Energy* 2015, **160:** 681-686.

77. Abate A, Saliba M, Hollman DJ, Stranks SD, Wojciechowski K, Avolio R*, et al.* Supramolecular Halogen Bond Passivation of Organic–Inorganic Halide Perovskite Solar Cells. *Nano Lett* 2014, **14**(6)**:** 3247-3254.

78. Li X, Dar MI, Yi C, Luo J, Tschumi M, Zakeeruddin SM*, et al.* Improved performance and stability of perovskite solar cells by crystal crosslinking with alkylphosphonic acid omega-ammonium chlorides. *Nat Chem* 2015, **7**(9)**:** 703-711.

79. Kaltenbrunner M, Adam G, Glowacki ED, Drack M, Schwodiauer R, Leonat L*, et al.* Flexible high power-per-weight perovskite solar cells with chromium oxide-metal contacts for improved stability in air. *Nat Mater* 2015, **14**(10)**:** 1032-1039.

80. Yang S, Wang Y, Liu P, Cheng Y-B, Zhao HJ, Yang HG. Functionalization of perovskite thin films with moisture-tolerant molecules. *Nat Energy* 2016, **1:** 15016.

81. Leijtens T, Eperon GE, Noel NK, Habisreutinger SN, Petrozza A, Snaith HJ. Stability of Metal Halide Perovskite Solar Cells. *Adv Energy Mater* 2015, **5**(20)**:** 1500963.

82. Wang D, Wright M, Elumalai NK, Uddin A. Stability of perovskite solar cells. *Sol Energy Mater Sol Cells* 2016, **147:** 255-275.

83. Bryant D, Aristidou N, Pont S, Sanchez-Molina I, Chotchunangatchaval T, Wheeler S*, et al.* Light and oxygen induced degradation limits the operational stability of methylammonium lead triiodide perovskite solar cells. *Energy Environ Sci* 2016, **9**(5)**:** 1655-1660.

84. Sin DH, Jo SB, Lee SG, Ko H, Kim M, Lee H*, et al.* Enhancing the Durability and Carrier Selectivity of Perovskite Solar Cells Using a Blend Interlayer. *ACS Appl Mater Inter* 2017, **9**(21)**:** 18103-18112.

85. Saliba M, Matsui T, Seo J-Y, Domanski K, Correa-Baena J-P, Nazeeruddin MK*, et al.* Cesium-containing triple cation perovskite solar cells: improved stability, reproducibility and high efficiency. *Energy Environ Sci* 2016, **9**(6)**:** 1989-1997.

86. Wang Z, McMeekin DP, Sakai N, van Reenen S, Wojciechowski K, Patel JB*, et al.* Efficient and Air-Stable Mixed-Cation Lead Mixed-Halide Perovskite Solar Cells with n-Doped Organic Electron Extraction Layers. *Adv Mater* 2017, **29**(5)**:** 1604186-n/a.

87. Tsai H, Nie W, Blancon J-C, Stoumpos CC, Asadpour R, Harutyunyan B*, et al.* High-efficiency two-dimensional Ruddlesden–Popper perovskite solar cells. *Nature* 2016, **536**(7616)**:** 312-316.

88. Smith IC, Hoke ET, Solis-Ibarra D, McGehee MD, Karunadasa HI. A Layered Hybrid Perovskite Solar-Cell Absorber with Enhanced Moisture Stability. *Angew Chem* 2014, **126**(42)**:** 11414-11417.

89. Grancini G, Roldán-Carmona C, Zimmermann I, Mosconi E, Lee X, Martineau D*, et al.* One-Year stable perovskite solar cells by 2D/3D interface engineering. *Nat Commun* 2017, **8:** 15684.

90. Bush KA, Palmstrom AF, Yu ZJ, Boccard M, Cheacharoen R, Mailoa JP*, et al.* 23.6%-efficient monolithic perovskite/silicon tandem solar cells with improved stability. *Nat Energy* 2017, **2:** 17009.

91. Brinkmann KO, Zhao J, Pourdavoud N, Becker T, Hu T, Olthof S*, et al.* Suppressed decomposition of organometal halide perovskites by impermeable electron-extraction layers in inverted solar cells. *Nat Commun* 2017, **8:** 13938.

92. Kaltenbrunner M, Adam G, Glowacki ED, Drack M, Schwodiauer R, Leonat L*, et al.* Flexible high power-per-weight perovskite solar cells with chromium oxide-metal contacts for improved stability in air. *Nat Mater* 2015, **14**(10)**:** 1032-1039.

93. Chen W, Wu Y, Yue Y, Liu J, Zhang W, Yang X*, et al.* Efficient and stable large-area perovskite solar cells with inorganic charge extraction layers. *Science* 2015, **350**(6263)**:** 944-948.

94. Yan W, Li Y, Li Y, Ye S, Liu Z, Wang S*, et al.* Stable high-performance hybrid perovskite solar cells with ultrathin polythiophene as hole-transporting layer. *Nano Res* 2015, **8**(8)**:** 2474-2480.

95. Zheng L, Chung YH, Ma Y, Zhang L, Xiao L, Chen Z*, et al.* A hydrophobic hole transporting oligothiophene for planar perovskite solar cells with improved stability. *Chem Commun (Camb)* 2014, **50**(76)**:** 11196-11199.

96. Ciro J, Mesa S, Uribe JI, Mejia-Escobar MA, Ramirez D, Montoya JF*, et al.* Optimization of the Ag/PCBM interface by a rhodamine interlayer to enhance the efficiency and stability of perovskite solar cells. *Nanoscale* 2017.

97. Zhu Z, Chueh C-C, Lin F, Jen AKY. Enhanced Ambient Stability of Efficient Perovskite Solar Cells by Employing a Modified Fullerene Cathode Interlayer. *Advanced Science* 2016, **3**(9)**:** 1600027-n/a.

98. Zhang M, Wang J, Li L, Zheng G, Liu K, Qin M*, et al.* High-Mobility p-Type Organic Semiconducting Interlayer Enhancing Efficiency and Stability of Perovskite Solar Cells. *Advanced Science* 2017**:** 1700025-n/a.

99. Li Y, Zhao Y, Chen Q, Yang Y, Liu Y, Hong Z*, et al.* Multifunctional Fullerene Derivative for Interface Engineering in Perovskite Solar Cells. *J Am Chem Soc* 2015, **137**(49)**:** 15540-15547.

100. Li B, Zheng C, Liu H, Zhu J, Zhang H, Gao D*, et al.* Large Planar π-Conjugated Porphyrin for Interfacial Engineering in p-i-n Perovskite Solar Cells. *ACS Appl Mater Inter* 2016, **8**(41)**:** 27438-27443.

101. !!! INVALID CITATION !!!

102. Ogomi Y, Morita A, Tsukamoto S, Saitho T, Shen Q, Toyoda T*, et al.* All-Solid Perovskite Solar Cells with HOCO-R-NH3+I– Anchor-Group Inserted between Porous Titania and Perovskite. *J Phys Chem C* 2014, **118**(30)**:** 16651-16659.

103. Zhu LF, Xu YZ, Shi JJ, Zhang HY, Xu X, Zhao YH*, et al.* Efficient perovskite solar cells via simple interfacial modification toward a mesoporous TiO2 electron transportation layer. *RSC adv* 2016, **6**(85)**:** 82282-82288.

104. Şahin Y, Alem S, de Bettignies R, Nunzi J-M. Development of air stable polymer solar cells using an inverted gold on top anode structure. *Thin Solid Films* 2005, **476**(2)**:** 340-343.

105. Wang Z-K, Gong X, Li M, Hu Y, Wang J-M, Ma H*, et al.* Induced Crystallization of Perovskites by a Perylene Underlayer for High-Performance Solar Cells. *ACS Nano* 2016, **10**(5)**:** 5479-5489.

106. Kim G-H, García de Arquer FP, Yoon YJ, Lan X, Liu M, Voznyy O*, et al.* High-Efficiency Colloidal Quantum Dot Photovoltaics via Robust Self-Assembled Monolayers. *Nano Lett* 2015, **15**(11)**:** 7691-7696.

107. Liu S, Zhang G, Lu J, Jia J, Li W, Huang F*, et al.* An alcohol soluble amino-functionalized organoplatinum(ii) complex as the cathode interlayer for highly efficient polymer solar cells. *J Mater Chem C* 2015, **3**(17)**:** 4372-4379.

108. Lin Z, Chang J, Xiao J, Zhu H, Xu Q-H, Zhang C*, et al.* Interface studies of the planar heterojunction perovskite solar cells. *Sol Energy Mater Sol Cells* 2016, **157:** 783-790.

109. Valles-Pelarda M, Hames BC, García-Benito I, Almora O, Molina-Ontoria A, Sánchez RS*, et al.* Analysis of the Hysteresis Behavior of Perovskite Solar

Cells with Interfacial Fullerene Self-Assembled Monolayers. *J Phys Chem Lett* 2016, **7**(22)**:** 4622-4628.

110. Cao T, Wang Z, Xia Y, Song B, Zhou Y, Chen N*, et al.* Facilitating Electron Transportation in Perovskite Solar Cells via Water-Soluble Fullerenol Interlayers. *ACS Appl Mater Inter* 2016, **8**(28)**:** 18284-18291.

111. Shih Y-C, Lan Y-B, Li C-S, Hsieh H-C, Wang L, Wu C-I*, et al.* Amino-Acid-Induced Preferential Orientation of Perovskite Crystals for Enhancing Interfacial Charge Transfer and Photovoltaic Performance. *Small* 2017**:** 1604305-n/a.

112. Sun W, Li Y, Xiao Y, Zhao Z, Ye S, Rao H*, et al.* An ammonia modified PEDOT: PSS for interfacial engineering in inverted planar perovskite solar cells. *Org Electron* 2017, **46:** 22-27.

113. Unsworth NK, Hancox I, Argent Dearden C, Sullivan P, Walker M, Lilley RS*, et al.* Comparison of dimethyl sulfoxide treated highly conductive poly(3,4-ethylenedioxythiophene):poly(styrenesulfonate) electrodes for use in indium tin oxide-free organic electronic photovoltaic devices. *Org Electron* 2014, **15**(10)**:** 2624-2631.

114. Li X, Zhang W, Wang X, Wu Y, Gao F, Fang J. Critical role of the external bias in improving the performance of polymer solar cells with a small molecule electrolyte interlayer. *J Mater Chem A* 2015, **3**(2)**:** 504-508.

115. Dong Y, Li W, Zhang X, Xu Q, Liu Q, Li C*, et al.* Highly Efficient Planar Perovskite Solar Cells Via Interfacial Modification with Fullerene Derivatives. *Small* 2016, **12**(8)**:** 1098-1104.

116. Zuo L, Chen Q, De Marco N, Hsieh Y-T, Chen H, Sun P*, et al.* Tailoring the Interfacial Chemical Interaction for High-Efficiency Perovskite Solar Cells. *Nano Lett* 2017, **17**(1)**:** 269-275.

117. Goh C, Scully SR, McGehee MD. Effects of molecular interface modification in hybrid organic-inorganic photovoltaic cells. *J Appl Phys* 2007, **101**(11)**:** 114503.

118. Shao S, Liu F, Fang G, Zhang B, Xie Z, Wang L. Enhanced performances of hybrid polymer solar cells with p-methoxybenzoic acid modified zinc oxide nanoparticles as an electron acceptor. *Org Electron* 2011, **12**(4)**:** 641-647.

119. Zhang WJ, Min C, Zhang Q, Li XD, Fang JF. Zwitterionic ammonium and neutral amino molecules as cathode interlayer for inverted polymer solar cells. *Org Electron* 2014, **15**(12)**:** 3632-3638.

120. Wang Z, Li Z, Xu X, Li Y, Li K, Peng Q. Polymer Solar Cells Exceeding 10% Efficiency Enabled via a Facile Star-Shaped Molecular Cathode Interlayer with Variable Counterions. *Adv Funct Mater* 2016, **26**(26)**:** 4643-4652.

121. Shih YC, Wang LY, Hsieh HC, Lin KF. Enhancing the photocurrent of perovskite solar cells via modification of the TiO2/CH3NH3PbI3 heterojunction interface with amino acid. *J Mater Chem A* 2015, **3**(17)**:** 9133-9136.

122. Zhang Q, Zhang D, Li X, Liu X, Zhang W, Han L*, et al.* Neutral amine based alcohol-soluble interface materials for inverted polymer solar cells: realizing high performance and overcoming solvent erosion. *Chem Commun* 2015, **51**(50)**:** 10182-10185.

123. Wang X, Qi B, Li H, Qi Z, Wang J. Improvement of organic solar cells with ammonium salt, tetrabutylammonium tetraphenylborate, as cathode buffer layer. *Synth Met* 2014, **191:** 36-40.

124. Fu P, Guo X, Wang S, Ye Y, Li C. Aminosilane as a Molecular Linker between the Electron-Transport Layer and Active Layer for Efficient Inverted Polymer Solar Cells. *ACS Appl Mater Inter* 2017, **9**(15)**:** 13390-13395.

125. Meroni D, Lo Presti L, Di Liberto G, Ceotto M, Acres RG, Prince KC*, et al.* A Close Look at the Structure of the TiO2-APTES Interface in Hybrid Nanomaterials and Its Degradation Pathway: An Experimental and Theoretical Study. *J Phys Chem C* 2017, **121**(1)**:** 430-440.

126. Song CK, Luck KA, Zhou N, Zeng L, Heitzer HM, Manley EF*, et al.* "Supersaturated" Self-Assembled Charge-Selective Interfacial Layers for Organic Solar Cells. *J Am Chem Soc* 2014, **136**(51)**:** 17762-17773.

127. Wang J, Xiang X, Yao X, Xiao W-J, Lin J, Li W-S. Efficient perovskite solar cells using trichlorosilanes as perovskite/PCBM interface modifiers. *Org Electron* 2016, **39:** 1-9.

128. Bai Y, Dong Q, Shao Y, Deng Y, Wang Q, Shen L*, et al.* Enhancing stability and efficiency of perovskite solar cells with crosslinkable silane-functionalized and doped fullerene. *Nat Commun* 2016, **7:** 12806.

129. Kim J, Khang D-Y, Kim J-H, Lee HH. The surface engineering of top electrode in inverted polymer bulk-heterojunction solar cells. *Appl Phys Lett* 2008, **92**(13)**:** 133307.

130. Nian L, Zhang W, Zhu N, Liu L, Xie Z, Wu H*, et al.* Photoconductive Cathode Interlayer for Highly Efficient Inverted Polymer Solar Cells. *J Am Chem Soc* 2015, **137**(22)**:** 6995-6998.

131. Hains AW, Chen H-Y, Reilly TH, Gregg BA. Cross-Linked Perylene Diimide-Based n-Type Interfacial Layer for Inverted Organic Photovoltaic Devices. *ACS Appl Mater Inter* 2011, **3**(11)**:** 4381-4387.

132. Xie Z, Würthner F. Hybrid Photoconductive Cathode Interlayer Materials Composed of Perylene Bisimide Photosensitizers and Zinc Oxide for High Performance Polymer Solar Cells. *Adv Energy Mater* 2017**:** 1602573-n/a.

133. Xie Z, Xiao B, He Z, Zhang W, Wu X, Wu H*, et al.* Self-assembled perylene bisimide J-aggregates as promising cathode modifiers for highly efficient inverted polymer solar cells. *Mater Horiz* 2015, **2**(5)**:** 514-518.

134. Sun J-P, Hendsbee AD, Dobson AJ, Welch GC, Hill IG. Perylene diimide based all small-molecule organic solar cells: Impact of branched-alkyl side chains on solubility, photophysics, self-assembly, and photovoltaic parameters. *Org Electron* 2016, **35:** 151-157.

135. Zhang W, Zhong S, Nian L, Chen Y, Xie Z, Liu L*, et al.* Perylene bisimide as the cathode modifier in organic photovoltaics: the role of aggregation morphology on the interlayer performance. *RSC adv* 2015, **5**(50)**:** 39973-39977.

136. Jia T, Han J, Zhou W, Wang L, Wu M, Chen W*, et al.* Application of a water-soluble metallophthalocyanine derivative as a cathode interlayer for the polymer solar cells. *Sol Energy Mater Sol Cells* 2015, **141:** 93-100.

137. Jia T, Zhou W, Chen Y, Han J, Wang L, Li F*, et al.* Highly efficient polymer solar cells based on a universal cathode interlayer composed of metallophthalocyanine derivative with good film-forming property. *J Mater Chem A* 2015, **3**(8)**:** 4547-4554.

138. Zeng H, Zhu X, Liang Y, Guo X. Interfacial Layer Engineering for Performance Enhancement in Polymer Solar Cells. *Polymers* 2015, **7**(2)**:** 333-372.

139. Wang H, Mativetsky JM, Ren Y, Gomez ED, Jaye C, Schwartz J*, et al.* Fluorinated and hydrogenated self-assembled monolayers (SAMs) on anodes: Effects of SAM chemistry on device characteristics of polymer solar cells. *Org Electron* 2014, **15**(11)**:** 3333-3340.

140. Hu Z, Miao J, Liu M, Yang T, Liang Y, Goto O*, et al.* Enhanced performance of inverted perovskite solar cells using solution-processed carboxylic potassium salt as cathode buffer layer. *Org Electron* 2017, **45:** 97-103.

141. Cao F-Y, Lai Y-Y, Chen Y-L, Cheng Y-J. Self-assembled tri-, tetra- and penta-ethylene glycols as easy, expedited and universal interfacial cathode-modifiers for inverted polymer solar cells. *J Mater Chem A* 2016, **4**(22)**:** 8707-8715.

142. Cao J, Yin J, Yuan S, Zhao Y, Li J, Zheng N. Thiols as interfacial modifiers to enhance the performance and stability of perovskite solar cells. *Nanoscale* 2015, **7**(21)**:** 9443-9447.

143. Chang C-Y, Chang Y-C, Huang W-K, Liao W-C, Wang H, Yeh C*, et al.* Achieving high efficiency and improved stability in large-area ITO-free perovskite solar cells with thiol-functionalized self-assembled monolayers. *J Mater Chem A* 2016, **4**(20)**:** 7903-7913.

144. Chang C-Y, Chang Y-C, Huang W-K, Lee K-T, Cho A-C, Hsu C-C. Enhanced Performance and Stability of Semitransparent Perovskite Solar Cells Using Solution-Processed Thiol-Functionalized Cationic Surfactant as Cathode Buffer Layer. *Chem Mater* 2015, **27**(20)**:** 7119-7127.

145. Zhou Y, Fuentes-Hernandez C, Shim J, Meyer J, Giordano AJ, Li H*, et al.* A Universal Method to Produce Low–Work Function Electrodes for Organic Electronics. *Science* 2012, **336**(6079)**:** 327-332.

146. Ulman A. Formation and Structure of Self-Assembled Monolayers. *Chem Rev* 1996, **96**(4)**:** 1533-1554.

147. Love JC, Estroff LA, Kriebel JK, Nuzzo RG, Whitesides GM. Self-Assembled Monolayers of Thiolates on Metals as a Form of Nanotechnology. *Chem Rev* 2005, **105**(4)**:** 1103-1170.

148. Harris AL, Rothberg L, Dubois LH, Levinos NJ, Dhar L. Molecular vibrational energy relaxation at a metal surface: Methyl thiolate on Ag(111). *Phys Rev Lett* 1990, **64**(17)**:** 2086-2089.

149. Azzaroni O, Vela ME, Fonticelli M, Benítez G, Carro P, Blum B*, et al.* Electrodesorption Potentials of Self-Assembled Alkanethiolate Monolayers on Copper Electrodes. An Experimental and Theoretical Study. *J Phys Chem B* 2003, **107**(48)**:** 13446-13454.

150. She Z, Di Falco A, Hähner G, Buck M. Electrodeposition of gold templated by patterned thiol monolayers. *Appl Surf Sci* 2016, **373:** 51-60.

151. Fontanesi C, Tassinari F, Parenti F, Cohen H, Mondal PC, Kiran V*, et al.* New One-Step Thiol Functionalization Procedure for Ni by Self-Assembled Monolayers. *Langmuir* 2015, **31**(11)**:** 3546-3552.

152. Vega A, Thissen P, Chabal YJ. Environment-Controlled Tethering by Aggregation and Growth of Phosphonic Acid Monolayers on Silicon Oxide. *Langmuir* 2012, **28**(21)**:** 8046-8051.

153. Guerra VLP, Altamura D, Trifiletti V, Colella S, Listorti A, Giannuzzi R*, et al.* Implications of TiO2 Surface Functionalization on Polycrystalline Mixed Halide Perovskite Film and Photovoltaic Devices. *J Mater Chem A* 2015, **3**(41)**:** 20811-20818.

154. Keszthelyi T, Pászti Z, Rigó T, Hakkel O, Telegdi J, Guczi L. Investigation of Solid Surfaces Modified by Langmuir–Blodgett Monolayers Using Sum-Frequency Vibrational Spectroscopy and X-ray Photoelectron Spectroscopy. *J Phys Chem B* 2006, **110**(17)**:** 8701-8714.

155. Azad I, Ram MK, Goswami DY, Stefanakos E. Fabrication and Characterization of ZnO Langmuir–Blodgett Film and Its Use in Metal–Insulator–Metal Tunnel Diode. *Langmuir* 2016, **32**(33)**:** 8307-8314.

156. Wei Y, Liu P-J, Lee R-H, Chen C-P. Thermally evaporable 5,10-dihydroindeno[2,1-a]indenes form efficient interfacial layers in organic solar cells. *RSC adv* 2015, **5**(11)**:** 7897-7904.

157. Huo L, Liu T, Sun X, Cai Y, Heeger AJ, Sun Y. Single-Junction Organic Solar Cells Based on a Novel Wide-Bandgap Polymer with Efficiency of 9.7%. *Adv Mater* 2015, **27**(18)**:** 2938-2944.

158. Huang J, Gu Z, Zuo L, Ye T, Chen H. Morphology control of planar heterojunction perovskite solar cells with fluorinated PDI films as organic electron transport layer. *Sol Energy* 2016, **133:** 331-338.

159. Qu Q, Geng H, Peng R, Cui Q, Gu X, Li F*, et al.* Chemically Binding Carboxylic Acids onto TiO2 Nanoparticles with Adjustable Coverage by Solvothermal Strategy. *Langmuir* 2010, **26**(12)**:** 9539-9546.

Chapter 2 Theory

Contents

2.1 Introduction

In this chapter, the theory behind the techniques and measurements used in this project is described.

2.2 Semiconductors and band structures

Based on their conductivity, solid materials can be classed as conductors, semiconductors and insulators. In a conductor, the conduction band and the valence band have a very small gap, and the conduction band is partially filled. Only tiny energy is needed to excite the valence electron, therefore it has high conductivity. While in a semiconductor or an insulator, the conduction band and the valence band are separated, and in an undoped wide band gap semi-conductor the concentration of free carriers at room temperature is very small. Thus the conductivity of semiconductors and insulators are lower than conductors. As shown in **Figure 2-1**, the conductivity of a semiconductor is in the range of 10^{-10} S/cm to 10^{4} S/cm, and its band gap is in the medium range with respect to an insulator and conductor. As the core part of a solar cell, semiconductors determine the optical properties of a device, and are critical to the charge generation efficiency and the output photovoltage that a device can achieve.

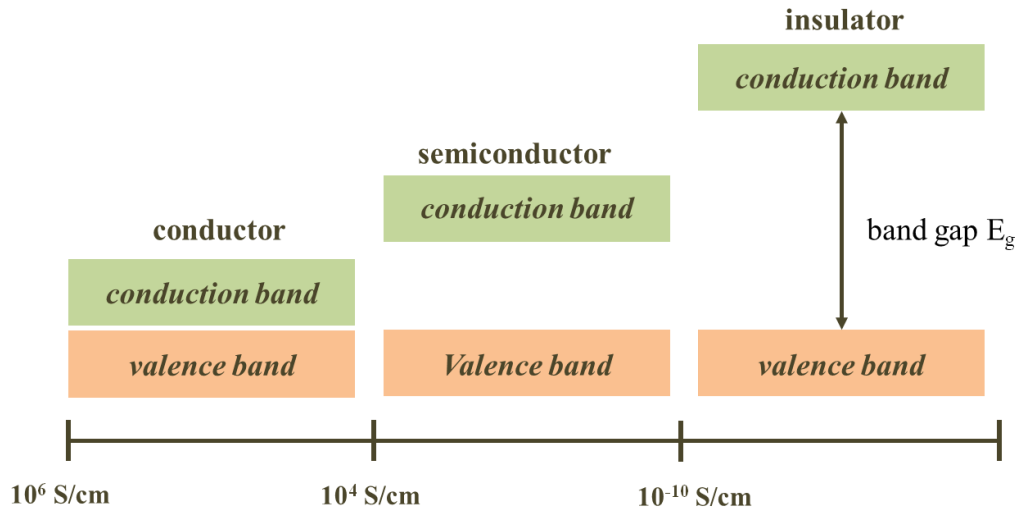

Figure 2-1 Band structures and conductivity of a conductor, semiconductor and insulator.

Depending on the majority charge carrier (electron or hole), semiconductors can be categorised as intrinsic, n-type and p-type semiconductors as demonstrated in Figure **2-2**. An intrinsic semiconductor has equal densities of electrons and holes and the Fermi

energy level (E_F) is located in the middle of the band gap, an n-type semiconductor (n type doping, i.e. introducing electron donors) has an excess of electrons with the E_F close to the conduction band and a p-type semiconductor (p type doping, i.e. introducing electron acceptors) has an excess of holes with the E_F close to the valence band. In perovskite solar cells methylammonium lead iodide ($CH_3NH_3PbI_3$) perovskite is well accepted as an intrinsic semiconductor[1], thus the junction it forms with electron transporting materials and hole transporting materials is so-called a "p-i-n" junction.

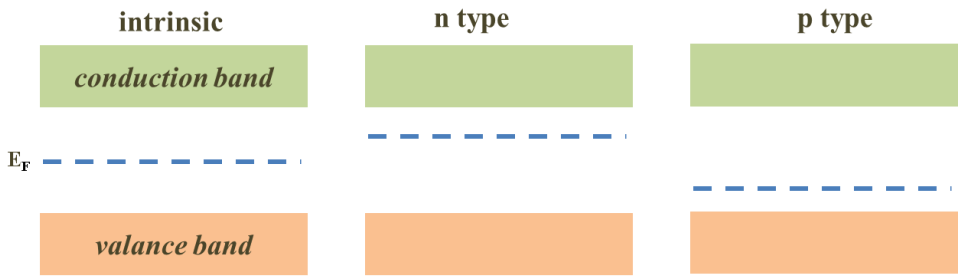

Figure 2-2 Classification of semiconductors. E_F represents Fermi energy level.

2.3 Energy alignment in a solar cell

Efficient solar cells also rely on effective charge separation and transport in addition to charge generation. It is of great importance to have appropriate energy level alignments between the different layers in a device, such as between semiconductor/semiconductor (e.g. p-n junction) and between the semiconductor/electrode (semiconductor/metal junction).

2.3.1 Energy alignment of p-n junctions and metal-semiconductor junctions

Band bending generally happens at the interface of materials with different Fermi levels. As illustrated in Figure **2-3**, where a "p-n" junction is used as an example, band bending occurs at the interface of the junction and Fermi levels are aligned. The as-established potential step caused by the alignment of Fermi levels is called the built-in potential (V_{bi}); the bending area (depletion region) is depleted of majority carriers.

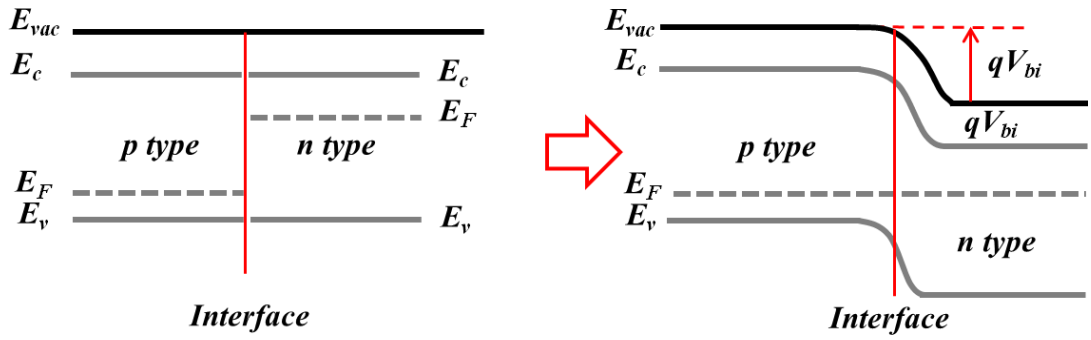

Figure 2-3 Energy alignment of a p-n junction in a solar cell at equilibrium at dark.

The energy alignment at the interface of a semiconductor and an electrode (i.e. metal) is critical for charge collection in a solar cell. If the Fermi level of a semiconductor is higher (lower work function) than a metal (i.e. mismatch of energy levels), a barrier can form at equilibrium with respect to the conduction band of the semiconductor. Figure **2-4** shows an n type semiconductor in contact with a metal. The metal has a lower Fermi level than the semiconductor. Once equilibrium is reached, an energy barrier, a so called Schottky Barrier, is generated at the interface, which acts to retard the electron flow to the metal. This mismatch in the energy levels should be avoided in order to reduce energy loss and improve the efficiency of charge collection.

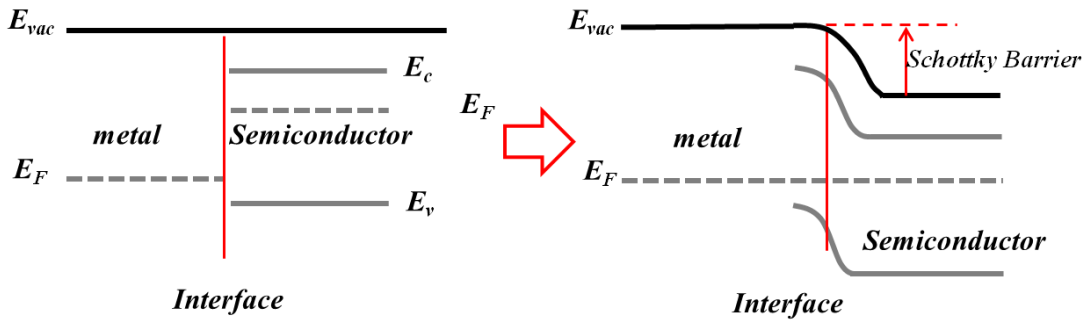

Figure 2-4 Energy alignment of a semiconductor-metal junction at dark.

2.3.2 p-i-n junction of the perovskite solar cell

The alignment of the energy levels in a p-i-n junction is demonstrated in Figure **2-5**. The built-in voltage is determined by the Fermi level differences which is the same as the p-n junction. But the electric field is uniformly extended over the thickness of the intrinsic semiconductor. Charge carriers in the intrinsic semiconductor generally show

extended lifetimes as the photogenerated carriers can be driven by the electric field and survive for a longer distance.

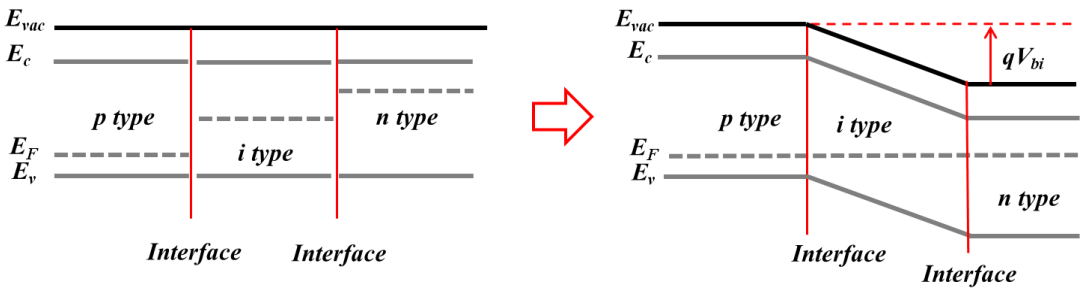

Figure 2-5 Energy alignments of p-i-n junction at dark.

2.3.3 Surface dipole and the charge collection at the metal contacts

Molecules with dipole moments are frequently used to tune the work function of modified substrates[2]. The direction of the surface dipole greatly influences the charge collecting efficiency (e.g. electron collection and hole collection). As illustrated in Figure **2-6**, for electron collection ((A), (B)and (C)), a surface dipole with the direction facing away from the metal will reduce the work function of the metal and decrease the barrier for electron collecting. In contrast, a surface dipole with the direction facing toward the metal will increase the work function of the metal and raise the barrier for electron collecting. The mechanism is the same for hole collecting. However, a surface dipole that is directed toward the metal is beneficial to hole collection Figure **2-6**(D), (E) and (F).

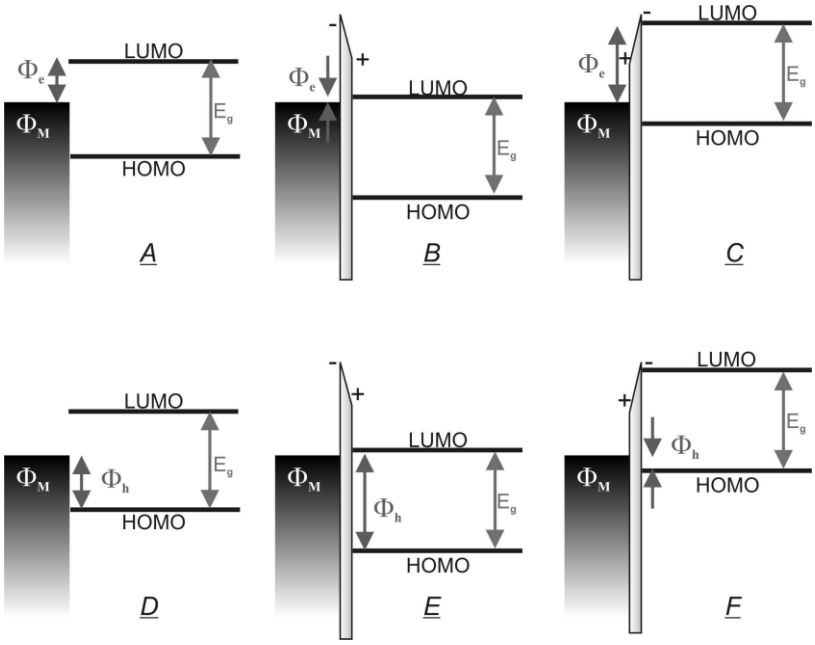

Figure 2-6 surface dipole and work function tuning in an organic solar cell. [2, 3] Φ_M is the work function of a metal contact. (A)(B)(C) demonstrate the impacts of molecular dipoles on electron collection. (D)(E)(F) demonstrate the impacts of molecular dipoles on hole collection.

2.4 Recombination and trap states in semiconductors

The photocurrent/photovoltage of a solar cell is the result of a balance between charge generation and charge recombination.[4] In a photovoltaic cell energy is needed to generate electron-hole pairs that then disappear by recombination, releasing energy. Recombination can release photons (radiative recombination), give energy to another carrier at the same time (Auger recombination) or excite lattice phonons (non-radiative recombination) Trap-mediated recombination (non-radiative recombination) occurs when the charge release (from the trap state) time is longer than the time to capture the opposite charge. e.g. when an electron relaxes from the conduction band to a trap state and a hole is then captured as well before the electron is released from the trap state The detailed processes are described in Figure **2-7**, where radiative recombination, non-radiative recombination and Auger recombination are all demonstrated.

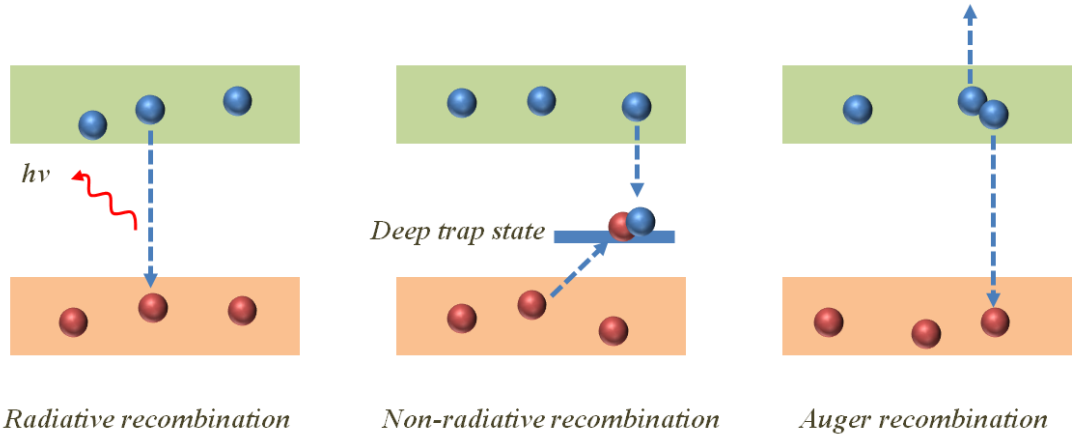

Figure 2-7 Recombinations in a solar cell

A 'trap' is a localised energy state within the band gap. Trap states are caused by impurities or defects in the crystal structure and can be classed as deep trap states and shallow trap states depending on the energy level the state is located. Charges trapped into shallow trap states can still be thermally excited. Charges which fall into deep trap states are more likely to recombine. As charge separation happens at an interface (i.e. depletion region) of a junction, the trap states can reduce the charge mobility and the recombination centres at surfaces can affect the charge collection. Decreasing the density of surface traps and recombination centres improves the PCE of perovskite solar cells[5].

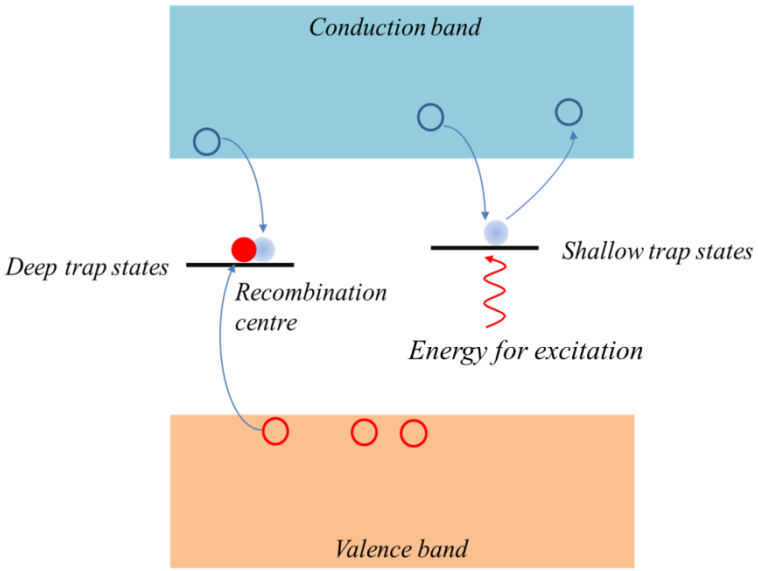

Figure 2-8 Deep and shallow trap states in a semiconductor.

2.5 Power conversion efficiency of perovskite solar cells

The power conversion efficiency (PCE) is an important parameter used to estimate the performance of a solar cell. It indicates how effectively solar energy can be converted into electricity. It can be obtained by carrying out J-V scans, where a bias is applied to the cell, as shown in **Figure 2-9**. Under certain test conditions (e.g. standard test condition: AM 1.5, 100 mW/cm^2 at a temperature of 25°C) parameters such as open circuit voltage (V_{oc}), short circuit current density (J_{sc}), and fill factor (FF) can be measured. The FF is calculated according to equation 2-1. The PCE can then be calculated by equation 2-2.

$$\mathbf{FF} = \frac{V_{max} \times J_{max}}{V_{oc} \times J_{sc}} \qquad \text{Equation 2-1}$$

$$\mathbf{PCE}(\eta, \%) = \frac{P_{\text{max output}}}{P_{input}} = \frac{V_{oc} \times J_{sc} \times FF}{P_{input}} \qquad \text{Equation 2-2}$$

Where $P_{\text{max output}}$ is the maximum power output and P_{input} is the power of incident solar energy.

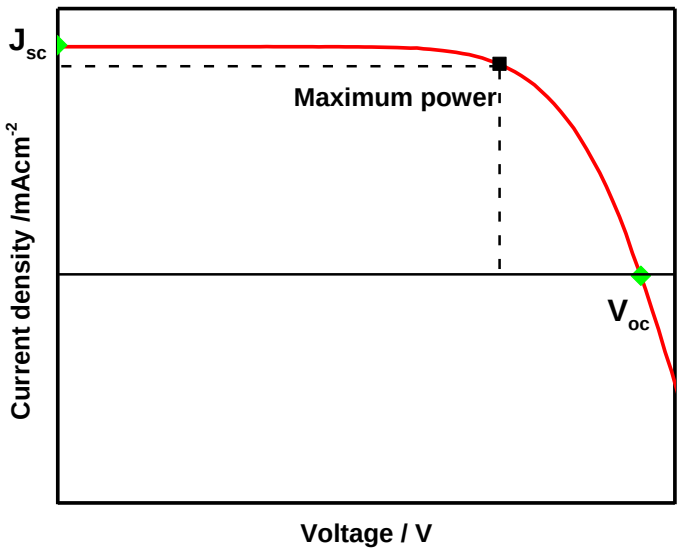

Figure 2-9 J-V curve of a solar cell under illumination.

Due to the diode character of a solar cell in the dark, the J-V curve under illumination is an overlap of the dark current and the light-generated current. As illustrated in Figure **2-10**, the J-V curve for a solar cell in the dark shows typical diode characteristics (Figure **2-10** (a)), and the direction of the dark current is opposite to the light generated

current which is also demonstrated in an equivalent circuit (Figure **2-10**(b)). The output current can be illustrated as equation 2-3

$$\boldsymbol{I = I_L - I_0[\exp\left(\frac{qV}{nkT}\right)]} \qquad \text{Equation 2-3}$$

Where I_L is the light generated current, I_0 is saturated dark current, I is the output current of a device and n is the ideality factor.

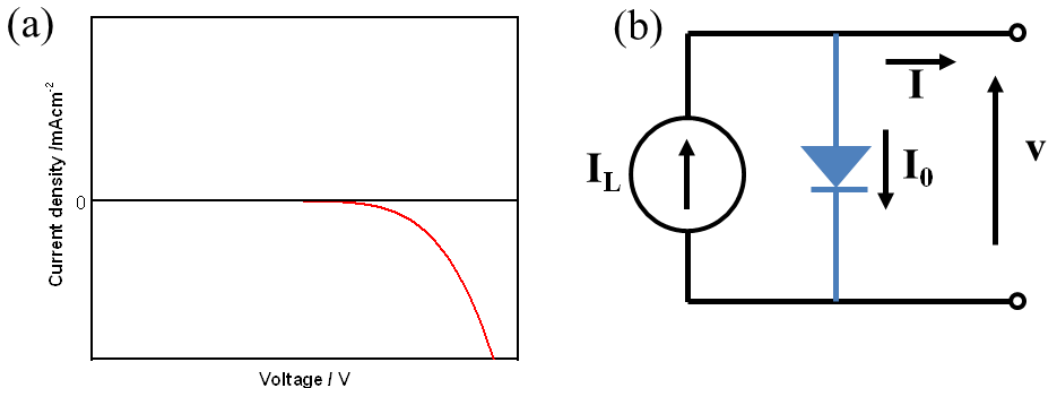

Figure 2-10 J-V curve of a solar cell at dark and equivalent circuit of a solar cell.

2.6 Cyclic voltammetry and HOMO/LUMO energy levels of organic molecules

Cyclic voltammetry is a frequently used electrochemical technique to study both the kinetics and thermodynamics of chemical systems.[6] A triangular waveform is applied (shown in Figure **2-11**(a)), and the current response is recorded as a function of potential, as demonstrated in Figure **2-11**(b).

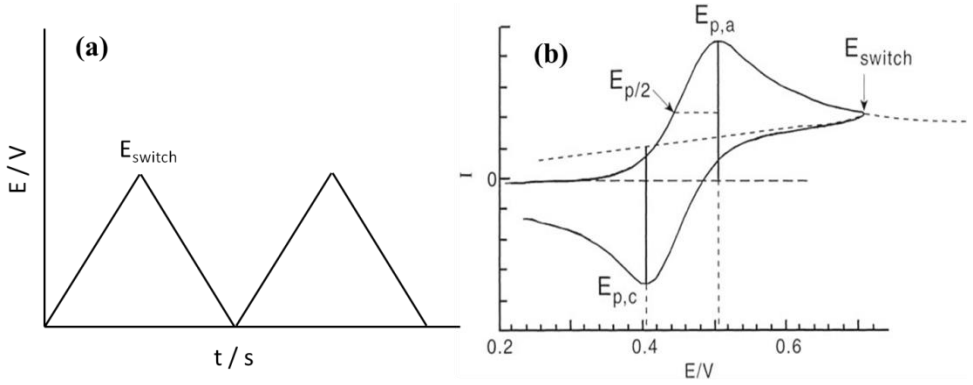

Figure 2-11 Cyclic voltammetry technic.(a) Applied voltage signal over time, (b) Plot of current-voltage response.[6] $E_{p,c}$ is redox peak current potential, $E_{p,a}$ is oxidation peak current potential, $E_{p/2}$ is half peak current potential and E_{switch} is the potential where the scan direction changes.

The reduction peak occurs when the species in solution or on the surface is reduced. As illustrated in Figure **2-12**, electrons transfer from the electrode into the LUMO of the molecule when the Fermi level of electrons in the metal electrode is driven to a position where an electron can relax to the LUMO of the molecule. In contrast, oxidation occurs when the Fermi level for electrons is driven to a position where it can accept electrons from the molecule. Therefore, the HOMO and LUMO energy levels of a molecule can be estimated. This method is only used to estimate the energy levels. It cannot determine exactly where the HOMO and LUMO are, since the reorganisation energy is not taken into account.

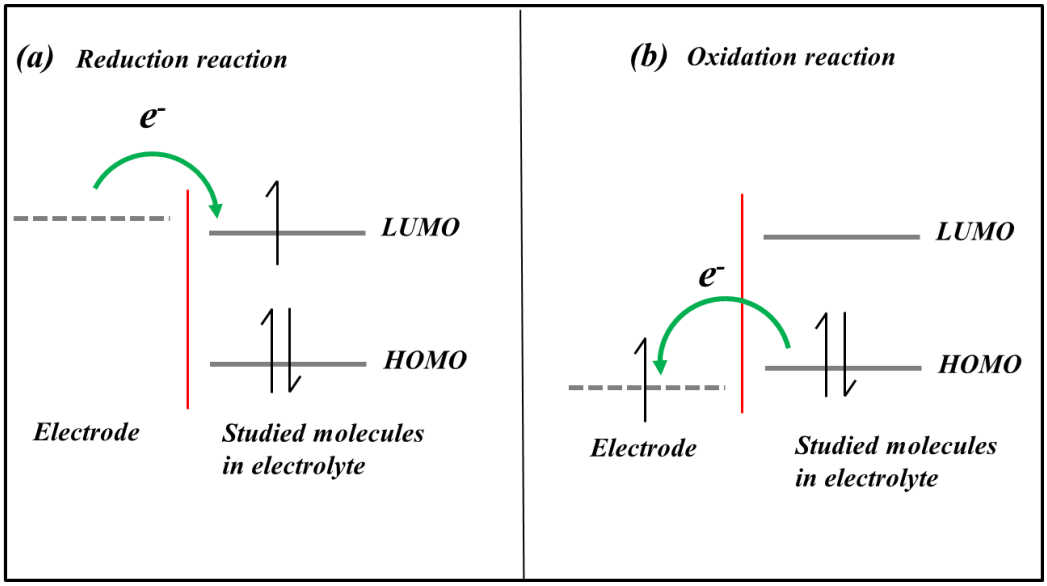

Figure 2-12 Reduction and oxidation reactions of molecules in the electrolyte by electrochemical methods.[7]

To carry out measurements, a three-electrode system is employed, which includes a working electrode (WE), a counter electrode (CE) and a reference electrode (RE). Sometimes the system to be studied needs to be kept under an inert environment to prevent dissolved oxygen reacting at the electrode. A three-electrode cell is shown in Figure **2-13**, the cell is held under Argon to keep an inert environment, and a thermometer can be used to check the temperature.

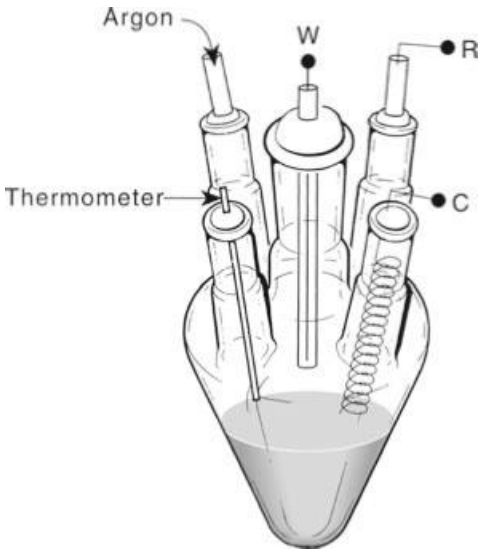

Figure 2-13 A cell with three-electrode system and inert environment.[6]

2.7 Impedance Spectroscopy

Impedance spectroscopy is a dynamic measuring technique, which can be used to study the kinetics of a system[8]. A small perturbation signal is applied to the system, generally a sinusoidally varying voltage E(t) with a small amplitude (e.g. 10mV), and the impedance (Z) is detected over a range of frequencies. The impedance is defined by Equation 2-4[9]

$$Z = \frac{E(t)}{I(t)} = \frac{E_m \sin(\omega t)}{I_m \sin(\omega t+\theta)} = \frac{E_m \sin(2\pi f t)}{I_m \sin(2\pi f t+\theta)} = z' + jz'' \qquad \text{Equation 2-4}$$

Here I(t) is the current, E_m and I_m are the amplitudes of the voltage and the current, θ is the phase difference between the applied voltage and the measured current, and Z′ and Z″ are the real and imaginary part of the impedance.

For a resistance, the phase difference between the applied voltage and the detected current are zero, the impedance can then be described by Equation 2-5, indicating the impedance of a resistance is a constant.

$$\mathbf{Z} = \frac{E(t)}{I(t)} = \frac{E_m \sin(\omega t)}{I_m \sin(\omega t+\theta)} = \frac{E_m \sin(2\pi f t)}{\frac{E_m}{R}\sin(2\pi f t)} = \mathbf{R} \qquad \text{Equation 2-5}$$

For a capacitance (C), its impedance changes as a function of frequency according to Equation 2-6. It is easy to find that the phase change between the voltage and current are 90°.

$$\mathbf{Z} = \frac{E(t)}{I(t)} = \frac{E_m \sin(2\pi ft)}{C\frac{dE(t)}{dt}} = \frac{E_m \sin(2\pi ft)}{C\frac{d(E_m \sin(2\pi ft))}{dt}} = \frac{E_m \sin(2\pi ft)}{C\frac{2\pi f E_m \cos(2\pi ft)dt}{dt}} = \frac{E_m \sin(2\pi ft)}{2\pi fCE_m \sin(2\pi ft + 90^\circ)}$$ Equation 2-6

According to Laplace Transform[8], the impedance of the capacitance can be written as Equation 7

$$\mathbf{Z} = \frac{1}{jwC}$$ Equation 2-7

For an inductance (L), the impedance can be described as the equation and the phase difference is also 90°.

$$\mathbf{Z} = \frac{E(t)}{I(t)} = \frac{L\frac{dI(t)}{dt}}{I(t)} = \frac{L\frac{d(I_m \sin(2\pi f))}{dt}}{I_m \sin(2\pi ft)} = \frac{LI_m(2\pi f)\cos(2\pi ft)}{I_m \sin(2\pi ft)} = \frac{LI_m(2\pi f)\sin(2\pi ft + 90^\circ)}{I_m \sin(2\pi ft)}$$ Equation 2-8

After transforming, the impedance of the inductance can represent as following[8]:

$$\mathbf{Z} = \mathbf{j\omega L}$$ Equation 2-9

Two typical plots, the Nyquist and Bode plots are used represent the information of the impedance spectroscopy. As demonstrated in Figure **2-14**, a Nyquist plot shows the information in a complex plane where the real and imaginary part of the impedance are displayed. However, the frequency is not obvious. In the plot the points from left to right represent the high frequency to low frequency signal. A bode plot displays the clear relation of the phase change or the absolute impedance change as a function of frequency, which is shown in bottom graph in Figure **2-14**.

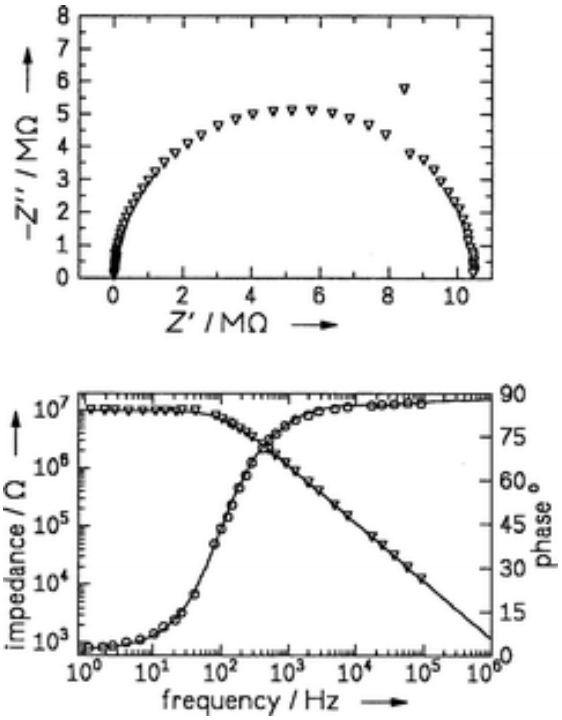

Figure 2-14 Impedance spectrum. Nyquist plot (top) and Bode plot (bottom)[10]

An equivalent circuit with different electrical elements (e.g. resistance, capacitance and inductance) is used to model the reality of an electrochemical system. In terms of the complex processes in perovskite solar cells, the impedance spectra are still not fully understood. Recently, it has been reported that the spectrum can be modelled using an equivalent circuit shown in Figure 2-15.[11, 12] The equivalent circuit can display the series resistance and reveal the charge movements in a perovskite solar cell. In the circuit, R_s is series resistance, Z_{rec} represents the recombination resistance which is frequency-dependent, C_{geo} is the geometric capacitance. R_{shunt} is the shunt resistance which is generally very high and rarely noticed in impedance. R_{ionic} and C_{dl} are the ionic resistance and double layer resistance which are related to the ionic moving in the device.

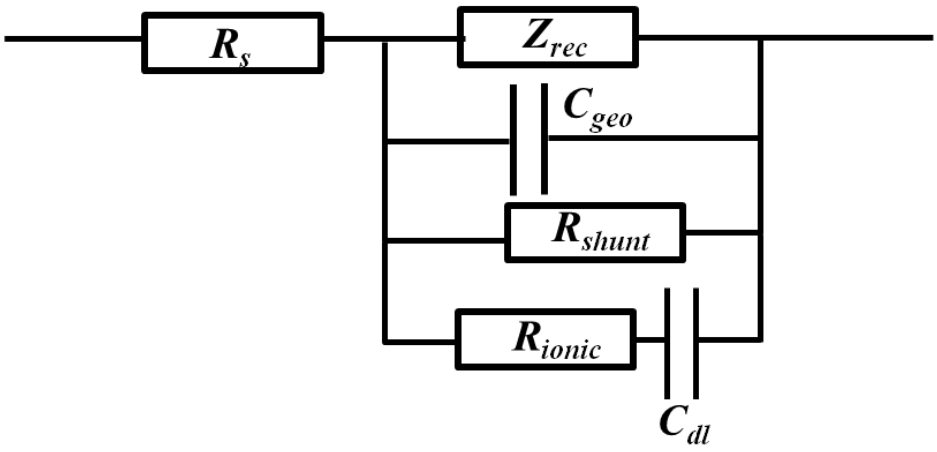

Figure 2-15Equivalent circuit for impedance spectrums of perovskite solar cells[11] .

2.8 Steady state and transient photoluminescence

Photoluminescence (PL) is a photon-excited light emission process. It includes three steps which are charge carrier generation following light absorption, diffusion of carriers and radiative recombination. Figure **2-16** shows light absorption to create an excited electron in an organic molecule. However, electrons can only be kept at the excited state for a short time. They speedily relax from a higher energy level to a lower energy and photoluminescence (i.e. fluorescence and phosphorescence) can be observed when the electrons relax from a singlet excited state or a triplet excited state to the ground state

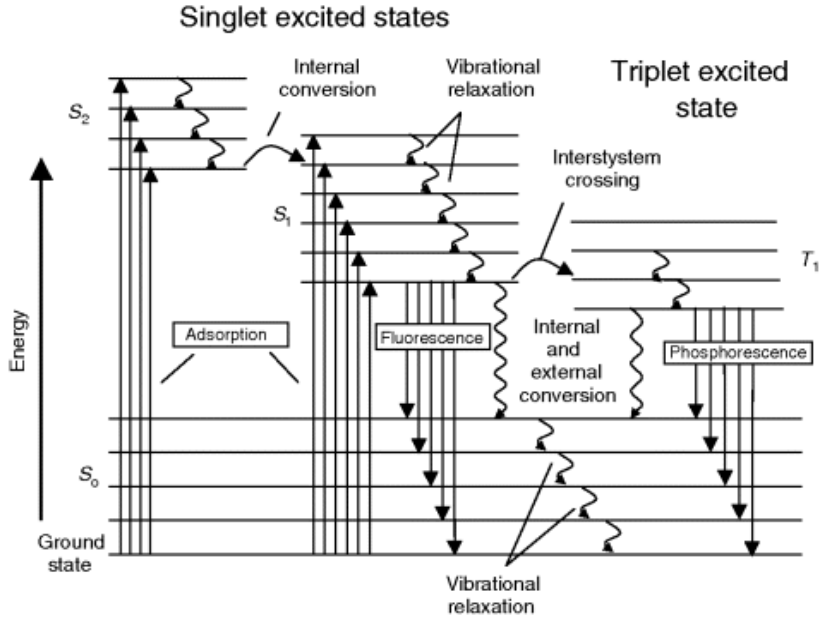

Figure 2-16 Jablonski Energy Diagram shows the light absorption and light emission process.[13]

In an inorganic semiconductor, PL refers to fluorescence. The energy of emitted light is related to the recombination processes. As illustrated in Figure 2-17, 5 different radiative transitions can be observed with PL. (a) is direct band to band recombination in the figure. (b) is the recombination of free excitons (bound electron hole pairs). In this situation some energy is used to counteract the binding energy. Therefore, the emission has a lower energy than the band gap. (c) is the recombination of the bound excitons of a free hole and a neutral donor, (d) represents bound excitons of a free electron and a neutral acceptor, and (e) is the recombination happening between an electron on a neutral donor and a hole on a neutral acceptor.

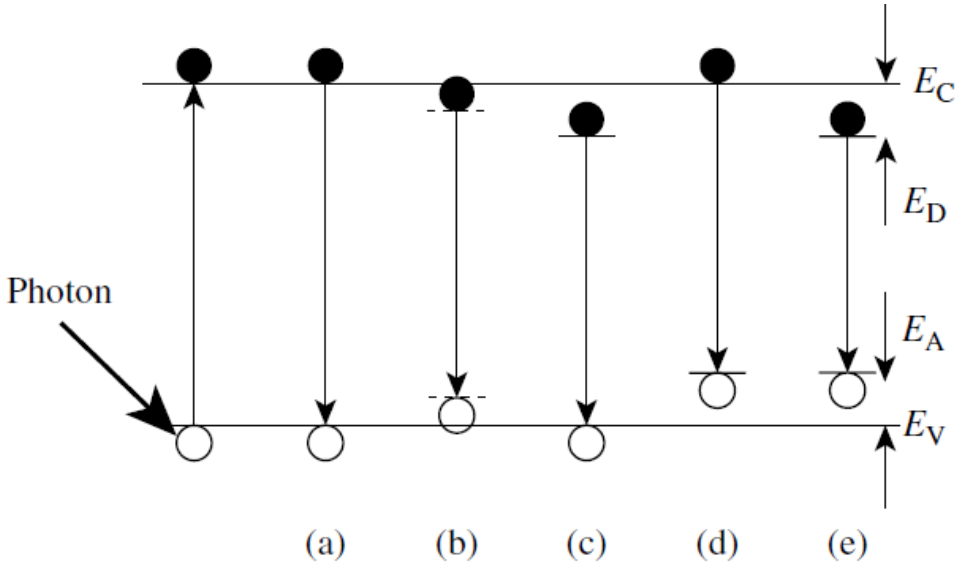

Figure 2-17 Different radiative transitions observed with photoluminescence[14]

Photoluminescence is a useful tool to estimate (or identify) the defect and determine the charge carrier lifetime of a semiconductor[5, 14, 15]. As mentioned above, the defects in a semiconductor can act as centres for non-radiative recombination. The density of the defects can significantly influence the intensity of the PL which is generated when radiative recombination happens. The more defects there are, the lower the PL intensity is. There are two PL techniques that have been used to characterise solar cells, which are steady-state PL and transient PL. In a steady-state PL measurement, continuous laser illumination is used to excite the charges. The PL intensity at different wavelengths is detected which, in the case of direct band to band recombination can be used to estimate the band gap. In a transient PL measurement, a transient laser pulse is generally applied. The decay PL intensity following a laser pulse at a certain

wavelength is recorded over time. This test can be used to investigate the charge carrier lifetime and calculate the charge diffusion length.

2.9 References

1. Chung C-C, Narra S, Jokar E, Wu H-P, Wei-Guang Diau E. Inverted planar solar cells based on perovskite/graphene oxide hybrid composites. *J Mater Chem A* 2017, **5**(27)**:** 13957-13965.

2. de Boer B, Hadipour A, Mandoc MM, van Woudenbergh T, Blom PWM. Tuning of Metal Work Functions with Self-Assembled Monolayers. *Adv Mater* 2005, **17**(5)**:** 621-625.

3. de Boer B, Hadipour A, Mandoc MM, van Woudenbergh T, Blom PWM. Tuning of Metal Work Functions with Self-Assembled Monolayers. *Proceedings of SPIE* 2004, **5464**.

4. Nelson J. *The physics of solar cells*. World Scientific Publishing Co Inc, 2003.

5. Noel NK, Abate A, Stranks SD, Parrott ES, Burlakov VM, Goriely A*, et al.* Enhanced Photoluminescence and Solar Cell Performance via Lewis Base Passivation of Organic–Inorganic Lead Halide Perovskites. *ACS Nano* 2014, **8**(10)**:** 9815-9821.

6. A.M. Bond RGC, D.A. Fiedler, G. Inzelt,, H. Kahlert ŠK-L, H. Lohse, M. Lovric,F. Marken, A. Neudeck, U. Retter, F. Scholz, Z. Stojek. *Electroanalytical methods*, vol. 1. Springer, 2010.

7. Bard AJ, Faulkner LR, Leddy J, Zoski CG. *Electrochemical methods: fundamentals and applications*, vol. 2. wiley New York, 1980.

8. Lasia A. *Electrochemical impedance spectroscopy and its applications*. Springer, 2014.

9. Xiao-Zi Yuan CS, Haijiang Wang, Jiujun Zhang. Impedance and its Corresponding Electrochemical Processes. *Electrochemical Impedance Spectroscopy in PEM Fuel Cells: Fundamentals and Applications*. Springer London: London, 2010, pp 95-138.

10. Buscher C, Stohr U, Freyland W. Electronic excitation spectra and transport of ligand stabilized crystalline Cu2-SeL-cluster compounds:

spectroellipsometric and impedance studies. *Phys Chem Chem Phys* 2000, **2**(10)**:** 2261-2264.

11. Pockett A, Eperon GE, Sakai N, Snaith HJ, Peter LM, Cameron PJ. Microseconds, milliseconds and seconds: deconvoluting the dynamic behaviour of planar perovskite solar cells. *Phys Chem Chem Phys* 2017, **19**(8)**:** 5959-5970.

12. Pockett A, Eperon GE, Peltola T, Snaith HJ, Walker A, Peter LM*, et al.* Characterization of Planar Lead Halide Perovskite Solar Cells by Impedance Spectroscopy, Open-Circuit Photovoltage Decay, and Intensity-Modulated Photovoltage/Photocurrent Spectroscopy. *J Phys Chem C* 2015, **119**(7)**:** 3456-3465.

13. Liu T. Pressure- and Temperature-Sensitive Paints. *Encyclopedia of Aerospace Engineering*. John Wiley & Sons, Ltd, 2010.

14. Dieter KS. Optical Characterization. *Semiconductor Material and Device Characterization*. Wiley-IEEE Press, 2006, pp 563-626.

15. deQuilettes DW, Vorpahl SM, Stranks SD, Nagaoka H, Eperon GE, Ziffer ME*, et al.* Impact of microstructure on local carrier lifetime in perovskite solar cells. *Science* 2015, **348**(6235)**:** 683-686.

Chapter 3 Experimental

Contents

3.1 Introduction

In this chapter, the methods used to fabricate solar cell devices are described and the most important characterization techniques used throughout this project are discussed. All the chemicals were ordered from Sigma-Aldrich or Dyesol, and they were used without further purification.

Table 3-1 Chemicals used in this project

Chemicals	Supplier	Purity	Size
CH_3NH_3I	Dyesol	-	5 g
PbI_2	Sigma-Aldrich	99%	50g
$PbCl_2$	Sigma-Aldrich	98%	250g
Titanium isopropoxide	Sigma-Aldrich	99.999%	5mL
Titanium diisopropoxide bis(acetylacetonate)	Sigma-Aldrich	75% in isopropanol	100 mL
Spiro-OMeTAD	Sigma-Aldrich	99%	5 g
Li-TFSI	Sigma-Aldrich	99.95%	5g
4-(aminomethyl) benzoic acid	Sigma-Aldrich	97%	5g
4-amino benzoic acid	Sigma-Aldrich	99%	5g
4-(methylamino) benzoic acid	Sigma-Aldrich	97%	10g
Ammonium hydroxide	Sigma-Aldrich	28%-30% aq. solution	500 mL

3.2 Device fabrication

In this project "n-i-p", both planar and mesoporous, perovskite solar cells were prepared. The structure of planar and mesoporous cells are shown in **Figure 3-1.** The cells were prepared by depositing one layer at a time from the bottom FTO substrate upwards. Devices were prepared either in a dry box or in an ambient environment.

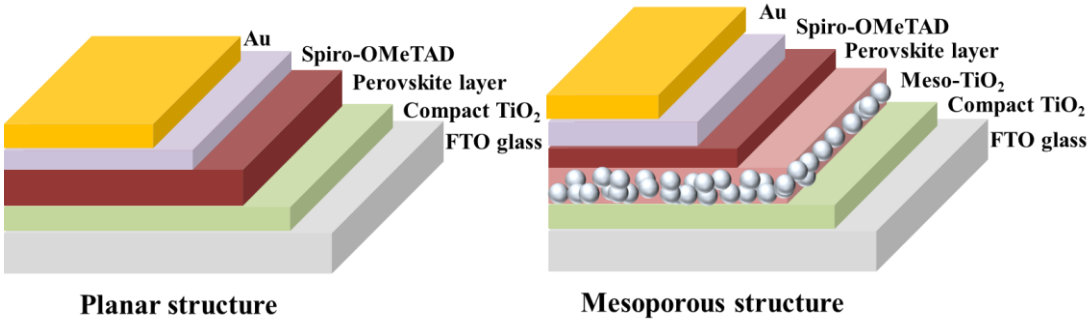

Figure 3-1 Planar and mesoporous perovskite solar cells

3.2.1 TCO glass cleaning and etching

FTO and ITO glasses were used as the charge collecting electrodes. They were cut into a size of 2.5cm×2.5cm and etched with Zn powder and 2 moldm^{-3} aqueous HCl to achieve the desired pattern. The pattern is displayed in **Figure 3-2** where the blue part is etched and not conductive. Subsequently, substrates were cleaned by using a 5-step cleaning process. Substrates were sonicated at 80°C in 2% hellmanex solution, ultrapure water, isopropanol, acetone and ethanol respectively, each sonication step lasted 15mins. Substrates were then dried with N_2 flow before deposition of the next layer.

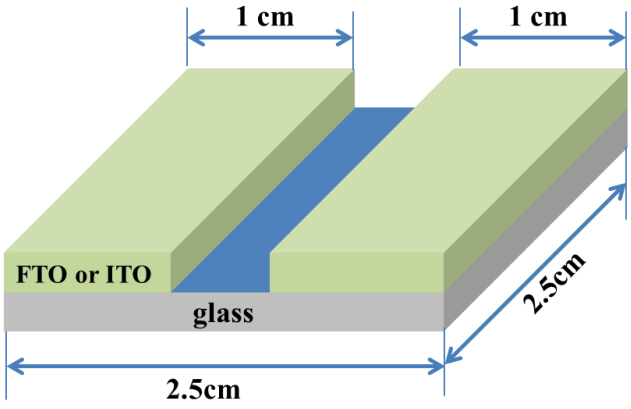

Figure 3-2 Etching pattern on FTO and ITO glass

3.2.2 Electron transporting layer (ETL)

A compact TiO_2 film works as an electron transporting layer in planar and mesoporous solar cells. It is prepared either through spin coating or spray pyrolysis. Depending on the methods used, different titanium precursor solutions are employed. For the spin coating method, an ethanolic solution of titanium isopropoxide (TTIP,) was used[1]. HCl solution was added into 0.2 mol/L TTIP in ethanol. The ETL is deposited by firstly spin coating the precursor solution at 2k rpm for 60s, followed by annealing the substrate at 150°C for 15min to remove the residue solvent, and then sintering at 500°C for 30min to get anatase TiO_2. For spray pyrolysis, a solution of titanium diisopropoxide bis(acetylacetonate) in ethanol was used. TiO_2 was prepared by spraying the precursor solution on substrates kept on a hotplate at 500°C with a chromatography sprayer (provided by Sigma-Aldrich). This step was repeated for 10 times and then post-annealing the substrates for 10min to get anatase TiO_2.

3.2.3 Mesoporous layer

The mesoporous TiO_2 precursor solution was prepared by dispersing a TiO_2 paste (Dyesol 18NR-T) into ethanol with a weight ratio of 2:7. The suspension was stirred at room temperature for at least 30min before use. The mesoporous layer was deposited by spin coating the precursor solution at 5k rpm for 30 s. The film was then heated at 150°C for 15min to remove the solvent and subsequently annealed at 500°C for 30min.

3.2.4 Hole transporting layer (HTL)

To prepare the precursor solution for making the hole transporting layer, 9.6 µL tert-butyl-pyridine and 30 µL bis(trifluromethane)sulfonimide lithium salt (Li-TFSI) solution (175 mg/mL of) in acetonitrile were added into 1mL of a 0.78 mol/L solution of N2,N2,N2′,N2′,N7,N7,N7′,N7′-octakis(4-methoxyphenyl)-9,9′-spirobi[9H-fluorene]-2,2′,7,7′-tetramine (spiro-OMeTAD) in chlorobenzene. The precursor solution was spin coated on top of the perovskite layer at 3k rpm for 30s to get the desired HTL.

3.2.5 Back contact electrode

The Au back contact was deposited by thermal evaporation (Moorfield nanoPVD). The deposition speed and thickness were monitored. The film was deposited at 0.1 nm/s for the first 5 nm and then at a rate of ~1 nm/s to obtain a 50 to 70 nm film.

3.3 Perovskite layer deposition

In this thesis, the perovskite layer is either $CH_3NH_3PbI_3$ or $CH_3NH_3PbI_{3-x}Cl_x$, depending on the type of perovskite film required. Two types of perovskite film deposition are used in this thesis. The first is a one-step method where the perovskite film is deposited using a single precursor solution. The second method is a vapour-assisted solution method in which the perovskite layer is deposited by a two-step method.

3.3.1 One step method

The one-step solution processing method is very widely used to prepare perovskite layers[1, 2]. It is simple and the layer is generally made by spin coating the precursor solution directly on the substrates. Two recipes were used in this work, and they are both 41% precursor solution. One has DMF as the solvent solution with MAI (methylammonium iodide): PbI_2:$PbCl_2$=4:1:1(molar ratio), named the 4:1:1 recipe. The other one is also a DMF solution but with MAI: $PbCl_2$=3:1(molar ratio), named the 3:1 recipe. The details of the recipes can be found in **Table 3-2**. After spin coating, the wet films were usually annealed at 100°C for 90 min to get full conversion to the dark brown/black perovskite films.

Table 3-2 Precursor solutions for preparing perovskite films

Recipes	MAI (Dysol,)(mg/mL)	PbI_2 (Sigma Aldrich,)(mg/mL)	$PbCl_2$ (Sigma Aldrich,)((mg/mL)	Solvent	Spin coating speed (rpm)	Spin coating time (s)
4:1:1	307.1	222.6	134.3	DMF	3 k	30
3:1	419.5	-	244.5	DMF	2 k	60

3.3.2 Vapour assisted method

A two-step vapour assisted method was also used to prepare perovskite films. The films were prepared in air under low vacuum. To get perovskite films, a PbI_2 layer was first deposited by spin coating a PbI_2 in DMF solution (400 mg/mL) on a compact TiO_2 substrate at 4k rpm for 60s, and then annealed at 120°C for 1 h to get the PbI_2 film.[3] The precursor solution and FTO substrates were both kept at 60°C before the deposition of PbI_2 films. MAI powder and the substrates with PbI_2 films were then put on a hotplate at 150°C. The samples were covered with a desiccator lid which was connected to a pump (Edwards 5 E2M5 Rotary Vane Dual Stage Mechanical Vacuum Pump) to evacuate the chamber as shown in **Scheme 3-1**. The yellow PbI_2 film turned into dark perovskite films, following the reaction of PbI_2 with MAI vapour. A complete color transition was observed after the substrates were treated for 70 mins under the dessicator lid.

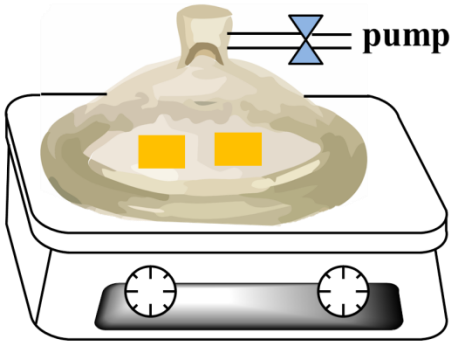

Scheme 3-1 Vapour assisted solution method for making perovskite films in air

3.4 Characterization Techniques

3.4.1 Cyclic voltammetry (CV)

CV was carried out using the Metrohm Autolab electrochemistry platform. A three-electrode set-up was used and measurements were carried out in an earthedFaraday Cage. A piece of Pt foil was used as the counter electrode, Pt wire was used as a pseudo-reference electrode and a Pt disc electrode (ø=2mm) as the working electrode. The electrolyte (PDIs in DMSO solution) was bubbled with argon gas for at least 15 min before the measurement to remove oxygen, and the system was kept under Ar

atmosphere until the measurements were finished. Ferrocene was added into the electrolyte as an internal reference after the CV measurements of active materials.

3.4.2 Current density-voltage scan (J-V scan)

J-V scans were controlled by a homemade programme supported by LabVIEW. The power was provided by a Keithley (2601A System) source meter and the light illumination was simulated by a solar simulator to match one sun, AM1.5. Both forward (e.g. from 0V to 1.1V) and reverse scans (e.g. from 1.1V to 0V) at dark and under illumination were tested. Before scanning under illumination, devices were soaked under light for 5s to to ensure the scans started from steady state. All devices were tested in the ambient environment without encapsulating.

3.4.3 Stability test

The stability of perovskite solar cells were monitored by measuring J-V scans of a device over time. For example, devices were first tested straight after fabrication, which is the data point collected at 0 h. More data points were then collected by taking JV curves at regular intervals, for instance, 1h, 2h, 24h, 48h or longer. The PCE change in the devices was used to estimate the stability. Between each test point, devices were kept in a desiccator box where the RH was around 20%.

3.4.4 Impedance Spectroscopy (EIS)

Impedance was measured on a ModulabXm (Solartron analytical). Solar cells were held at the open circuit voltage under illumations with a red LED (660nm) for measurements at single illumination intensity. Measurements at different light intensities were also carried out on the same instrument, but with a blue LED (470nm) as the light source. A frequency range of 1MHz to 10 mHz and an AC amplitude of 10 mV were applied in the test. Measurements were carried out in a earthed Faraday cage at room temperature.

3.5 References

1. Wojciechowski K, Stranks SD, Abate A, Sadoughi G, Sadhanala A, Kopidakis N, *et al.* Heterojunction Modification for Highly Efficient Organic–Inorganic Perovskite Solar Cells. *ACS Nano* 2014, **8**(12)**:** 12701-12709.

2. Eperon GE, Burlakov VM, Docampo P, Goriely A, Snaith HJ. Morphological Control for High Performance, Solution-Processed Planar Heterojunction Perovskite Solar Cells. *Advanced Functional Materials* 2014, **24**(1)**:** 151-157.

3. Casaluci S, Cinà L, Pockett A, Kubiak PS, Niemann RG, Reale A*, et al.* A simple approach for the fabrication of perovskite solar cells in air. *Journal of Power Sources* 2015, **297:** 504-510.

Chapter 4 Optimization of baseline perovskite solar cells

Contents

4.1 Introduction

There are two key factors correlated to the power conversion efficiency of perovskite solar cells as shown in equation 4-1. They are charge generation efficiency (including light harvesting, exciton generation and separation) and charge collection efficiency of devices. The optimization of solar cell device performance can be achieved by improving both processes.

$$IPCE = \eta_{generation} \times \eta_{collection} \qquad \text{Equation 4-1}$$

To enhance the charge generation efficiency, improvements can be achieved by increasing the light harvesting and charge generation, such as reducing light loss and band gap, . As demonstrated in **Figure 4-1**, three important processes happen in a solar cell. They are the light harvesting, charge generation (e.g. excitation generation) and charge collection process (including the charge separation, recombination and transporting). It is an effective solution to improve the charge generation efficiency by, for example, reducing losses due to light reflection and absorption of transparent conductive oxides (TCO) glass substrates, and the electron transporting material (ETM) helps to improve the light harvesting efficiency. Lowering the band gap of the perovskite can improve the harvesting of visible light. The addition of additives into perovskite precursor solution[1, 2] and use of mixed anions ($MAPbI_{1-x}Cl_x$)[3, 4] have been used to improve the absorbance of the perovskite. Mixed cation systems (e.g. $Cs_xFA_yMA_{1-x-y}PbX_3$) can be used to reduce the band gap of perovskite[5, 6]. Charge collection efficiency can be improved through enhancing the charge separation and charge transporting and decreasing non-radiative recombination in the device. For instance, decreasing the energy loss at interfaces by optimizing the energy alignments of different layers either through interface engineering or selection of a well-matched contact layer can effectively improve the charge collection efficiency. In addition, avoidance of the non-radiative recombination by reducing the concentration of defects of semiconductors is also an effective way to improve the charge collection efficiency.

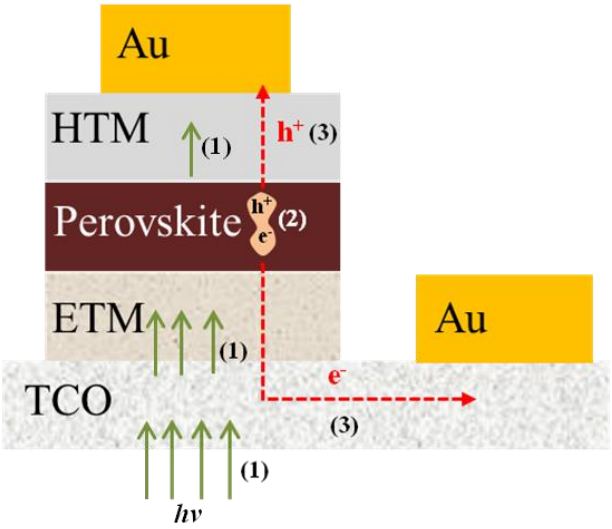

Figure 4-1 Working mechanism of n-i-p structure hybrid perovskite device. The three processes displayed are (1) light harvesting, (2) excition generation and (3) charge collection.

In this chapter, studies are based on conventionally structured perovskite solar cells, which have a "n-i-p" architecture with TiO_2 as the electron transporting layer. The optimization described in this chapter mainly targets the performance enhancement of mixed halide perovskite ($MAPbI_{1-x}Cl_x$) solar cells fabricated in air or in a dry box. Research was carried out on different layers of the devices, from selection of the TCO substrates, studying of the blocking layers made by different methods and modification of perovskite layers to device configuration improvement. Most of the work focuses on the modification of the techniques used to prepare thin films, including the blocking layer and the perovskite layer. Factors such as film preparation method, humidity of the environment, solvent atmosphere and film annealing procedure were explored and their effect on device performance investigated in detail. In addition, hysteresis in planar and mesoporous devices is also discussed. The work in this chapter was important to create baseline solar cells for the following study of small molecules and their applications in perovskite solar cells.

4.2 Experimental

Device Fabrication: All devices in this chapter were prepared by one step solution method unless specifically mentioned. The details can be found in Chapter 3.

Samples preparation for profilometer: When films were spin coated or sprayed on FTO substrates, the edges of FTO were covered in order for the thickness difference to be measured.

Film coverage estimation. The coverage of perovskite films were estimated according to the colour gradient of the AFM images using Matlab image analysing function. Detailed codes of the program can be found in the supporting information at the end of this chapter.

4.3 Transparent conductive oxide (TCO) glass substrates

FTO (TEC15, TEC7) and ITO glass are three widely used substrates for rigid perovskite solar cells.[7, 8, 9] They are employed as electrodes in conventional structure hybrid perovskite solar cells[6, 10, 11]. Their properties are listed in

Table **4-1**, including transmittance, resistance and average roughness. The transmittance of substrates can affect how much solar illumination can reach the light absorbing layer, thus affecting the external quantum efficiency (EQE) of the devices. The sheet resistance can increase the series resistance of devices, and ultimately influence the fill factor (FF). The roughness of substrates can impact the film quality of the layer deposited directly on top of the glass which in turn can influence the short circuit current (J_{sc}), open circuit voltage (V_{oc}) and FF.

To work out the difference in morphology, glass substrates were characterized by Atomic Force Microscopy (AFM), the three substrates showed distinctly different morphology. As shown in Figure 4-2, ITO glass is the smoothest substrate and composed of big oxide particles. Its average roughness is approximately 1nm. TEC15 has a medium roughness, 8nm on average. TEC7 is the roughest substrate with an average roughness of 25nm. According to the optical and electrical information demonstrated in

Table **4-1**, TEC15 is very transparent but with relatively high sheet resistance, TEC7 has lower sheet resistance but a very rough surface and is inferior in transparency. ITO is very smooth but costs more than the other two substrates. It is worth noting that the resistance of ITO will increase severely when it is heated at high temperature (e.g. 500°C)[12]. For this reason, most of the work related to use of ITO is usually done at low-temperature[13] or in inverted structure perovskite solar cells. However, it is still

necessary to explore how the cell performance can be changed in comparison with substrates which have better tolerance of high temperature. It is important to mention that when the perovskite film is annealed on a hotplate, the thickness of the glass substrate could cause significant surface temperature differences. For example, it was found that when the hotplate was heated up to 103°C, the temperature of the substrates surface was 88°C, 88.7°C and 95.6°C for TEC15, TEC7 and ITO, respectively. In order to find the most suitable substrate for conventional structure (n-i-p) perovskite solar cells, standard device preparation procedures were used for solar cells with different glass substrates, and effects of the substrate on the power conversion efficiency were investigated.

Table 4-1 Properties of TCO substrates

Substrate	**Transmittance**[a]	**Sheet resistance**[a]	**Surface roughness**[b]	**thickness**[a]	**Surface temperature (substrate/hotplate)**	**Price**[c] **/per substrate**
FTO TEC15	82~84.5%	~13Ω /sq	~ 8 nm	2.3 mm	88°C/103°C	£0.37
FTO TEC7	80~82%	~7 Ω /sq	~25 nm	2 mm	88.7°C/103°C	£0.37
ITO	84%	8-12 Ω /sq	~ 1 nm	1.1mm	95.6°C/103°C	£10.6

[a] data from Sigma-Adrich;
[b] average roughness obtained by using AFM;
[c] price calculated according to the size of the substrates (2.5×2.5cm) used in the lab

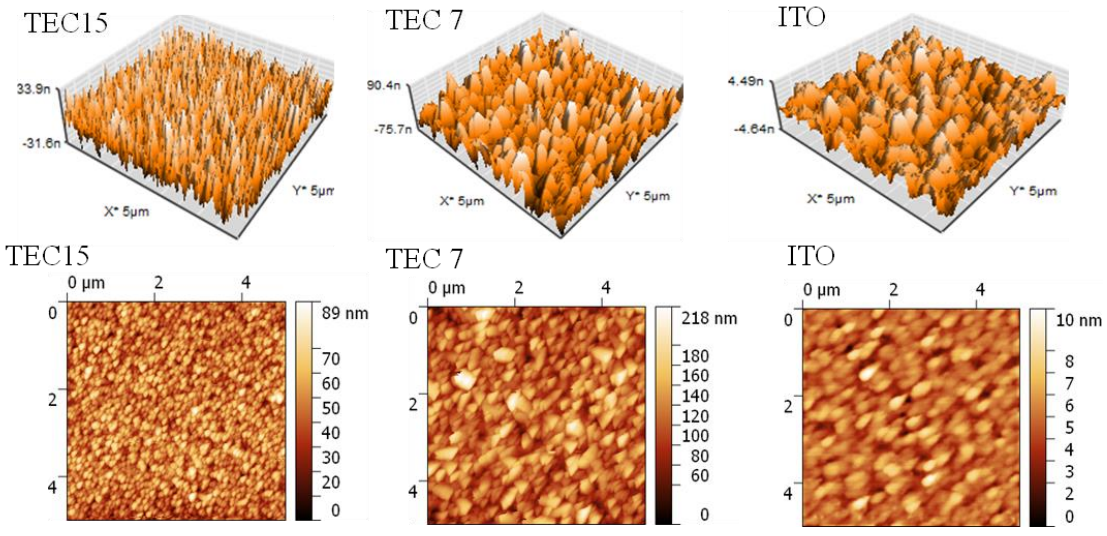

Figure 4-2 AFM images of TCO substrates. Images shown at the top are Z-axis 3D topography, and images shown at the bottom are Z-axis 2D colour map.

Devices were prepared in N_2 filled dry box, and the one step method was used to deposit mixed halide perovskite films. The details of the device preparation methods can be found in chapter 3. Current density-voltage (J-V) tests were carried out for all the devices. The calculated device parameters from J-V curves are shown using box plots (Figure **4-3**) to monitor the performance change. All the parameters can be found in detail in Table **4-2**.

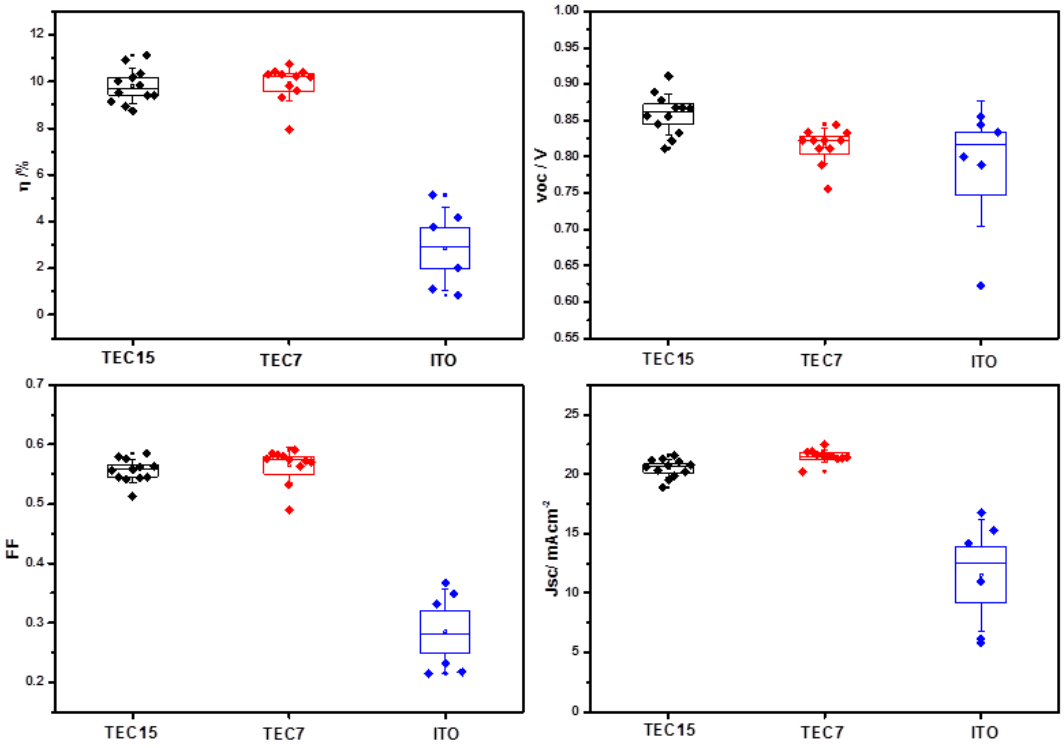

Figure 4-3 Perovksite solar cell performances. Devices with different substrates were labelled as TEC15, TEC7 and ITO. The box and whisker represent 0.5 SD and 1 SD. Data were from reverse scan of current density-voltage measurement at one sun AM1.5 at room temperature. The scan rate was 200mV/s. The active area under illumination was 7.5mm^2. Device configuration was glass substrate/TiO_2/$MAPbI_{1-x}Cl_x$/spiro-OMeTAD/Au.

It can be concluded TEC15 and TEC7 are better candidates than ITO to work as rigid substrates for conventional devices. The damage to the conductivity of ITO by the high temperature annealing procedure causes a significant PCE drop. As shown in the figure and the table, devices using ITO show inferior V_{oc}, FF and J_{sc} in comparison with the other two samples, especially the FF which is much lower than the other two. The PCE of devices using ITO substrates is 2.9% on average. For devices TEC15 and TEC7, they showed very similar PCE, giving average efficiencies of 9.8% for TEC15 and 9.9% for TEC7. When being analysed in detail, it can be found that the FF of device TEC7 is higher than device TEC15 (0.57 vs. 0.56) due to better conductivity. TEC7 also has a

higher J_{sc} but a lower V_{oc} than device TEC15. This could be due to the low sheet resistance (i.e. effective charge collection caused Jsc to increase) but high surface roughness (i.e. high recombination caused V_{oc} drop). Overall, ITO is not an appropriate substrate for conventional structure perovskite solar cells, while TEC7 and TEC15 display similar device performance, indicating no preferences when these two substrates are used.

Table 4-2 Device parameters under AM1.5 illumination

Samples	PCE /%	Voc / V	Jsc / $mAcm^{-2}$	FF
TEC15	9.8 ± 0.8	0.86 ± 0.03	20.5 ± 0.8	0.56 ± 0.02
TEC7	9.9 ± 0.8	0.82 ± 0.02	21.5 ± 0.6	0.57 ± 0.03
ITO	2.9 ± 1.8	0.80 ± 0.09	11.5 ± 4.7	0.29 ± 0.07

4.4 Hole-blocking layer optimization

High quality selective contacts are very critical to make a good device. A good blocking layer film should be highly selective to either electrons or holes, which ideally means no "pin holes". The surface should be good for the following layer to be deposited, which means its morphology and wetting properties are appropriate for the control of the following layer. In this part, the preparation of the hole blocking TiO_2 films is described. The films were prepared using spin coating and spray pyrolysis methods. Films were characterized by AFM, contact angle measurement and XRD, and the effects of the blocking layer on perovskite films were studied.

4.4.1. Spin-coated TiO_2 and sprayed TiO_2

Two different methods, spray pyrolysis and spin coating, were employed to make the TiO_2 layers. The details of blocking layer preparation were copied from references[14, 15] and are described in detail in chapter 3. The morphologies of two blocking layers were characterized by AFM and they were noticed to be similar. As shown in Figure **4-4**, AFM images of both films show particles with the size around 200nm, which is likely to be the structure of the TEC15 substrate[14]. Due to the fine structure of TiO_2, its morphology is hard to detect by AFM or even SEM when it is deposited on TCO glass. Films display similar average roughness of 4.9 nm and 6.5 nm for spin coated and sprayed film, respectively.

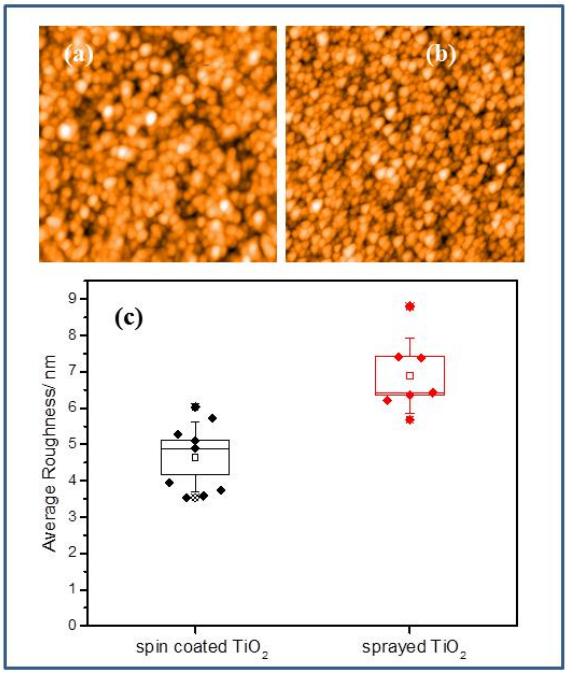

Figure 4-4 AFM images of spin coated TiO_2 (a), sprayed TiO_2 (b) and average roughens of TiO_2 films by box plot(c). The size of AFM images is 5×5μm

The thickness of the spin coated TiO_2 layers was estimated to be around 50nm by FESEM cross-section measurements, while the sprayed TiO_2 was found to be thicker and was around 120 nm measured by profilometer.

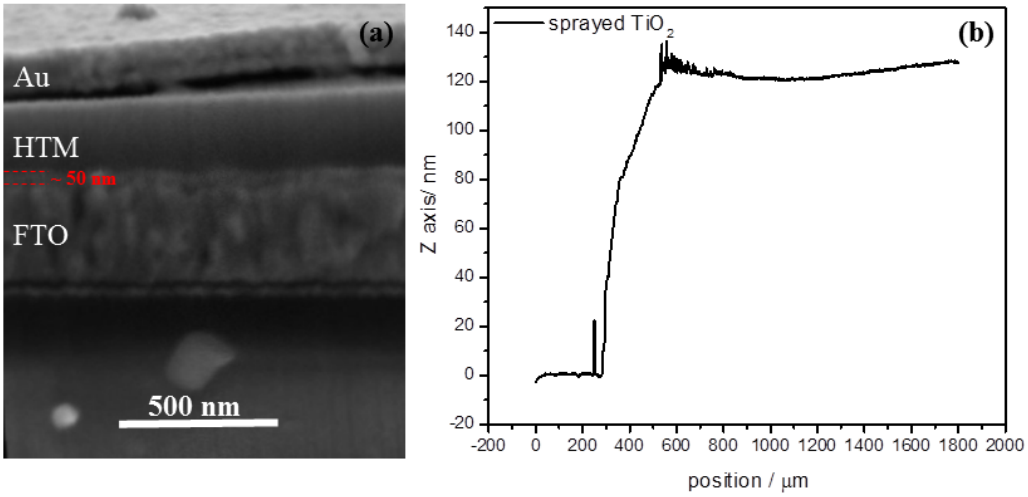

Figure 4-5 Thickness of TiO_2 (a) FESEM cross section of device without perovskite to determine spin coated TiO_2. (b) profilometer measurement to determine thickness of sprayed TiO_2

Advancing contact angle measurements indicate that TiO_2 layers prepared by spray pyrolysis are more hydrophilic than layers made by spin coating. The water contact angle of sprayed TiO_2 is 25.5°± 1.3°, and it is 30.7°± 1.8° for spin coated TiO_2. Since

the perovskite films are typically deposited from DMF, which is miscible with water, we have observed that low contact angles are beneficial for perovskite layer deposition.

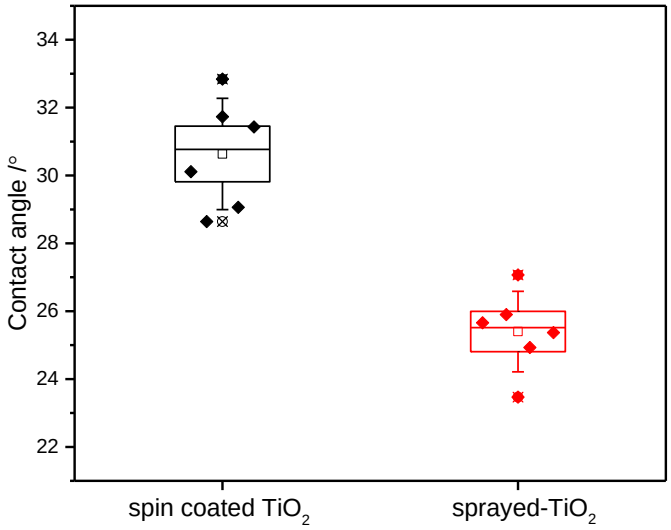

Figure 4-6 Advancing contact angle to monitor wetting properties of TiO_2 blocking layer. Liquid used for test is water.The range of the box is one standard deviation (SD) and the range of the whisker is 2SD

XRD curves of TiO_2 films reveal that films prepared by spray pyrolysis are in the anatase phase, and the peak at 25.3° is the (101) lattice plane of the crystal. The characteristic peaks of spin coated TiO_2 are not obvious which is either due to the layer being too thin or an amorphous layer being formed on the FTO surface.

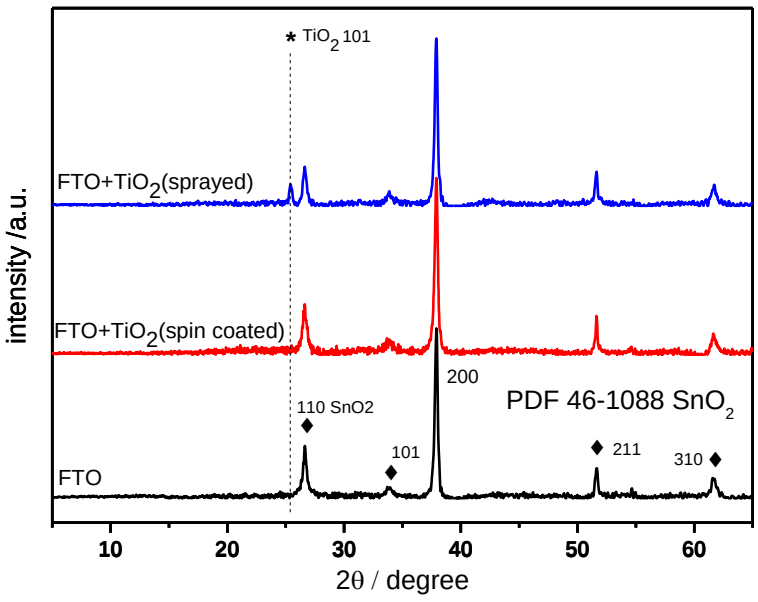

Figure 4-7 X-ray diffraction of TiO_2 by spin coating or spray pyrolysis.

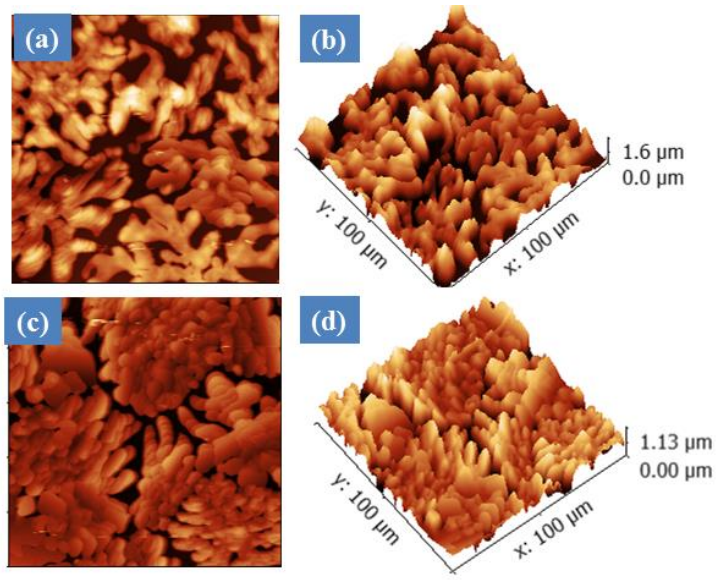

Figure 4-8 AFM images of perovskite films. (a) AFM colour map (b) 3D view of perovksite film deposited on spin coated TiO_2, (c) AFM colour map (d) 3D view of perovskite film deposited on sprayed TiO_2. Image sizes are 100µm×100µm. Perovskite film was prepared by the one step method in air.

As shown in Figure **4-8**, perovskite films deposited on blocking layers prepared by different methods display some differences. Films on sprayed TiO_2 appear to be more compact and have bigger grains than those deposited on spin coated TiO_2. Besides, the 3D view images reveal that perovskite film deposited on spin coated TiO_2 have a rougher surface as shown by a wider range of undulations on the Z axis. The average roughness is 255nm for films on spin coated TiO_2 and 142nm for films on sprayed TiO_2. In addition, as an important parameter, the coverage is estimated to be 68.5% for films on spin coated TiO_2, while it is 91% on sprayed TiO_2. In a word, regardless of the thickness (which can be easily controlled), TiO_2 prepared via spray pyrolysis shows better performance than the spin coated TiO_2 when it is used as the blocking layer in perovskite solar cells.

4.5 Perovskite film quality control

Generally, perovskite film preparation is carried out under carefully controlled conditions such as in a glove box or in a clean room. The humidity, as well as the dust and oxygen levels in the environment can then be controlled. However, in terms of the expense, these facilities are very high cost and also expensive to maintain. Thus, it will be very useful if the operations can be done in ambient environment with cheap equipment. In this part, perovskite solar cells were prepared in a dry box which was

filled with dry inert gas to control the humidity and atmosphere. Perovskite film quality was monitored under various preparation conditions such as different lead sources, different film annealing processes and dry box atmosphere control.

4.5.1. Humidity

Humidity is one of the key factors that affect perovskite solar cells' performances. As MAI can easily dissolve in water, the humidity of the environment will significantly influence the crystallization of the perovskite film and the stability of devices as well. However, it has also been reported that at certain humidity ranges (35% ± 5%)[16], the moisture can assist the perovskite growth and is beneficial to make good quality perovksite films. This work shows the possibility to make devices without glove box, which is high cost and expensive to maintain. In order to obtain more information about how humidity affects the film morphology, perovskite layers prepared at different humidity (i.e. 32%, 37%, 42% and 47%) via one step method were characterized by AFM. As demonstrated in Figure **4-9**, though the humidity difference is only 5%, the coverage of perovskite films decreases obviously with the increase of humidity, and films roughness rises nearly in direct proportion. Especially, from 42% to 47% there is remarkable increase of roughness (from 70nm to 150nm), and the coverage decreases sharply as well. Thus, we believe when the humidity is above 42%, the moisture is detrimental to perovskite film preparation, and all devices preparations reported in this thesis were carried out for humidity below 42% when devices were prepared in ambient environment. Otherwise if devices were fabricated in a dry box, the humidity is kept at around 6% by filling with dry N_2.

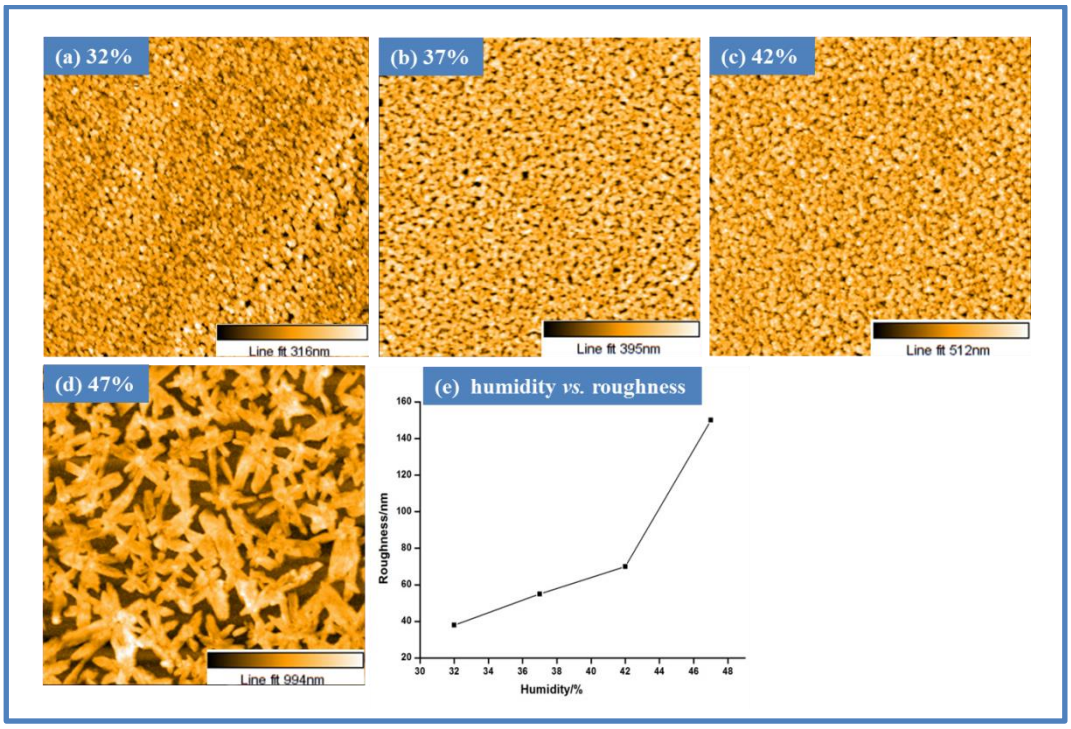

Figure 4-9 Changes of perovskite film morphology with humidity.

4.5.2. Perovskite layer annealing process control

Control of the annealing procedure for making perovskite films is vital since the speed of solvent evaporation can significantly influence the crystallization process. When the precursor solution is deposited on substrates, the transformation from the liquid state to solid state via an intermediate phase ($CH_3NH_3PbI_3$·solvent) plays an important role in obtaining perovskite films with desired morphologies[17]. Researchers have used solvent engineering or vapour assisted methods to either control the intermediate phase or skip the process that forms intermediates[17, 18, 19]. In the present work, a 15min pre-annealing process was introduced to control the crystallization when making planar structure devices and mesoporous devices. After spin coating of perovskite precursor solution, instead of being transferred to hotplate directly, wet films were kept at room temperature for 15min before being annealed at high temperature. The pre-annealing process slows down the evaporation of the solvent, and it will ultimately affect the film qualities. Its impacts were found to be different for planar and mesoporous structure devices. It assists the planar device by improving the performance, while it causes a decrease in the PCE for mesoporous solar cells.

As shown in Figure **4-10**, (a) and (b), when wet samples for making planar devices were taken out for annealing directly after spin coating, the films showed inferior coverage (77%) and the average roughness was 128 nm. However, if samples were kept at room temperature for a while (e.g.15min), an obvious increase of coverage (85%) and reduction of roughness (88 nm) were observed, as displayed in (c) and (d). In addition, perovskite particles are big and compact in samples with pre-annealing. We suppose the pre-annealing process allows enough time for PbI_2 interacting with MAI in the state of intermediates (PbI_2-MAI-DMF), and it reduces the influences of the solvation which is responsible for the poor coverage of perovskite film. The pre-annealing process decreases the solvation problem which caused needle-shaped uncovered areas on the substrate and helps the crystal compactly cover the substrate.

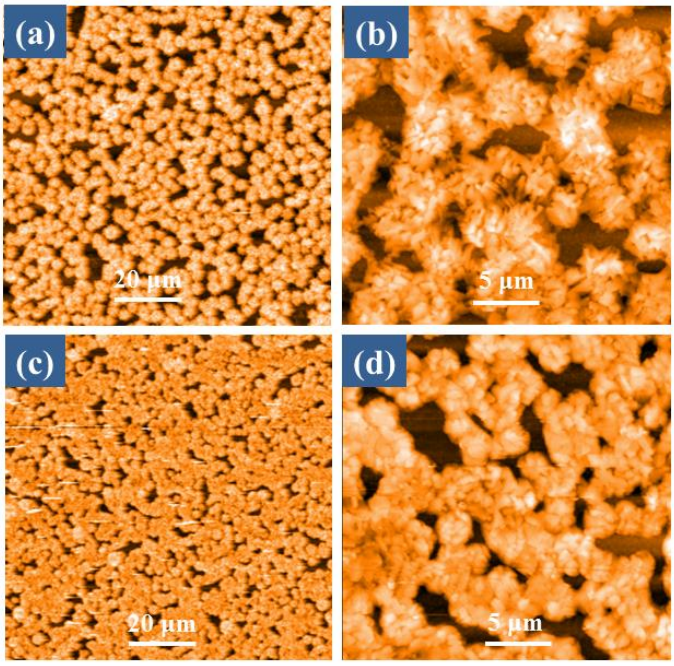

Figure 4-10 AFM images of perovskite films without pre-annealing (a),(b), and (c)(d) with pre-annealing (c),(d). Perovskite films were deposited on compact TiO_2.

Devices were also made with the corresponding perovskite films and the device performance is displayed in Figure **4-11** as box plots, based on 12 devices. The PCE of planar solar cells with the pre-annealing procedure is observed to be higher in comparison with the ones without pre-annealing. The increase in average V_{oc} (from 0.84 V to 0.89 V) and average J_{sc} (from 9.18 $mAcm^{-2}$ to 11.08 $mAcm^{-2}$) could be due to the better coverage of perovskite films shown in Figure **4-10** which decreases shunt path and results in the improvement of device performance. The FF of both types of

devices is almost the same, indicating the resistance was not changed after pre-annealing.

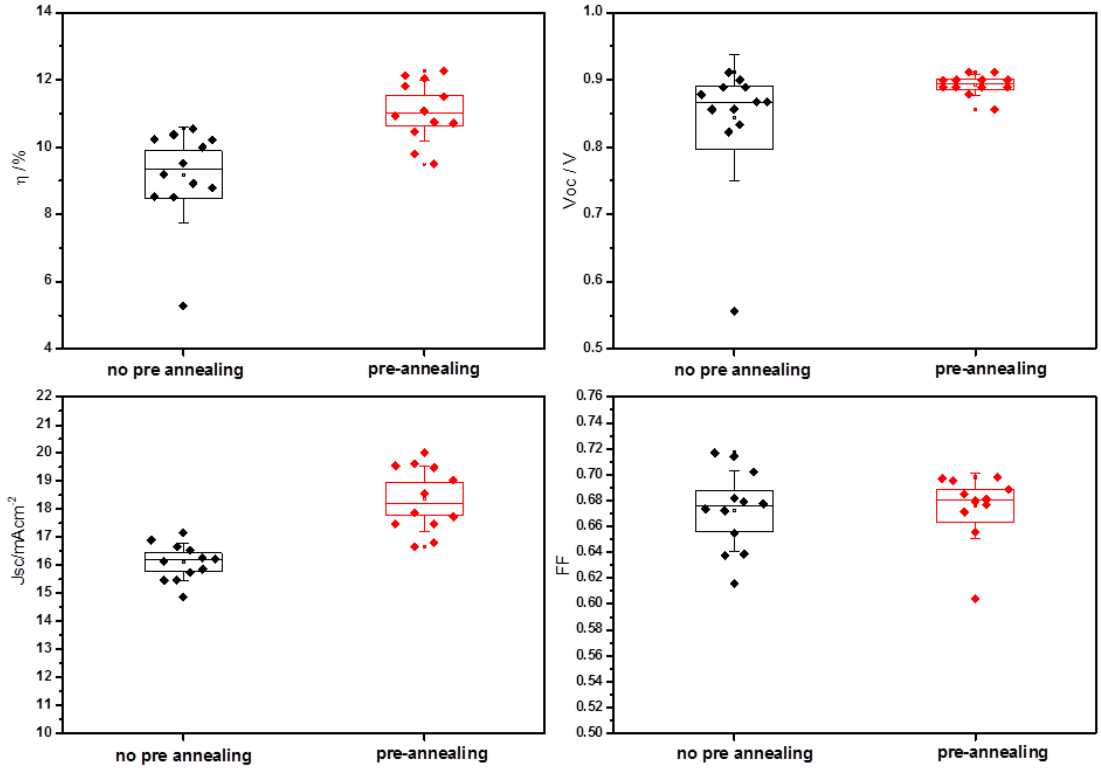

Figure 4-11 Device performance of planar perovskite solar cells prepared with and without pre-annealing.

Table 4-3 AM 1.5 parameters of planar devices prepared with and without pre-annealing

Preparation procedure	PCE / %	J_{sc} / $mAcm^{-2}$	V_{oc} / V	FF
Without pre-annealing	9.18 ± 1.43	16.01 ± 0.66	0.84 ± 0.09	0.67 ± 0.03
With Pre-annealing	11.08 ± 0.90	18.40 ± 1.17	0.89 ± 0.02	0.68 ± 0.03

The effects of the pre-annealing were also investigated on mesoporous devices. The perovskite films were compared by AFM characterization. As shown in Figure **4-12**(a) and (c), the roughness and coverage of films are very similar. The average roughness is 50 nm and coverage is 92% for sample with pre-annealing, and 48 nm and 94% for sample without pre-annealing. It indicates that films without pre-annealing have a slightly smoother surface and better coverage. The grain size distribution was also worked out for both samples to further explore the morphology. As revealed in Figure **4-12** (b) and (d), the median grain size is around 0.45 μm^2 for the pre-annealed sample, and around 0.55 μm^2 for the sample without pre-annealing, indicating grain size is

reduced when the pre-annealing process is used. It is noteworthy that what the AFM images show is the film morphology of capping layers. When spin coated on mesoporous layer, the precursor solution will infiltrate the porous structure, and perovskite crystals then form in pores as well as on top of the mesoporous layer. This implies that the pre-annealing process cannot influence the crystallization of perovskite in the same way it does in planar devices.

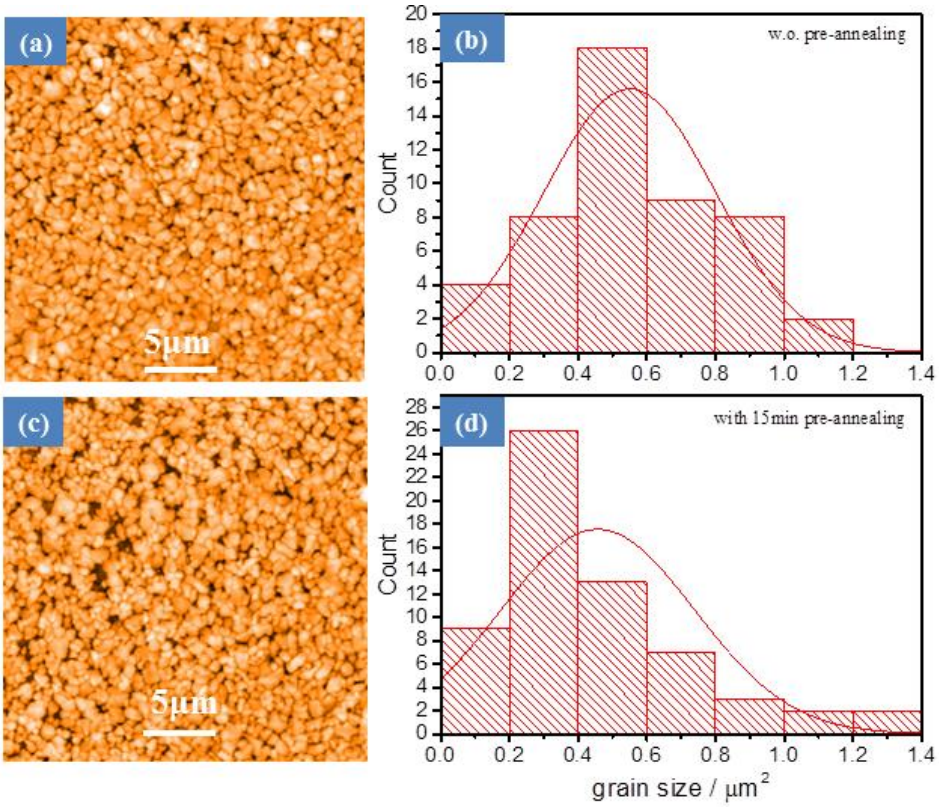

Figure 4-12 AFM images and grain size distribution of perovskite films without (a)(b) and with (c)(d)pre-annealing. Perovskite films were deposited on mesoporous TiO_2.

Mesoporous devices fabricated with and without pre-annealing show different performances. Instead of enhancing the device performance, the pre-annealing process causes a decrease in the PCE of mesoporous devices. As demonstrated in Figure **4-13** and Table **4-4**, the PCE drops when pre-annealing is used for device preparation. It is 9.96% on average for devices prepared without pre-annealing, while it is 9.42% in average for pre-annealed devices. Other parameters J_{sc}, V_{oc} and FF all decreased when pre-annealing was employed.

It is interesting to notice that the effects of the pre-annealing process are different on solar cells with different architectures. It is assumed that the pre-annealing could reduce the needle-shaped solvation intermediates in planar devices[19], and it can be confirmed by the increased coverage and grain size shown in AFM images. However, the coverage and grain size change show the opposite trend in mesoporous solar cells. We think this is a result of the different architecture of mesoporous solar cells which includes the mesoporous layer and the capping layer. It is very likely that the crystallization processes of perovskite in titania pores and in the capping layer are different. The hypothesis is that once slower crystallization occurs in pores, the formed perovskite fills the pores, and it makes the escape of the solvent more difficult. The capping layer could be supposed to be influenced by pre-annealing in the same way as the planar perovskite film. However, the delayed quick solvent removal procedure (when heated) will drive the solvent from mesoporous layer to pass through the capping layer, and ultimately cause a decrease in coverage of the capping layer.

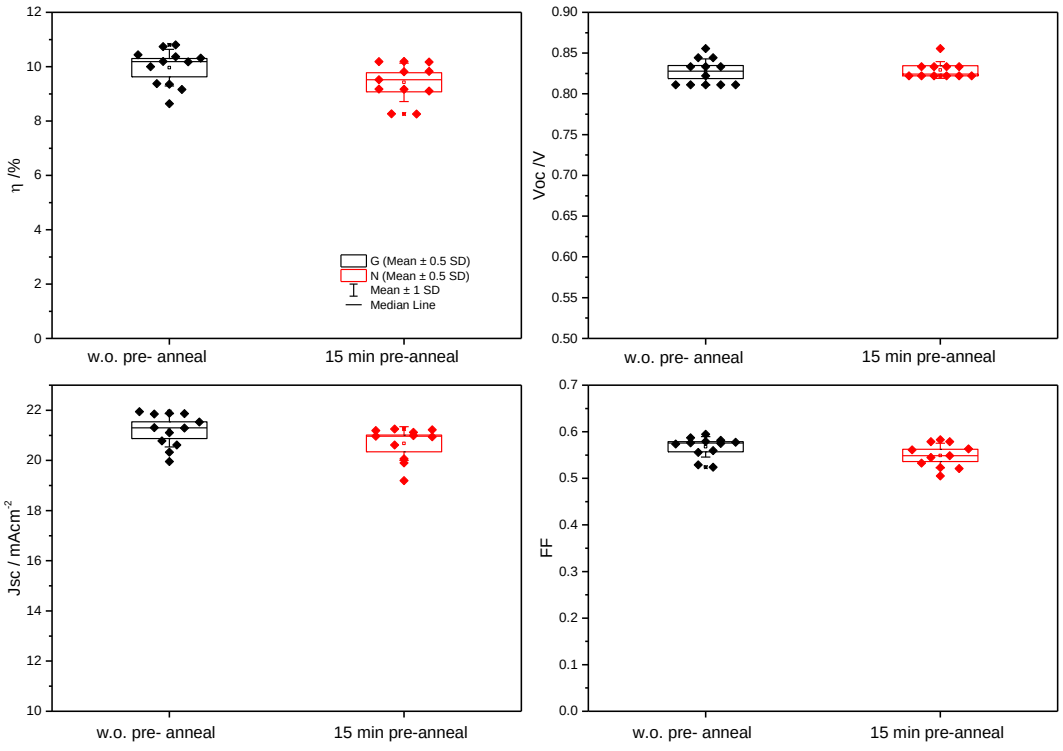

Figure 4-13 Perovskite solar cell performances shown by box plots. Devices with and without pre-annealing are labelled as 15 min pre-anneal and w.o. pre-anneal. The box and whisker represent 0.5 SD and 1 SD. Data are from reverse scan of current density-voltage measurement at one sun AM1.5 at room temperature. The scan rate was 200mV/s. The active area under illumination was 7.5mm2. Device configuration is glass substrate/c-TiO_2/meso-TiO_2/$MAPbI_{1-x}Cl_x$/spiro-OMeTAD/Au.

Table 4-4 AM 1.5 parameters of mesoporous devices prepared with and without pre-annealing

Preparation procedure	PCE / %	J_{sc} / $mAcm^{-2}$	V_{oc} / V	FF
Without pre-annealing	9.96 ± 0.68	21.20 ± 0.66	0.83 ± 0.02	0.57 ± 0.02
Pre-annealing	9.42 ± 0.71	20.68 ± 0.67	0.83 ± 0.01	0.55 ± 0.03

The J-V curves of the best pixels show clear trend of V_{oc} and J_{sc} decrease after employing the pre-annealing process. This could be because the perovskite film crystallinity is reduced, and the decreased coverage causes more "shunt paths" for recombination.

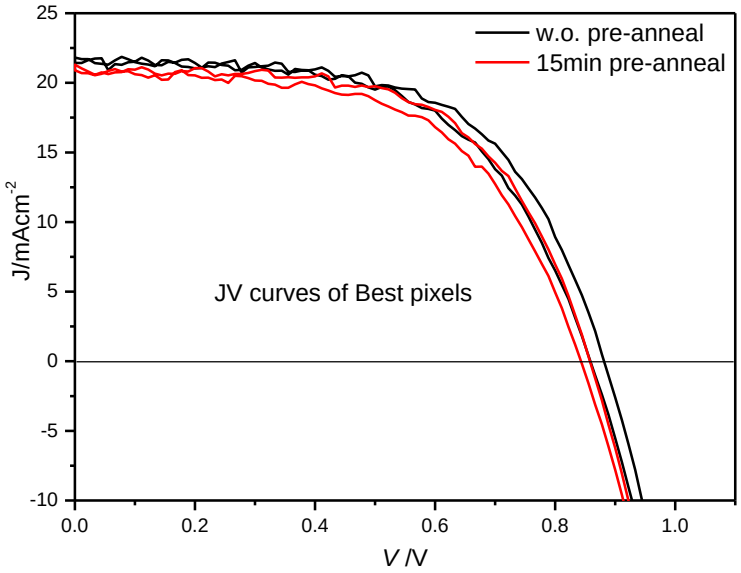

Figure 4-14 AM 1.5 J-V curves of mesoporous devices. Both the reverse scan (showing higher efficiency) and the forward scan (showing lower efficiency) are displayed.

4.5.3. Lead source

There are numerous potential ways to optimize $CH_3NH_3PbI_3$ film quality by controlling the crystallization process, such as solvent engineering[17], and varying the materials in precursor solutions.[3, 4] Usage of mixed halides in the perovskite is a very effective approach. For example, a 3:1 ratio of MAI and $PbCl_2$ precursor solution is used to improve the film quality[20], and the resulted perovskite is known as $CH_3NH_3PbI_{3-x}Cl_x$. With the addition of $PbCl_2$, the kinetics of crystallization change and the resulting film is more compact and uniform. In 2015, Zhang et.al. found that $PbAc_2$ can significantly speed up the crystallization of perovskite and make the perovskite films ultra-smooth.[21] However, when those optimized parameters are taken as reference, the variation in results needs to be considered as the fabrication of perovskite devices is affected by a

great many factors and highly depends on the circumstances in the lab where they are being made. For instance, in Zhang's work[21], PbI_2 was not completely converted into $CH_3NH_3PbI_3$ when annealed at 100°C for 12 h, while in some other studies, it was fully converted within a few hours[22]. In order to investigate the effects of different lead sources on perovskite films prepared in a dry box, the perovskite film morphology was characterized, and device performances were monitored.

Here, lead acetate and lead chloride were used as lead sources in precursor solutions for the one step method of perovskite film preparation. The precursor solutions are composed of MAI and PbX_2(X=Cl^- or Ac^-) in a 3:1 ratio. Spin coated films were annealed at 100°C for 5min ($PbAc_2$) and 100min ($PbCl_2$) respectively, and the device fabrication procedures can be found in chapter 3. The resulting perovskite films were found to be remarkably different in morphology, as shown in Figure **4-15**. AFM colour maps and 3D images indicate that perovskite film made from $PbCl_2$ has bigger grains and a rougher surface (127nm) than the one from $PbAc_2$ (48nm), and film from $PbAc_2$ has a better coverage of the substrate but with smaller grains, which could mean more recombination at grain boundaries. The 3D images (b) and (d) roughly reveal the thickness of the perovskite films. Due to the large increase in the roughness, perovskite films made from $PbCl_2$ (Figure **4-15**(b)) appeared to be much thicker than the one from PbAc2 (Figure **4-15**(d)).

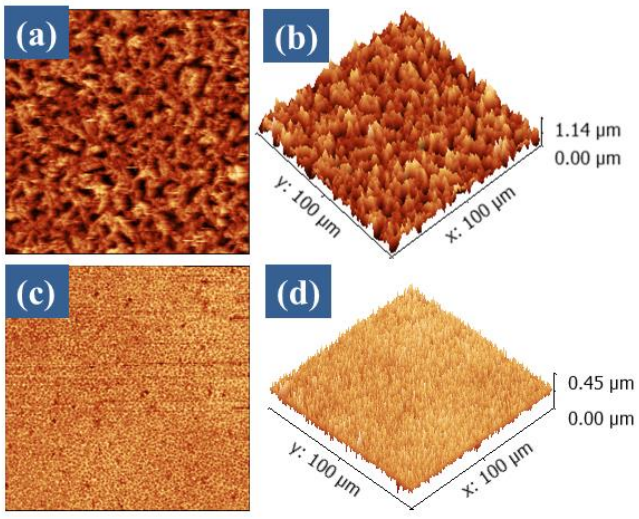

Figure 4-15 AFM images of perovskite films from different lead sources. (a) colour map and (b) 3D view of perovskite films made by using $PbCl_2$, (c) colour map and (d) 3D view of perovskite films made by using $PbAc_2$. Image sizes are all 100µm ×100µm. Perovskite films were made by that one step method and deposited on compact spray pyrolysisTiO_2

Perovskite films were also characterized by XRD. No PbI_2 peaks were observed in the two spectra shown in Figure 4-16, indicating that the lead sources in two samples are fully converted. A strong diffraction peak at 14.2° is observed, which is the (110) lattice plane of $MAPbI_3$ crystal. The FWHM of the perovskite films are 0.24° ($PbAc_2$) and 0.18° ($PbCl_2$), indicating that the particles of the perovskite film from $PbCl_2$ is bigger than that from $PbAc_2$. The characteristic peak of FTO at 26.6° is not found in the spectrum of the perovskite sample made from $PbCl_2$, which can be ascribed to the strong intensity of perovskite peaks.

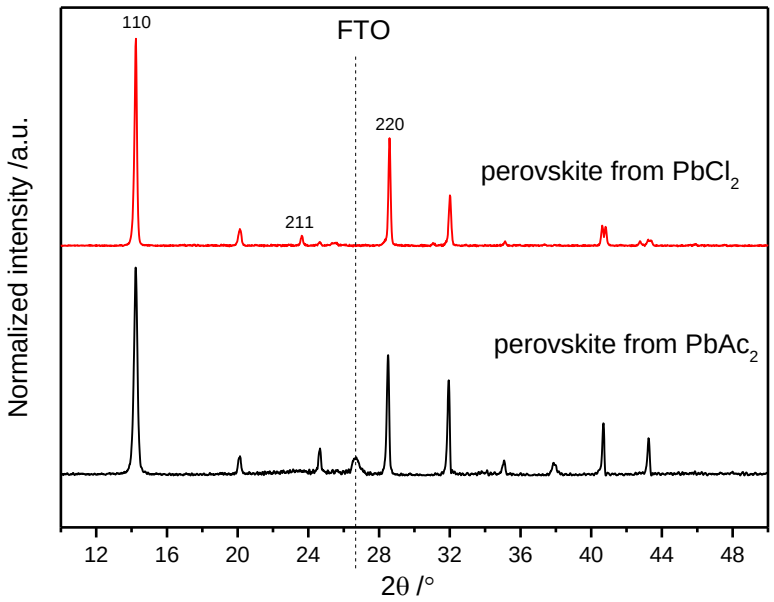

Figure 4-16 XRD curves of perovskite made from $PbCl_2$ and $PbAc_2$. Samples were detected by Cu Kα (000) Diffraction intensity was normalized to [0,1].

Devices were fabricated by using different lead sources, and the performance of solar cells was demonstrated in Table **4-5**. The standard deviation in efficiency of devices prepared from $PbAc_2$ was quite narrow, implying the active layer is uniform, which is consistent with the AFM images. However, the average J_{sc} is 16.26 $mAcm^{-2}$, much lower than that of devices from $PbCl_2$. This is within expectation, since the XRD has revealed the crystallinity of perovskite from $PbAc_2$ is not as good as that from $PbCl_2$.

Table 4-5 device parameters of solar cells made from different lead sources.

Lead source	PCE / %	J_{sc}/ $mAcm^{-2}$	V_{oc} / V	FF
$PbCl_2$	9.20 ± 3.17	17.45 ±1.65	0.87 ± 0.16	0.59 ± 0.12
$PbAc_2$	10.22 ± 0.47	16.26 ± 0.36	1.02 ± 0.01	0.61 ± 0.01

The J-V curves of best-performing pixel in each case are shown in Figure **4-17**. When $PbAc_2$ was used as the lead source, the V_{oc} is enhanced, but the J_{sc} is decreased in comparison with $PbCl_2$ device. The modified V_{oc} can be attributed to the improved coverage which can reduce the 'shunt path', and decrease the recombination.

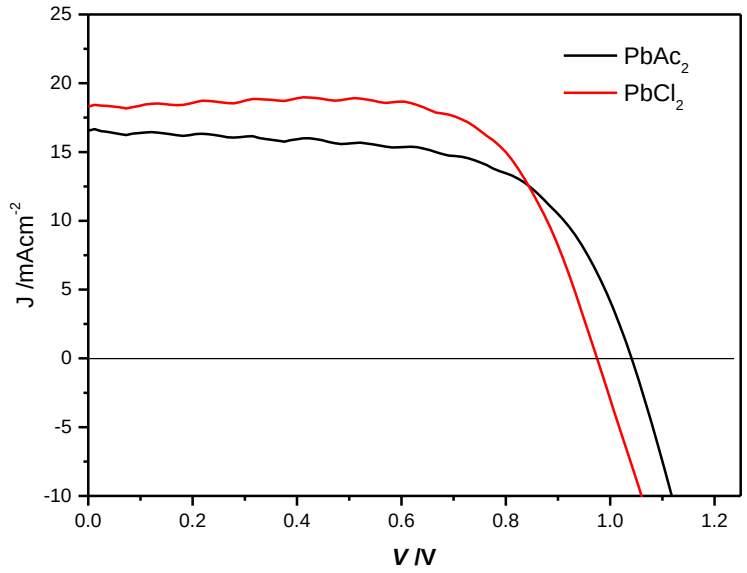

Figure 4-17 AM 1.5 J-V curves of perovskite solar cells made from $PbAc_2$ and $PbCl_2$. Devices tested at one sun AM1.5 at room temperature. The active area is $7.5mm^2$

The study into varying the lead sources reveals that $PbAc_2$ can significantly speed up crystallization of the perovskite film. The resulting film was uniform and compact, and the V_{oc} of devices was improved compared with $PbCl_2$ devices. Though the champion device had a lower efficiency than the champion $PbCl_2$ one, the average efficiency was found to be higher than for $PbCl_2$ and distributed in a narrow range. To further achieve better devices by using $PbAc_2$, the crystallinity of the perovskite film needs to be improved. More research therefore should be done to control the perovskite film annealing process, such as the annealing temperature or annealing time. This study shows how important it is to optimise perovskite film preparation for the specific lab conditions since minor changes in humidity or solvent atmosphere in the dry box can greatly change to observed results.

4.6 Efficiency measurement of solar cells - scan rates and hysteresis

The phenomenon of hysteresis was noticed when J-V scans were used to evaluate the device performances, and it was found to be related to the architectures of devices and

the processing conditions. Hysteresis has been discussed by many researchers.[23, 24] However, the reasons behind the phenomenon still remain unclear. Researchers have reported that trap states at the interfaces, charge collection at interfaces and properties of perovskite itself (e.g. mobile ions, a ferroelectric effect, capacitive character) can attribute to the hysteresis[25]. It is observed to change with scan directions and scan rates of J-V curves, as well with illumination conditions and temperature[23, 26, 27]. Generally, the hysteresis is more evident in planar structure solar cells and less pronounced in mesoporous structure solar cells. Since the hysteresis is highly dependent on processing conditions, we monitored the hysteretic behaviours for devices made in our laboratory, and both the planar solar cells and mesoporous solar cells were studied.

Devices were prepared with mixed halide perovskite layers ($MAPbI_{3-x}Cl_x$) deposited using the one-step method and devices were assembled in a dry box. The hysteresis was measured by recording the J-V curves at different scan rates from 4000mV/s to 10mV/s. All the scans start at open circuit to short circuit, before scanning to short circuit then back to open circuit. Before scanning, the devices were polarized at 1.1V for 5s. Both planar solar cells and mesoporous solar cells were investigated and the obtained J-V curves are displayed in Figure **4-18** and Figure **4-20** respectively. J-V curves of planar solar cells show very evident hysteresis within a certain range of scan rates, and the hysteresis disappears when scanning at very low or very high speed. Similar trends have been seen in some other studies[13].

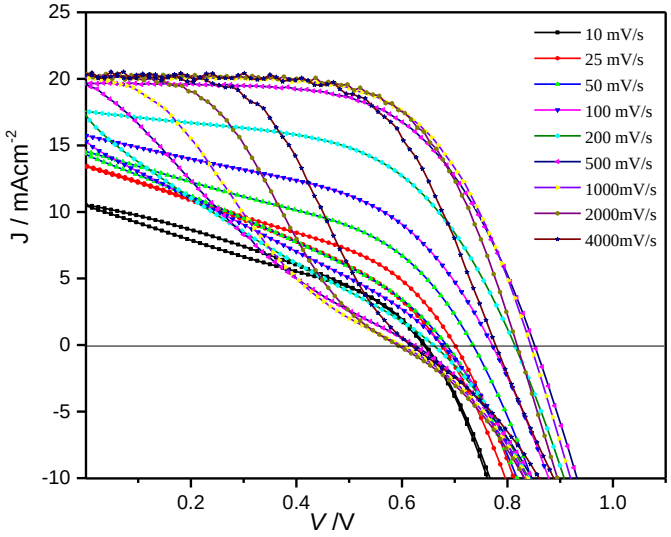

Figure 4-18 J-V curves of reverse scans and forward scans of planar structure devices at different scan rates. Devices tested at one sun AM1.5 at room temperature. The active area is 7.5mm^2

The hysteresis phenomenon is very pronounced when the efficiencies calculated from the reverse scan and the forward scan are compared. Shown in Figure **4-19**, the efficiency calculated based on reverse scan (open circuit to short circuit) is much higher than that from the forward scan (short circuit to open circuit) within the middle range of scan rates, and the difference reduces when at high and low scan rates. Interestingly, the efficiency of the forward scan was found to be higher than that of the reverse scan when tested at 10 mV/s.

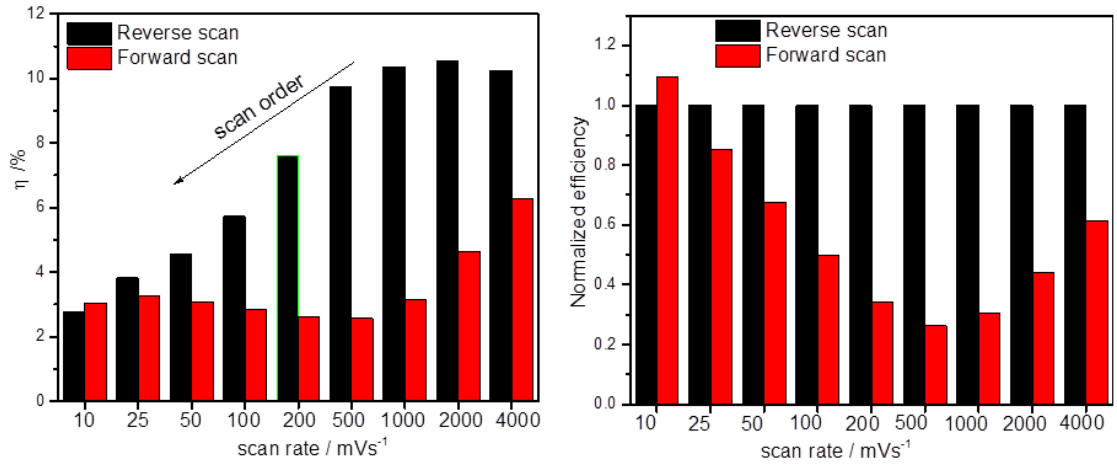

Figure 4-19 Hysteresis of planar solar cells shown by comparing device efficiencies of reverse scan and forward scan at different scan rates. Devices tested at one sun AM1.5 at room temperature. The active area is 7.5mm^2

The J-V curves of mesoporous devices at various scan rates are displayed in Figure **4-20**. Unlike the planar solar cells, the hysteresis of mesoporous devices is negligible. The efficiency shown in the reverse scan and forward scan are very close. This is consistent with reported studies[23].

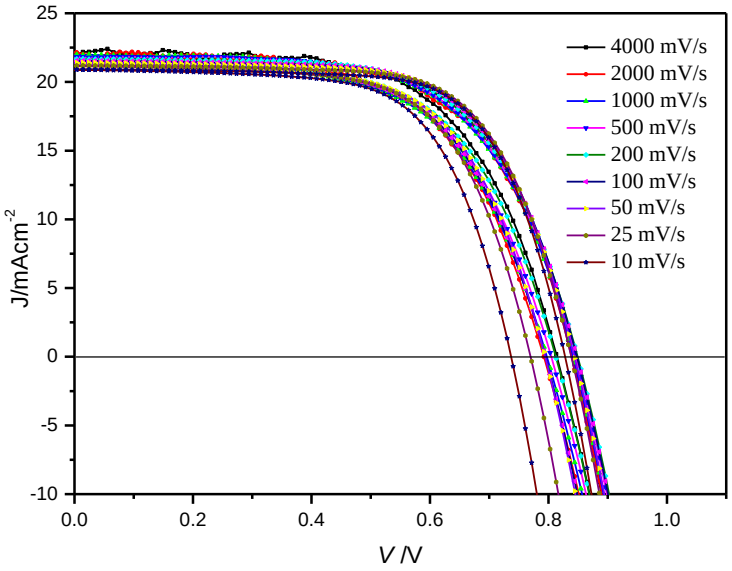

Figure 4-20 J-V curves of reverse scans and forward scans of mesoporous structure devices at different scan rates. Devices tested at one sun AM1.5 at room temperature. The active area is 7.5mm^2

Figure **4-21** gives the comparison of efficiencies calculated via reverse scan and forward scan. It is clear that the efficiencies from different scan directions are very close, and the dependence of efficiency on scan rates is not as apparent as the planar device. From the normalized efficiency figure, the hysteresis shows similar trend as the planar device which decreases at very high and low scan rates, though not distinctly.

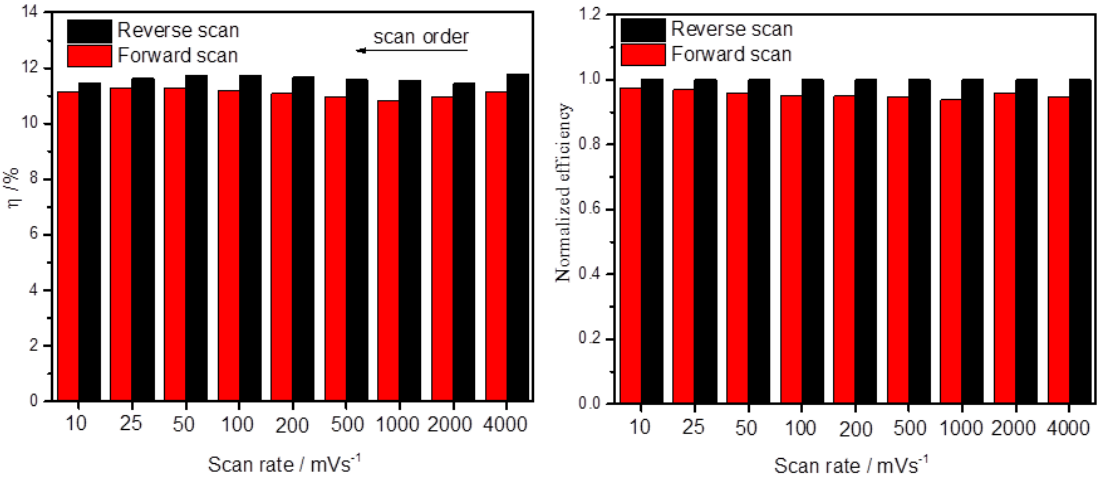

Figure 4-21 Mesoporous structure device efficiency and hysteresis comparison at different scan rates. Devices tested at one sun AM1.5 at room temperature. The active area is 7.5mm^2 and the device architecture is TEC15/c-TiO_2/m-TiO_2/$CH_3NH_3PbI_{1-x}Cl_x$/spiro-OMeTAD/Au

4.7 The configuration of devices

The configuration of devices is very important as it decides whether accurate parameters can be obtained when characterising the cells. As demonstrated in Scheme **4-1**, our first-generation device has 10 independent pixels on each substrate. The cathode electrode for electron collecting, a conductive strip, was located in the middle, and the 10 pixels were symmetrically aligned at the two sides. However, we found the pixels close to the edge (e.g. 1, 6 5, 10) frequently showed inferior performance compared to other pixels on the same substrates. We supposed that it is due to the non-uniformity in film thickness at the edge of the active layers, which is possibly caused by edge effects of the spin coating. The upgraded configuration (configuration-2) has 6 pixels which are more centred. The deposition of the gold contact is finely controlled by using a mask. The final area is calculated by taking a digital image of the active area and the dimensions are then measured in image J in order to make the characterization more accurate. As shown in Scheme **4-1**, no pixel was found to be working improperly.

Configuration-1

Pixels	1	2	3	4	5	6	7	8	9	10
Device-1				*						
Device-2							*			
Device-3									*	

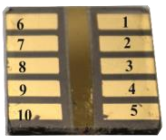

Configuration-2

Pixel	1	2	3	4	5	6
Device-1			*			
Device-2		*				
Device-3	*					

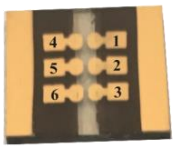

Scheme 4-1 Configurations of solar cell devices. * represents the best-performing pixel, and green colour represents the pixel functioning properly, and the red colour represents the pixel does not work or showed an unusually inferior performance.

4.8 Conclusions

In addition to standard perovskite solar cells preparation procedures, some factors that could severely influence the device performance were studied in order to optimize the device PCE in our lab. The work in this chapter is basic, but it was important to establish baseline devices to support the later research projects. The optimization considered the substrate, the compact layer, perovskite layer and ultimately the whole

device configuration. Different TCO glasses were compared. TEC7 and TEC15, though having different electric and electronic characters, were found to show similar performance when used as conducting substrates. ITO glass was unsuitable due to the high cost and the loss of conductivity when it was used to prepare conventional TiO_2 based devices. TiO_2 compact layers prepared by spray pyrolysis were more easily wetted by the perovskite precursor solution than spin coated TiO_2 layers, which was beneficial to make more compact and uniform perovskite films. Further studies on the perovskite layer show that if device are to be fabricated in the ambient environment, the humidity should be below 42%, as the coverage decreases dramatically for only a 5% humidity increase. The pre-annealing process is good for making planar perovskite films but disadvantageous to mesoporous perovskite films. The type of lead used in precursor solutions has important impacts on the perovskite film morphology. $PbAc_2$ was observed to significantly improve the coverage of perovskite film but to decrease the grain size and crystallinity. More work needs to be done to find the optimal process to prepare perovskite film from $PbAc_2$ under our laboratory conditions. The hysteresis of planar and mesoporous devices made in our lab was compared and the mesoporous solar cells has negligible hysteresis. The configuration of the solar cell was upgraded from 10 pixel substrate to 6 pixel substrate in order to make the characterization of devices more accurate and reproducible.

4.9 Acknowledgements

The author thanks Isabella Poli for help with the investigation about the effects of the lead source (lead acetate PCE study). The author also thanks Dr. Ralf Niemann and Dr. Adam Pockett for designing the pixel configurations.

Supporting Information

Code of Matlab package for estimating film coverage

```
function[coverRate]=CalculateCoverage()

data=imread('warm.bmp'); % read the image you need

grayIm = rgb2gray(data); % turn it into the gray level

imshow(grayIm);

level = 0.25; % computing the level used for binary im,
```

```
binaryIm = im2bw(grayIm, level);% turn it into the binary im

imshow(binaryIm);

[m, n] = size(binaryIm); % get the dimension of the image

totalArea = m*n; % total area of this image

coverageArea = sum(sum(binaryIm)); % the area that be covered

coverRate = coverageArea / totalArea; % get the final coverage rate
```

4.10 References

1. Ke W, Xiao C, Wang C, Saparov B, Duan H-S, Zhao D*, et al.* Employing Lead Thiocyanate Additive to Reduce the Hysteresis and Boost the Fill Factor of Planar Perovskite Solar Cells. *Adv Mater* 2016, **28**(26)**:** 5214-5221.

2. Liang P-W, Liao C-Y, Chueh C-C, Zuo F, Williams ST, Xin X-K*, et al.* Additive Enhanced Crystallization of Solution-Processed Perovskite for Highly Efficient Planar-Heterojunction Solar Cells. *Adv Mater* 2014, **26**(22)**:** 3748-3754.

3. Lee MM, Teuscher J, Miyasaka T, Murakami TN, Snaith HJ. Efficient Hybrid Solar Cells Based on Meso-Superstructured Organometal Halide Perovskites. *Science* 2012, **338**(6107)**:** 643-647.

4. Colella S, Mosconi E, Fedeli P, Listorti A, Gazza F, Orlandi F*, et al.* MAPbI3-xClx Mixed Halide Perovskite for Hybrid Solar Cells: The Role of Chloride as Dopant on the Transport and Structural Properties. *Chem Mater* 2013, **25**(22)**:** 4613-4618.

5. Saliba M, Matsui T, Seo J-Y, Domanski K, Correa-Baena J-P, Nazeeruddin MK*, et al.* Cesium-containing triple cation perovskite solar cells: improved stability, reproducibility and high efficiency. *Energy Environ Sci* 2016, **9**(6)**:** 1989-1997.

6. Burschka J, Pellet N, Moon S-J, Humphry-Baker R, Gao P, Nazeeruddin MK*, et al.* Sequential deposition as a route to high-performance perovskite-sensitized solar cells. *Nature* 2013, **499**(7458)**:** 316-319.

7. Ball JM, Stranks SD, Horantner MT, Huttner S, Zhang W, Crossland EJW*, et al.* Optical properties and limiting photocurrent of thin-film perovskite solar cells. *Energy Environ Sci* 2015, **8**(2)**:** 602-609.

8. Zhang Y, Liu M, Eperon GE, Leijtens TC, McMeekin D, Saliba M*, et al.* Charge selective contacts, mobile ions and anomalous hysteresis in organic-inorganic perovskite solar cells. *Mater Horiz* 2015, **2**(3)**:** 315-322.

9. Yang B, Mahjouri-Samani M, Rouleau CM, Geohegan DB, Xiao K. Low temperature synthesis of hierarchical TiO2 nanostructures for high performance perovskite solar cells by pulsed laser deposition. *Phys Chem Chem Phys* 2016, **18**(39)**:** 27067-27072.

10. Liu M, Johnston MB, Snaith HJ. Efficient planar heterojunction perovskite solar cells by vapour deposition. *Nature* 2013, **501**(7467)**:** 395-398.

11. Liu D, Kelly TL. Perovskite solar cells with a planar heterojunction structure prepared using room-temperature solution processing techniques. *Nat Photon* 2014, **8**(2)**:** 133-138.

12. Nishimoto N, Yamada Y, Ohnishi Y, Imawaka N, Yoshino K. Effect of temperature on the electrical properties of ITO in a TiO2/ITO film. *physica status solidi (a)* 2013, **210**(3)**:** 589-593.

13. Tress W, Marinova N, Moehl T, Zakeeruddin SM, Nazeeruddin MK, Gratzel M. Understanding the rate-dependent J-V hysteresis, slow time component, and aging in CH3NH3PbI3 perovskite solar cells: the role of a compensated electric field. *Energy Environ Sci* 2015, **8**(3)**:** 995-1004.

14. Yongzhen W, Xudong Y, Han C, Kun Z, Chuanjiang Q, Jian L*, et al.* Highly compact TiO 2 layer for efficient hole-blocking in perovskite solar cells. *Applied Physics Express* 2014, **7**(5)**:** 052301.

15. Jeon NJ, Lee J, Noh JH, Nazeeruddin MK, Grätzel M, Seok SI. Efficient Inorganic–Organic Hybrid Perovskite Solar Cells Based on Pyrene Arylamine Derivatives as Hole-Transporting Materials. *J Am Chem Soc* 2013, **135**(51)**:** 19087-19090.

16. You J, Yang Y, Hong Z, Song T-B, Meng L, Liu Y*, et al.* Moisture assisted perovskite film growth for high performance solar cells. *Appl Phys Lett* 2014, **105**(18)**:** 183902.

17. Jeon NJ, Noh JH, Kim YC, Yang WS, Ryu S, Seok SI. Solvent engineering for high-performance inorganic–organic hybrid perovskite solar cells. *Nat Mater* 2014, **13**(9)**:** 897-903.

18. Ahn N, Son D-Y, Jang I-H, Kang SM, Choi M, Park N-G. Highly Reproducible Perovskite Solar Cells with Average Efficiency of 18.3% and Best Efficiency of 19.7% Fabricated via Lewis Base Adduct of Lead(II) Iodide. *J Am Chem Soc* 2015, **137**(27)**:** 8696-8699.

19. Hao F, Stoumpos CC, Liu Z, Chang RPH, Kanatzidis MG. Controllable Perovskite Crystallization at a Gas–Solid Interface for Hole Conductor-Free Solar Cells with Steady Power Conversion Efficiency over 10%. *J Am Chem Soc* 2014, **136**(46)**:** 16411-16419.

20. Deschler F, Price M, Pathak S, Klintberg LE, Jarausch D-D, Higler R*, et al.* High Photoluminescence Efficiency and Optically Pumped Lasing in Solution-Processed Mixed Halide Perovskite Semiconductors. *J Phys Chem Lett* 2014, **5**(8)**:** 1421-1426.

21. Zhang W, Saliba M, Moore DT, Pathak SK, Hörantner MT, Stergiopoulos T*, et al.* Ultrasmooth organic–inorganic perovskite thin-film formation and crystallization for efficient planar heterojunction solar cells. *Nat Commun* 2015, **6:** 1- 10.

22. Heo JH, Song DH, Han HJ, Kim SY, Kim JH, Kim D*, et al.* Planar CH3NH3PbI3 Perovskite Solar Cells with Constant 17.2% Average Power Conversion Efficiency Irrespective of the Scan Rate. *Adv Mater* 2015, **27**(22)**:** 3424-3430.

23. Snaith HJ, Abate A, Ball JM, Eperon GE, Leijtens T, Noel NK*, et al.* Anomalous Hysteresis in Perovskite Solar Cells. *J Phys Chem Lett* 2014, **5**(9)**:** 1511-1515.

24. Unger EL, Hoke ET, Bailie CD, Nguyen WH, Bowring AR, Heumuller T*, et al.* Hysteresis and transient behavior in current-voltage measurements of hybrid-perovskite absorber solar cells. *Energy Environ Sci* 2014, **7**(11)**:** 3690-3698.

25. Fan R, Huang Y, Wang L, Li L, Zheng G, Zhou H. The Progress of Interface Design in Perovskite-Based Solar Cells. *Adv Energy Mater* 2016, **6**(17)**:** 1600460-n/a.

26. Levine I, Nayak PK, Wang JT-W, Sakai N, Van Reenen S, Brenner TM*, et al.* Temperature-dependent Hysteresis in MAPbI3 Solar Cells. *arXiv preprint arXiv:160403907* 2016.

27. Zhang C, Sun D, Liu X, Sheng C-X, Vardeny ZV. Temperature-Dependent Electric Field Poling Effects in CH3NH3PbI3 Optoelectronic Devices. *J Phys Chem Lett* 2017, **8**(7)**:** 1429-1435.

Chapter 5 Perylene Diimdes as Interlayers in Hybrid Perovskite Solar Cells

Contents

5.1 Introduction

In a conventional "n-i-p" structured hybrid perovskite solar cell, TiO_2 is the most commonly used inorganic electron transporting layer (or hole blocking layer) due to its good electrical and electronic properties. It has a band gap of 3.2 eV[1] which is transparent to visible light and has a low lying valance band maximum (VBM, -7.6 eV) which is good for hole blocking. Besides, it is easy to get a uniform, continuous and compact anatase TiO_2 layer through spin coating[2], spray pyrolysis[3] and other methods such as chemical vapour deposition (CVD) and atomic layer deposition(ALD)[4, 5]. Despite its numerous advantages as a blocking layer, TiO_2 has some drawbacks, such as surface defects and relatively low conductivity. The reported conductivity of TiO_2 used in perovskite solar cells is around $10^{-5} \sim 10^{-6}$ S /cm[6 7], and for a thick layer, this can limit the device PCE. Moreover, surface defects resulting from an imperfect crystal structure or chemical impurities can act as deep trap states that cause non-radiative recombination.

Interface engineering by using organic small molecules is an effective way to change the electrical and electronic properties of TiO_2. It can reduce the number of surface defects and adjust the work function as well as the surface energy. For example molecules with carboxyl groups (e.g. benzoic acids) can interact with non-bonded atoms on TiO_2 surface [8]. There are a few different groups of molecules can be used as interlayer in solar cells, among which, perylene diimide derivatives reported as typical n-type interlayer have attracted interest in organic solar cells and perovskite solar cells for their good conductivity(e.g. 10^{-5} S/cm)[9, 10]. In this chapter, we studied the optimization of hybrid perovskite solar cells' performance via interfacial engineering, and two perylene diimides, N, N'-di(L-histidine)-perylene-3,4:9,10-tetracarboxylic acid diimide (PDIH) and N, N'-di(L-valine)-perylene-3,4:9,10-tetracarboxylic acid diimide (PDIV) were used as interlayers. They both have carboxyl groups which are able to bind to metal oxides, and the interlayers prepared by these two molecules succeeded in changing surface properties of the TiO_2. Two different interlayer preparation methods spin coating and dip coating were used, and their effect on interlayer quality and device performance was investigated. The two organic materials were provided by Professor David Adams, University of Liverpool. The procedures to prepared two molecules can be found in reference 9 .[11]

5.2 Experimental

Solutions 0.05mM PDIV or PDIH solutions were prepared by dissolving the solid in anhydrous DMSO. The solutions were kept under magnetic stirring overnight to make a fully dissolved clear dipping solution. 0.5mM solutions were made by the same procedure.

PDIs films PDIs films were prepared either through the spin coating method or the dip coating method.

1) By spin coating method. 1 equivalent 0.1 mol/L KOH was added into 2mg/mL PDIs aqueous solutions to improve the materials' solubility. Solutions were then stirred for 4 hours at room temperature (RT) and filtered with a 0.45 μm filter before use. PDIs films were deposited at 1k rpm, 2k rpm or 3k rpm with 100 μL solution and annealed at 120°C for 1h. Samples are labeled as 1k rpm, 2k rpm and 3k rpm.
2) By dip coating method. Before being immersed into the solution, FTO substrates with compact TiO_2 were heated to 150°C to remove any moisture and then cooled down to 70°C. The 70 °C substrates were then dipped into 0.05mM PDIs DMSO solutions contained in sealable glass cleaning jars and kept for 3 hours or 24 hrs. Once being taken out, the substrates were rinsed with 2-isopropanal (IPA) and dried with dry N_2 flow. The as-prepared substrates were sealed in a clean petri dish before perovskite layer deposition.

Device fabrication the perovskite layers described in this chapter were prepared by a one-step spin coating method or a two-step vapour-assisted solution processing method. More details about these two methods can be found in Chapter 3 and reported procedures in reference 10[12]

Characterization

1) ***Photoluminescence*** perovskite film samples (deposited on glass or glass with TiO_2) were illuminated via the air/perovskite interface under vacuum at around 10^{-3} mbar. For steady state photoluminescence, a laser wavelength of 510nm was used. For transient photoluminescence (TRL) measurements were carried out by using a laser pulse with a width of approximately 20ps FWHM and

wavelength of 510 nm. The laser power was measured to be 0.2mW using a power meter. The TRPL signal was collected at 770nm.

5.3 Perylene diimides (PDIs) molecular structure and properties

5.3.1 Molecular structure and solubility

The molecular structures of the two molecules used in this work are shown in **Figure 5-1** . They both have –COOH functional groups, which allow them to chemically bind to the metal oxide surface. Because of the conjugated core, the PDIs showed low solubility in many commonly used solvents. As listed in **Table 5-1**, PDIH and PDIV are practically insoluble in chlorobenzene, toluene and chloroform and are partially soluble in DMSO and DMF. In this work, anhydrous DMSO was used as the solvent in the dip coating process for solubility and safety purposes, and KOH was used as an additive to prepare the precursor solution for spin coating process.

(1) PDIH

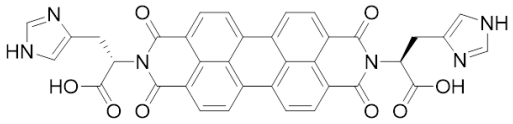

(2) PDIV

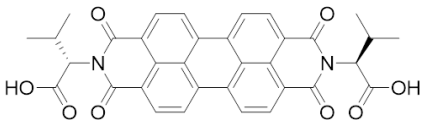

Figure 5-1 Structures of the perylene diimides used in this work

Table 5-1 Solubility of PDIs in common solvents

Material	chlorobenzene	chloroform	DMSO	DMF	toluene	acetonitrile	H_2O
PDIH	-	-	±	±	-	-	±
PDIV	-	-	±	±	-	±	±

± partially soluble, less than 1mg/mL

- not soluble

5.3.2 Optical property and thermal stability

PDIV and PDIH were dissolved into DMSO to make 0.05mM solutions. Clear red solutions were obtained after overnight magnetic stirring. The optical properties and thermal stability of the two molecules were characterized by UV-Vis and TGA

measurements. As shown in Figure **5-2**, PDIV and PDIH have almost the same absorption onsets which are around 550nm, indicating a HOMO-LUMO gap of ~2.2 eV. They both show peaks at around 490nm and 530nm, which represent the 0-1 and 0-0 vibronic bands of the S0/S1 transition , respectively[13].

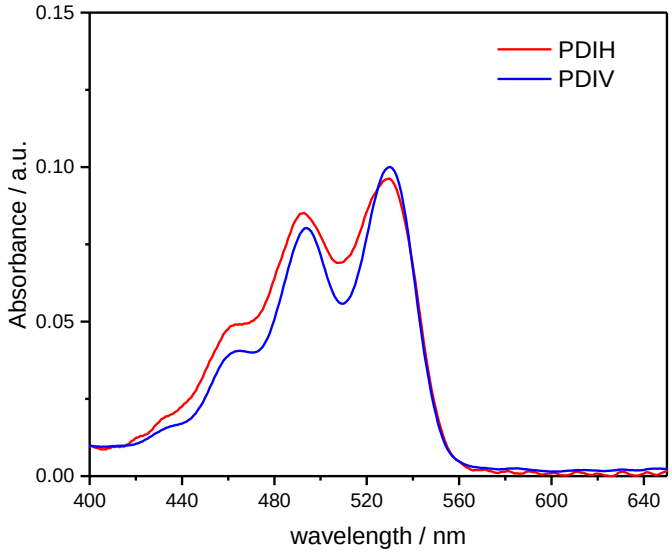

Figure 5-2 UV-Vis absorption of 0.05 mM PDIs DMSO solutions.

In order to find out whether thermal decomposition of the interlayer might occur during the perovskite layer annealing procedure, a study of the thermal stability study of PDIV and PDIH below 200°C was carried out. The results of the thermogravimetry (TGA) are shown in **Figure 5-3**. The mass loss started from the beginning of heating for both the PDIV and PDIV samples. For the PDIV sample, the weight stop dropping after 140°C and stayed stable until around 200°C. The weight loss is around 5%, and it can be attributed to the remove of the moisture in the sample. For the PDIH sample, the moisture removal process is slow and it keeps losing mass until reaching the temperature for the 2nd mass loss. The mass loss in the first step is around 8.8%. With further increase of the temperature, a 2nd stepped decrease in mass occurred. But the mass loss starts above 200°C, indicating that PDIV and PDIH will both be stable at the temperature at which perovskite film is made (typically. below 150°C).

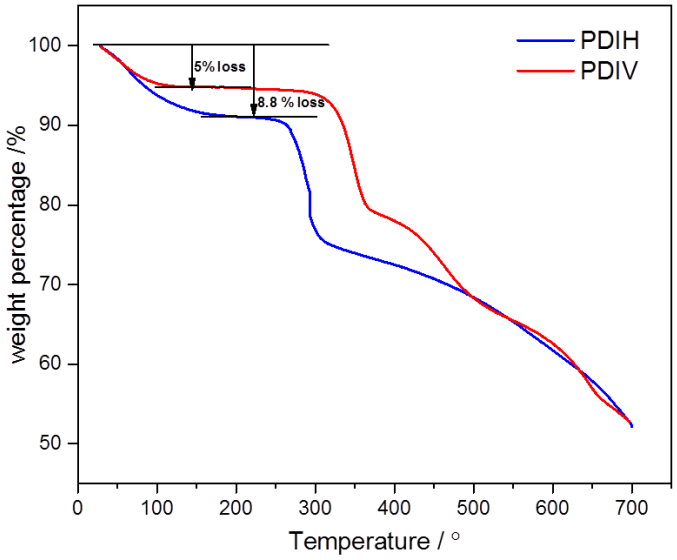

Figure 5-3 Thermogravimetric analysis (TGA) of PDIV and PDIH. Experiments were carried out under N_2 gas flow and a heating rate of 5 °C/min from 30°C to 700°C.

5.3.3 Electrochemistry

Cyclic voltammetry (CV) and UV-Vis measurement were used to estimate the highest occupied molecular orbital (HOMO) and the lowest unoccupied molecular orbital (LUMO) energy levels of the PDIV and PDIH molecules. The energy level of the HOMO can be related to the first oxidation process measured by cyclic voltammetry. The LUMO can be related to the first reduction peak[14]. The CV measurements were carried out under an argon atmosphere and ferrocene was used as an internal standard which was added into the same solution where the CV curves of PDIs were obtained.,[15] The HOMO and LUMO values were then estimated using the equations below:

$$\boldsymbol{E_{LUMO} \approx -[e\left(E_{onset}^{red} - E_{\frac{1}{2}}Fc/Fc^{+}\right) + 4.8\ eV]} \qquad \text{Equation 5-1}$$

$$\boldsymbol{E_{HOMO} \approx -[e\left(E_{onset}^{oxd} - E_{\frac{1}{2}}Fc/Fc^{+}\right) + 4.8\ eV]} \qquad \text{Equation 5-2}$$

$$\boldsymbol{E_{HOMO} \approx E_{LUMO} - E_{g}^{opt}} \qquad \text{Equation 5-3}$$

In which -4.8eV is the absolute energy of ferrocene–ferricenium couple[16], $E_{1/2}$ Fc/Fc$^+$ is the half-wave potential of the ferrocene-ferricenium redox couple, E_g^{opt} is the optical band gap of the material and the E_{onset}^{oxd} and E_{onset}^{red} are the onset potentials of the oxidation peak and redox peak, respectively.

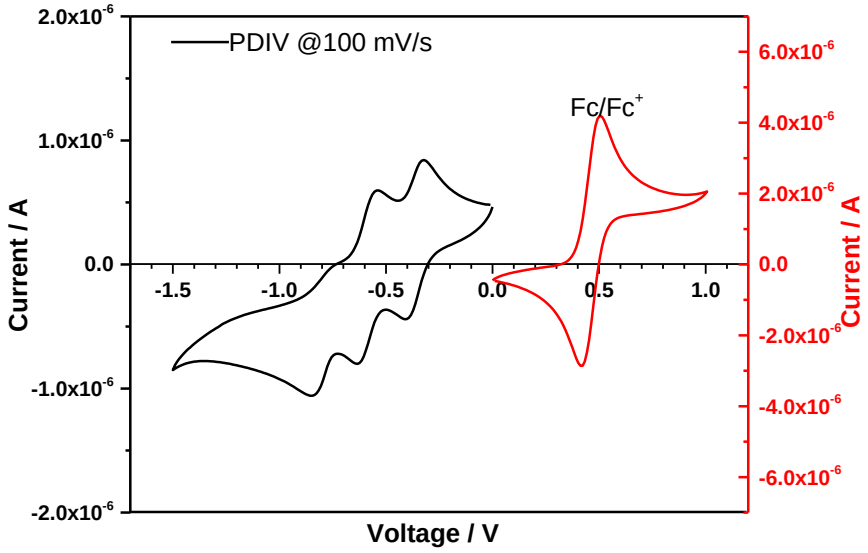

Figure 5-4 Cyclic Voltammetry of PDIV (0.25mM) in 0.1M $TBAPF_6$ DMSO soltuion with ferrocene as the internal standard(ferrocene was added into the solution of PDIs after PDIs curves were collected). Scan rate 100mV/s and the scan direction is from 0V to -1.6V. Counter electrode: Pt, working electrode: Pt column (2mm diameter) and reference electrode: Pt wire.

The cyclic voltamogram of PDIV is illustrated in Figure 5-4. The onset potential of the first redox peak is -0.35V and the $E_{1/2}$ Fc/Fc^+ is 0.47V. The LUMO of PDIV is calculated to be -4.0 eV by using equation 5-1. Since the oxidation peak corresponding to the HOMO is not clear, equation 5-3 can be used to estimate the HOMO by using the LUMO and the optical band gap. As the E_g^{opt} is 2.25eV which was obtained from UV-Vis the absorption onset of PDIV solution (Figure 5-2), the HOMO of PDIV can then be estimated. The energy levels of PDIH were determined by the same method. As shown in Table **5-2**, the HOMO and LUMO of PDIV and PDIH are all listed. They have very close energy levels due to the high similarity of the structure, and the energy levels are close to some reported PDIs (-3.63eV/-5.96eV) as well.[15] It should also be made clear that the reorganization energy was not considered when the equations were used to calculate the HOMO and LUMO. In addition, when E_g^{opt} was used to calculate the HOMO, the binding energy between the electron and hole was not considered. Therefore, equation 5-3 and CV can only be used to give a rough estimate of the energy levels, but it is useful to have an estimate to compare with literature values for other PDIs.

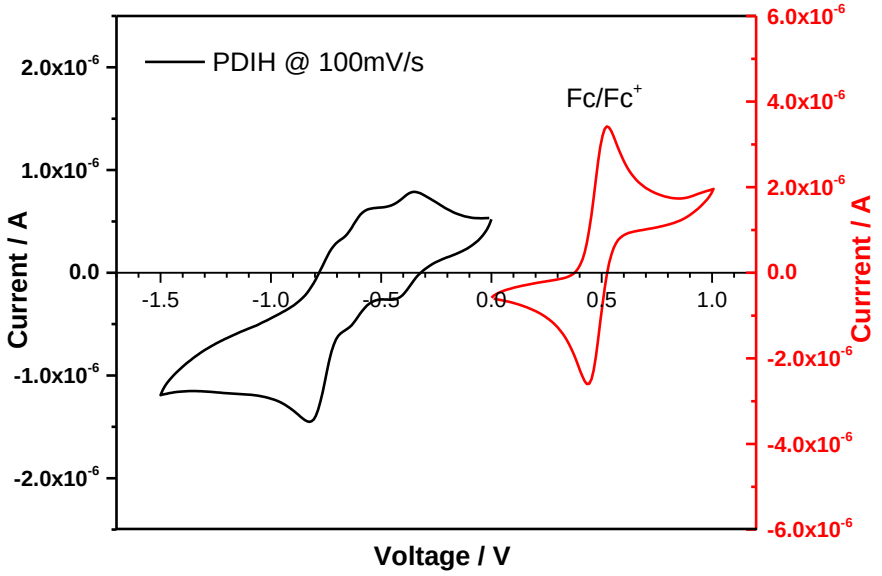

Figure 5-5 Cyclic Voltammetry of PDIH (0.2mM) dissolved in 0.1M $TBAPF_6$ DMSO solution with ferrocene as internal standard. Scan rate: 100mV/s, counter electrode: Pt, working electrode: Pt column (2mm diameter) and reference electrode: Pt wire. Scans strart from 0V to -1.6V.

Table 5-2 HOMO and LUMO of PDIs calculated according to CV tests.

Material	E_{onset}^{red} / V	$E_{1/2(}Fc/Fc^{+}$) / V	E_g^{opt} / eV	LUMO /eV	HOMO /eV
PDIV	-0.35	0.47	2.25	-3.98	-6.23
PDIH	-0.32	0.48	2.24	-4.00	-6.24

5.3.4 Dipole moment estimation

Molecular dipoles of PDIV and PDIH can be estimated based on the non-relaxed structures (the 3D structure provided by chem3D is displayed in Figure **5-6**) using the software Avogadro, and the equation used to determine dipoles is as following:

$$\vec{\mu} = \sum_i q_i \vec{r_i} \qquad \text{Equation 5-4}$$

Where $\vec{\mu}$ is the dipole moment vector, q_i is the charge of the i^{th} atom, and $\vec{r_i}$ is the vector representing the position of the i^{th} charge. The absolute value of PDIV dipole is 6.30D, and it is 6.96D for PDIH. Note that the geometries of the molecules are not relaxed by ab initio calculations, thus the numbers are merely a rough estimation and should not be taken into quantitative account. Since the PDIH and PDIV have molecular dipoles, interlayers based on these molecules are expected to affect the work functions of the modified substrates.

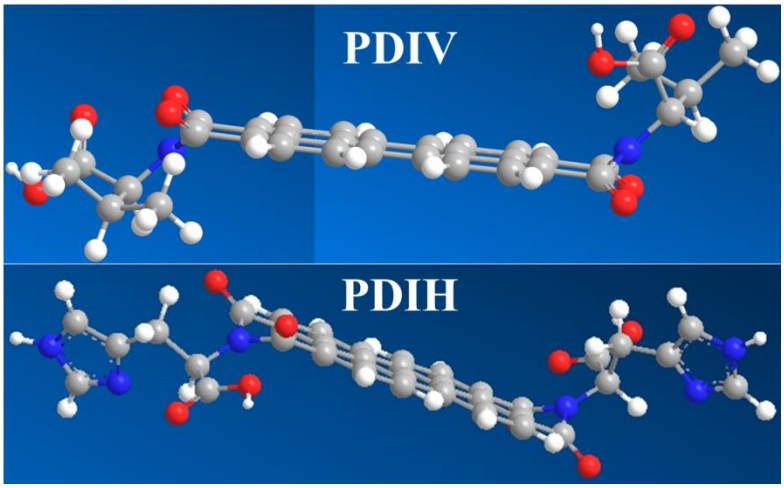

Figure 5-6 3D view of PDIs molecules through Chem3D.

5.4 Interlayer preparation through spin coating method

5.4.1 Results and discussion

In this part, PDIH interlayers were prepared using a spin coating method, and the deposition of mixed halide perovskite layer was then carried out in a dry box by a one-step method which is described in detail in Chapter 3. The sample without interlayers was labelled as the control and the other 3 samples were labelled according to the spin coating speeds at which the interlayer was prepared (i.e. 1k rpm, 2k rpm and 3k rpm). Figure 5-7 displays digital images of the deposited PDIH films. The visible colour change of the substrate after the deposition of a PDIH interlayer shows the successful deposition of PDIH film. The substrate with the PDIH interlayer deposited at 1k rpm is darker than the other samples. According to the UV-Vis curve (shown in Figure 5-8) of the film deposited at 1k rpm, which should be the sample with the thickest PDIH film. The absorption peak indicates the presence of PDIH, and suggests the spin coated layer is not a monolayer but a multilayer film as it is unlikely this UV/Vis system would be sensitive enough to measure a single monolayer. The fact that a pinkish colour can also be seen by eye again suggests a multi-layer is formed.

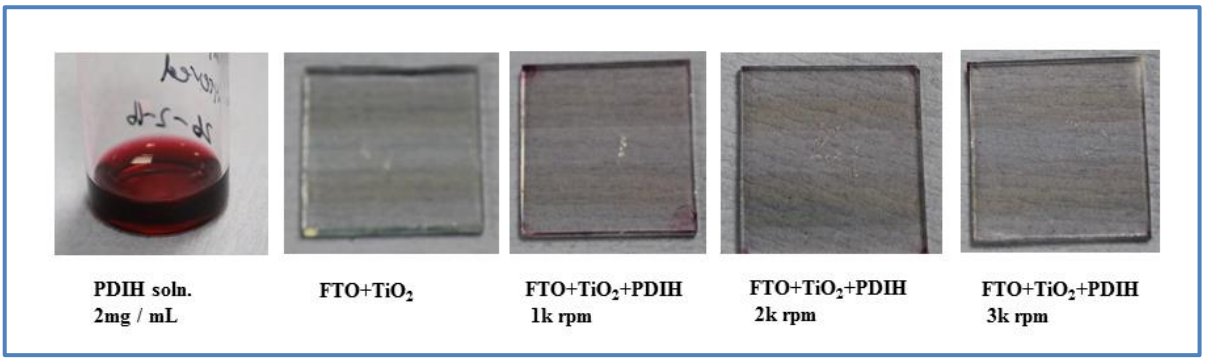

Figure 5-7 Digital image of precursor solution and spin coated thin film

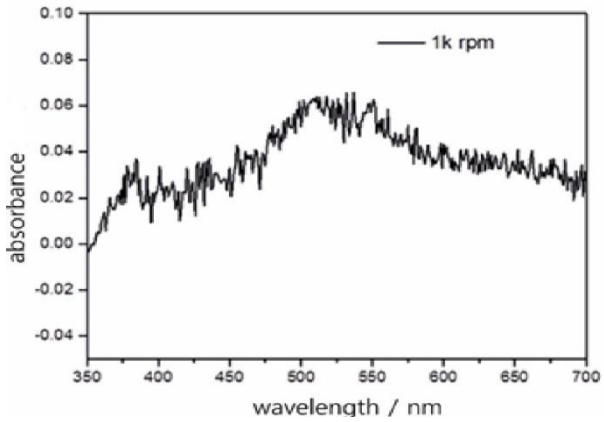

Figure 5-8 UV-Vis of the 1k rpm deposited PDIH film.

To investigate the morphology of the PDIH interlayer, AFM was carried out. It is very hard to distinguish the difference between the bare TiO_2 and the sample with PDIH as both layers (TiO_2 and PDIH) appears to mirror the surface of the underlying FTO film. As shown in Figure 5-9 (a) the image of the thin TiO_2 film looks very similar to the image of the underlying FTO (has been discussed in Chapter 4), and TiO_2 with PDIH on top also show very similar morphology. The average roughness for samples before and after interface engineering is almost the same, both around 7 nm. Thus, the morphology of the PDIH interlayer cannot be resolved – although no large aggregates of PDIH were observed. Though the film cannot be observed directly through characterization methods such as AFM or SEM, Some spectroscopic methods can be employed to study the material properties indirectly.

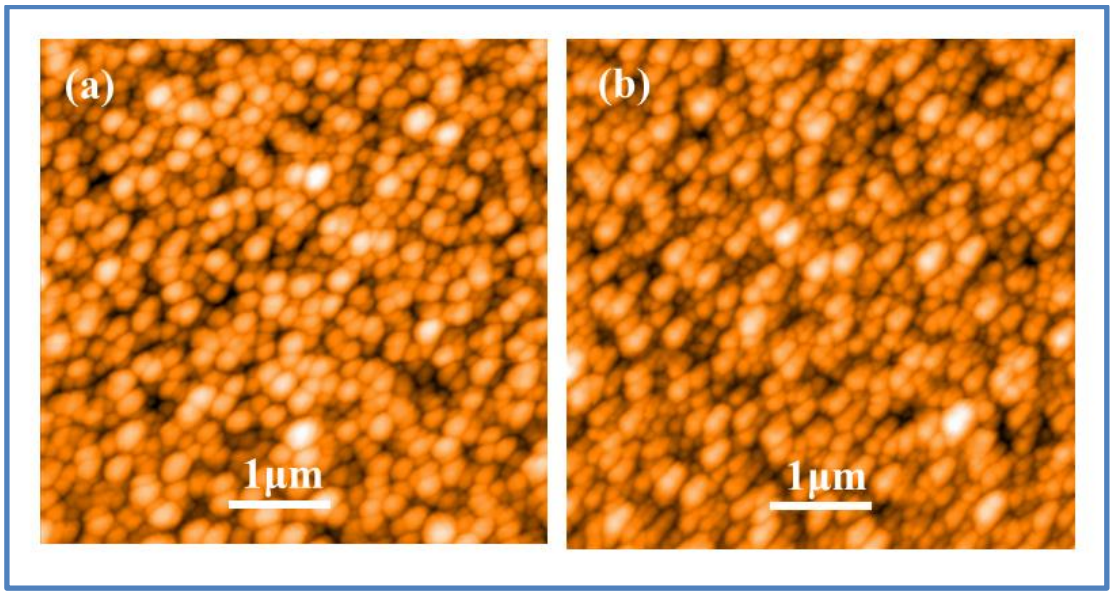

Figure 5-9 AFM images of TiO_2 (a) and TiO_2 with PDIH spin coated at 2k rpm (b).

In order to confirm the existence of the PDIH interlayer and to investigate the effects of the PDIH interlayer on the interface, X-ray photoelectron spectroscopy (XPS) and Kelvin probe force microscopy (KPFM) were used to characterize the surface properties. XPS is shown in **Figure 5-10**(a), the peaks at the binding energies 284eV and 399 eV represent C1s and N1s respectively, indicating the existence of PDIH on the TiO_2 surface.[17] KPFM results in **Figure 5-10**(b) reveal that after deposition of the PDIH interlayer, the work function of the substrate is decreased by 30 meV compared with bare TiO_2, confirming the work function adjustment function of the PDIH interlayer.

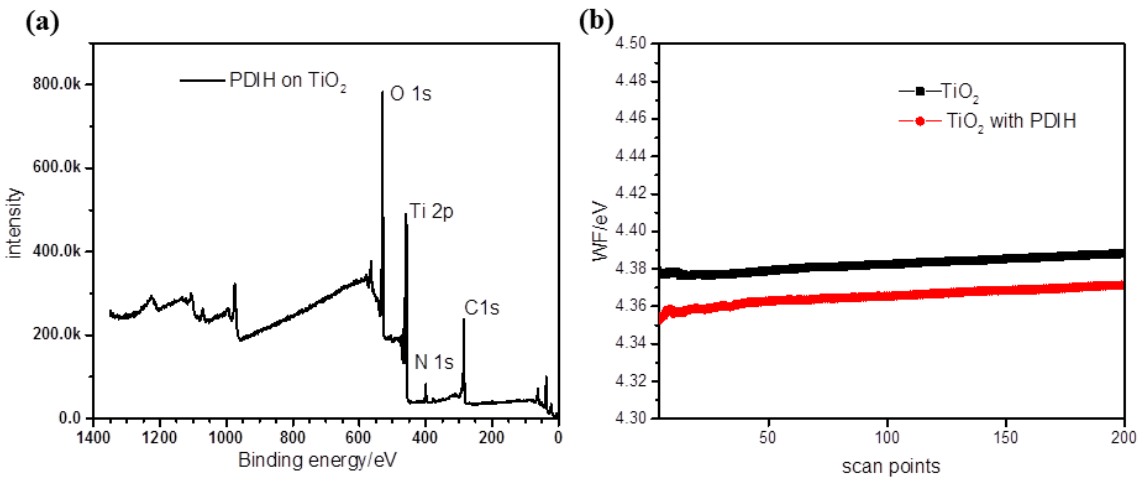

Figure 5-10 Surface properties characterization.(a) XPS and (b) KPFM of PDIH film spin coated at 2k rpm

Since the wetting properties of the substrate surface has a critical effect on the morphology of the film to be deposited, it is important to study the variation in the contact angles of the substrates before and after interface engineering. As shown in **Figure 5-11**, bare TiO_2 shows an average contact angle (to water) of 17.6°, while after being coated with a PDIH interlayer, the contact angle of the substrate is around 28°. This indicates that the PDIH has changed the surface energy and actually has made the substrate less hydrophilic. However, it cannot be concluded that the PDIH will induce worse morphology in the perovskite film as the crystallization of the perovskite is a complex process which is affected by quite a few factors (e.g. temperature, solvent).

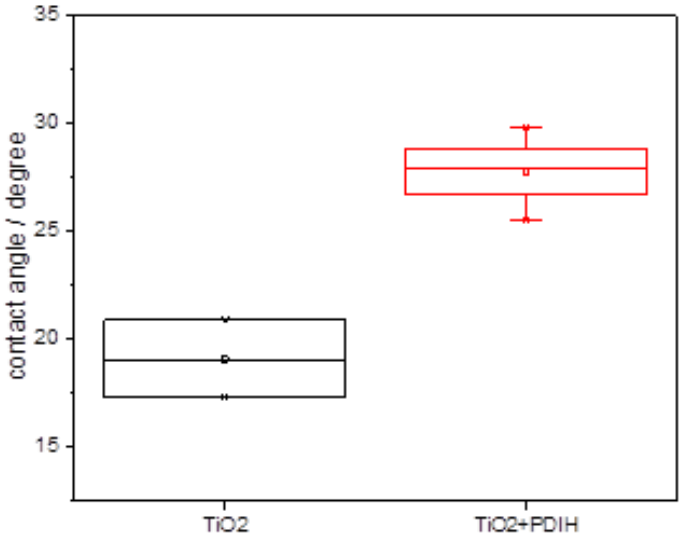

Figure 5-11 Contact angle of TiO_2 and TiO_2 with PDIH interlayer. Measurements were carried out by dropping ultrapure water on the substrate.

UV-Vis spectra of $CH_3NH_3PbI_{3-x}Cl_x$ perovskite films deposited on different substrates were measured to characterise the optical properties of perovskite layers after interface engineering. As displayed in **Figure 5-12**, all the samples show similar absorption curves. The band gap is not changed after the interface engineering and is calculated to be around 1.57eV which agrees with reported data[18]. There is no obvious absorption enhancement observed after interface engineering.

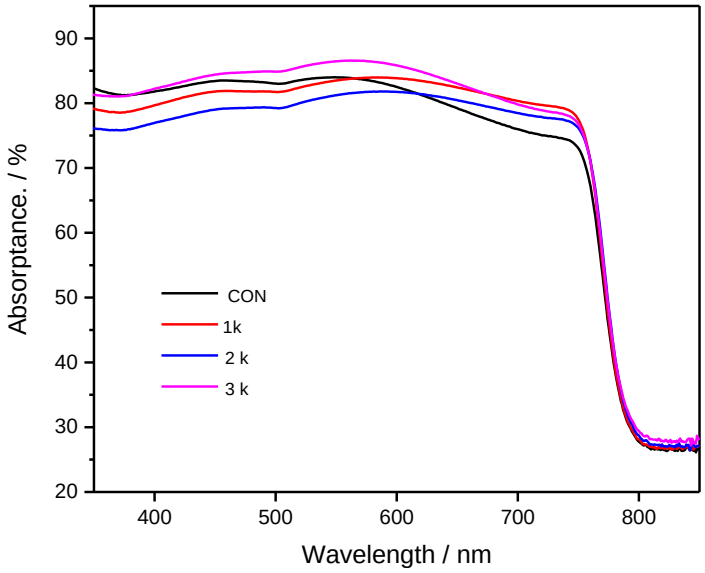

Figure 5-12 UV-Vis absorption of perovskite layer on PDIH film spin coated at different speeds.

As mentioned above surface energy and contact angle of substrates have changed after deposition of PDIH interlayers, the morphology of the perovskite layers was expected to change with the interface engineering. AFM was used to investigate the effects of the interface engineering on the morphology of mixed halide perovskite layers. In **Figure 5-13** AFM images of the control sample (**Figure 5-13**(a)) and samples with interlayers (**Figure 5-13** (b) (c) & (d)) are displayed. Grain sizes in the perovskite films were observed to change with the introduction of interlayers: samples with PDIH show smaller grain sizes across the entire field of view compared with the control sample. In addition, the average roughness of samples (shown in Table **5-3**) indicate that perovskite films are smoother on interlayers compared to on bare TiO_2 layer except the 2k deposited sample. However, the standard deviations of samples deposited on interlayers are much higher than the control samples, indicating the perovskite films on the interlayers are less uniform.

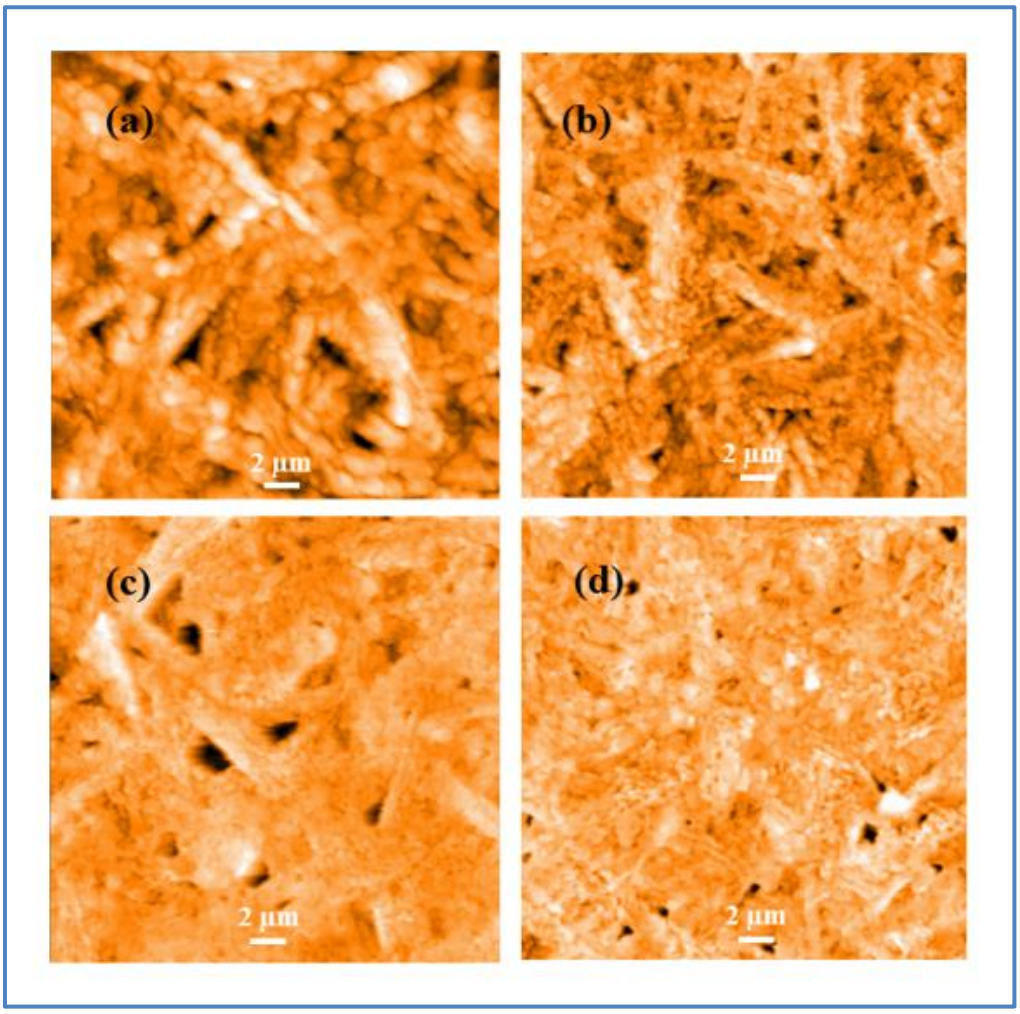

Figure 5-13 AFM images of mixed halide perovskite films. (a) Control, (b) with PDIH 1k rpm, (c) 2k rpm, (d) 3krpm

Table 5-3 Average roughness (from AFM tests) of mixed halide perovskite films deposited on different substrates

Samples	Control	1k rpm	2k rpm	3k rpm
Average roughness/nm	67.5 ± 0.6	56.3 ± 4.7	87.1 ± 16.2	57.0 ± 12.0

To further explore the crystal structure of the prepared perovskite films, X-ray diffraction was used and the patterns are illustrated in **Figure 5-14**. All the samples show a weak peak at 12.7° which is attributed to PbI_2, revealing the incomplete conversion of PbI_2 in perovskite film. The diffraction peaks at 14.2°, 23.5, 24.5°, 28.2°, 28.5°, 31.9° and 43.3°, exhibited in the four curves, were assigned to be the (110), (211), (202), (004), (220), (312) and (314) lattice planes of the tetragonal crystal structure of $CH_3NH_3PbI_3$, implying that interface engineering does not change the material crystal structure. Besides, enlarged scale plots (Figure 5-15) for peaks at 14.2° and 28.5 show differences in the full width half-maximum (FWHM) of the four samples. The control

sample gives the smallest FWHM, indicating a bigger particle size which is consistent with the AFM images. The control also shows higher peak intensity, revealing that the crystallintiy is better than the films deposited on PDIH interlayers.

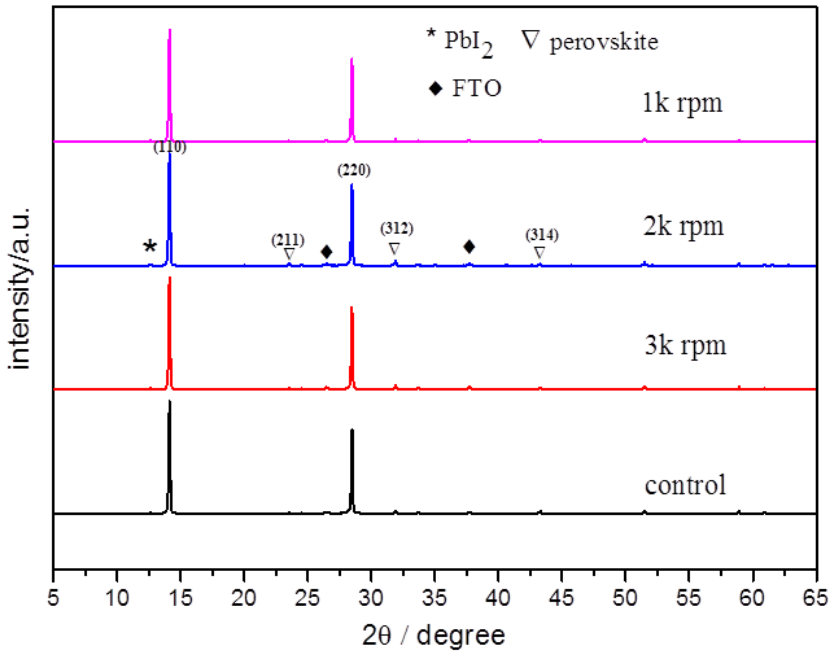

Figure 5-14 XRD of perovskite films (intensity normalized) on different substrates. Samples are perovskite layer on FTO glass with TiO_2 with and without PIDH layer. (the peak for TiO_2 is not certain)

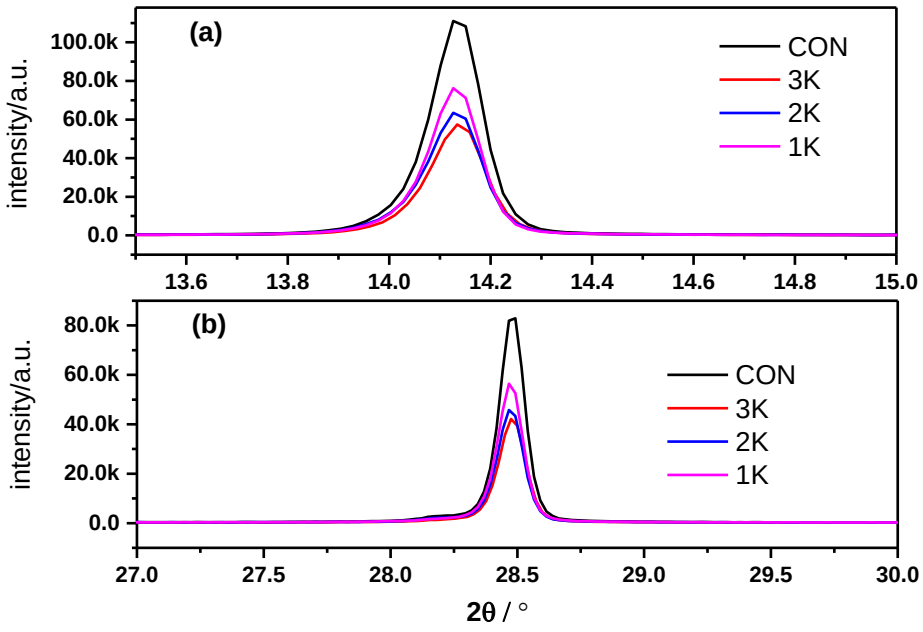

Figure 5-15 Enlarged scale plots of normalized peaks at 14.15° and 28.5°.

To explore the influence of the interlayer on device performance, conventionally structured (i.e. "n-i-p') planar solar cells were prepared. The details about device fabrication can be found in chapter 3. All the devices were tested directly after Au was deposited and measured at 1 sun AM1.5 (100 mW/cm^2) with a masked area of 0.075cm^2. **Figure 5-16** shows all the parameters (i.e. power conversion efficiency (PCE, η), open circuit voltage (V_{oc}), short circuit current density (J_{sc}) and fill factor (FF)) of devices with and without PDIH interlayers. The data is presented in box plots and the whisker is 1 standard deviation (Further details can be found in Table 5-4). As demonstrated in the figure and the table, the PCE of devices with PDIH films that have various thicknesses are lower than the control samples. This is found to originate from the decrease of V_{oc}, FF and J_{sc}. In particular, the V_{oc} drops sharply after the introducing of the interlayer, which could be a result of the introduction of surface defects that act as recombination centres. However, the work function of TiO_2 with an interlayer was reduced by 30 meV (KPFM measurement shown in **Figure 5-10**) which is supposed to increase the V_{bi} and benefit charge collection. Thus, we suppose the decrease of device parameters is owing to the interlayer film quality (e.g. coverage, thickness and uniformity), as the thickness and uniformity of interlayer films are critically important to the charge collection. The hypothesis can be proved by varying the thickness of the interlayer. As demonstrated in **Figure 5-16** , the best-performing devices are those with interlayers deposited at 2k rpm. There is an obvious increase of J_{sc}, FF and V_{oc} for devices with 2krpm deposited PDIH compared with those deposited at1k rpm and 3k rpm.

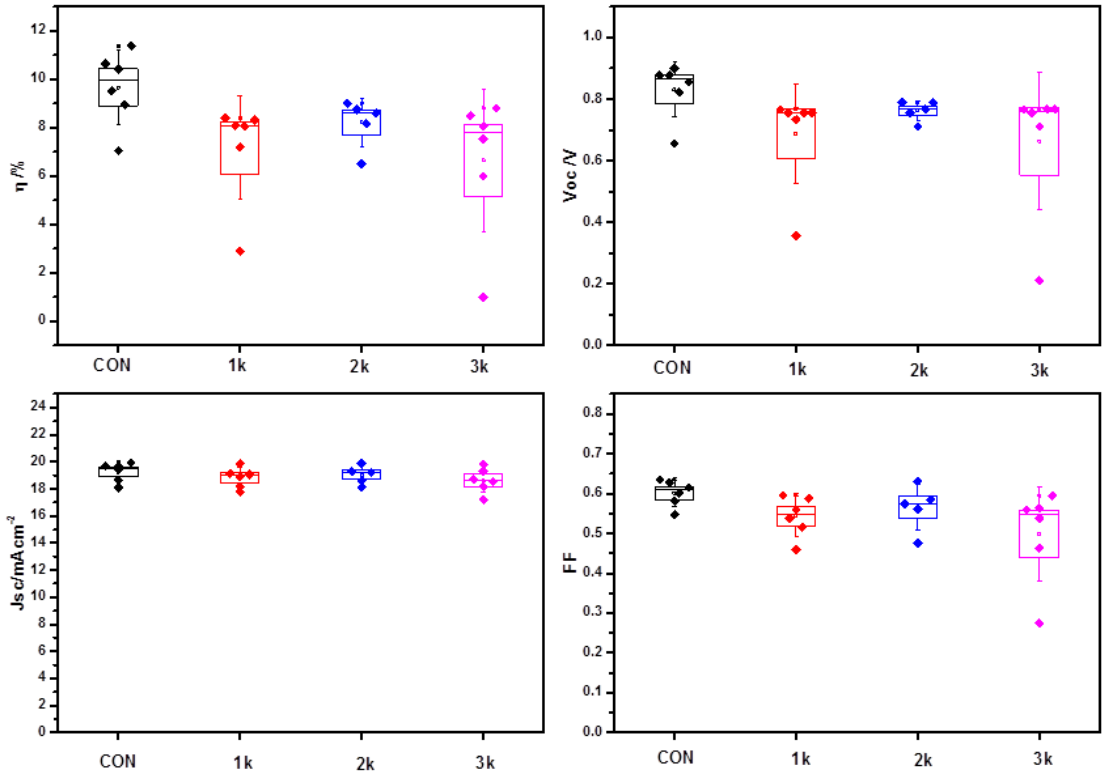

Figure 5-16 Device performances. The box and whisker represent 0.5 SD and 1 SD. Data were from reverse scan of current density-voltage measurement at one sun AM1.5 at room temperature. The scan rate was 200mV/s. The active area under illumination was 7.5mm^2. Control device configuration was TEC15/TiO_2/$MAPbI_{1-x}Cl_x$/spio-OMeTAD/Au,, and the interface engineered device was TEC15/TiO_2/PDIH/$MAPbI_{1-x}Cl_x$/spio-OMeTAD/Au 6 pixels were tested which were on one substrate.

The current density-voltage characteristics (J-V curves) of the best performing solar cell tested under illumination and in the dark are shown in Figure 5-17 J-V curves taken in the dark indicate both the control and devices with interlayers have typical diode character. The best performing cells shown the same trend as the wider study outlined above, e.g.the control solar cell gave the best performance and the 2k rpm deposited solar cell showed the best performance among solar cells with interlayers.

Table 5-4 Device performance parameters. Devices are the same as demonstrated in Figure 5-16.

Devices	PCE /%	V_{oc} / V	J_{sc} / mAcm^{-2}	FF
Control	9.7 ± 1.5	0.83 ± 0.09	19.2 ± 0.7	0.60 ± 0.03
1k rpm deposited PDIH	7.2 ± 2.1	0.68 ± 0.16	18.8 ± 0.7	0.54 ± 0.05
2k rpm deposited PDIH	8.2 ± 1.0	0.76 ± 0.03	19.0 ± 0.7	0.57 ± 0.06
3k rpm deposited PDIH	6.6 ± 2.9	0.66 ± 0.22	18.6 ± 0.9	0.50 ± 0.12

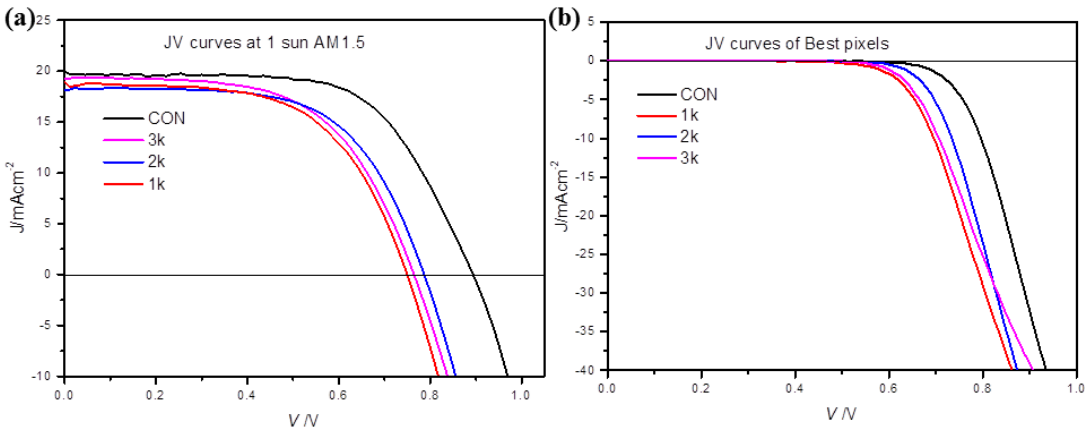

Figure 5-17 J-V curves of solar cells scanned at 200 mV/s under illumination (a), and at dark (b). The curves are from best-performing pixels.

Hysteresis and long-term stability of devices were also monitored to further understand the impacts of interface engineering. The ratio of the PCE at forward scan (J_{sc} to V_{oc} direction) and reverse scan (V_{oc} to J_{sc} direction) was used to estimate the hysteresis change. As shown in Figure **5-18**(a), the hysteresis is less serious with the decrease of the spin coating speed used to deposit the PDIH interlayer. It suggests that the increase of the interlayer thickness could decrease the hysteresis, implying that a PDIH interlayer could reduce the hysteresis in perovskite solar cells.

Control and 2k rpm devices were tested immediately after fabrication and after 480h under standard test conditions to investigate the effects of interlayers on the stability of perovskite solar cells. All the devices were kept in a sealed container with a relative humidity of 20% at room temperature when not being tested. The PCE variation for both devices is shown in **Figure 5-18**(b). It shows that the devices with PDIH interlayers (deposited at 2k rpm) were observed to be more stable than the control. It impressively keeps 97% of the initial efficiency. While the control devices only keep 79% of their initial efficiencies. This very stable character of the devices with 2k rpm deposited PDIH interlayer reveals that the long-term stability of solar cells can be significantly improved through an appropriate interface engineering process.

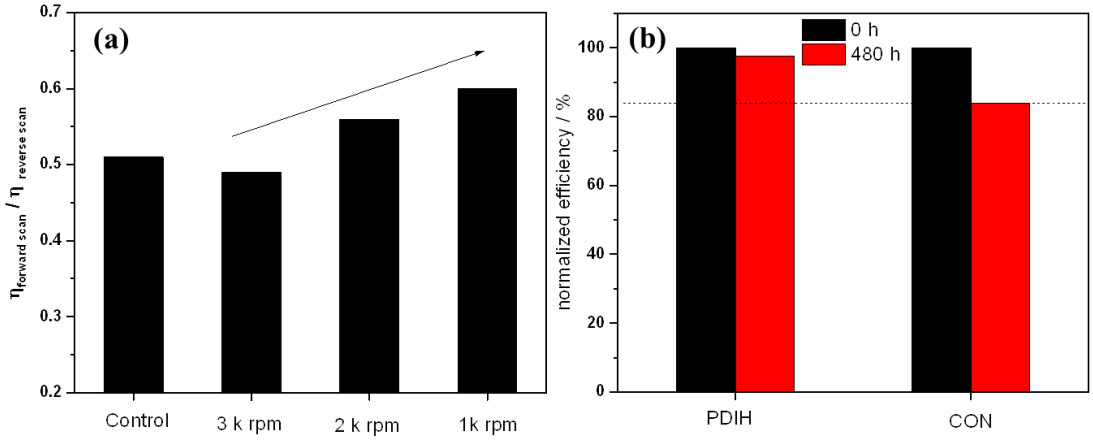

Figure 5-18 Hysteresis and long-term stability of devices with and without PDIH interlayers.Devices were tested at 200 mV/s under room temperature at AM1.5. Devices were stored in a desiccator box(RH%~20%) when not being tested.)

5.4.2 Conclusion

To conclude, PDIH films were deposited on TiO_2 as interlayers by spin coating for perovskite solar cells. The work function of the compact layer TiO_2 can be decreased by around 30 meV due to the dipole moment of PDIH molecules. However, the corresponding solar cells displayed a reduction in open circuit voltage. It is supposed to be caused by the increased recombination after adding a PDIH interlayer. A further study on interlayer thickness was carried out by varying the spin coating speeds. After optimization of layer thickness, the V_{oc} of the devices increased, and in our study a maximum V_{oc} was shown for 2k rpm deposited devices, though the V_{oc} was still lower than the control. In addition, 2k rpm deposited samples displayed less hysteresis and better long-term stability compared with the control. In order to make better quality interlayers, a dip coating method was used and is discussed below.

5.5 Interlayer preparation through dip coating method

As illustrated in the last part, the interlayer film quality plays an important role in determining device performances. Results discussed previously indicated that the spin coating method may not be a perfect approach to make thin and uniform interlayers, especially for PDIs which can easily aggregate in the precursor solution (e.g. π-π stacking). Therefore, in this part, employed dip coating method was used to prepare PDI interlayers. This method takes advantages of the functional groups of the PDIs molecules, introducing a self-assembly process on the substrate surface. The self-

assembly process involves the interaction of the –COOH functional group of PDIs with –OH functional groups or non-bonded Ti^{4+} on the TiO_2 surface. It takes longer to form a film; however, the film is expected to be more uniform.

5.5.1 Results and discussion

After being immersed into the precursor solution (0.05mM PDIV or PDIH in DMSO solution) for a certain time, substrates were taken out to measure the UV-Vis absorption to see if any PDI had adhered to the surface. Figure 5-19 shows the absorption spectra of the substrate (FTO/TiO_2/PDIs) after it has been dipped for different times. The characteristic peaks for PDI (seen in solution at 490 and 530 nm) were not observed after 3 and 6 hour dipping, but it was hard to obtain a good quality spectrum on the TiO_2 surface. After 18 hrs peaks appeared at around 530 and 630 nm (PDIV 525 and 627nm, PDIH 532 and 632nm) which could indicate PDIs on the surface, the signal is red shifted compared to the solution suggesting that the molecules are aggregated. It is possible that there is PDIs on the surface after 3 and 6 hours but the spectrometer is not sensitive enough to detect it.

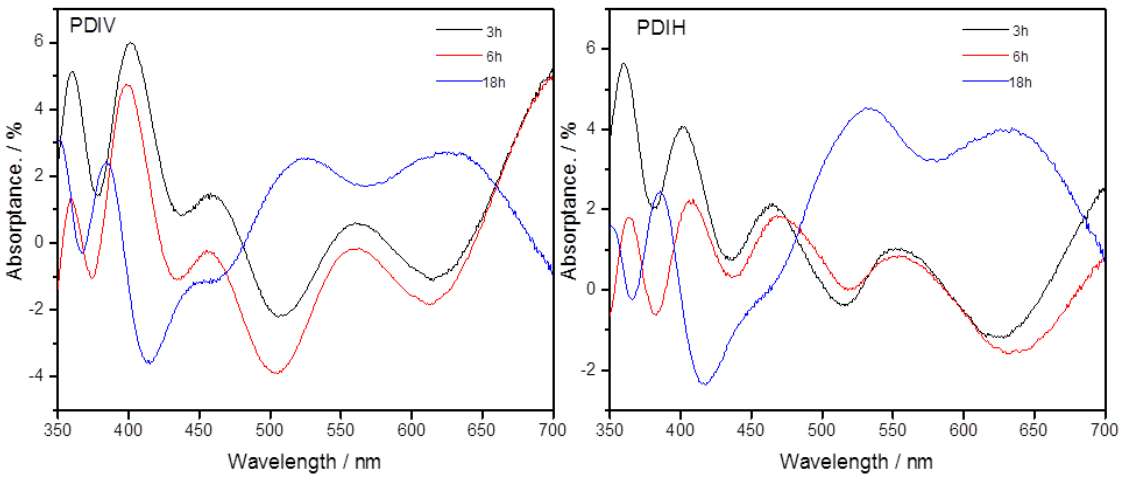

Figure 5-19 UV-Vis of PDIV and PDIH films by dip coating method. Samples are substrates immersed into PDIH/PDIV solutions for 3h, 6h and 18h.Spectra were obtained by subtracting the background (FTO/TiO_2)

In order to further investigate the existence of the interlayer, desorption experiments were carried out. Substrates which were already coated with PDIs were immersed into 0.1M KOH aqueous solution for 2h to desorb any adsorbed molecules. The remained solution was then measured by UV-Vis spectroscopy. The results are shown in Figure 5-20. There is no obvious absorption peaks for PDIV samples immersed for 3h and 6h,

and very weak peak appears at around 500nm of sample immersed for 18h, indicating the amount of absorbed PDIV is very limited. In contrary, all the three samples of PDIH (immersed for 3h, 6h and 18h) are observed to display characteristic peaks at around 500 nm and the signal increases with the immersion time.

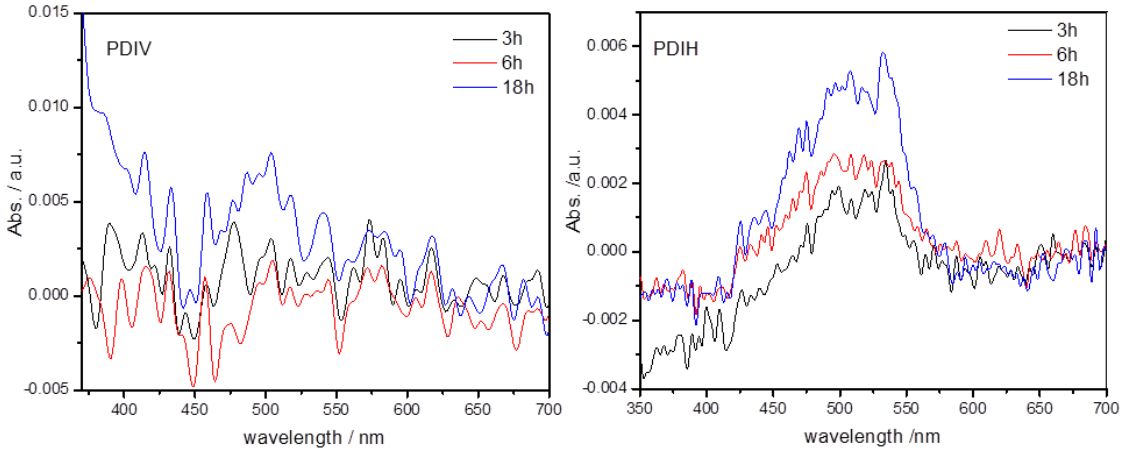

Figure 5-20 desorption of PDIV and PDIH films. Substrates were immersed into 2mL 0.1M KOH solution separately for 2h at room temperature.

Contact angle measurements were used to find the surface energy change after the film had been deposited. Figure 5-21 demonstrates there is only slight increase of the contact angles between the control sample and those with PDIV interlayers shown in the digital images. It is consistent with the UV-Vis curves in desorption experiments, revealing the inefficient adsorption of the PDIV molecules on the TiO_2 surface. In contrast the substrates with PDIH interlayers give a different response compared with the control sample, and the contact angle goes up when immersed for a longer time. The box plots in Figure 5-21 also show the contact angles before and after interface engineering. The contact angle of the TiO_2 blocking layer is 10° on average, the angle increases to 26.5°, 27.5° and 34.5°for the 3h, 6h and 18h PDIH interlayer samples. The contact angle change for the PDIV is not obvious. They are 6°, 14.2° and 13.5° for 3h, 6h and 18h immersed samples respectively, indicating poor adsorption of PDIV onto the TiO_2 surface. Therefore, we assume that the interaction of the PDIs samples with the TiO_2 is not mainly based on the –COOH. The difference in the adsorption for the two molecules also implies that the imidazole ring in the PDIH structure plays an important role in improving the adsorption on the TiO_2 surface.

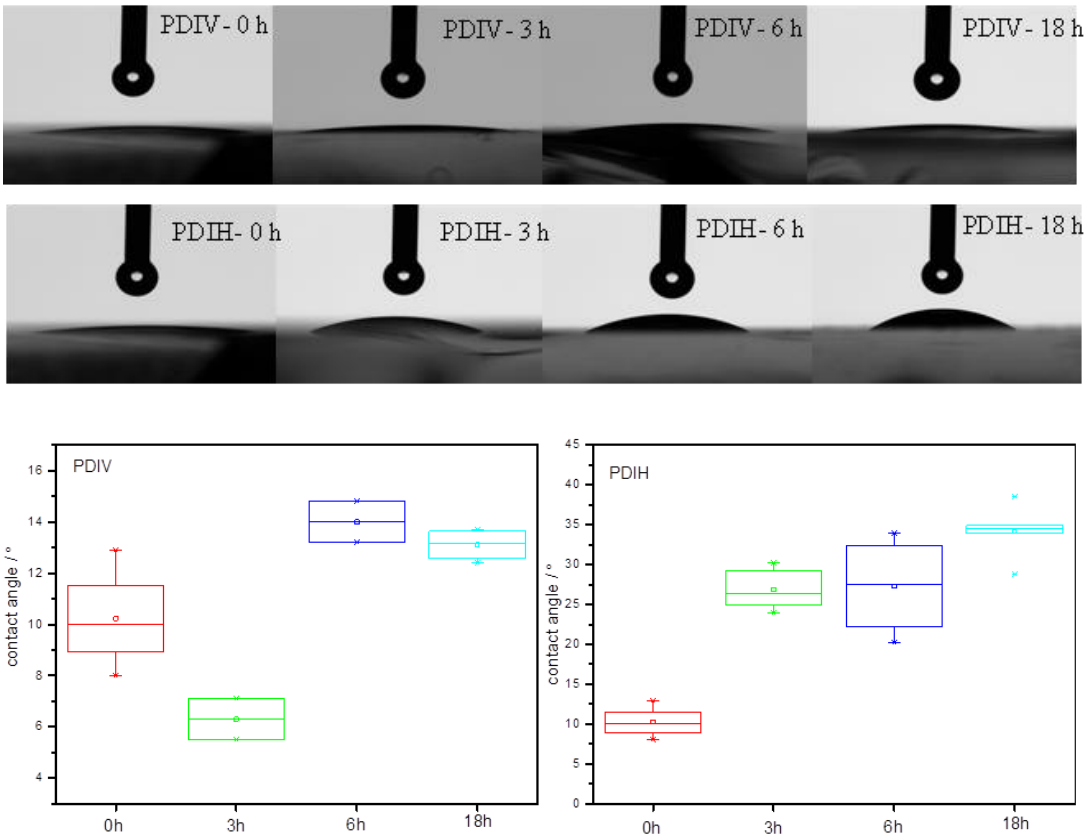

Figure 5-21 Advancing contact angle measurements on PDIV and PDIH films by using water as the working liquid. Samples were rinsed with IPA and dried with dry N_2 flow. Digital images were taken in the measurements and shown at the top are PDIV and PDIH samples. They are TiO_2 substrates immersed into PDIV or PDIH for 3h, 6h and 18h. The bottom box plots show the contact angle data. The whisker and box indicate the 25%, 50%, 75% and 100% of data distribution.

A two-step method (vapour assisted solution method) was used to prepare perovskite layers. A PbI_2 layer was first deposited on substrates with interlayers by spin coating. The morphology of the PbI_2 layer was investigated by AFM. As shown in Figure 5-22, (a), (b) and (c) are the AFM topography images of PbI_2 on PDIV, PDIH and the control sample, respectively. PDIV sample shows very different PbI_2 morphology. The film is rougher and has bigger grain sizes than the other samples. While the PDIH and control sample show smooth surfaces and compact grains. The average roughness of all the samples is given in Table 5-5. The control sample gives the smallest average roughness 14.5 nm, and the PDIV gives the biggest roughness 36.2 nm.

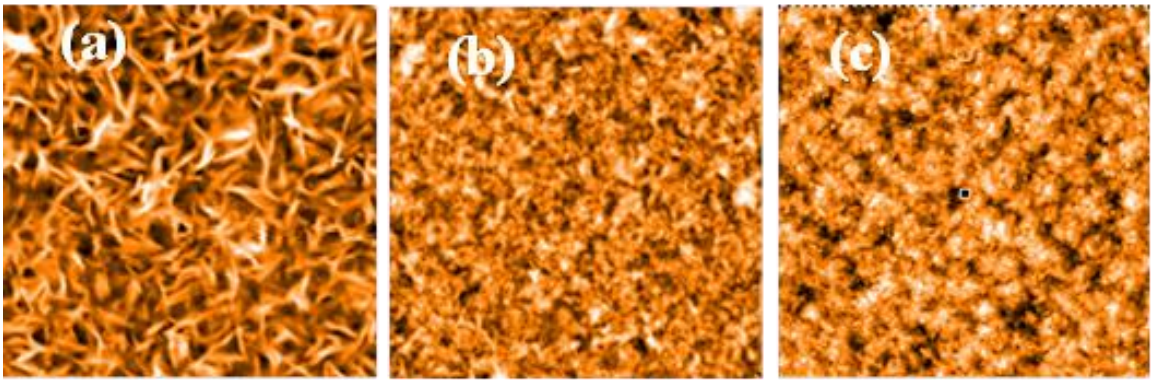

Figure 5-22 AFM images of PbI_2 films on different substrates (a) TiO_2/PDIV, (b) TiO_2/PDIH and (c) bare TiO_2 (control). Image size is 20μm ×20 μm.

Table 5-5 Average roughness of PbI_2 films from AFM

Sample	PDIV	PDIH	Control
Average roughness/nm	36.2 ± 3.8	20.1 ± 1.5	14.5 ± 1.2

After reacting with CH_3NH_3I vapour, PbI_2 was converted into the hybrid perovskite. The morphologies of perovskite layers on different substrates were also investigated by AFM and are displayed in Figure 5-23. It is clear that the perovskite layer morphology is related to the PbI_2 layer. Shown as (a), (b) and (c) in Figure 5-23, PDIV, PDIH and control samples imply a similar trend of roughness to the PbI_2 layer. The PDIV sample shows a rougher texture, while PDIH and the control exhibit relatively smooth surfaces. The detailed average roughness information can be found in Table 5-6. However, unlike information demonstrated in Table 5-5 where control sample has the lowest average roughness, PDIH sample give the smoothest film surface in all the samples, with a roughness of 19.1 nm. It was also observed from the AFM images that the PDIH film shows better surface coverage. Enlarged images(e), (f), (g) below show the corresponding fine structure of the perovskite films shown in images (a), (b) and (c). It is obvious that both the perovskite on PDIH and PDIV have smaller grains than the control sample, which is consistent to the character shown in samples prepared by spin coating methods. We then can conclude that the application of PDIH and PDIV organic interlayers will decrease the grain size of the perovskite film. Although PDIH sample is composed of smaller grains, it shows smoother surface than the control sample, implying fewer “shunt paths” through the perovskite film.

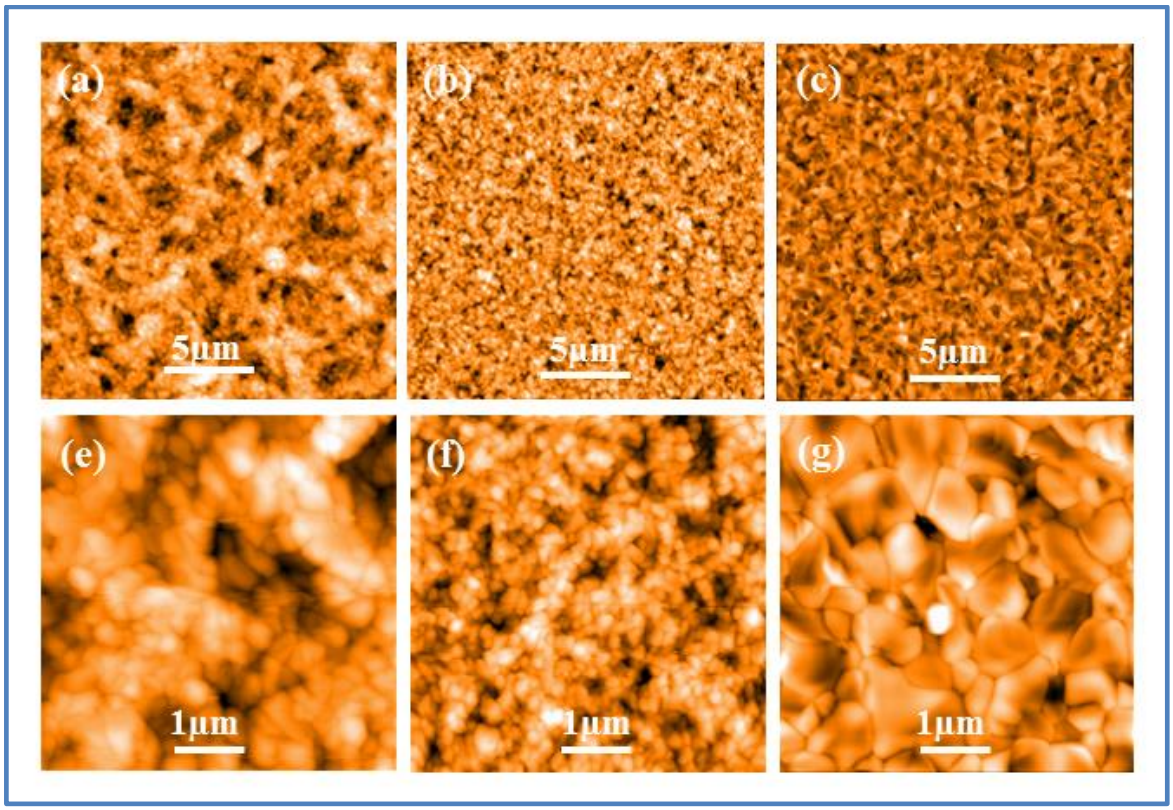

Figure 5-23 AFM images of perovskite films in different scales. (a) and (e) TiO_2/PDIV/Perovskite, (b)and(f) TiO_2/PDIH/Perovskite, (c)and(g) TiO_2/Perovskite (Control)

Table 5-6 Average roughness of perovskite films from AFM

Samples	PDIV	PDIH	Control
Average roughness /nm	45.7 ± 1.6	19.1 ± 0.9	35.7 ± 2.9

Information about the particle size was further analysed and the grain size statistics for perovskite films in different samples are given in Figure 5-24. As shown in the 5-25 (a) the PDIV sample has particles mainly distributed around 0.079 ± 0.058 μm^2. Figure 5-25(b) shows the distribution for the perovskite film on PDIH. The particles mainly distribute at 0.026 ± 0.010 μm^2. Figure 5-25(c) shows the control sample, it shows micrometre grain size (0.43 ± 0.29 μm^2), and the particles are one order of magnitude larger than PDIV and PDIH samples.

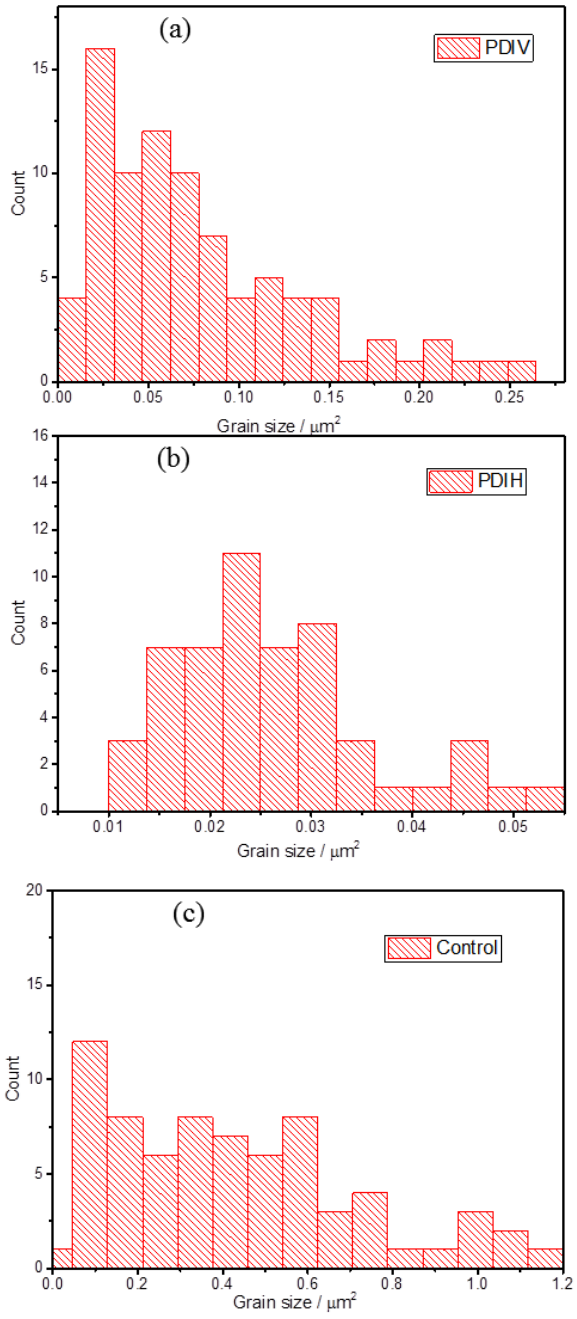

Figure 5-24 perovskite film grain size distribution. (a) PDIV, (b) PDIH, (c) Control

The AFM shows that interface engineering can significantly change the film morphology of perovskite layers. To understand if interlayers can change the crystal structure and crystallinity in addition to the morphology, XRD measurements were carried out, and the results are shown in Figure 5-25. The sharp and strong peaks at 14.2° (110) and 28.5° (220) indicate tetragonal perovskite crystals are formed in all samples. The peak at 12.7° in PDIV and the control are the (101) lattice plane of PbI_2, indicating the incomplete conversion of lead source in these two samples. In addition, crystal size

information can be obtained from the FWHM of the peaks. In the enlarged scale graph, it is observed that the control sample has a lower FWHM than PDIV and PDIH sample. It suggests that the perovskite layer in the control sample has bigger particles than the other two samples after interface engineering. The reduced particle size of perovskite film may cause increase of recombination in perovskite layer.

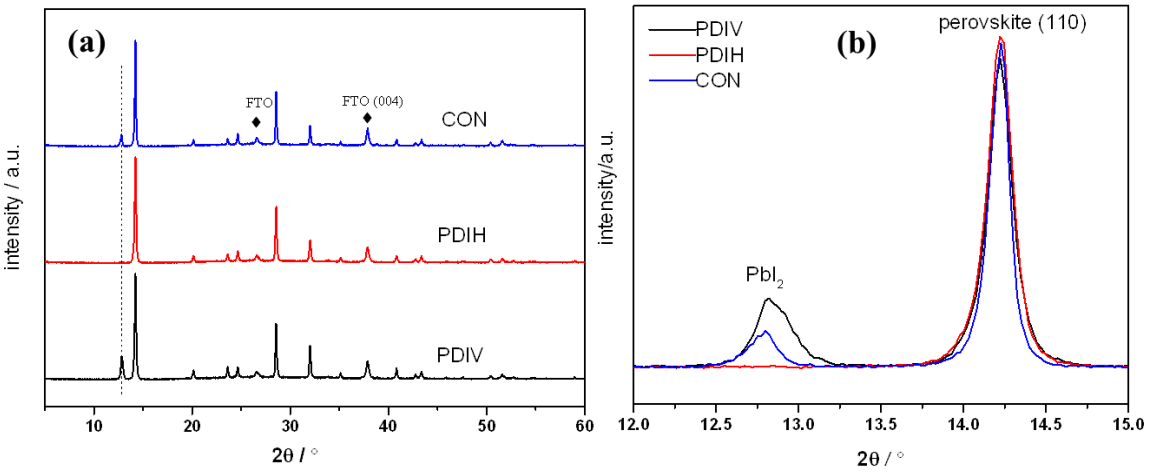

Figure 5-25 XRD patterns of perovskite films. Samples are CON(FTO/TiO_2/perovskite), PDIH(FTO/TiO_2/PDIH/perovskite) and PDIV(FTO/TiO_2/PDIH/perovskite) Peaks for different samples are aligned with peaks of FTO, and all the patterns in (a) are normalized.

Steady state photoluminescence and transient photoluminescence measurements were carried out to investigate trap states and the charge transfer dynamics. Samples with configurations glass/perovskite, glass/TiO_2/perovskite and glass/TiO_2/PDIs/perovskite were prepared. As shown in Figure 5-26(a), perovskite emission peaks at around 772nm (~1.6 eV) are observed in all samples, which roughly agrees with the published band gap of MAPI perovskites (~1.55eV) in references[19]. When the perovskite was deposited on TiO_2, the peak was slightly red-shifted ($\Delta\lambda$=3 nm, 0.006 eV) indicating light emitted has a lower energy than the control (glass/perovskite), and the luminescence intensity was strongly increased. The peak shift suggests a slight shift of the band edge, which has also been observed in other reported work.[20] However, samples with PDIH or PDIV interlayers showed a blue-shift in luminescence peak (767nm, 771nm respectively) and lower luminescence intensity. It indicates the band-gap of the perovskite is slightly increased. Li et al have reported that the steady state PL intensity is linked to the number of surface defects in the perovskite film[21]; where the surface defects act as recombination centres to reduce the PL intensity. If this is true it suggests that the PDI

introduces more surface defects than the TiO_2 (in fact the film on TiO_2 seems to have fewer surface defects than the film on glass). It is important to note that the PL signal could also be decreased by the introduction of bulk defects in the perovskite – this could be due to changes in the crystal size and structure when the films are spin coated onto different substrates. In contrast, You et al[22] have stated that reduced PL signals are due to better quenching of the excited state due to effective charge transfer from the perovskite to the contact layer, however they do not discuss what happens to the carriers after they have been transferred to the contact. If more effective quenching is occurring it suggests that the PDI is a better electron extracting layer than the TiO_2. It is very difficult to prove which mechanism is happening in the perovskite films. In these experiments the films were illuminated from the perovskite side and the perovskite film was approximately 300-400 nm thick. Given that the absorption coefficient of MAPI is ~$10^5 cm^{-1}$, this suggests that all the incident light at 510nm would be absorbed in the first ~100nm of the film[23]. This suggests that PL is more likely to be indicative of the number of bulk recombination sites in the film. Again this suggests that the film morphology (e.g. crystallite size and number of grain boundaries) is highly dependent on the substrate it is deposited on.

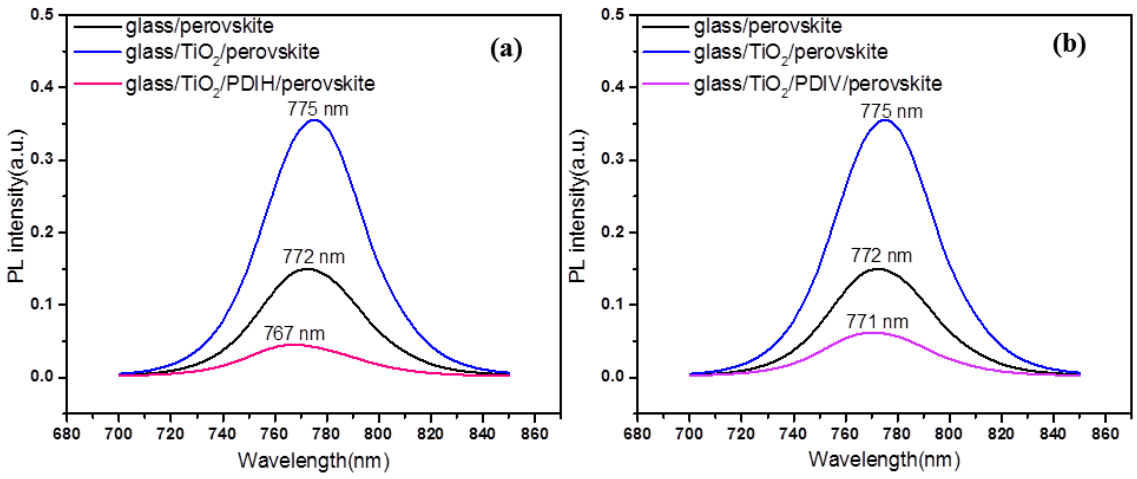

Figure 5-26 Steady state photoluminescence of perovskite films. (a) PDIH and corresponding reference samples, (b) PDIV and corresponding reference samples.

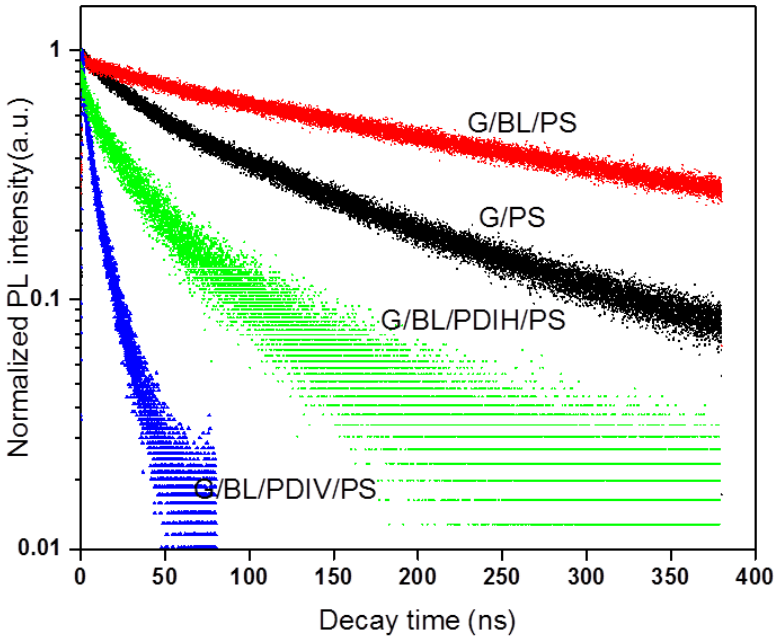

Figure 5-27 Transient photoluminescence decay of perovskite films. G represents glass, BL represents TiO_2 blocking layer and PS represents perovskite. Lifetime calculation follows the definition.

Transient photoluminescence (or time-resolved photoluminescence, TRPL) was used to detect PL decay. As displayed in **Figure 5-27**, the spectra for PDIH, PDIV and the reference samples show significant differences in decay kinetics. In the literature it is often suggested that faster decay kinetics are linked to more efficient charge transfer to the electron (or hole) selective contact[24]. The calculated lifetime is 90ns for sample G/PS (glass/peroskite), 250ns for G/BL/PS (glass/TiO_2/perovsite), 20ns for G/BL/PDIH/PS (glass/TiO_2/PDIV/perovskite) and 6ns for G/BL/PDIV/PS (glass/TiO_2/PDIV/perovskite). If the theory about improved quenching is correct then the TiO_2 blocking layer, is a less effective selective contact than the PDIs. After introducing the perylene diimide interlayers, the electron could be extracted to electron transporting layer more efficiently. However if the rate of PL decay is controlled by charge transfer to the selective contact it is not clear why a shorter lifetime is observed for the perovskite film on glass compared to a film on titania – glass is not able to accept electrons. This also suggests that the rate of PL decay is more likely to be linked to the properties of the bulk perovskite layer.

Based on the characterisation shown above, it appears that the interlayers change the perovskite morphology and this has a large effect on the film properties. In order to

investigate the overall impact on the device, full devices were fabricated in air (PDIH and PDIV films were obtained by dipping in solution for 3 hrs). Devices were tested under standard condition (AM1.5, one sun, 25°C). The parameters of devices were acquired from current density-voltage analysis. The PCE, J_{sc}, V_{oc} and FF are shown in box plot in **Figure 5-28**, and the results in detail are shown in Table 5-7.

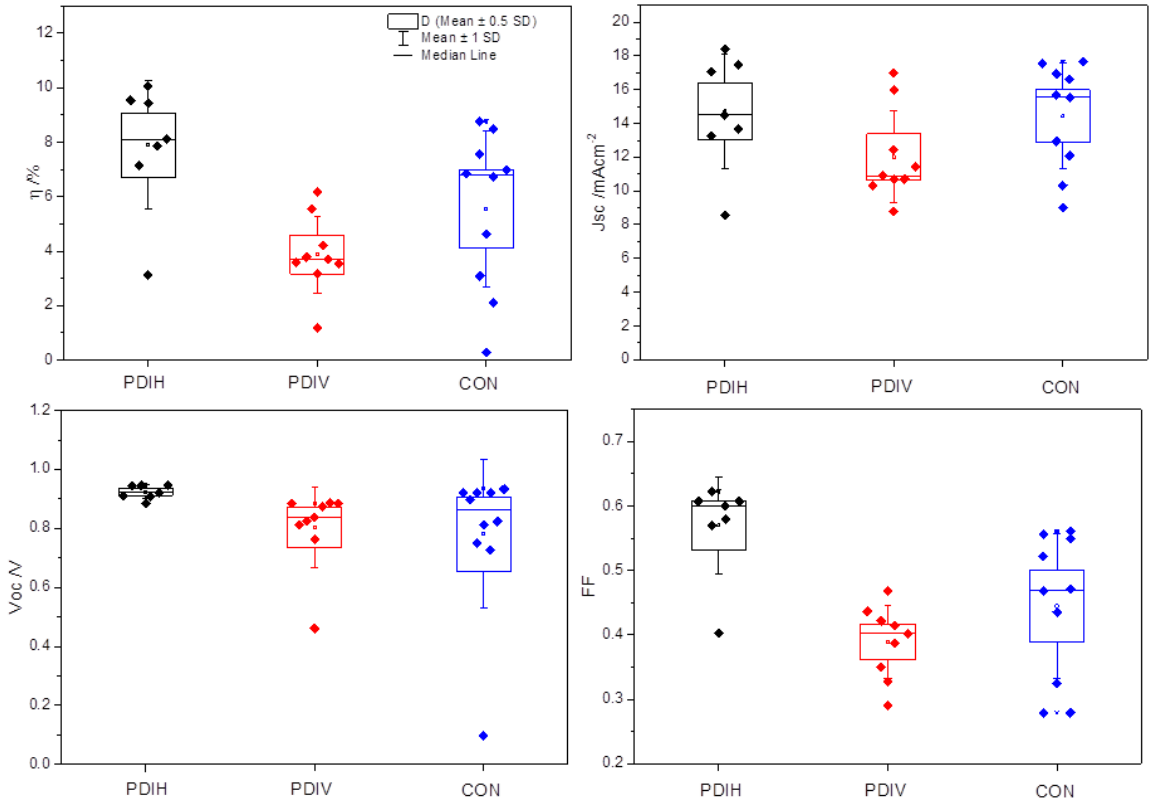

Figure 5-28 solar cell performances of devices in box plot. At least 6 devices were fabricated to analyse the statistic parameters for each type of samples. Data were from reverse scan of current density-voltage measurement at one sun AM1.5 at room temperature. The scan rate was 200mV/s. The active area under illumination was 7.5mm^2. Control device configuration was TEC15/TiO_2/$MAPbI_{1-x}Cl_x$/spio-OMeTAD/Au, and the interface engineered device was TEC15/TiO_2/PDIs/$MAPbI_{1-x}Cl_x$/spio-OMeTAD/Au

Table 5-7 Solar cell parameters of different devices. Shown as average with standard deviation.

Samples	PCE /%	V_{oc} / V	J_{sc} / mAcm^{-2}	FF
PDIV	3.9±1.4	0.80±0.13	12.0±2.7	0.39±0.06
PDIH	7.9±2.3	0.93±0.02	14.4±3.4	0.57±0.08
Control	5.6±2.9	0.78±0.25	14.4±3.1	0.44±0.11

It is observed that the PCE of devices with PDIH interlayers is significantly enhanced compared with the control, while devices with PDIV interlayers display inferior

performance. The PCE of the best performing solar cell is 10.5% for PDIH sample, 8.5% for control and 5.3% for PDIV samples. The superior performance of devices with PDIH interlayers is mainly due to an increase of the V_{oc} and FF, which could be attributed to the smooth perovskite film which has small crystallites and fewer pinholes. Meanwhile, the J_{sc} for PDIH and the control devices is very similar. However for PDIV samples, the J_{sc} and FF are much lower than the others, though the average V_{oc} is close to control devices, could be due to the rough perovskite film (more possible shunt paths).

The J-V curves of best-performing devices are shown in Figure 5-29. The V_{oc} and FF of PDIH are significantly enhanced in comparison with the control. The result is consistent with the corresponding KPFM and PL measurements. Besides, the PDIH is a conjugated material with very good conductivity, the series resistance (R_s) could be reduced as well.

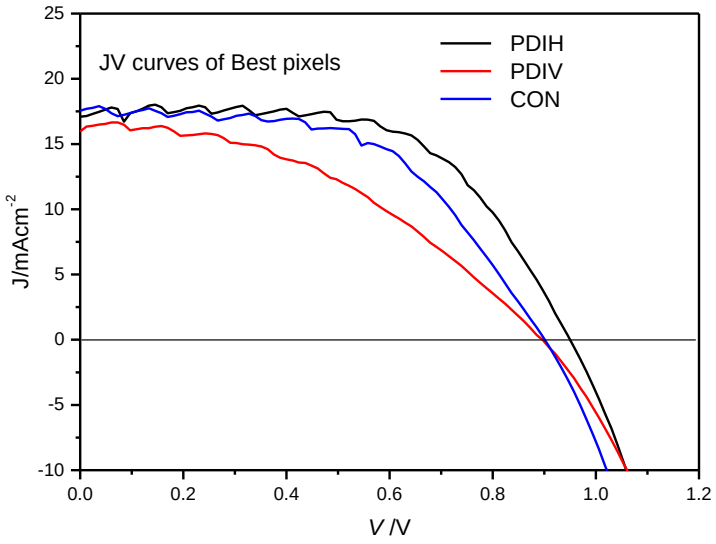

Figure 5-29 J-V curves of devices. Devices are with configurations of PDIH: FTO/TiO_2/PDIH/perovskite/spiro-OMeTAD/Au, PDIV: FTO/TiO_2/PDIV/perovskite/spiro-OMeTAD/Au and CON: FTO/TiO_2/perovskite/spiro-OMeTAD/Au. Devices tested at room temperature at one sun AM1.5. Scan rate is 200 mV/s. Active area with Au is 9mm^2, and the area under illumination is 7.5mm^2

The interlayer also impact the stability of devices. As shown in Figure **5-30**, average efficiencies of different devices were monitored over time. Significant degradation was found in all three device types when they were tested after being kept at ambient environment for 360 h and 500h. However, the PDIH device was noticed to be the most stable device with ~ 32% decrease of its original efficiency after being kept for 360h.

The control device, by contrast, has a 48% decrease of efficiency at 360h. The PDIV device shows the most serious degradation which can be ascribed to the rougher perovskite film which presents a larger surface area and many grain boundaries where moisture could attack the film.

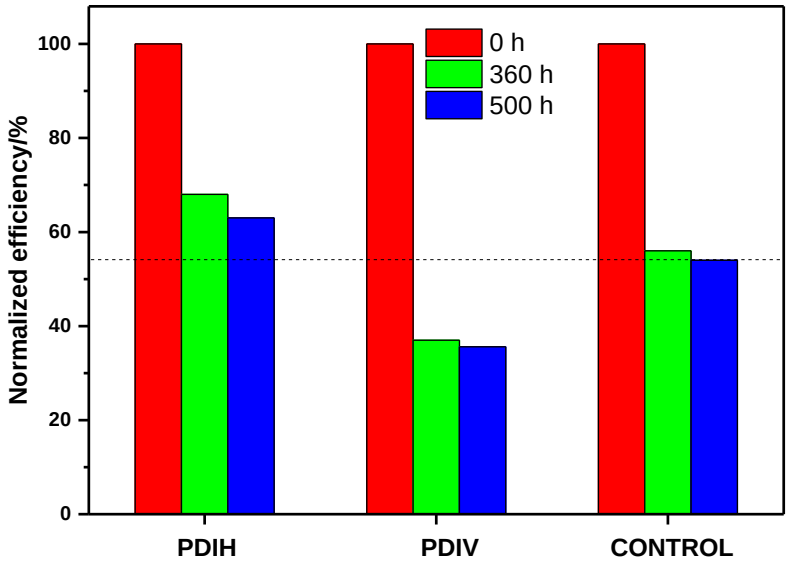

Figure 5-30 stability of solar cells with and without PDIs interlayers. Devices were kept at desiccator box with a humidity of ~20%

5.5.2 Conclusion

In this part, interlayers of PDIH and PDIV molecules were prepared by dip coating method. By using this method, perylene diimides can chemically bond the surface of TiO_2 through the interaction of their functional groups (e.g. –COOH) with the TiO_2 surface. Though this process takes longer time than the spin coating method, thin and strongly attached interlayers should be achieved. All the procedures for device fabrication were carried out in air, and perovskite layers were prepared through vapour assisted two-step solution method. The characterization of interlayers indicates that interface engineering significantly changed the surface energy, and perovskite films on PDIH and PDIV interlayers both show reduced particle sizes. Samples with PDIH interlayers show smoother perovskite films relative to the control; while samples with PDIV interlayers displayed a higher roughness than the control. Solar cells fabricated with and without interlayers demonstrate very distinct differences in performance. Devices with PDIH interlayer has an optimized performance, the V_{oc} and FF are both improved and the PCE increased by 24%, from 8.5% (average 5.6%) of control devices

to 10.5% (average 7.9%) . However, devices with PDIV show inferior performance which can be attributed to the change of the surface energy which leads to a less favourable film morphology. The improved performance of devices is also shown by the stability measurements. In the presence of a PDIH interlayer, the efficiency remained at 68% of the initial value after 360h, which is better than the control (52% retained).

5.6 The effects of the interlayer preparation method on device performance

It is very critical to control the interlayer film quality when interface engineering is employed to optimize the solar cell performance. Theoretically, the interlayer should be very thin to avoid an increase in series resistance and the formation of recombination sites. It can be prepared by spin coating a low concentration precursor solution (1-2mg/ml or lower) or through dip coating method by immersing the substrates into dilute solution (a few mM or lower) for a certain time.

In this chapter, both methods were tried and the devices display different performance when the same interlayer material was used (PDIH interlayer as an example.) The device with PDIH interlayers prepared through dip coating showed enhanced PCE compared to the control. However, the device with PDIH interlayer prepared by spin coating method displays a lower PCE than the control. As discussed before, we suppose the thickness and the uniformity of the interlayer can be the two key factors that affect the device efficiency. The hypothesis is partly confirmed by changing the thickness of interlayers through varying the spin coating speeds. We then analysed how the optimization of interlayers changes the device parameters. As shown in the discussions in sections 5.4 and 5.5, the parameters of devices vary with the interlayer preparation methods. In the end, the device with spin coated PDIH shows a V_{oc} and J_{sc} decrease (*vs.* control), while the one with dip coated PDIH interlayer shows increased V_{oc}, and similar J_{sc} (vs. control).

5.7 Conclusion and future work

This chapter discussed the importance of the interface engineering in the performance improvement of perovskite solar cells. Introducing interlayers in devices can improve

the built in voltage and control the morphology of the active layer. In our work, PDIH and PDIV were used modify titania layers. It is found that the interlayer film quality is extremely critical in determining the device performance. The thickness, coverage and morphology are all important since they can effectively affect properties of the layer deposited on interlayers. When a PDIH interlayer was prepared through spin coating, the V_{oc} and FF both decreased, and the optimization of spin coating speed causes an increase of V_{oc} and FF. Thus we believe the films prepared through spin coating method are thicker than they are expected to be. We then used a dip coating method to make the interlayers and the results show that when the substrates were dipped into PDIH solution for 3h, the PCE was 24% higher than the control sample. The V_{oc} and FF were both found to have increased after interface engineering with PDIH. The inferior performance of devices with dip coated PDIV interlayer can be attributed to the low coverage of the interlayer on the substrate surface, which can be obtained from contact angle and UV-Vis measurements. Moreover, PDIH cells are more stable than PDIV or control cells, revealing that interface engineering also impacts the long-term stability of devices. More work needs to be carried out to investigate how to control the quality of interlayer and how the interlayer interacts with the TiO_2. For example, thickness control of a PDIH interlayer through immersing for different times, PDIH film thicknesses can be measured via ellipsometry, and the kinetics of PDIH or PDIV absorption on TiO_2 could be further investigated. All this work should be done to find the optimal conditions to prepare interlayers in order to get enhanced performance of perovskite solar cells.

5.8 Acknowledgements

Dr Emily Draper and Prof David Adams are greatly appreciated for providing PDIH and PDIV. The author also thanks Ruoxi Yang for the computational work of molecular dipoles, Prem Thongchai for help in TGA measurements, Ben Freestone for photoluminescence tests and Laxman Gouda for KPFM measurements.

5.9 References

1. Chung I, Lee B, He J, Chang RPH, Kanatzidis MG. All-solid-state dye-sensitized solar cells with high efficiency. *Nature* 2012, **485**(7399)**:** 486-489.

2. Wojciechowski K, Saliba M, Leijtens T, Abate A, Snaith HJ. Sub-150 [degree]C processed meso-superstructured perovskite solar cells with enhanced efficiency. *Energy Environ Sci* 2014, **7**(3)**:** 1142-1147.

3. Kavan L, Tétreault N, Moehl T, Grätzel M. Electrochemical Characterization of TiO2 Blocking Layers for Dye-Sensitized Solar Cells. *J Phys Chem C* 2014, **118**(30)**:** 16408-16418.

4. Yongzhen W, Xudong Y, Han C, Kun Z, Chuanjiang Q, Jian L*, et al.* Highly compact TiO 2 layer for efficient hole-blocking in perovskite solar cells. *Applied Physics Express* 2014, **7**(5)**:** 052301.

5. Ke W, Fang G, Wang J, Qin P, Tao H, Lei H*, et al.* Perovskite Solar Cell with an Efficient TiO2 Compact Film. *ACS Appl Mater Inter* 2014, **6**(18)**:** 15959-15965.

6. Zhou H, Chen Q, Li G, Luo S, Song T-b, Duan H-S*, et al.* Interface engineering of highly efficient perovskite solar cells. *Science* 2014, **345**(6196)**:** 542-546.

7. Chen W, Wu Y, Yue Y, Liu J, Zhang W, Yang X*, et al.* Efficient and stable large-area perovskite solar cells with inorganic charge extraction layers. *Science* 2015.

8. Yip H-L, Hau SK, Baek NS, Ma H, Jen AKY. Polymer Solar Cells That Use Self-Assembled-Monolayer- Modified ZnO/Metals as Cathodes. *Adv Mater* 2008, **20**(12)**:** 2376-2382.

9. Zhang Z-G, Qi B, Jin Z, Chi D, Qi Z, Li Y*, et al.* Perylene diimides: a thickness-insensitive cathode interlayer for high performance polymer solar cells. *Energy Environ Sci* 2014, **7**(6)**:** 1966-1973.

10. Hains AW, Chen H-Y, Reilly TH, Gregg BA. Cross-Linked Perylene Diimide-Based n-Type Interfacial Layer for Inverted Organic Photovoltaic Devices. *ACS Appl Mater Inter* 2011, **3**(11)**:** 4381-4387.

11. Draper ER, Walsh JJ, McDonald TO, Zwijnenburg MA, Cameron PJ, Cowan AJ*, et al.* Air-stable photoconductive films formed from perylene bisimide gelators. *J Mater Chem C* 2014, **2**(28)**:** 5570-5575.

12. Casaluci S, Cinà L, Pockett A, Kubiak PS, Niemann RG, Reale A*, et al.* A simple approach for the fabrication of perovskite solar cells in air. *J Power Sources* 2015, **297:** 504-510.

13. Balakrishnan K, Datar A, Naddo T, Huang J, Oitker R, Yen M*, et al.* Effect of side-chain substituents on self-assembly of perylene diimide molecules: morphology control. *J Am Chem Soc* 2006, **128**(22)**:** 7390-7398.

14. Bard AJ, Faulkner LR, Leddy J, Zoski CG. *Electrochemical methods: fundamentals and applications*, vol. 2. wiley New York, 1980.

15. Kozma E, Kotowski D, Catellani M, Luzzati S, Famulari A, Bertini F. Synthesis and characterization of new electron acceptor perylene diimide molecules for photovoltaic applications. *Dyes and Pigments* 2013, **99**(2)**:** 329-338.

16. Shin WS, Jeong H-H, Kim M-K, Jin S-H, Kim M-R, Lee J-K*, et al.* Effects of functional groups at perylene diimide derivatives on organic photovoltaic device application. *J Mater Chem* 2006, **16**(4)**:** 384-390.

17. Zhou Y, Fuentes-Hernandez C, Shim J, Meyer J, Giordano AJ, Li H*, et al.* A Universal Method to Produce Low–Work Function Electrodes for Organic Electronics. *Science* 2012, **336**(6079)**:** 327-332.

18. Lee MM, Teuscher J, Miyasaka T, Murakami TN, Snaith HJ. Efficient Hybrid Solar Cells Based on Meso-Superstructured Organometal Halide Perovskites. *Science* 2012, **338**(6107)**:** 643-647.

19. Eperon GE, Stranks SD, Menelaou C, Johnston MB, Herz LM, Snaith HJ. Formamidinium lead trihalide: a broadly tunable perovskite for efficient planar heterojunction solar cells. *Energy Environ Sci* 2014, **7**(3)**:** 982-988.

20. Cho KT, Paek S, Grancini G, Roldan-Carmona C, Gao P, Lee Y*, et al.* Highly efficient perovskite solar cells with a compositionally engineered perovskite/hole transporting material interface. *Energy Environ Sci* 2017, **10**(2)**:** 621-627.

21. Li B, Chen Y, Liang Z, Gao D, Huang W. Interfacial engineering by using self-assembled monolayer in mesoporous perovskite solar cell. *RSC adv* 2015, **5**(114)**:** 94290-94295.

22. You J, Hong Z, Yang Y, Chen Q, Cai M, Song T-B*, et al.* Low-Temperature Solution-Processed Perovskite Solar Cells with High Efficiency and Flexibility. *ACS Nano* 2014, **8**(2)**:** 1674-1680.

23. De Wolf S, Holovsky J, Moon S-J, Löper P, Niesen B, Ledinsky M*, et al.* Organometallic Halide Perovskites: Sharp Optical Absorption Edge and Its Relation to Photovoltaic Performance. *J Phys Chem Lett* 2014, **5**(6)**:** 1035-1039.

24. Chen W, Li K, Wang Y, Feng X, Liao Z, Su Q*, et al.* Black Phosphorus Quantum Dots for Hole Extraction of Typical Planar Hybrid Perovskite Solar Cells. *J Phys Chem Lett* 2017, **8**(3)**:** 591-598.

Chapter 6 Benzoic acids interlayers for hybrid perovskite solar cells

Contents

6.1 Introduction

Dyes with carboxylic acid pendant groups are typically used in dye-sensitized solar cells (DSSCs) as the carboxylic acid group can interact strongly with the titania surface. For example, the –COOH anchoring group interacts strongly with the titania[1, 2]. Benzoic acids have also been used to modify oxide layers in organic and perovskite solar cells[3, 4, 5]. As mentioned in previous chapters, a compact TiO_2 film is also commonly employed as the hole blocking layer for hybrid perovskite solar cells. However several studies have shown that titania blocking layers induce hysteresis in perovskite solar cells and that surface modification is needed to improve the J-V characteristics[6, 7, 8]. Considering all the advantages, the study of benzoic acids as modifiers for the TiO_2 layer is meaningful, since it promises to substantially improve the perovskite solar cells' performance. To date, only a few studies have been reported where benzoic acids have been used as surface modifiers in hybrid perovskite solar cells[5, 9].

Benzoic acids have been shown to reduce the surface defects on the surface of the TiO_2 layer by chemically bonding with non-bonded Ti^{4+} on the surface, since the non-bonded Ti^{4+} can act as a site to trap electrons[10]. In addition, benzoic acids and their derivatives can be used to adjust the work function at the interface as they have dipole moments. They can be functionalized easily to get various derivatives with different dipole moments. [4] It has been reported that benzoic acids with para-position functional groups such as amino, methoxyl, bromide, cyano and nitro groups have dipoles of -4.5D, -3.9D,1.4D, 3.4D and 3.8D respectively[4]. The negative or positive dipole moment can be introduced at the interface according to the structure of devices to improve the energy level alignment.

Recent research using benzoic acids in hybrid perovskite solar cells generally targets the mesoporous TiO_2 layer in mesoporous devices. To date no study about modifying the compact TiO_2 layer has been reported. Zhu and co-authors used a group of benzoic acids (i.e. 4-amino benzoic acid, 4-chloride benzoic acid, benzoic acid and 4-nitro benzoic acid) to modify the mesoporous TiO_2 in mixed cations and mixed halides perovskite solar cells.[5] Benzoic acids interlayers did not change the morphology and crystallinity of perovskite, but they significantly improved charge extraction. Out of all the molecules, 4-chlorobenzoic acid was observed to improve the device PCE from 17.5 % to 18.4%, while 4-nitrobenzoic acid and 4-aminobenzoic acid were found to

have a negative effect on the device PCE. Li *et.al.*[9] employed 4-aminobenzoic acid in their mesoporous $CH_3NH_3PbI_3$ perovskite solar cells. However, unlike the studies above, they found the morphology of perovskite layer was modified, and the device performance was improved from 9.6% to 10.6%.

In this chapter, the effects of benzoic acids interlayers on hybrid perovskite solar cells is discussed. Three benzoic acids with different amino groups, 4-aminobenzoic acid (ABA), 4-(aminomethyl) benzoic acid (AMBA) and 4-(methylamino) benzoic acid (MABA) were investigated. They were all used to modify the compact TiO_2 layers in planar perovskite solar cells, and their impact on the surface energy of the TiO_2 layer, perovskite layer morphology and crystallinity were studied. As the functional groups have different substitutions, the effects on perovskite crystallization caused by them were also discussed. Inconsistent results have been reported in literature studies (as mentioned above) containing the same benzoic acid derivatives and reasons for the differences are discussed. Experiments were also designed to figure out the factors that could cause the inconsistencies.

6.2 Experimental

Interlayer preparation

By spin coating: 10mM of the benzoic acid derivative was dissolved into H_2O with one equivalent of NH_4OH as the additive to make the interlayer precursor solutions. Interlayer films were prepared by spin coating the precursor solution at 500 rpm, 1000 rpm, 2000 rpm, 3000 rpm or 4000 rpm on TiO_2 blocking layer and then annealed at 120°C for 1 hour to remove the solvent.

By dip coating: TiO_2 substrates were heated to 60°C and then immersed into 0.1mM benzoic acid derivative MeOH solution for 3h, 6h, 12h or 24h. Substrates were then taken out from the solution and rinsed with EtOH to remove any physically adsorbed molecules. N_2 flow was used to dry the substrates.

Device Fabrication: TiO_2 blocking layers were made by spray pyrolysis method unless specifically mentioned. Devices were fabricated by using a one-step solution method in air unless mentioned specifically. The substrates and precursor solutions were kept at 60°C before depositing the perovskite layer. More details can be found in Chapter 3.

6.3 Structure of benzoic acids with amino groups and their potential roles as interlayers

ABA, AMBA and MABA show limited solubility in water. The solubility of ABA can be significantly increased when the pH is reduced below 4 or increased above 9. As shown in **Figure 6-1**, the reported solubility (calculated) at pH 7 is around 10mg/mL (~66 mM).[11] In this work, when a basic additive is added to deprotonate the carboxyl functional group, the solubility in water can reach 25 mg/mL. NH_4OH was therefore used to improve the solubility of all the solutions (**Figure 6-2**).

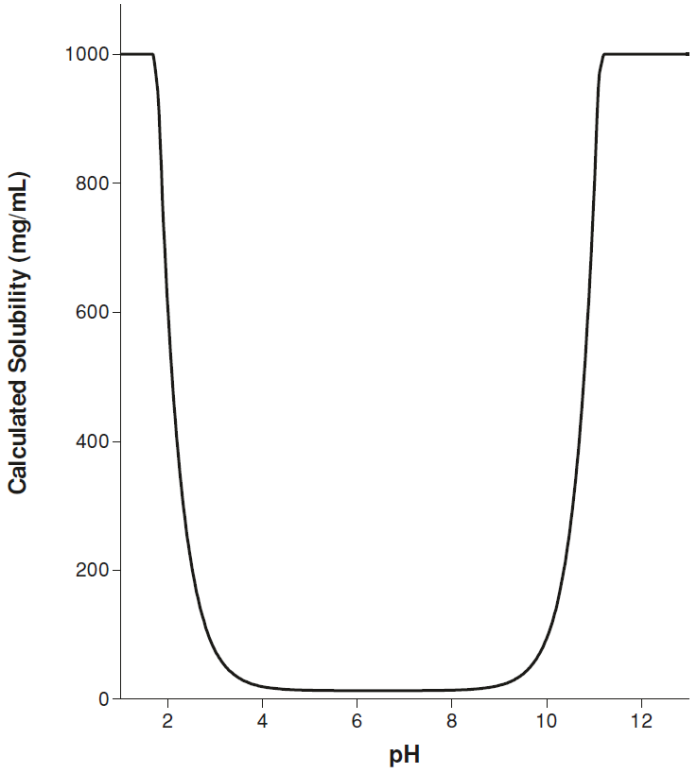

Figure 6-1 Calculated pH dependence of the aqueous solubility of 4-(aminomethyl) benzoic acid, generated using the program PhysChem 7.0 (Advanced Chemistry Development, Toronto, CA)[11].

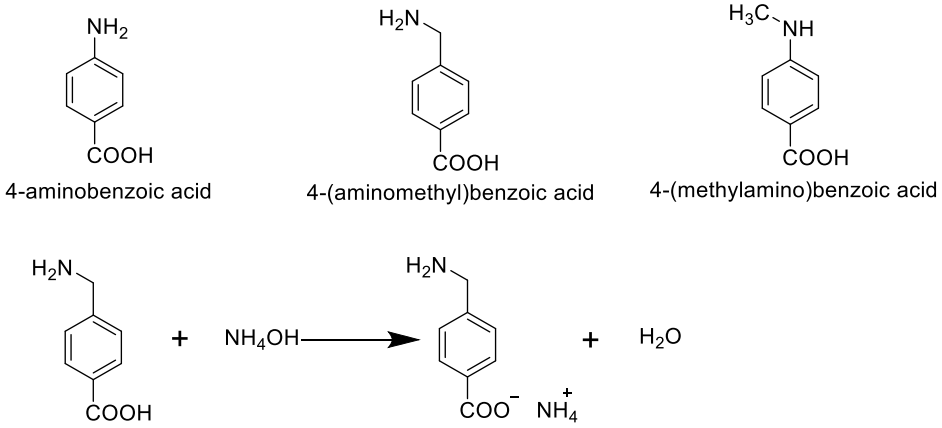

Figure 6-2 Molecular structure of amino benzoic acids

These three molecules have dipoles that point from the carboxylate group (negative end of the dipole) to the amino group (positive end of the dipole). As mentioned in the introduction chapter, aligned molecular dipoles can help interfacial band alignment in perovskite devices. Since the carboxyl group interacts with TiO_2 surface, the dipole introduced by the molecule will point away from the TiO_2 surface, and the work function of the TiO_2 should be reduced. Theoretically, as a result the built-in voltage of the p-i-n junction is expected to increase, and it is beneficial to charge collection in the device.. In addition, molecules with amino groups have been reported to be able to coordinate with the non-bonded Pb^{2+} , the amino benzoic acid layer could therefore affect the defects at the interface and could also possibly affect the crystallinity of the perovksite films[5, 12].

6.4 4-(Aminomethyl) benzoic acid

6.4.1 Solubility of AMBA--effects of NH_4OH

AMBA was the first molecule to be studied. As mentioned in the experimental part, NH_4OH was added into the spin coating solution to improve its solubility. It was observed that the optical properties of AMBA have not been changed. The UV-vis absorption signal of the AMBA solution and its salt are the same, and are shown in **Figure 6-3**. The molecule AMBA and its salt only absorb light in the UV region, which makes it a good candidate as the interlayer, since it doesn't affect the light harvesting of the perovskite layer. In addition, the absorption of UV light could improve the stability of devices (though the UV light absorbed by a interlayer may be negligible), as UV light is one of the factors that causes the degradation of the perovskite.[13]

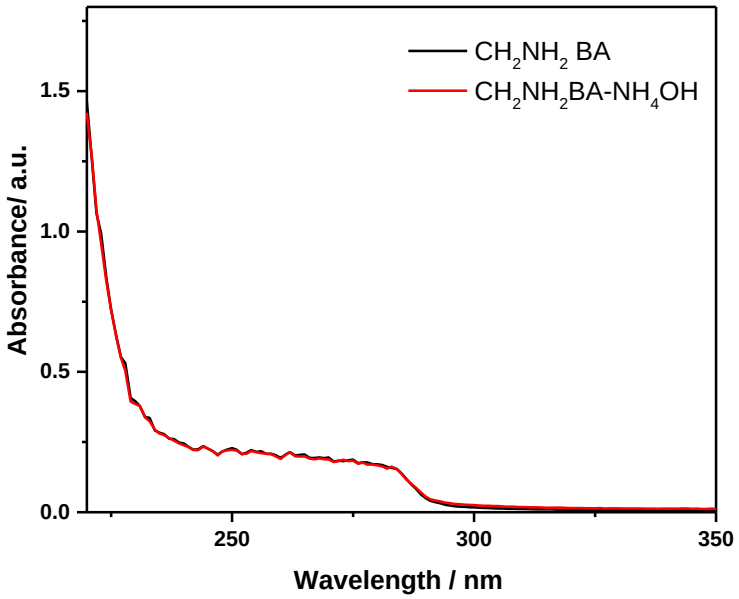

Figure 6-3 UV-Vis of solutions with and without the addition of NH_4OH

To investigate the influence of the NH_4OH additive on the solar cell performance, devices were fabricated based on interlayers made from solutions with and without NH_4OH, and the performance of these devices was characterized through J-V scans. As shown in **Figure 6-4** and Table **6-1**, the J_{sc} is obviously improved from 11.37 to 12.82 $mAcm^{-2}$ in devices with AMBA interlayers made from the basic solution. The V_{oc} increases slightly as well from 0.92 V to 0.94 V. The changes in J_{sc} and V_{oc} indicate that the usage of the basic additive in interlayer preparation solution can modify the device performance.

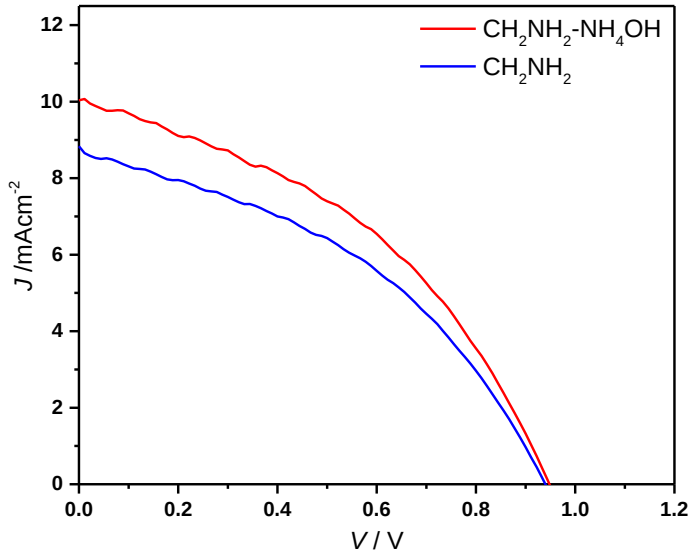

Figure 6-4 J-V curves of devices. CH_2NH_2-NH_4OH represents interlayers prepared from the AMBA solution with NH_4OH additive, and CH_2NH_2 represents the one without basic additive. Device structures are: FTO/TiO_2/AMBA/$CH_3NH_3Pb_{1-x}ICl_x$/spiro-OMeTAD/Au and FTO/TiO_2/AMBA-NH_4OH/ $CH_3NH_3Pb_{1-x}ICl_x$/spiro-OMeTAD/Au respectively. Devices were tested at one sun AM1.5 with a scan rate of 200 mV/s at ambient environment. The active area of each device is 0.075cm^2.

Table 6-1 Device parameters.

Device	J_{sc} / $mAcm^{-2}$	V_{oc} / V	FF	PCE /%
CH_2NH_2	11.37 ± 1.04	0.92 ± 0.02	0.35 ± 0.04	3.63 ± 0.44
CH_2NH_2-NH_4OH	12.82 ± 0.88	0.94 ± 0.01	0.35 ± 0.04	4.17 ± 0.55

6.4.2 Optimisation of 4-(Aminomethyl) benzoic acid interlayer

Optimization of the spin coating process for interlayer preparation was carried out by varying the spin coating speeds from 500 rpm to 4000 rpm. All the interlayer precursor solutions had NH_4OH as an additive. The corresponding devices were characterized by J-V scans in the dark and under illumination, and the results are shown in Figure **6-5**. All devices show typical diode characteristics as shown in Figure **6-5**(b) when tested at the dark. When tested under illumination, it is observed that the J_{sc} of devices changed significantly with the variation of the spin coating speeds for making the interlayers. The J_{sc} increases with the spin coating speed in the range of 0.5k to 3k rpm and decreases from 3 k to 4 k rpm. It peaks for devices prepared at 3k rpm, with an average J_{sc} of 16.81 $mAcm^{-2}$ (shown in Table **6-3**). There is also a change in the FF, and it peaks

in the 3k rpm deposited devices. The FF is 0.64 on average which is 45% higher than the cells prepared at the lowest spin rate (0.5k).

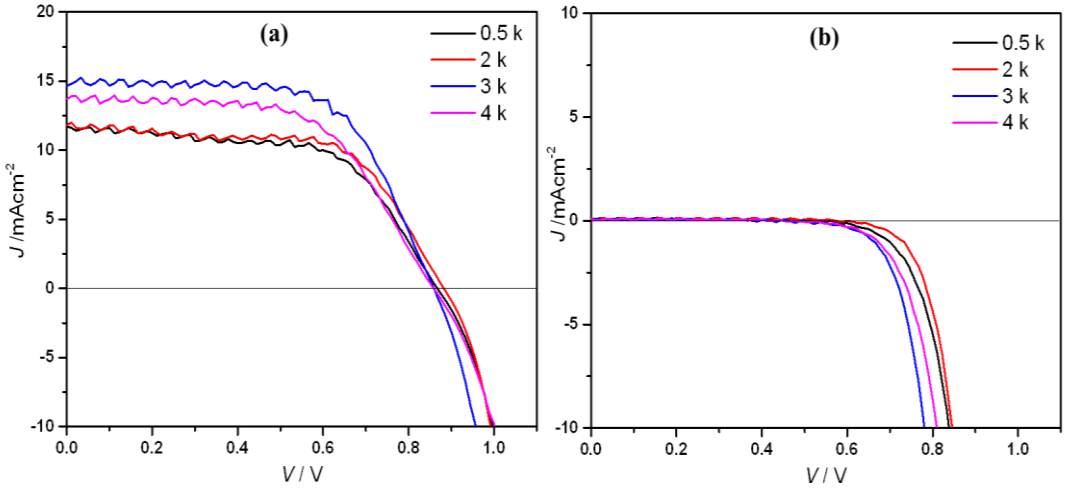

Figure 6-5 J-V curves of devices with different spin speed deposited AMBA under illumination (a) and at dark (b). Devices are labelled according to the spin coating speed and their structure is FTO/TiO_2/AMBA-NH_4OH/$CH_3NH_3Pb_{1-x}ICl_x$/spiro-OMeTAD/Au. Devices were tested at one sun AM1.5 with a scan rate of 200 mV/s at ambient environment. The active area of each device is 0.075cm^2.

Table 6-2 Device parameters. Devices are labelled according to the spin coating speeds for making the interlayers.

Device	J_{sc} / $mAcm^{-2}$	V_{oc} / V	FF	PCE /%
0.5k	7.72 ± 5.81	0.83 ± 0.14	0.41 ± 0.05	2.66 ± 2.09
2k	11.80 ± 3.00	0.82 ± 0.15	0.56 ± 0.07	5.62 ± 2.32
3k	16.81 ± 1.30	0.85 ± 0.02	0.64 ± 0.02	8.98 ± 0.89
4k	12.87 ± 5.39	0.74 ± 0.08	0.59 ± 0.05	5.79 ± 2.83

6.4.3 AMBA interlayer for planar hybrid perovskite solar cells

After the optimization of preparation conditions, AMBA interlayers were deposited using the optimized parameters to make hybrid perovskite solar cells, and the performance was compared with the standard device. J-V curves under illumination (Figure **6-6** (a)) show that the J_{sc} of the device is increased with the interface engineering, and Table **6-3** shows that the J_{sc} increases from 15.98 ± 0.79 $mAcm^{-2}$ to 16.58 ± 0.41 $mAcm^{-2}$ after interface engineering with AMBA. The improved J_{sc} could be due to enhancing the film quality of the perovskite layer as the amino functional groups in the interlayer are believed participate into the crystallization process of

perovskites[14], and XRD measurements were carried out in the following work in order to find the evidence about changes in crystallisation for the perovskite films after interface engineering. The V_{oc} is largely unchanged by surface modification (**Figure 6-6** and Table **6-3**). Though the J_{sc} is improved after interface engineering, the FF is decreased obviously and it causes the PCE to drop. As can be observed from the J-V curves under illumination (**Figure 6-6** (a)), the reason for the FF drop is the increase of the series resistance and the shunt resistance.

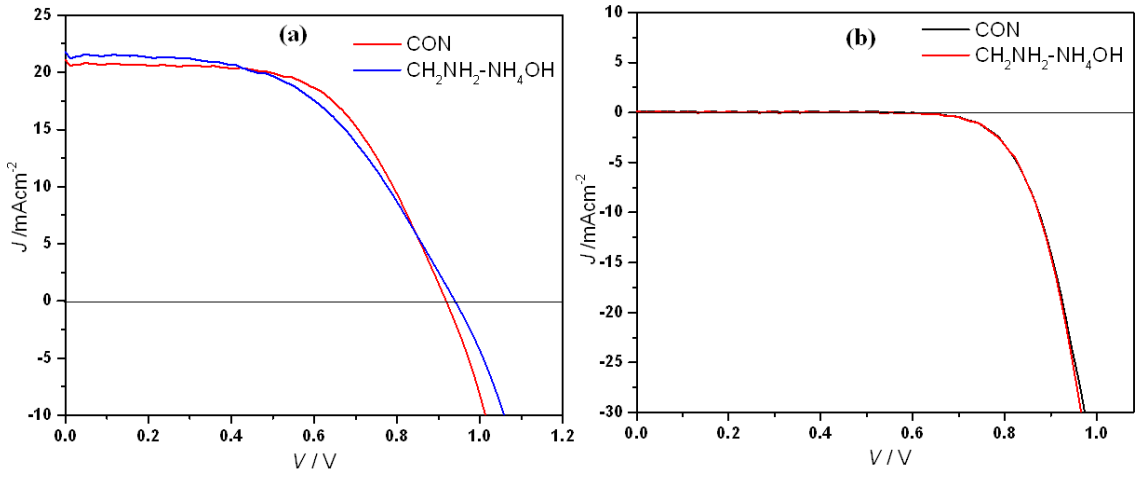

Figure 6-6 J-V curves of best performing devices with and without AMBA interlayers under illumination (a) and at dark (b). Devices structure is CH_2NH_2-NH_4OH: FTO/TiO_2/AMBA-NH_4OH/$CH_3NH_3Pb_{1-x}ICl_x$/spiro-OMeTAD/Au, CON: FTO/TiO_2/AMBA-NH_4OH/$CH_3NH_3Pb_{1-x}ICl_x$/spiro-OMeTAD/Au. Devices (12 devices in total) were tested at one sun AM1.5 with a scan rate of 200mV/s at ambient environment. The active area of each device is 0.075cm^2. RH=22%.

Table 6-3 Device parameters. Devices were measured at standard condition (AM1.5, 100mW/cm^2)

Device	J_{sc} / $mAcm^{-2}$	V_{oc} / V	FF	PCE / %
CON	15.98 ± 0.79	0.88 ± 0.08	0.53 ± 0.06	9.58 ± 1.34
AMBA	16.58 ± 0.41	0.92 ± 0.02	0.44 ± 0.05	8.70 ± 1.09

6.4.4 Other characterizations

X-ray photoelectron spectroscopy was used to prove the existence of the AMBA interlayer. As displayed in Figure **6-7**, a peak at around 400 eV and a peak at 285 eV are clearly observed due to the binding energy of N 1S and C1s respectively, showing the presence of benzoic acid on the surface.

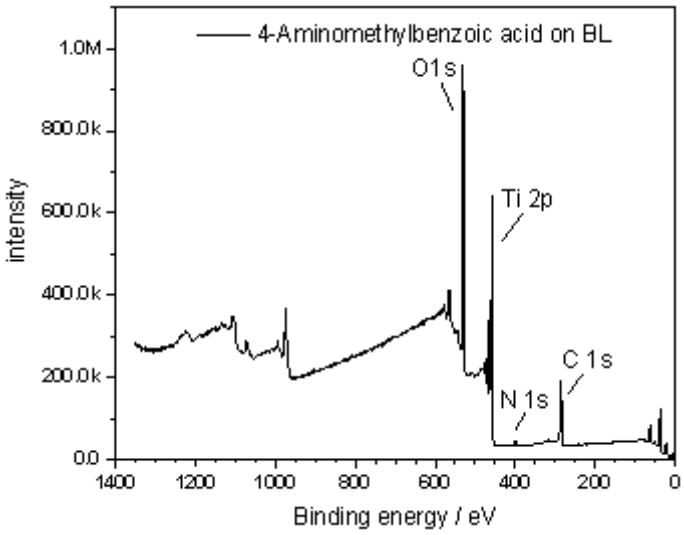

Figure 6-7 XPS of AMBA interlayer deposited on TiO_2

To understand how the overlying perovskite films were affected, contact angle measurements, AFM and XRD were used out study the substrate surface, the perovskite layer morphology and the perovskite film crystallinity. As demonstrated in Figure **6-8**, the advancing contact angle of the TiO_2 surface increased from around 12° to 27° on average after the deposition of the AMBA interlayer. The surface is therefore less hydrophilic than the control, which will influence the wetting of the precursor solutions when preparing the film.

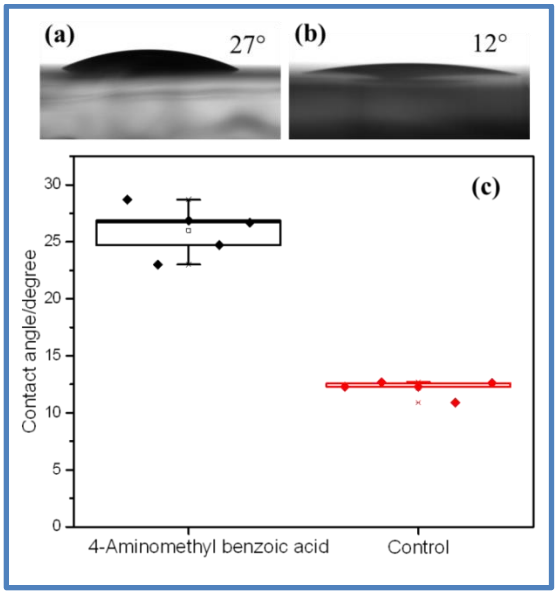

Figure 6-8 Contact angle of TiO_2 substrates. Photos shows contact angle of (a) TiO_2 with spin coated AMBA and (b) TiO_2, (c) box plot showing average contact angles of different TiO_2 substrates.

Since any change in the surface energy can possibly change the morphology of perovskite films, we used AFM measurements to investigate the perovskite films' morphology when interface engineering is employed. As shown in Figure **6-9**, the morphologies of the perovskite films display distinct differences in the grain size and coverage. It is noticed that with the AMBA interlayer, the deposited perovskite films have a more compact surface and bigger grains than the control sample. The average roughness of the control sample was around 154.7±9.1 nm, while the sample with an AMBA interlayer showed a much lower roughness, 83.9±1.3nm as calculated.

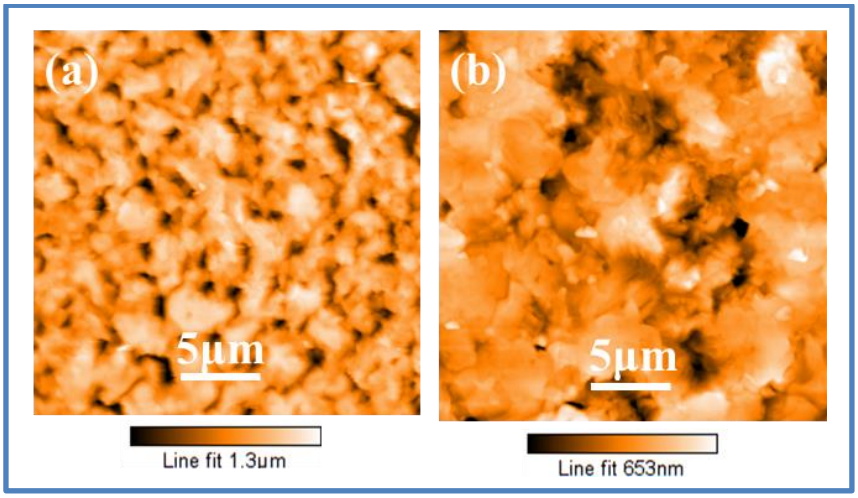

Figure 6-9 AFM of perovskite films deposited (a) on the TiO_2 compact layer (control), (b) on the TiO_2 with AMBA interlayer

X-ray diffraction was used to further understand the effect of the AMBA interlayer on the crystals of the perovskite films, and the diffraction patterns are shown in Figure **6-10**. The characteristic peaks at 14.1°(110) and 28.5°(220) displayed in the patterns indicate that both the perovskite samples(e.g. control and AMBA) are in the tetragonal phase. No peak of PbI_2 is observed in both samples, indicating the full conversion of PbI_2 to the perovskite. The peaks at 14.1° are given in an enlarged-scale figure (Figure **6-10** (right)), where the intensity and FWHM are compared. It reveals that the particle sizes of the two perovskite samples are almost the same and the crystallinity is largely unchanged. This suggests that increased J_{sc} is not caused by the film quality change (in this measurement at least-there is some inconsistency between measurements on different batches of films)-more discussion is presented below.

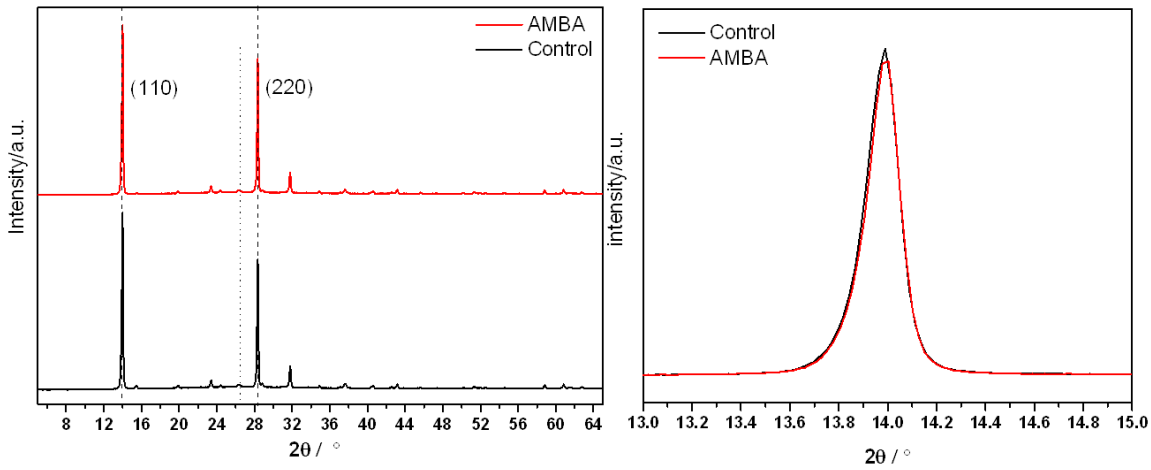

Figure 6-10 XRD of perovskite films deposited on TiO_2 and TiO_2 with AMBA.

6.4.5 4-aminobenzoic acid and 4-(methylamino) benzoic acid

In order to monitor the effects of different amino groups on solar cell performance, the other two benzoic acids were also introduced as interlayers, and the devices were made by using the same optimized procedures for making AMBA film. Devices with AMBA were also fabricated in this batch. After analysing the J-V curves of different devices (Figure **6-11**), it is interesting to notice that the device parameters vary with the amino groups' positions and substitutions. 4-aminobenzoic acid (ABA) and 4-(aminomethyl)benzoic acid(AMBA) are primary amines, while 4-(methylamino)benzoic acid is a secondary amine, and it has been reported that the interaction of these molecules with perovskite crystals are different[15]. The primary amines are less hindered than the secondary amines and therefore could more easily affect the passivation of perovskite films, as the lone pair electrons of N are more flexible. As shown in Figure **6-11**, devices with ABA and AMBA which have primary amino groups show higher J_{sc} than MABA devices (secondary amine), and the J_{sc} is also higher than the standard devices. The average J_{sc} is 18.42 $mAcm^{-2}$ for ABA devices, 18.51 $mAcm^{-2}$ for AMBA devices and 15.48 $mAcm^{-2}$ for MABA devices. The J_{sc} of the control devices is 15.77 $mAcm^{-2}$ as demonstrated in Table **6-4**, which is located between the secondary amine and primary amine devices. In this experiment, the hypothesis was that the terminal function group interacted with the perovskite film which could change the perovskite crystallinity . This hypothesis seems to be supported by the trend in the J_{sc} values and crystallinity of the films (**Figure 6-15**). However, from the last batch experiment, the J_{sc} was improved after adding AMBA, while the

crystallinity didn't change. Thus it is believed that interface engineering caused crystallinity change could be one of the origins of the J_{sc} increase, but not the only one.

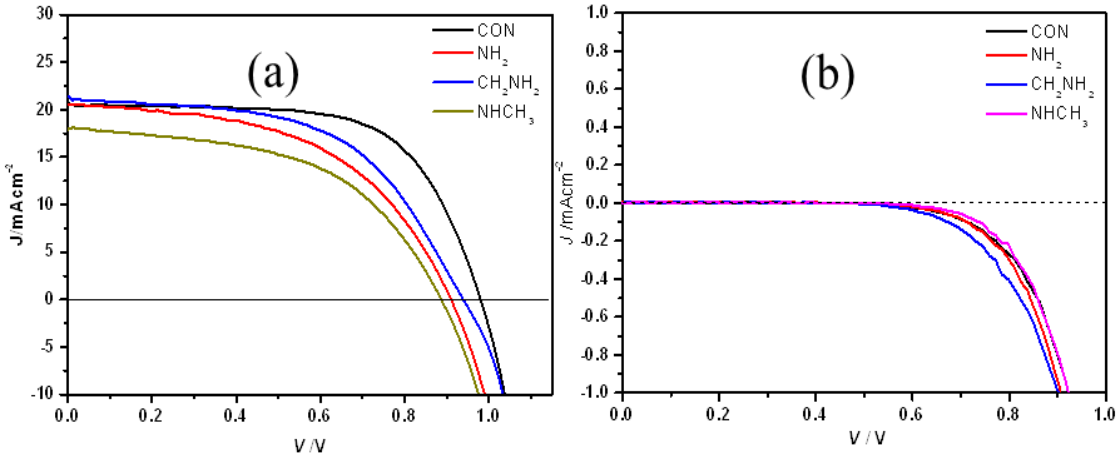

Figure 6-11 J-V curves of best performing devices with and without interlayers. CON: FTO/TiO_2/bezoic acids-$NH_4OH/CH_3NH_3Pb_{1-x}ICl_x$/spiro-OMeTAD/Au, and device with interlayers are: FTO/TiO_2/bezoic acids-$NH_4OH/CH_3NH_3Pb_{1-x}ICl_x$/spiro-OMeTAD/Au. All devices (12 devices for each type) were tested at one sun AM1.5 with a scan rate of 200mV/s at ambient environment. The active area of each device is 0.075cm^2. RH%=37%

Table 6-4 Device parameters. Devices (12 devices for each type) are labelled according to the amino groups.

Device	V_{oc} / V	J_{sc} /$mAcm^{-2}$	FF / %	PCE / %
CON	0.96 ± 0.03	15.77 ± 4.99	0.58 ± 0.08	9.1 ± 3.9
-NH_2 (ABA)	0.88 ± 0.05	18.42 ± 3.24	0.49 ± 0.03	7.9 ± 1.2
-CH_2NH_2 (AMBA)	0.93 ± 0.02	18.51 ± 2.02	0.50 ± 0.03	8.7 ± 1.4
-$NHCH_3$ (MABA)	0.90 ± 0.03	15.48 ± 3.07	0.51 ± 0.03	7.0 ± 1.1

The influence of the terminal functional groups of the benzoic acids in the perovskite crystal is also illustrated in Scheme **6-1**. Due to the similarities to the methyl ammonium ion, the amino groups of ABA and AMBA are supposed to interact with the Pb^{2+} via the lone pair electrons provided by the nitrogen. They therefore could affect the perovskite crystallization because of their competition with $CH_3NH_3^+$. In contrast the secondary amine MABA finds it slightly more difficult to bond with Pb^{2+} due to the steric-hindrance caused by the methyl substitute. The $-NH_2$ in ABA is less flexible than that of AMBA, which makes it less effective in its involvement in the perovskite crystal. In a word, it is assumed that among the three interlayers, the activity of the terminal group interacting with Pb^{2+} in perovskite is AMBA > ABA > MABA.

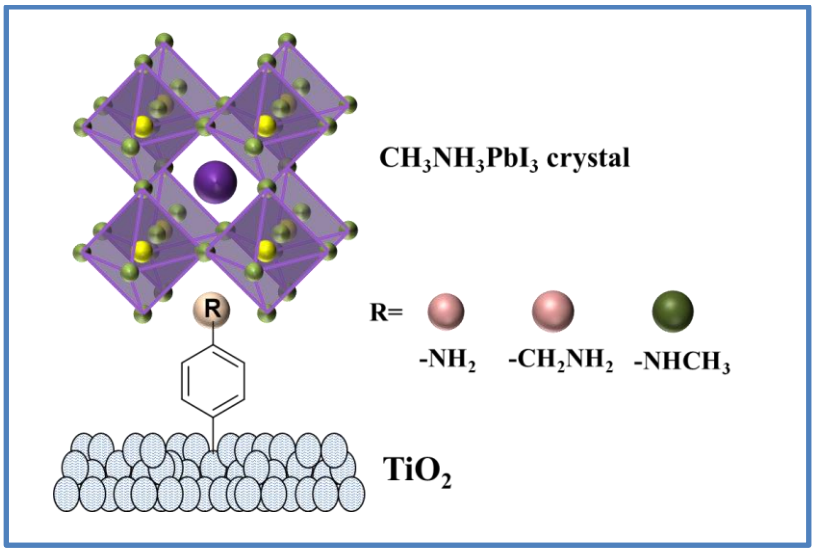

Scheme 6-1 The interactions of interlayers and the perovskite crystal.

According to the device parameters given by the J-V scans under illumination, the J_{sc} of ABA and AMBA devices are close when compared with that of MABA and control devices, though the J_{sc} of ABA devices is still slightly lower than the AMBA devices. This result is consistent with the hypothesis mentioned before as the perovskite film quality mainly determines the J_{sc} at least in these measurements. Once again, the V_{oc} of the devices are very similar (within experimental error), although it appears that the V_{oc} of the control is slightly higher. Though the J_{sc} is found improved, the PCE of devices with ABA and AMBA interlayers is decreased compared with the control devices. According to **Table 6-4**, the decrease is due to slightly lower FF. As it is observed in J-V curves, both the shunt resistance and series resistance are worse than the control, and the results are consistence with the last batch made devices. Theoretically benzoic acids should decrease the WF of TiO_2 and thus increase the V_{bi} of the junction which will improve the charge separation and collection. Improvement in charge collection will increase the J_{sc}, therefore, it is concluded that the J_{sc} increase could be attributed to two reasons, one is crystallinity changes caused by the interlayer, and the other one is the WF adjustment which leads to a charge collection improvement. The crystallinity change is not observed in the first batch of devices which could be resulted from the other factors that have more influence on the perovskite morphology (e.g. contact angle).

As shown in Figure **6-12**, contact angles for the bare TiO_2 and TiO_2 with benzoic acids were measured by using water as the testing liquid. The contact angle is slightly increased after the deposition of interlayers, and increased from around 35° to around

40°. AMBA has the lowest contact angle (~38°) out of the three molecules. ABA and AMBA both have $–NH_2$ as the terminal group, but the molecular dipole of AMBA is estimated to be bigger, as its electron donating group $–CH_2NH_2$ has a relatively high electron density than $–NH_2$. Due to the hydrophobic terminal group $–CH_3$, MABA surface has a higher contact angle than AMBA. It is interesting to notice that, after the deposition of interlayers, the standard deviation of the contact angle becomes smaller, indicating the wetting is more uniform on interlayers. Correspondingly, it is observed in the parameter table (Table **6-4**) that the PCE of solar cells has a lower standard deviation that the PCE for the control.

In addition to the contact angle change, it is also important to notice that the contact angle of the control TiO_2 is around 35° which is much higher than the same type of sample shown before (Figure **6-8**) where it was around 12°. The difference of the contact angle could be due to the roughness difference or the film age caused a surface energy change (details can be found in Figure **6-21**).

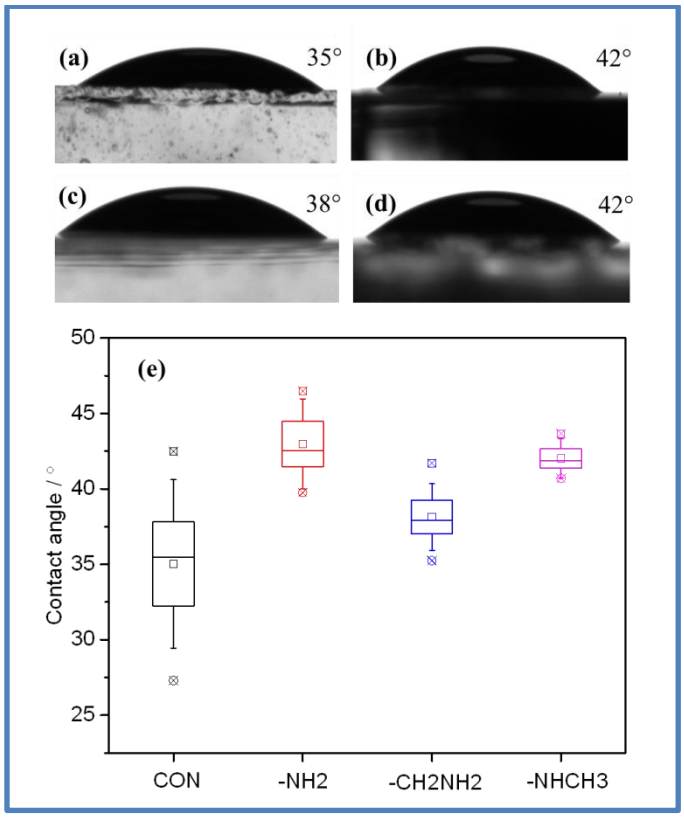

Figure 6-12 Contact angle of TiO_2 before and after interface engineering.

AFM images shown in Figure **6-13** display the morphology of perovskite films deposited on TiO_2 and TiO_2 with different interlayers. Their morphologies are not distinctly different, but there are slight differences in roughness and grain sizes. The average roughness is around 86nm, 97nm, 91nm and 75nm for the control, ABA, AMBA and MABA respectively. MABA has the smoothest surface, but the grain size of the perovskite film is decreased. The decreased grain size raises the number of grain boundaries which is supposed to increase surface recombination and reduce the PCE. However, the morphology changes are different from what we observed for the control and AMBA sample in previous batch (Figure **6-9**). It is supposed that the humidity of the environment and the variation of the TiO_2 surface wetting properties between the two sample batches resulted in the inconsistencies in the perovskite morphology, and these factors make a bigger impact on the perovskite film than the interlayer properties. More details can be found in part 6.5 where all the possible reasons that caused the morphology difference are discussed. Although the perovskite morphology did vary between batches, the J_{sc} always increased and PCE always decreased when an interlayer was added.

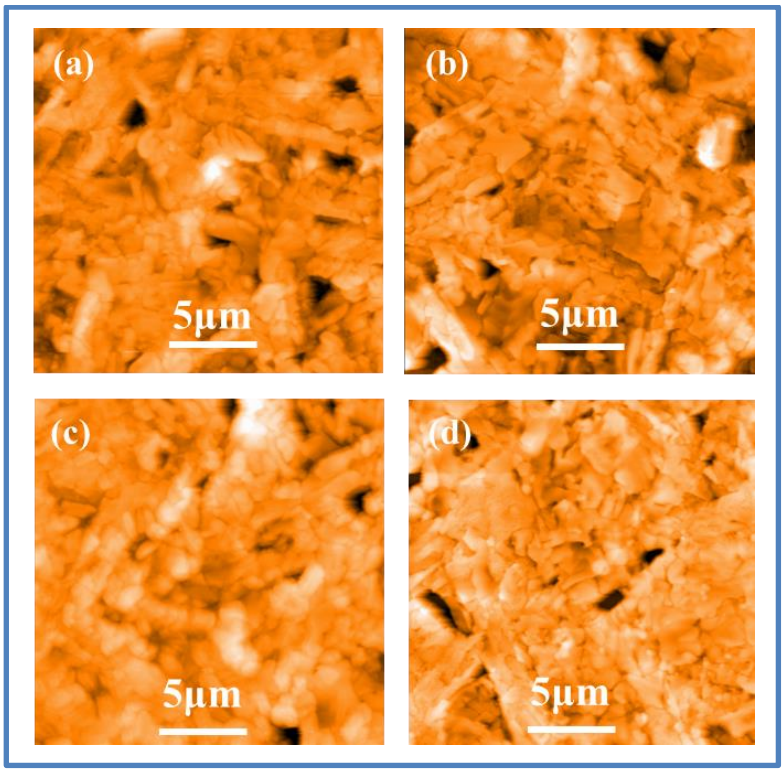

Figure 6-13 AFM images of perovskite films deposited on (a) TiO_2 , (b) ABA, (c) AMBA, (d) MABA.

UV-vis was used to further understand the effect of the interlayer on light harvesting. The absorption curves in Figure **6-14** show that interface engineering with benzoic acids does not change the band gap and the light absorbing ability of the perovskite. The absorption onsets are all around 790 nm which corresponds to a band gap of 1.57eV.

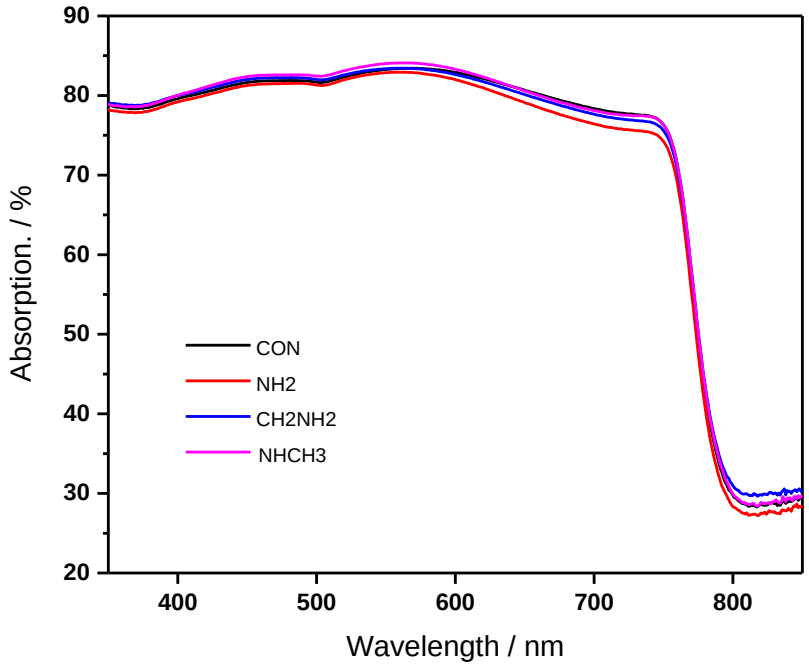

Figure 6-14 UV-vis of perovskite films deposited on TiO_2 with different interlayes.NH_2 represents the ABA interlayer, CH_2NH_2 represents AMBA interlayer and $NHCH_3$ represents MABA interlayer. Absorption is extracted by using Absorption%=100%-Transmission%-Reflection%.

In order to determine the crystal structure and obtain information on crystallinity, the four perovskite films were characterised by powder X-ray diffraction. As shown in Figure **6-15**(a), peaks at 14.2°(110) and 28.5°(220) indicate all films contain tetragonal phase $CH_3NH_3PbI_3$ crystals. It is also revealed that PbI_2 is not fully converted in all samples, as the characteristic peak of PbI_2 at 12.9° (101) is still noticed in the diffraction curves. Among these samples, AMBA shows the weakest intensity at 12.9°, indicating its relatively higher conversion ratio than the others. Table **6-5** exhibits the full width at half maximum (FWHM) of the peak at 14.2° which is the (110) lattice plane of the tetragonal perovskite crystal. It is revealed from the peak intensity displayed in Figure **6-15**(b) as well as the FWHM shown in the table that the sample deposited on an AMBA interlayer has the best crystallinity and largest particles as it has the highest peak intensity and narrow FWHM out of the 4 samples, while MABA has a similar crytallinity and particle size as the control. The results for the perovskite film

crystallinity are consistent with the J_{sc} variations among samples since film quality is closely related to J_{sc}.

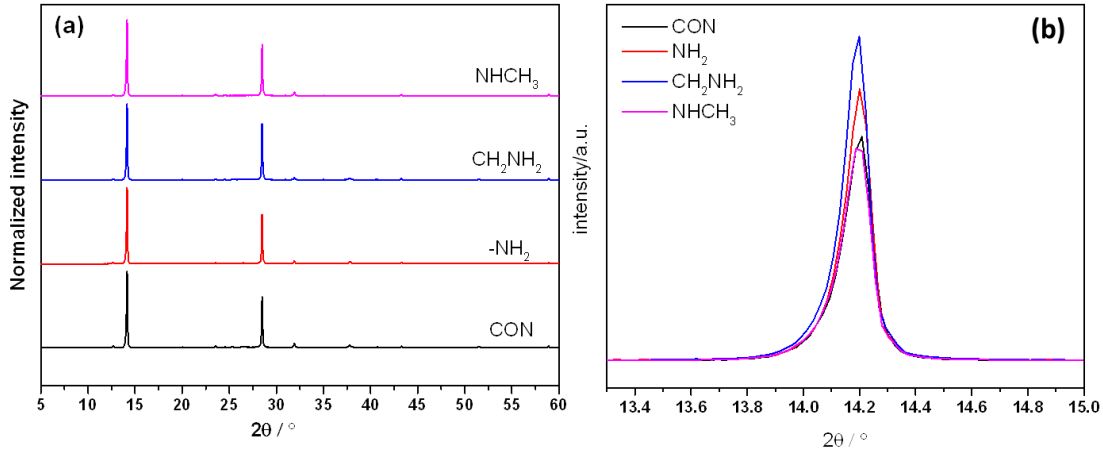

Figure 6-15 XRD of perovskite films deposited on TiO_2 and TiO_2 with different benzoic acids. (a) Diffraction patterns of the control and ABA (NH_2), AMBA (CH_2NH_2) and MABA ($NHCH_3$), (b) enlarged-scale of peak at 14.2° (110).

Table 6-5 FWHM of the diffraction peak at 14.2 (110 lattice plane)

Sample	CON	NH_2	CH_2NH_2	$NHCH_3$
FWHM	0.133	0.124	0.119	0.134

6.4.6 Impedance characterization

Impedance Spectroscopy (IS) was carried out at different light intensities for all the solar cell devices to understand the recombination behaviour of the charges. The measurements were operated at V_{oc} by using a blue LED (470nm) as the light source. According to Pockett et al[16], the recombination resistance is given by the intercept of the high frequency semi-circle with the real axis. However, a subsequent study by the same authors[16] proposed that the recombination should be represented by a complex impedance rather than a simple resistance in order to take into account time-dependent changes in recombination rate brought about by slow relaxation of the ionic distributions (and hence of the electric field profile) within the film. The equivalent circuit can therefore be shown as Figure **6-16**, in which R_s represents the series resistance, Z_{rec} represents the complex recombination impedance, C_{geo} represents the geometry capacitance, R_{shunt} is the shunt resistance, R_{ionic} is related to ionic transportresistance and C_{dl} is the double layer resistance. As a general condition in a

good cell, R_{shunt} is much higher than the R_{rec}. Furthermore the ionic transport resistance is expected to be sufficiently high that it can be neglected, which means that the model can be simplified to the one in the bottom in Figure 6-16.

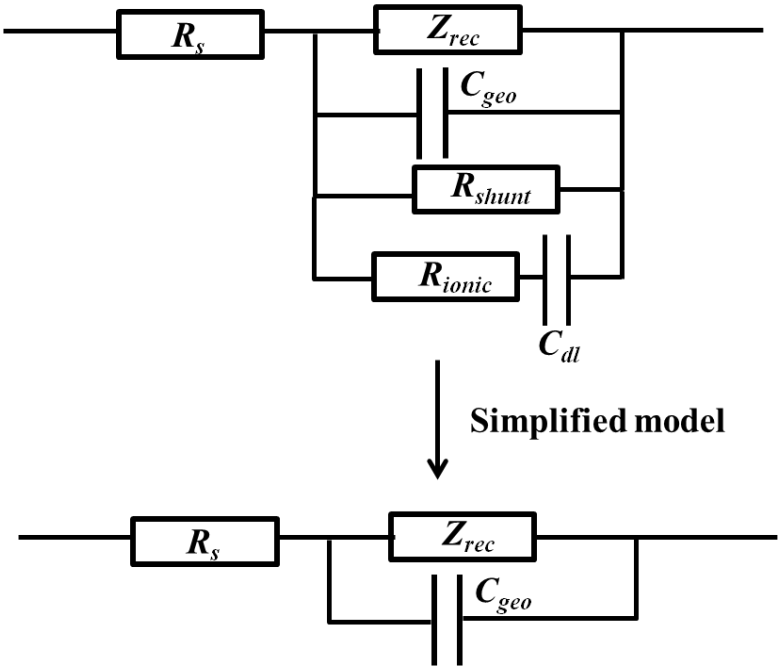

Figure 6-16 Equivalent circuit and simplified model of high frequency response for a planar structured perovskite solar cell.

As shown in Figure **6-17**, the RC response represented by the first semicircle shows that the R_{rec} decreases with light intensities for both the control and device with interlayers (AMBA (CH_2NH_2) as a representative). It can be ascribed to the increase in the number of excited charges when the illuminated light intensity is increased. More details about the relationship between the recombination resistance and the light intensity can be found in part 6.8.

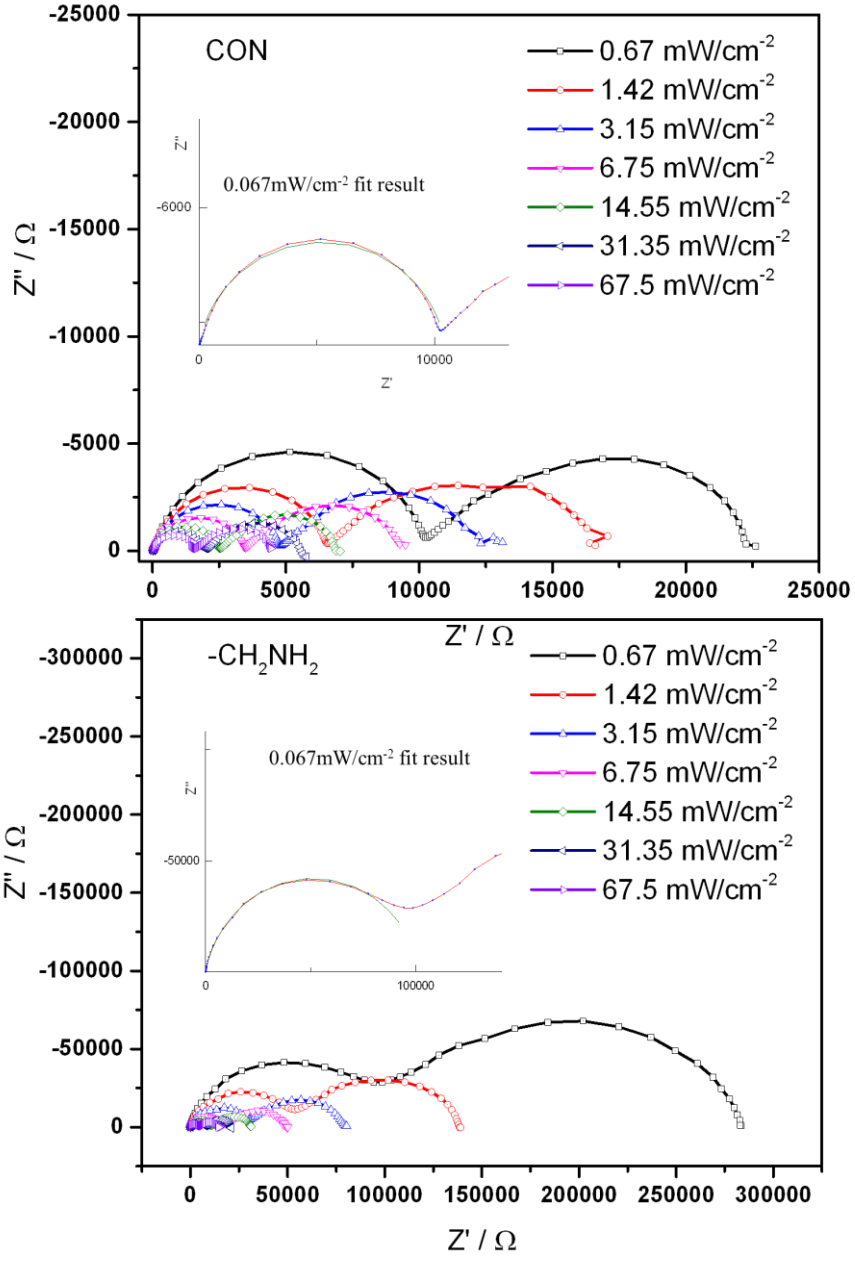

Figure 6-17 Nyquist plots of control device (CON) and AMBA device (CH_2NH_2) at different light intensities. Impedance spectrums were collected at V_{oc} from 10^6HZ to 5 mHZ at room temperature

To further understand the relationship between R_{rec} and the light intensity, R_{rec} obtained from the impedance spectra was plotted versus light intensity. It was found that the logplot of R_{rec} versus light intensity shows a linear relationship as displayed in Figure **6-18**. However, the slopes of the plots are less than 1, showing the R_{rec} is not inversely proportional to the light intensity as expected. (the deviation can be found in the supporting information at the end of this chapter). Notably, the R_{rec} of devices with interlayers are higher than the control, indicating that recombination in devices with

interlayers occurs less easily than in the control. Especially the R_{rec} of the device with AMBA (NH_2CH_2 or 4-(aminomethyl) benzoic acid) is one order of magnitude higher than in the control device, showing recombination is more difficult in devices with those benzoic acids interlayers.

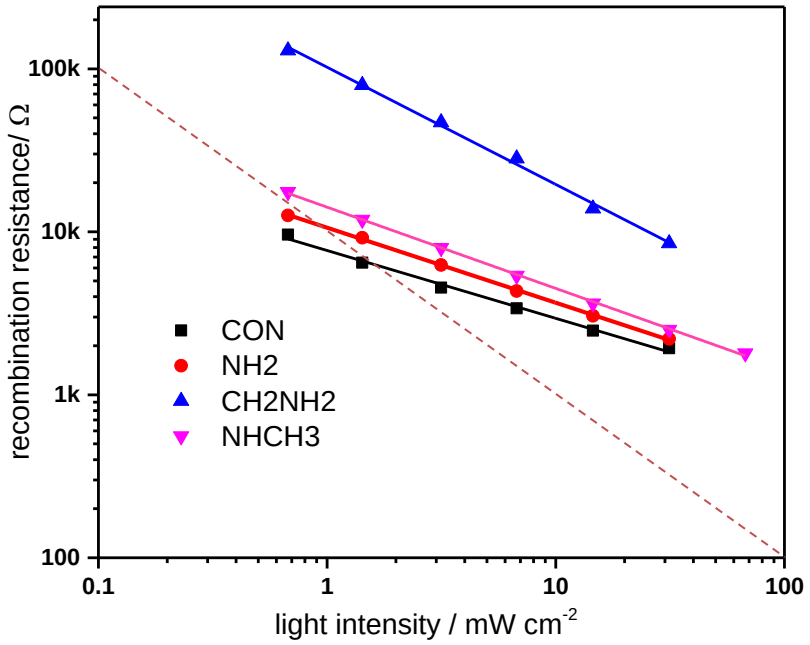

Figure 6-18 Recombination resistances of devices at different light intensities.CON is the control device, NH_2 is the ABA device, CH_2NH_2 is the AMBA device and $NHCH_3$ is the MABA device.

Table **6-6** lists the gradients of the linear fits shown above. It is interesting to notice that devices with interlayers containing 4-(aminomethyl) benzoic acid show a steeper gradient. It is possible that interlayers with terminal groups that are involved in the perovskite crystallization could have a higher impact on the recombination behaviour of solar cells. However, the mechanism of how the recombination process is affected by the interlayers remains unclear. It could be the reduction of surface defects due to the crystallinity improvements in the perovskite films.

Table 6-6 Gradients and other parameters of curves $\log R_{rec}$ vs. light intensity.

Device	Gradient	Geometric Capacitance / F	Geometric Capacitance / Fcm^{-2}	R^2 of curves
CON	-0.41	5.55E-08	7.44E-7	99.4%
NH_2	-0.46	1.48E-07	1.97E-6	99.9%
CH_2NH_2	-0.72	6.65E-08	8.87E-7	99.6%
$NHCH_3$	-0.50	2.35E-07	3.13E-6	99.9%

6.5 Discussion of inconsistency in device performance

Based on this study, the changes in perovskite morphology and some of the device parameters show very different trends after interface engineering of different batches of devices. The morphologies of the perovskite films with and without interface engineering are distinctly different among the first batch samples. However, the difference was observed to be negligible in the second batch. Interestingly, this phenomenon has been observed in other work. There are some reported studies, which used the same benzoic acids as the interlayers in devices with the same architecture, but reported opposite influences of the interlayer on device performances.[5, 9, 15] In Table 6-7, the interlayer deposition methods and the performance of corresponding devices reported in the two papers and those investigated in this chapter are displayed. From the information listed in the table, it seems the impacts of the benzoic acids are very hard to determine as the results from different experiments are not consistent. The differences in the reported studies come mainly from FF and J_{sc}. In our work the effect of AMBA on the J_{sc} and FF of devices was always the same.

It is noticed that the changes in perovskite film morphology are more distinct when the changes in contact angle are larger (column "perovskite morphology change" in Table 6-7). Therefore, it looks like the change in the contact angle is the main factor that dominates the change of the perovskite film morphology. Notably, in our study, the contact angle measurements reveal that the substrates' wetting properties vary differently from batch to batch. The contact angle increases from 12° to 27° (15° difference) in the first batch, while it changes from 35° to 38° (3° difference) in the second batch after the deposition of the interlayers. In the published studies, the contact angle variation is opposite (e.g. paper A and paper B). It seems that the original surface of the modified substrates (i.e. mesoporous TiO_2 in reported papers and compact TiO_2 in our study) is extremely important. The contact angle of the TiO_2 is highly related to how the TiO_2 and is made, and it can be different even when the same preparation method is used. For instance, the roughness of the TiO_2 film will affect the wetting of the liquid to be coated. Thus, the impacts of the interlayer are not the only factor that determines the contact angle. We assume other factors derived from the environment could be the origin of the inconsistency.

Table 6-7 Comparison of experiments and device performances in different papers where same interlayer was used. Performances of devices from different batches with the same interlayer in this chapter are also listed.

Origin	**Molecule interlayer**	**Target layer**	**Interlayer preparation method**	**Contact angle***	**Perovskite morphology change***	**Crystallinity***	**Impact on devices***
Paper A[5]	4-aminobenzoic acid	Meso TiO_2	Immersion 2mM IPA	6° *vs.*12°	No obvious difference	No obvious change	J_{sc}↓, V_{oc}↓, FF↓, PCE↓
Paper B[9]	4-aminobenzoic acid	Meso TiO_2	Immersion 0.2mM EtOH	39° *vs.* 22°	Larger grain size	increased	J_{sc}↑, V_{oc}↓, FF↑, PCE↑
Batch 1	4-(aminomethyl) benzoic acid	Compact TiO_2	Spin-coating 10mM aqueous	12° *vs.* 27°	Larger grain size	No obvious change	J_{sc}↑, FF↓, PCE↓
Batch 2	4-(aminomethyl) benzoic acid	Compact TiO_2	Spin-coating 10mM aqueous	35° *vs.*38°	No obvious difference	Increased	J_{sc}↑, FF↓, PCE↓

* represents the changes (interlayer *vs.*control).

A planar perovskite solar cell based on TiO_2, with an interlayer to modify the TiO_2, is given in **Figure 6-19**. It illustrates the three possible interactions between different layers that could influence the device performance.①②③ represent all the interactions, including physical and chemical ones between those layers. For instance, in this study, ② comprises the influence the amino group has on the crystallization of the perovskite (chemical interaction) and the band edge changes caused by the surface dipole of the interlayers.

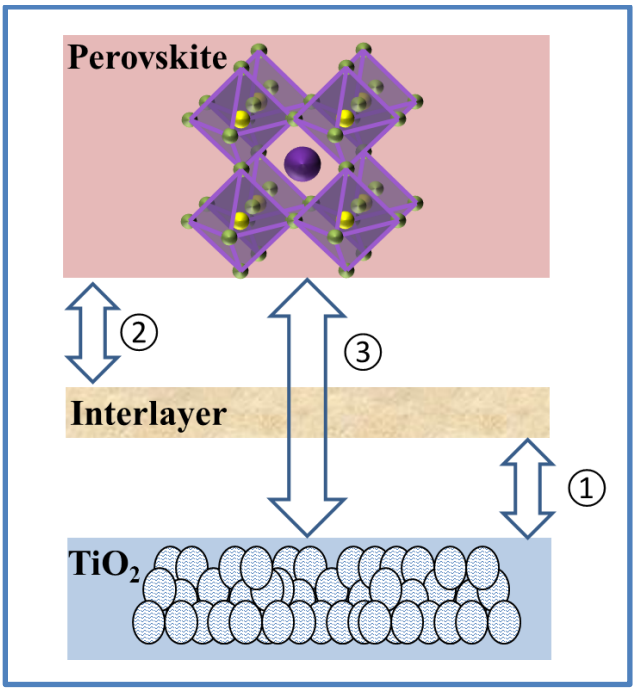

Figure 6-19 interactions between interlayers and other layers with a TiO_2 based planar perovskite solar cell as the example.①②③ represent the interactions between TiO_2 and the interlayer(TiO_2/interlayer), interlayer/perovskite and TiO_2/perovskite.

6.5.1 Humidity of the environment - possible inconsistency from the perovskite layer

Since the formation of perovskite films is extremely sensitive to the humidity of the environment, any change of the humidity will cause a variation in perovskite film morphology. Samples shown in Figure **6-9** and Figure **6-13** were prepared using exactly the same procedures. However there was a humidity difference of in the environment. It was 22% for the sample shown in Figure **6-9** and 38% for the one shown in Figure **6-13**. If the impact of the humidity on the morphology of the perovskite layer is larger than the change introduced by interface engineering, the influences of the interface engineering will not be evident in device performance.

6.5.2 Effects of the atmosphere-possible inconsistency from the TiO_2 layer

Another possible cause for inconsistent results could be the surface chemistry of the TiO_2 layer. This will directly affect interaction ① (TiO_2/interlayer) and indirectly affect interaction ②(interlayer/perovskite). It was noticed that the surface wetting properties of the blocking layer change significantly after being blown with N_2 even for a short time. As shown in Figure **6-20**, the contact angle of the TiO_2 layer increases from 22° to

42° after being blown with N_2 for 4 min. It could be attributed to the adsorption of N_2 onto the TiO_2, causing the surface to be less hydrophilic. It is also possible that exposure to a stream of dry nitrogen removes some water from the surface of the titania films, as these samples were exposed to the ambient environment for hours (stored in a petri dish) before being tested. When the perovskite solar cells were made, the blocking layers were generally prepared a few hours in advance, and the substrates with blocking layer were kept in a petri dish before the deposition of the perovskite layer. Therefore care must been taken when N_2 flow is used to dry the TiO_2 surface, and the atmosphere for storing TiO_2 substrates is also important.

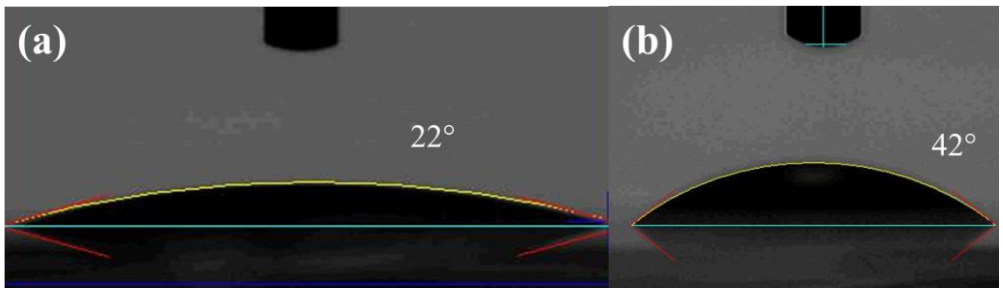

Figure 6-20 Water contact angle of TiO_2 (a) before and (b) after N_2 treatment for 4 min

It was found that after being stored under ambient conditions (in a covered petri dish) for 5 days, the contact angle of the TiO_2 also changed significantly (as displayed in Figure 6-21). The freshly made TiO_2 showed nearly zero contact angle to water, while after being stored for 5 days, the contact angle was 47°.

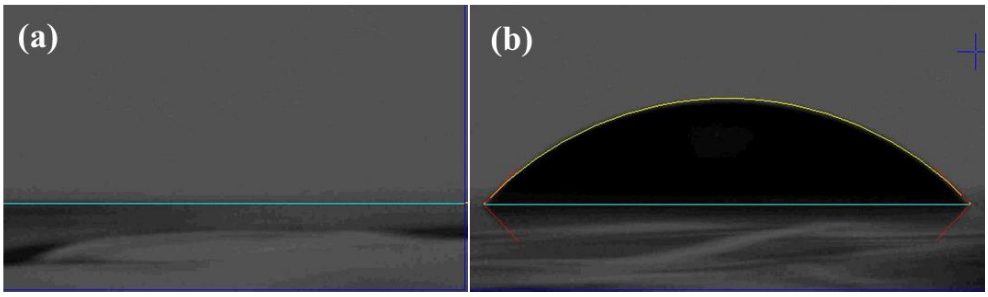

Figure 6-21 Water contact angle changes with the film age:(a) contact angle of freshly prepared film (b) contact angle of film after 5 days. Data provided by Isabella Poli.

6.5.3 Temperature of the ambient environment - possible inconsistencies in the interlayer

Interactions ①and ② can be affected if the state of the benzoic acid interlayer has been changed (e.g. coverage). One possible reason that could influence the interlayer is room

temperature variation. As the interlayers were prepared at room temperature, especially for the dip coating method, changes of ambient environment temperature could affect the binding kinetics However it seems unlikely that this would cause the big differences in perovskite morphology observed.

In a word, there are many reports on interface engineering in the literature, but care needs to be taken that any changes in the device are not due simply to differences in morphology of the perovskite film.

6.6 Conclusion and future work

In this chapter, three benzoic acids 4-aminobenzic acid, 4-(aminomethyl) benzoic acid and 4-(methylamino) benzoic acid) with different amino functional groups are used to modify the compact TiO_2 layer in perovskite solar cells. The procedures of interlayer preparation were optimized by adding NH_4OH and adjusting the spin coating parameters. Though the terminal amino groups can theoretically all become involve in the crystallization of perovskite layer, the changes caused by the substitutions are different. Primary amino groups (4-aminobenzoic acid and 4-(methylamino) benzoic acid) were found to display enhancement of J_{sc}, while secondary amino (4-aminomethyl benzoic acid) shows negative impact on J_{sc} when compared with control devices. Impedance spectroscopy was used to monitor the recombination in devices. It is observed that interface engineering can reduce the recombination, and 4-methylamino benzoic acid shows the best performance. In addition, the inconsistency showed in some of the film properties and in the literature was discussed. It is very likely that environment change (e.g. temperature, humidity and atmosphere) changed the perovskite morphology which can have a larger impact than the presence of an interlayer. This uncertainty can be removed by controlling those parameters strictly.

6.7 Acknowledgements

The author thanks Yaoming Li for helping in XPS characterization of benzoic acid interlayers. The contact angles of TiO_2 film aged for different times were provided by Isabella Poli.

6.8 Supporting Information

6.8.1 Relationship between recombination resistance and light intensity

Due to the opposite direction of light generated current and the saturated current, the net current collected can be displayed as:

$$\mathbf{j = j_L - j_{sat}\left[e^{\frac{qV}{nk_bT}} - 1\right]}$$

where j_L is light generated current density, j_{sat} is saturated current density. As the $e^{\frac{qV}{nk_bT}} \gg 1$, the equation can also be displayed as :

$$j = j_L - j_{sat}\left[e^{\frac{qV}{nk_bT}}\right]$$

As IS is generally tested at open circuit, where j=0, the current density equation can then be shown as:

$$j_L = j_{sat}\left[e^{\frac{qV}{nk_bT}}\right]$$

Then $R_{rec} = \frac{dV}{dj} = \frac{nk_bT}{j_L}$

So $\log R_{rec}$ is inversely proportional to $\log j_L$ which is proportional to the light intensity. More details can be found in Adam and co-authors' work.[17]

6.9 References

1. Kwon YS, Song IY, Lim J, Park S-H, Siva A, Park Y-C*, et al.* Reduced charge recombination by the formation of an interlayer using a novel dendron coadsorbent in solid-state dye-sensitized solar cells. *RSC adv* 2012, **2**(8)**:** 3467-3472.

2. Gupta A, Armel V, Xiang W, Bilic A, Evans RA. New organic sensitizers using 4-(cyanomethyl)benzoic acid as an acceptor group for dye-sensitized solar cell applications. *Dyes and Pigments* 2015, **113:** 280-288.

3. Krüger J, Bach U, Grätzel M. Modification of TiO2 Heterojunctions with Benzoic Acid Derivatives in Hybrid Molecular Solid-State Devices. *Adv Mater* 2000, **12**(6)**:** 447-451.

4. Goh C, Scully SR, McGehee MD. Effects of molecular interface modification in hybrid organic-inorganic photovoltaic cells. *J Appl Phys* 2007, **101**(11)**:** 114503.

5. Zhu LF, Xu YZ, Shi JJ, Zhang HY, Xu X, Zhao YH*, et al.* Efficient perovskite solar cells via simple interfacial modification toward a mesoporous TiO2 electron transportation layer. *RSC adv* 2016, **6**(85)**:** 82282-82288.

6. Jena AK, Chen H-W, Kogo A, Sanehira Y, Ikegami M, Miyasaka T. The Interface between FTO and the TiO2 Compact Layer Can Be One of the Origins to Hysteresis in Planar Heterojunction Perovskite Solar Cells. *ACS Appl Mater Inter* 2015, **7**(18)**:** 9817-9823.

7. Snaith HJ, Abate A, Ball JM, Eperon GE, Leijtens T, Noel NK*, et al.* Anomalous Hysteresis in Perovskite Solar Cells. *J Phys Chem Lett* 2014, **5**(9)**:** 1511-1515.

8. Li Y, Zhao Y, Chen Q, Yang Y, Liu Y, Hong Z*, et al.* Multifunctional Fullerene Derivative for Interface Engineering in Perovskite Solar Cells. *J Am Chem Soc* 2015, **137**(49)**:** 15540-15547.

9. Li B, Chen Y, Liang Z, Gao D, Huang W. Interfacial engineering by using self-assembled monolayer in mesoporous perovskite solar cell. *RSC adv* 2015, **5**(114)**:** 94290-94295.

10. Linsebigler AL, Lu G, Yates JT. Photocatalysis on TiO2 Surfaces: Principles, Mechanisms, and Selected Results. *Chem Rev* 1995, **95**(3)**:** 735-758.

11. Augustijns P, Brewster ME. *Solvent systems and their selection in pharmaceutics and biopharmaceutics*, vol. 190. Springer, 2007.

12. Yang G, Wang C, Lei H, Zheng X, Qin P, Xiong L*, et al.* Interface engineering in planar perovskite solar cells: energy level alignment, perovskite morphology control and high performance achievement. *J Mater Chem A* 2017, **5**(4)**:** 1658-1666.

13. Bella F, Griffini G, Correa-Baena J-P, Saracco G, Grätzel M, Hagfeldt A*, et al.* Improving efficiency and stability of perovskite solar cells with photocurable fluoropolymers. *Science* 2016, **354**(6309)**:** 203-206.

14. Shih Y-C, Lan Y-B, Li C-S, Hsieh H-C, Wang L, Wu C-I*, et al.* Amino-Acid-Induced Preferential Orientation of Perovskite Crystals for Enhancing

Interfacial Charge Transfer and Photovoltaic Performance. *Small* 2017, **13**(12)**:** 1604305-n/a.

15. Zuo L, Chen Q, De Marco N, Hsieh Y-T, Chen H, Sun P*, et al.* Tailoring the Interfacial Chemical Interaction for High-Efficiency Perovskite Solar Cells. *Nano Lett* 2017, **17**(1)**:** 269-275.

16. Pockett A, Eperon GE, Sakai N, Snaith HJ, Peter LM, Cameron PJ. Microseconds, milliseconds and seconds: deconvoluting the dynamic behaviour of planar perovskite solar cells. *Phys Chem Chem Phys* 2017, **19**(8)**:** 5959-5970.

17. Pockett A, Eperon GE, Peltola T, Snaith HJ, Walker A, Peter LM*, et al.* Characterization of Planar Lead Halide Perovskite Solar Cells by Impedance Spectroscopy, Open-Circuit Photovoltage Decay, and Intensity-Modulated Photovoltage/Photocurrent Spectroscopy. *J Phys Chem C* 2015, **119**(7)**:** 3456-3465.

Chapter 7 PDIH as blocking layer for low temperature fabricated hybrid perovskite solar cells

Contents

7.1 Introduction

In a conventional planar perovskite solar cell ("n-i-p" structure), inorganic hole blocking layers (electron transporting layers) such as TiO_2 and ZnO are widely used due to their easy preparation processes and good electronic and optical properties.[1, 2] For example, TiO_2 has been reported to exhibit good conductivity (e.g. 1.1×10^{-5}S cm^{-1})[3] and it is nearly transparent which means light can be harvested efficiently by the perovskite light absorber layer. However, these inorganic hole blocking layers either require a high-temperature sintering step or cause long-term device stability problems.[4] For instance, a high annealing temperature (e.g.500 °C) is needed to realize the phase transformation to get high quality, compact anatase TiO_2 films that can act as efficient electron transporting layers in solar cells.[5] The high operating temperature can result in a severe drop in conductivity of the TCO substrates, especially ITO glass whose sheet resistance is highly correlated to the annealing temperature[6]. Furthermore, it also makes the fabrication of flexible devices hard to achieve. Thus, to avoid the drawbacks of using inorganic hole blocking layers, some organic semiconductors with good conductivity and stability have been investigated.[7, 8] For example, fullerene and its derivatives are commonly used in organic solar cells and perovskite solar cells.[9, 10] In addition to costly fullerene derivatives, non-fullerene electron-transporting materials, especially perylene diimides (or perylene bisimides), are very popular for their cheap price and good electrical and electronic properties. As typical n-type small molecular semiconductors, perylene diimide and its derivatives have good electron mobility (10^{-5} S cm^{-1}) according to reported studies[11]. They are also solution-processable which means low temperature device fabrication can be easily realized. In this work, N, N'-di(L-histidine)-perylene-3,4:9,10-tetracarboxylic acid bisimide (PDIH) was introduced as an electron transporting layer in planar structure perovskite solar cell to replace the TiO_2 blocking layer. The PCE of the resulting devices is around 6%, and the device fabrication can be carried out below 150°C. PDIH film thickness and aggregation state were also studied in this work, and improvements to the device performance were made by modifying the PDIH film quality.

7.2 Experimental

7.2.1 PDIH blocking layer

PDIH precursor solution was prepared by dissolving 2.5mg PDIH into 1mL MeOH/NH_4OH=4:1(v/v) mixed solvent and stirring overnight before use. PDIH thin film was obtained through spin-coating the precursor solution on clean FTO substrates at 2k, 3k or 4k rpm and then annealed at 50°C, 100°C or 150°C for 1h to remove the solvent.

7.2.2 Device fabrication

A perovskite layer was deposited by using the one step solution method and a (3:1($MAI/PbCl_2$ molar ratio)) perovskite precursor solution. More film deposition and device fabrication details can be found in Chapter 3.

7.3 Results and discussions

An appropriate energy level alignment between semiconductors in a solar cell is important to achieve a good device performance. According to previous studies, the conduction band (CB) minimum of $CH_3NH_3PbI_3$ is around -3.9 eV and the valence band (VB) maximum is around -5.4 eV[12]. In chapter 5 the energy levels of PDIH molecule were studied using electrochemistry and spectroscopic methods. Its HOMO and LUMO are estimated to be -6.24 eV and -4.00 eV respectively. Its energy level matches very well with that of perovskite layer as demonstrated in Schematic **7-1**.

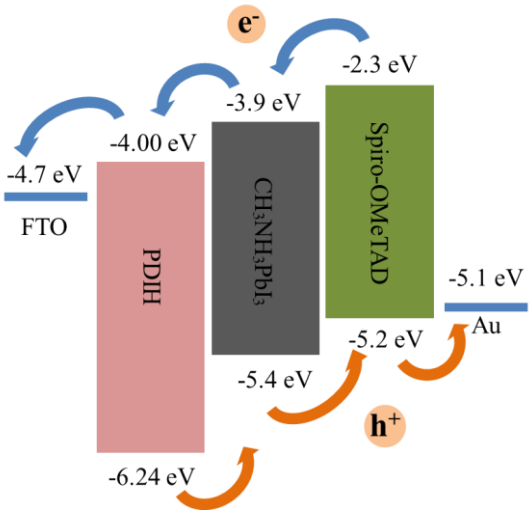

Schematic 7-1 Energy alignment of hybrid perovskite ($CH_3NH_3PbI_{1-x}Cl_x$) solar cells[12]

7.3.1 PDIH thin layer morphology and thickness control

PDIH is poorly soluble in most commonly used solvents as discussed in chapter 5. The two symmetrical carboxylic functional groups at the sides of the conjugation core make its solubility in water pH-dependant, and it will also dissolve in some alcohols. **Figure 7-1** shows the first tests of the solubility in different solvents. It rarely dissolves in solvents with low polarity such as toluene and chloroform, and it partially dissolves in DMF. However, 2 mg PDIH dissolves well in water and MeOH with the addition of base (KOH or NH_4OH). In **Figure 7-2**, (a) and (b) indicate that PDIH dissolves better in base-adjusted solvent than acid adjusted solvent which is due to the deprotonation of the carboxylic acids. When the pH is above 5(neutral at pH ≈5), the deprotonation of the carboxyl group improves the solubility of the molecule[13].

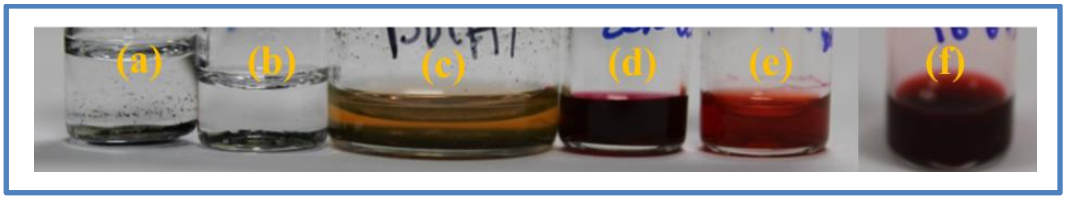

Figure 7-1 Photographs of PDIH dissolving in different solvents. From (a) to (f) are 2mg / mL PDIH in toluene, chloroform, DMF, water with KOH; 1mg/mL PDIH in MeOH with KOH and 2mg/mL PDIH in MeOH with NH_4OH.

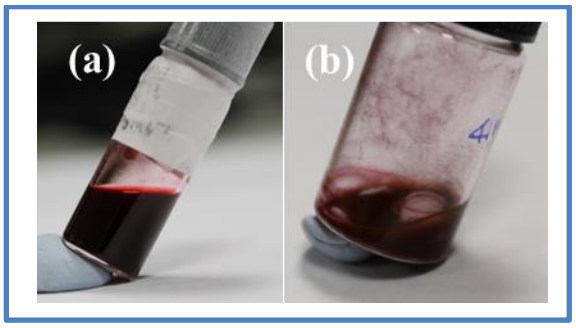

Figure 7-2 pH-dependant solubility of PDIH. (a) Photograph of 6.5mg PDIH in 1mL MeOH-KOH mixed solvent, (b) photographs of 6.5mg PDIH in 1mL MeOH-HAc mixed solvent.

The morphology of the deposited PDIH film (spin coated at 3k rpm for 30s from MeOH/NH_4OH precursor solution) is hard to distinguish using SEM and AFM. As displayed in **Figure 7-3**, the SEM and AFM images of TEC15 ((a) and (b)) show no evident difference in morphology compared with (c) and (d) which are SEM and AFM images of TEC15 with PDIH films. This is ascribed to the rough surface of TCO coated glass and the fact that a very thin (potentially sub-monolayer) of PDIH is deposited.

TCO glass surfaces show a wide distribution of particle sizes which can vary from tens of nanometers to hundreds of nanometers[14]. The roughnesses of FTO and FTO with PDIH were found to be very close as well, around 9 nm and 7nm respectively. As the PDIH film could not be detected on FTO glass, to investigate the surface morphology of PDIH, a film was deposited on a silicon wafer which has smooth surface.

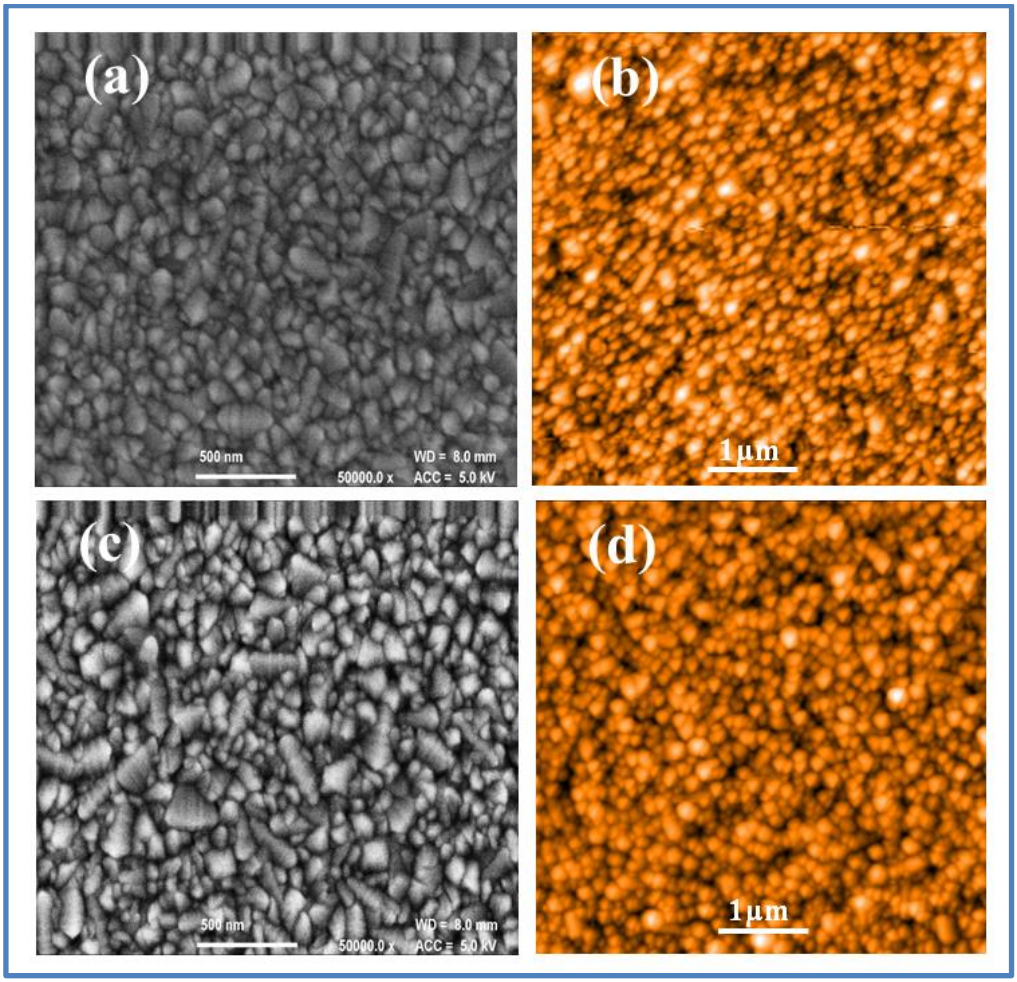

Figure 7-3 Morphology of PDIH films deposited on TCO glass. Sample are tested by SEM and AFM. (a) and (b) are TEC15,(c) and (d) are FTO TEC15 +PDIH. PDIH was deposited at 3k rpm for 30s from 2.5mg/mL PDIIH MeOH/NH_4OH solution.

The surface morphology of PDIH films deposited on Si wafer was also investigated by AFM and the images can be found in **Figure 7-4**. The difference in morphology is clear between samples with and without PDIH film on top. As clearly shown in **Figure 7-4**(b) the PDIH film is composed of nanoparticles with a size of around 70nm, while the Si wafer is composed of steps which around half a micrometre in width (**Figure 7-4**(a)). The PDIH particles form a compact film on the Si wafer and the film roughness is

around 2 nm, rougher than the Si wafer surface (~ 1nm), and the coverage of the substrate is reasonable.

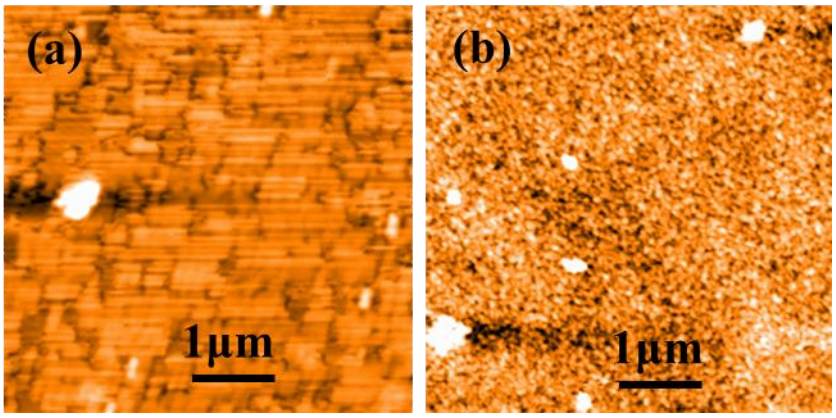

Figure 7-4 Morphology of si wafer (a), and PDIH film deposited on Si wafer (b) tested by AFM. PDIH was deposited at 3k rpm for 30s from 2.5mg/mL PDIIH MeOH/NH_4OH solution. Si wafer was cleaned by immersing it into H_2O:H_2O_2:HCl (5:1:1 v/v) and H_2O:NH_4OH:H_2O_2(6:1:1 v/v) solutions for 10 mins separately and rinsed with water after that.

As discussed in previous chapters, the morphology of the underlayer for depositing perovskite is extremely critical for obtaining high quality perovskite films. The roughness of the PDIH film was therefore monitored when varying the solvent, types of base added and the concentrations of PDIH precursor solutions. Though the film was deposited on a Si wafer rather than TCO glass, a study of changes in film morphology is still instructive. As shown in **Figure 7-5**, changing the solvent from H_2O to MeOH does not bring about a big change in the film roughness, while decreasing the PDIH concentration and changing the basic additive (from KOH to NH_4OH) caused a significant drop in film roughness from 7.5 ± 6.1nm to 3.5 ± 1.1 nm. Further reduction of roughness can be achieved by halving the concentration. However, the roughness only slowly decreases according to the curve in the figure, and almost does not change from 2.5mg/mL solution to 1mg/mL solution. The conclusion is that a weak base NH_4OH was better than KOH in assisting the dissolution of the PDIH molecules, and a low concentration of PDIH reduced aggregation of PDIH in the solution.

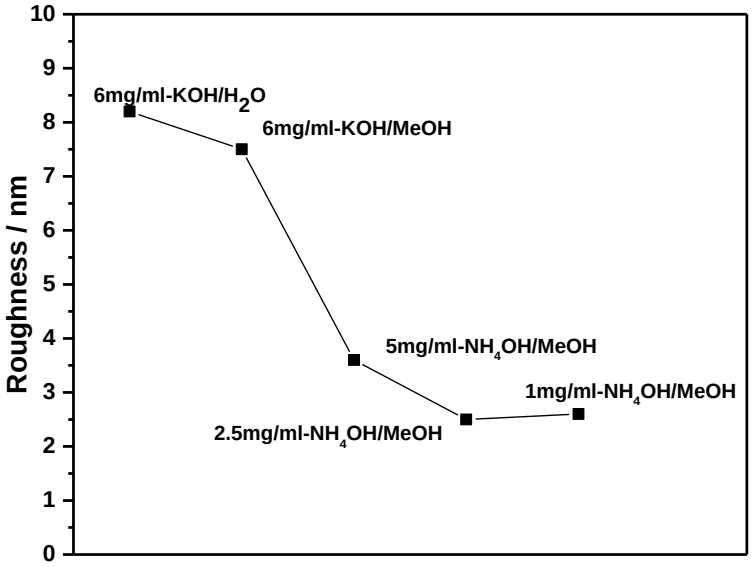

Figure 7-5 PDIH film roughness varies with changing of solvent and concentration. Films are deposited at 3k rpm for 30s, and the roughness data are from AFM.

The thickness of PDIH film deposited on Si wafers was also measured by AFM (Figure 7-6). Though it doesn't represent the actual thickness of PDIH films deposited on TCO, it gives useful information about the thickness variation with the spin coating speeds. As shown in Figure 7-6(a), the PDIH film was partially scratched to measure the thickness by AFM. The Z axis section shows the film was around 15nm when it was prepared at 3k rpm, and the thickness is proportional with the reciprocal of the square root of spin coating speed ((b) and (c)).

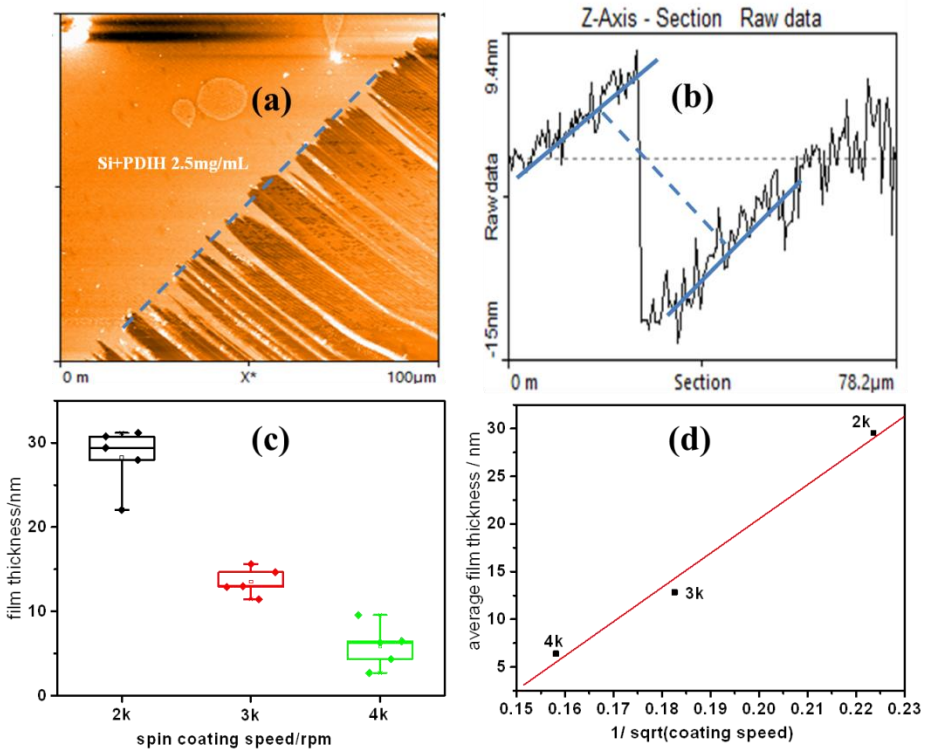

Figure 7-6 PDIH film thickness by AFM.(a)AFM image of PDIH film deposited on Si wafer, (b)AFM z axis line roughness, (c)thickness at different spin coating speeds, (d)relationship of spin coating speeds with the film thickness.

UV-Vis absorption of the precursor solution and the corresponding film were tested and are shown in **Figure 7-7**.The solution spectrum shows peaks at 490 and 522nm, which represent 0-1 and 0-0 vibronic transitions of the S0/S1 transition respectively[15]. The relative absorption intensity of the two peaks gives information on the degree of aggregation[16]. Free PDIH dominates in solution, while unsurprisingly the PDIH is aggregated in the film. In addition the peaks for the film are red-shifted relative the solution, showing maxima at 508nm and 550 nm.[17]

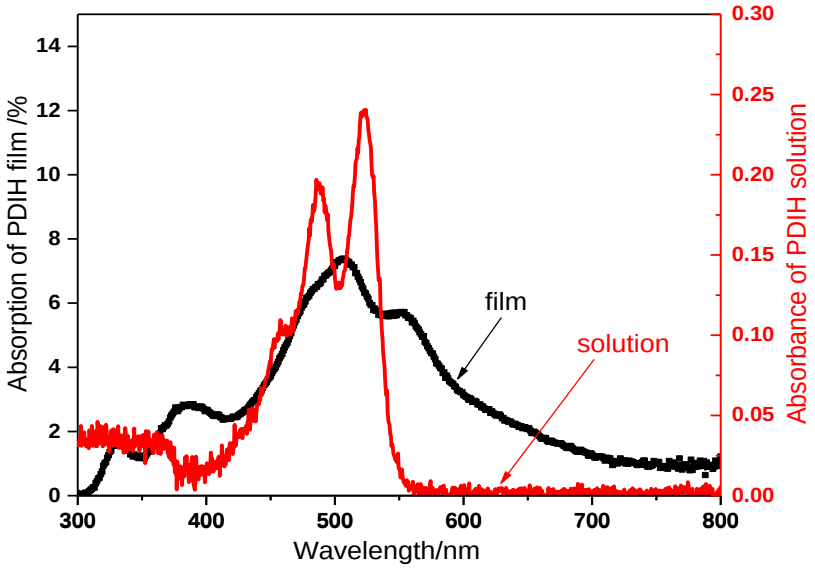

Figure 7-7 UV-Vis. of PDIH MeOH/NH_4OH solution and the corresponding thin film. Thin film on FTO was prepared by spin coating at 2k for 30s (1mg/mL PDIH solution) and annealing at 50°C for 1h. DMF washing was carried out using the same procedure as perovskite film preparation.

7.3.2 Effects of PDIH blocking layer on device performance

It is important to monitor any change in morphology of perovskite films deposited on new substrates (i.e. FTO or FTO with PDIH), as the presence of a PDIH layer can change the surface energy of the substrates. To explore the change, AFM was used to characterize perovskite films deposited on PDIH. Perovskite film deposited on standard TiO_2 blocking layers was also tested for comparison. As shown in **Figure 7-8**, the morphologies of the corresponding perovskite films exhibit pronounced differences. The coverage and grain sizes were found to be different for each sample. The perovskite film deposited on FTO showed the worst coverage. The film deposited on TiO_2 appears to be slightly more compact compared to the film on the FTO substrate. Films deposited on PDIH were compact and showed the best coverage. It was also noticed that the grain size decreased when perovskite was deposited on PDIH layer. With an increase in the PDIH film thickness (or decrease of the spin coating speed), smaller perovskite grains were found in the films, indicating that the FTO was more efficiently covered with PDIH at low spin coating speed. Perovskite films on PDIH, especially on sample PDIH-2k, were also smoother than those deposited on other samples. As shown in **Figure 7-9**, the roughness of perovskite films on FTO, 2.5mg PDIH-4k, 2.5mg PDIH-3k, 2.5mg PDIH-2 and TiO_2 is calculated to be around 103nm, 94nm, 89nm, 73nm and 92 nm

respectively. Out of all PDIH samples, PDIH-2k displays the smoothest surface. However, the distribution in the roughness values is wide, implying that the PDIH film is possibly not as uniform as the TiO_2 layer. It is also interesting to notice that perovskite films on FTO and TiO_2 have similar morphology and grain size, but the film on TiO_2 is more compact and smoother which can be proved by the average roughness. The morphology change after deposition of PDIH blocking layer indicates that PDIH can significantly adjust the morphology of perovskite films through changing the grain size and surface roughness.

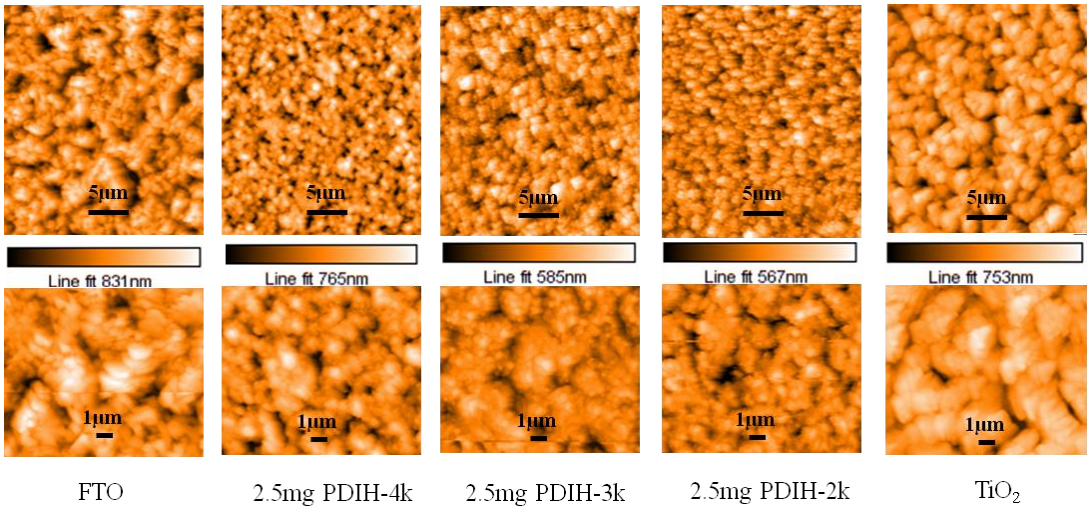

Figure 7-8 Perovskite films on different substrates. Images at the bottom are enlarged-scale graphs of the corresponding samples shown at the top. The scale bars are 5µm and 1µm respectively. 2.5mg PDIH-2k represents the PDIH film deposited at 2k rpm from a 2.5mg/mL precursor solution. Other samples of PDIH are labeled as the same way.

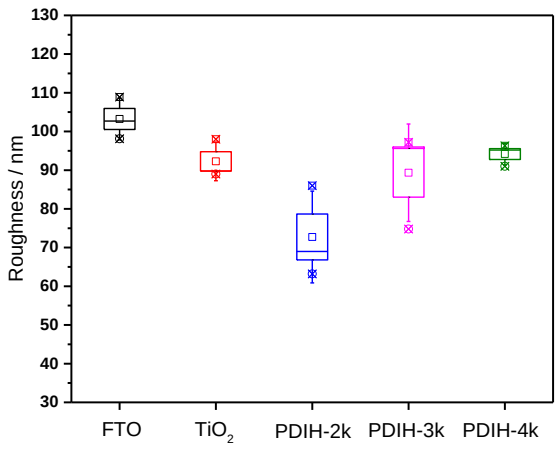

Figure 7-9 Average roughness of perovskite films deposited on different substrates. The box and whisker represent 0.5 SD and 1 SD.

The effects of PDIH blocking layers on device performance were also investigated by fabricating devices with corresponding contact layers. The device parameters were tested by current density-voltage (J-V) scans at one sun AM1.5. All parameters were obtained from reverse scans (direction: V_{oc} to J_{sc}) at 200 mV/s, and the parameters are all listed in **Table 7-1**. In the three different PDIH samples (deposited at different spin coating speeds), devices prepared with PDIH deposited at 2k-PDIH show the best PCE (6.02%), and the efficiency is also higher than devices prepared with no blocking layers (FTO, 4.16%) and conventional blocking layer TiO_2 (4.11%). The increased J_{sc} and FF are the two main sources of the PCE enhancement for device PDIH (2k), and the rise of J_{sc} corresponds with the improved morphology shown in **Figure 7-8**. The other two types of PDIH devices both showed inferior performances in comparison with the devices on FTO and TiO_2. This could be attributed to the PDIH blocking layers obtained at high spin coating speeds being too thin to block charge recombination efficiently. It is assumed that if the spin coating speed is too high (e.g. 4k rpm), the deposited thin film may not be able to uniformly cover the substrate. The possible coverage problem can be caused by several reasons. For instance, if the precursor solution is too dilute, the deposited film cannot significantly cover the substrate. Or if the solubility of the PDIH film to DMF (which is the solvent for the following perovskite layer) is high, the deposited PDIH can be removed by the solvent (related study can be found in the following context). The poor rectifying behaviour of the thickest PDIH film (deposited at 2k rpm) is shown below which can partially support this assumption. The inhomogeneity of the deposited PDIH and the possible exposed FTO in contact with the perovskite could easily form recombination and shunting sites, resulting in rapid decrease of V_{oc} and J_{sc}.

It is also worth noting that the FF of all the devices with PDIH is higher than the other samples. It may be due to the good conductivity of PDIH, as it can reduce the series resistance of devices. The device without the blocking layer (FTO) displays the worst FF, which could be due to the low shunt resistance caused by the low coverage of the perovskite film on the substrate. .

Table 7-1 Device performance parameters. Devices were measured at AM1.5 at room temperature.

Devices	PCE /%	V_{oc} / V	J_{sc} / mAcm^{-2}	FF /%
2k-PDIH*	6.02 ± 0.17	0.78 ± 0.01	11.09 ± 0.12	70.02 ± 0.48
3k-PDIH*	4.01 ± 1.30	0.64 ± 0.13	8.83 ± 1.14	68.98 ± 4.31
4k-PDIH*	2.60 ± 0.79	0.50 ± 0.05	7.87 ± 1.19	64.56 ± 9.05
FTO	4.16 ± 1.33	0.83 ± 0.11	9.98 ± 2.06	46.6 ± 6.77
TiO_2	4.11 ± 0.83	0.87 ± 0.05	7.53 ± 1.00	62.46 ± 4.56

* Devices labelled as 2k/3k/4k PDIH represent the devices FTO/PDIH/ $CH_3NH_3PbI_{3-x}Cl$/spiro-OMeTAD/Au, and PDIH layers were deposited at 2k, 3k or 4k rpm. FTO represents FTO/ $CH_3NH_3PbI_{3-x}Cl_x$/spiro-OMeTAD/Au and TiO_2 represents FTO/TiO_2/$CH_3NH_3PbI_{3-x}Cl_x$/spiro-OMeTAD/Au.

As another important parameter, the hysteresis was reduced in devices with blocking layers, especially in the device with 2k rpm deposited PDIH layer. In **Figure 7-10** the differences between the reverse J-V scan and the forward scan is demonstrated for different devices. Devices without a blocking layer (i.e. FTO) show the most serious hysteresis, while devices with 2k rpm deposited PDIH display the least hysteresis. This hysteresis reduction phenomenon is consistent with reported works in which organic contacts (e.g. PCBM) are used as blocking layers[18, 19]. Other devices with PDIH deposited at other speeds did not give the same trend, which can be ascribed to the inhomogeneity of PDIH films. It can also be found that the series resistances of devices with PDIH are all lower than that of the other devices, due to the good electrical properties of PDIH.

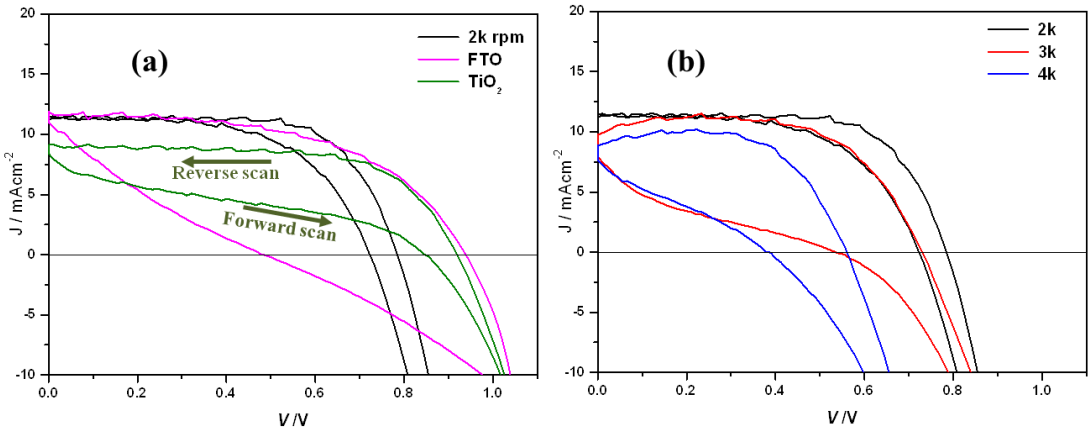

Figure 7-10 J-V curves of best performing devices with TiO_2 blocking layer, PDIH blocking layers deposited at different spin coating speeds(2k, 3k, 4k) and no blocking layer (FTO) Reverse scan is the curve (from open circuit to short circuit) showing higher efficiency (e.g. illustrated as the arrows in J-V curve of TiO_2)

The long-term stability of hybrid perovskite solar cells remains a challenge for their commercialization. To study stability, the PCE of devices was monitored over time. J-V curves of devices with TiO_2 blocking layer, PDIH blocking layer (2k rpm deposited) and no blocking layer (FTO) were tested at 0h (tested once devices were fabricated), 24h and 96h. As shown in **Figure 7-11**, the PCE of all devices is observed to increase within 24h, which could be caused by doping effects in the spiro-OMeTAD or a reduction in defects after aging under low humidity conditions.[20, 21] When tested after 96h, the PCE is found drop rapidly for the FTO device, while the decrease is much slower for devices with a TiO_2 blocking layer and a PDIH layer, indicating that blocking layers work to slow down device degradation. In addition, from 24h to 96h, the degradation of device with blocking layer PDIH is slightly slower than that with conventional blocking layer TiO_2.

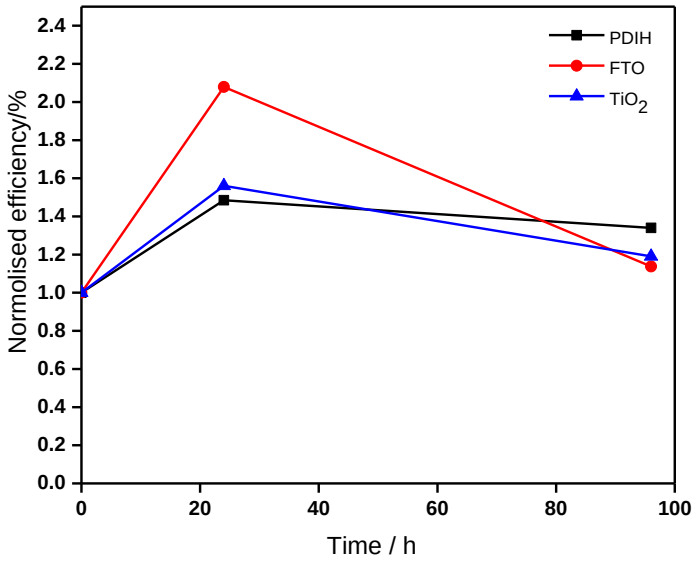

Figure 7-11 Device stability over time. Efficiencies were calculated according to reverse scans of J-V curves. When not being tested, devices were stored in a desiccator box (humidity ~ 20%) at dark. PDIH represents the sample with PDIH film deposited at 2k rpm from 2.5mg/mL MeOH/NH_4OH solution.

To further understand the performance of devices with PDIH (2k), UV-Vis absorption spectra of perovksite films deposited on PDIH (2k), FTO and TiO_2 were measured. The onsets of the perovskite absorption are almost the same and the calculated band gaps are all 1.55eV, indicating no change of the perovskite structure. The absorption in the tested region was observed largely unchanged from PDIH sample to the control (TiO_2 and FTO).

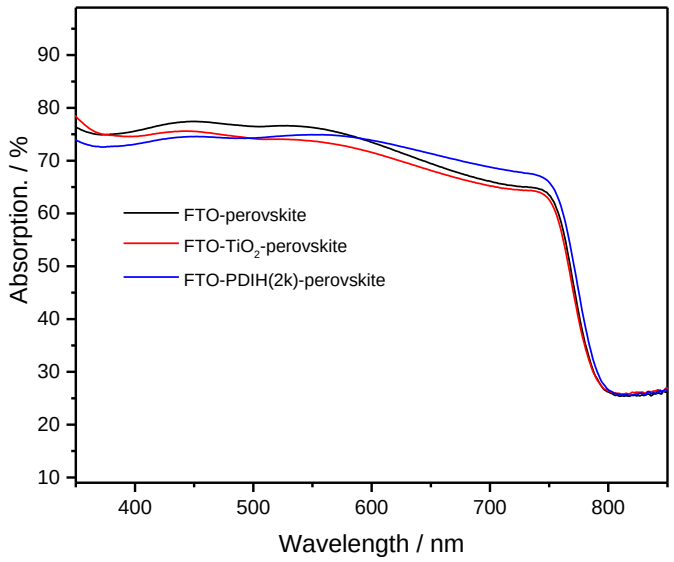

Figure 7-12 UV-Vis of perovskite films deposited on FTO, TiO_2 and 2k rpm(2.5mg/mL) spin coated PDIH film

Differences in XRD patterns can also assist in illustrating the PCE changes. As illustrated in **Figure 7-13**(a), perovskite films on FTO, TiO_2 and PDIH(2k) all show tetragonal structured $CH_3NH_3PbI_3$, showing strong peaks at 14.2°(110), 28.5°(220). The peaks at 12.9° represent the existence of PbI_2, indicating the incomplete conversion of PbI_2 to hybrid perovskite. However, PbI_2 peaks in PDIH (2k) and TiO_2 samples are obviously weaker than in the FTO sample, revealing that the conversion of samples with blocking layers is more complete than the sample without blocking layer (FTO). The calculated FWHM for the (110) peak of films deposited on PDIH (2k), TiO_2 and FTO is 0.152°, 0.143° and 0.158°, indicating that the perovskite film deposited on TiO_2 has the best crystallinity and the largest particles, and the one on FTO has the worst crystallinity and smallest particles.

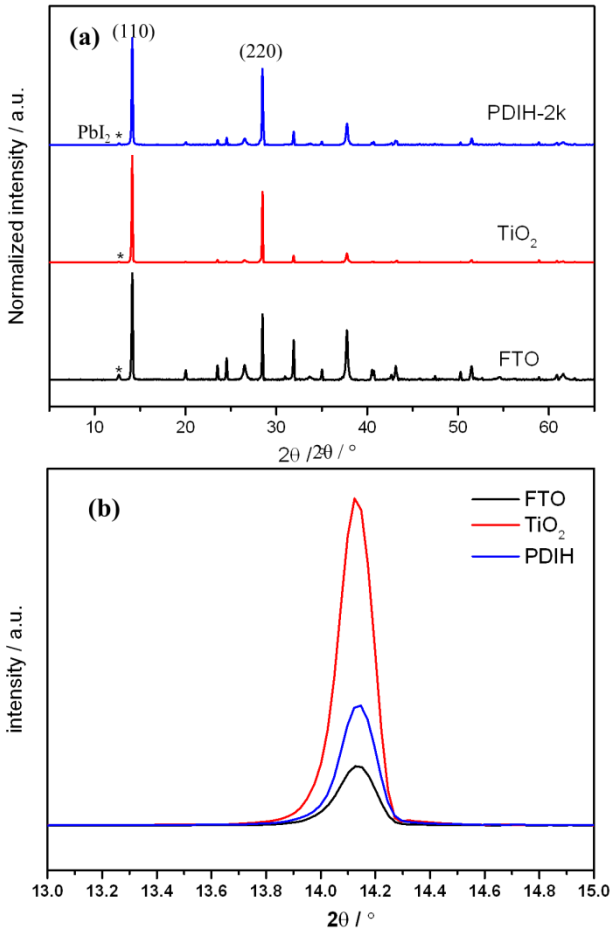

Figure 7-13 XRD patterns of perovskite films deposited on FTO, TiO_2 and PDIH (deposited at 2k rpm, 2.5mg/mL solution). (a)Normalized full range diffraction patterns for perovskite films, (b) diffraction peak of lattice plane (110)

The rectifying behaviour of the blocking layers was measured to better understand the behaviour of the PDIH films (Figure 7-14). The curve for sample TiO_2 (FTO/TiO_2/perovskite/Au) shows distinct rectifying behaviour, while the curves for FTO (FTO/perovskite/Au) and PDIH (FTO/PDIH/perovskite/Au) are not particularly rectifying. Both the responses of FTO and PDIH are close to linear, showing a resistive behaviour. This indicates that the perovskite film has many shunt paths which can be revealed from the near-linear IV curve of the FTO/perovskite/Au junction, and the PDIH did not work effectively as a blocking layer. We hypothesise that the weak rectifying character is due to the PDIH film not being thick enough, and the uniformity is poor as well. This also explains why PDIH films deposited at high speeds (3k or 4k) which are thinner than 2k deposited film, show much decreased V_{oc} and J_{sc} in comparison with the TiO_2 device. More work needs to be done by characterize the rectifying behaviour of PDIH film with different thicknesses.

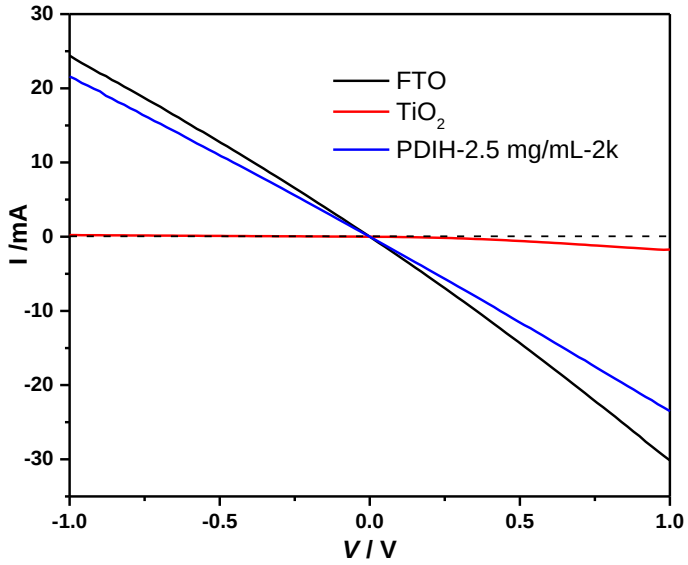

Figure 7-14 Rectifying character of PDIH (2k), FTO and TiO_2. Samples structures are FTO/PDIH/perovskite/Cu tape, FTO/perovskite/Cu tape and FTO/TiO2/perovskite/Cu tape. Samples were tested with DC scan at dark from -1.0V to 1.0V.

One potential problem is that the PDIH film may be damaged when the perovskite layer is spin coated on top. In the first part of this chapter, solubility of PDIH in different solvents was investigated (**Figure 7-2**), and importantly PDIH was observed to partially dissolve in DMF. Notably, most reports do not mention or consider this problem where the underlayers can dissolve in the solvent that used for following films to be deposited[8]. As the perovskite film is deposited as a DMF solution, this could cause some of the PDIH to be removed from the substrate.

To study the stability of the PDIH films to DMF, experiments were carried out by spin coating DMF solvent on the films. The effect was evaluated by testing the UV-Vis absorption of the film before and after the DMF rinse (shown in **Figure 7-15**). It was found that the position of the peaks was almost the same after solvent rinsing (509nm/549nm to 508nm/547nm) but the intensities of the peaks decreased, indicating solid PDIH can be partially removed through perovskite deposition step. As discussed before, the inhomogeneity could introduce recombination sites for trapping charge carrier. Therefore, more work on improving the solvent resistance of PDIH film needs to be carried out.

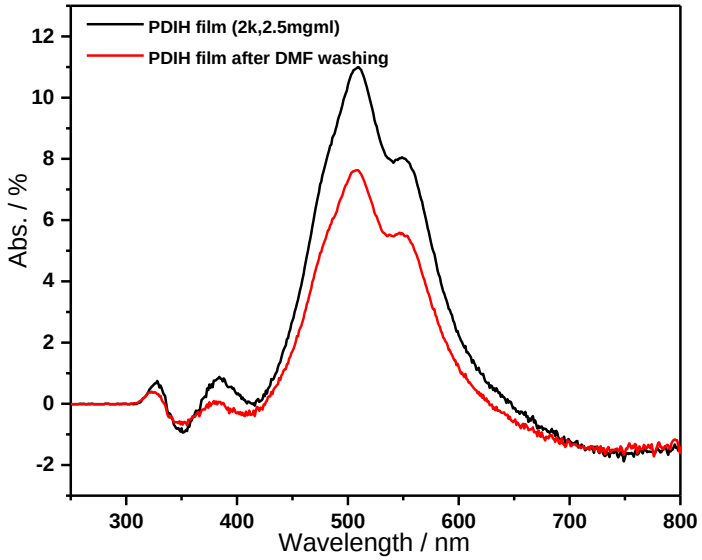

Figure 7-15 UV-Vis. of PDIH film (2k, 2.5mg / mL) before and after DMF rinse. DMF spin coating procedure was according to perovskite layer preparation process. The baseline is observed below zero which is ascribed to the subtraction of the FTO background and the FTO was not the one used for deposit PDIH.

Since annealing at controlled temperatures can be beneficial to promote the intermolecular chemical bonding of PDIH and the chemical bonding of PDIH to substrates,[22] it could be a useful way to improve the stability of deposited PDIH films to solvents (e.g. PDIH). To investigate the effects of annealing temperature on device efficiency, two different tests were carried out. In the experiments, PDIH films were annealed at 50°C and 100°C and rinsed with MeOH after annealing. MeOH rinsing was used previously to remove surface aggregates in the PDIH film, more details can be found in 7.3.3(a). J-V curves of corresponding devices were monitored and are shown in **Figure 7-16**(a). When the annealing temperature was increased from 50°C to 100 °C, the V_{oc} and J_{sc} of corresponding devices were both improved, possibly indicating that the increased annealing temperature can enhance the film's solvent resistance.

In the second set of experiments, no MeOH rinse step was employed. Studies were carried out by increasing the annealing temperature from 100°C to 150°C for PDIH film deposited at 2k rpm and 3k rpm, and related devices were fabricated by using a one-step solution method. The J-V curves of devices are demonstrated in **Figure 7-16**(b). When the PDIH film was annealed at 100°C, the device with PDIH deposited at 3k shows better performance than the device deposited at 2k. In the previous work, PDIH was annealed at 50°C, and the device showed opposite trend in performance. More experiments need to be carried out in future, but the results indicate that though

deposited at high speed (3k rpm), a thin film with improved stability to solvent rinsing enhances the device performance, and works better as a blocking layer than the thicker film (2k rpm deposited). An increase in the annealing temperature to 150°C is noticed to further improve the PCE. The V_{oc} increases by 12% from 0.65 V to 0.73V, and the Jsc increases by 33% from 15.75 $mAcm^{-2}$ to 20.98 $mAcm^{-2}$.

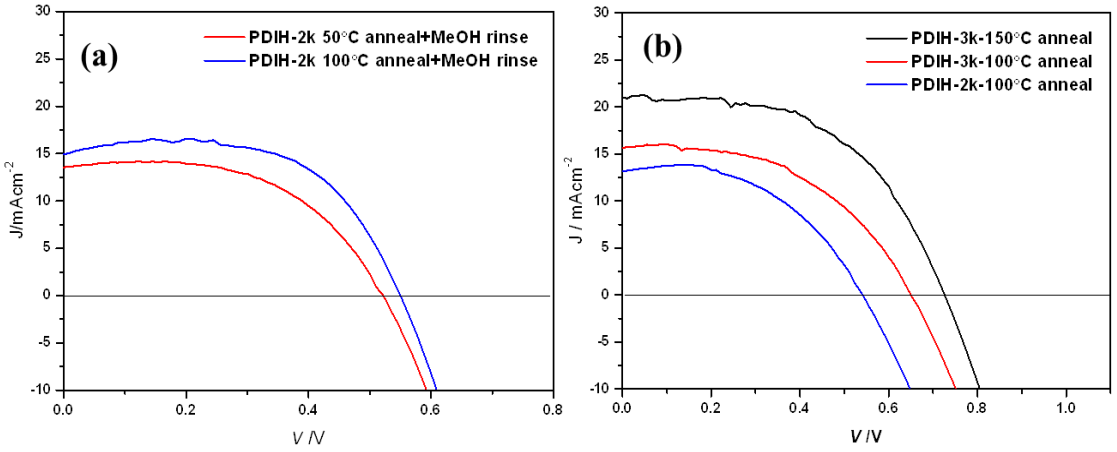

Figure 7-16 PDIH film stability over solvent after being annealed at different temperatures.

To understand the change in the PDIH films after varying the annealing temperature, UV-Vis measurements were used to look for changes in the absorption spectra of films annealed at different temperatures. **Figure 7-17** shows UV-Vis absorption spectra of films annealed at 50°C, 100°C, 150°C and 200°C. The curves all show peaks at around 509 nm and 549nm which represent the aggregation[16]. But the relative intensity of the two peaks changes with the annealing temperature. As reported in a previous study, the ratio of the peak intensity in solution reveals the aggregation state of the molecule[23, 24]. As demonstrated in **Table 7-2**, the ratio of peak intensities (509 nm *vs.* 549nm) rises with an increase of temperature from 0.75 to 0.84, indicating that the degree of π-π stacking is reduced (assuming that a similar process happens on the surface as in solution). Therefore, it can be concluded that the increased annealing temperature of PDIH films decreases the degree of π-π aggregation, and this improves the PCE of devices. Furthermore, the efficiency of the device could potentially be further improved by increasing the annealing temperature to 200°C.

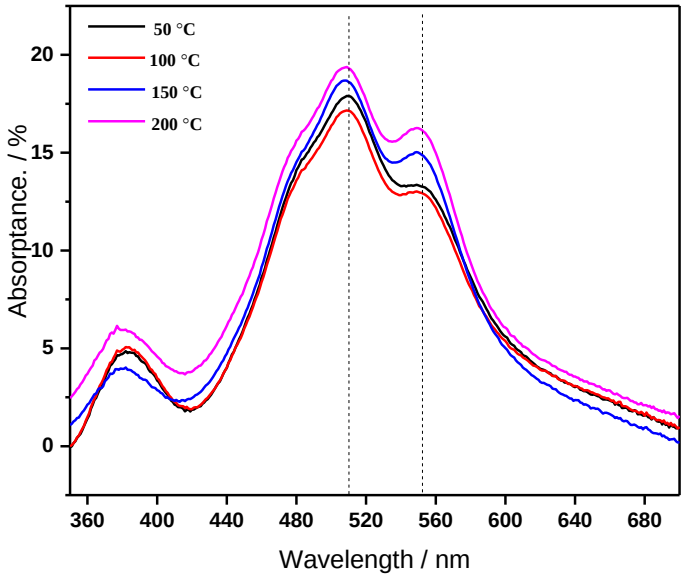

Figure 7-17 UV-Vis of films at different anneal temperatures.

Table 7-2 UV-Vis. absorption peak information of PDIH films (2k, 30s) annealed at different temperatures

Annealing temperature	Peak 1	Peak 2	Peak intensity ratio (peak 2/peak 1)
50 °C	509 nm	549 nm	0.75
100 °C	509 nm	549 nm	0.76
150 °C	508 nm	549 nm	0.81
200 °C	509 nm	549 nm	0.84

7.3.3 Optimization of device performance

a) Aggregates on PDIH film surface

As discussed above, the surface roughness of PDIH films can be modified by changing the concentration of the precursor solution and the type of base used. The average roughness can be reduced to around 2nm (**Figure 7-5**) if the film was deposited on Si wafer. However, it is still possible to find numerous PDIH aggregates on the film surface (shown in **Figure 7-18**). Aggregates are clearly present in **Figure 7-18** (enlarged graph). They are generally hundreds of nanometers in size and composed of PDIH particles with the size of around 60nm.

The formation of PDIH aggregates is due to the weak molecular-solvent interaction which causes strong aggregation that happens either in solution or during the annealing process[15, 17]. These big aggregates (some are micrometer size) seriously affect the surface roughness of PDIH blocking layer and could create uneven coverage of the perovskite layer.

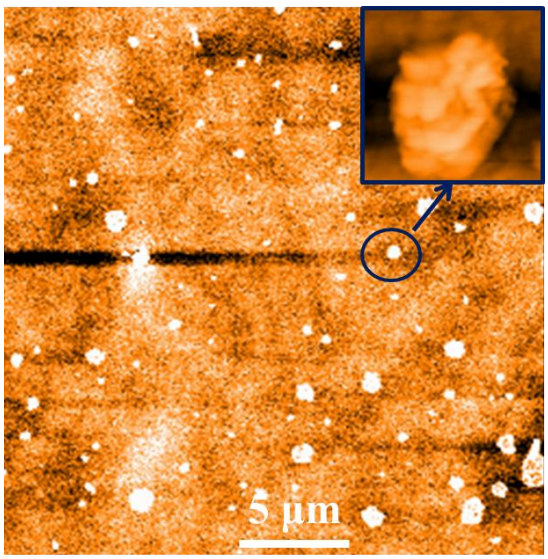

Figure 7-18 AFM images showing PDIH aggregates on film surface, and enlarged scale image. PDIH was deposited on Si wafer at 3k rpm from 2.5mg/mL solution.

In order to improve the film quality, a solvent rinsing step was considered to remove large aggregates. As MeOH is not a good solvent for dissolving PDIH (PDIH only dissolves well in MeOH when NH_4OH was added), therefore MeOH was used to rinse the prepared film. The force of the liquid flow should remove those aggregates which are physically adsorbed on the surface. The PDIH film was rinsed with MeOH for 10s after the annealing step, and then dried by N_2 flow. Corresponding hybrid perovskite solar cells were fabricated by using one-step solution method, and device performances are demonstrated in **Figure 7-19**. In contrast to what we expected, the performance of the device with MeOH rinse procedure decreases compared with the device without MeOH rinsing. Shown in the J-V curves, its V_{oc} and J_{sc} both drop severely. The V_{oc} decrease from 0.67V to 0.52V, and the J_{sc} decreases from 16.4 $mAcm^{-2}$ to 13.5 $mAcm^{-2}$ after the MeOH rinse. The decrease of PCE could be due to removal of too much PDIH

from the film even though PDIH has a very low solubility in MeOH. It could also happen if the aggregates are removed leaving behind pin holes in the PDIH layer.

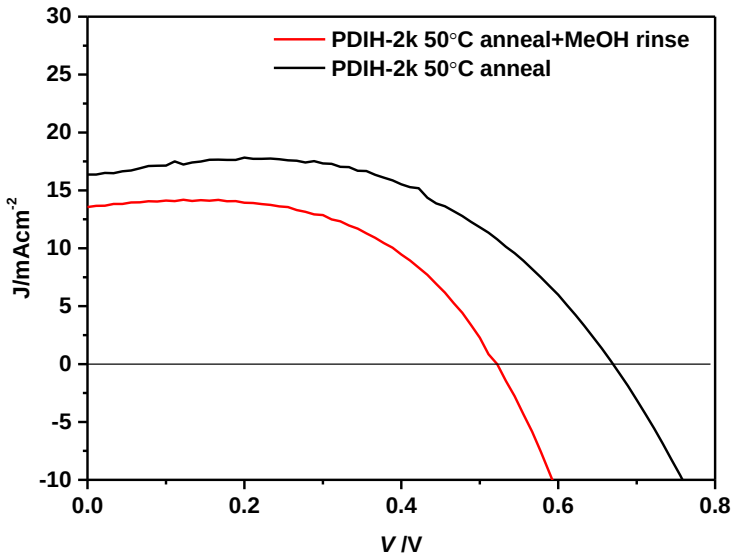

Figure 7-19 J-V curves of devices with and without MeOH rinse.

b) TCO substrates

As PDIH blocking layer can be created at low temperature (below 200°C), ITO is also appropriate to be used as a substrate. Compared with FTO TEC15, ITO (supplied by Sigma Aldrich, sheet resistance 8~12Ω) has a smoother surface and lower sheet resistance, which make it a better substrate in low temperature fabricated solar cells. The corresponding devices with PDIH deposited on ITO display better performance than those with TEC15 as substrates (shown in **Figure 7-20**). Improvements of V_{oc}, J_{sc} and FF are all observed to increase, and the main contribution to the PCE increase is the J_{sc} improvement. It increases from 13.86 to 14.88 $mAcm^{-2}$, resulting in a 12.5% increase of PCE.

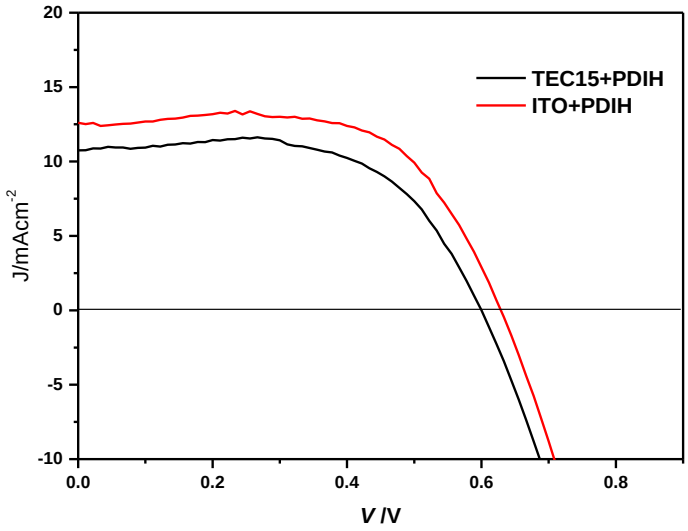

Figure 7-20 J-V curves of devices. Devices are FTO (ITO)/PDIH (2k,30s)/$CH_3NH_3PbI_{3-x}Cl_x$/spiro-OMeTAD/Au, and tested at 1 sun AM1.5 with a scan rate of 200 mV/s.

Table 7-3 device parameters from J-V curves reverse scan.

Devices	PCE /%	V_{oc} / V	J_{sc} / mAcm^{-2}	FF /%
TEC15	4.8 ± 0.2	0.58 ± 0.02	13.86 ± 0.38	0.60 ± 0.01
ITO	5.4 ± 0.9	0.59 ± 0.03	14.88 ± 1.51	0.61 ± 0.02

c) PDIH Precursor solution spin coating time

The effects of spin coating time to prepare PDIH blocking layer on device performance were also investigated. PDIH films were spin coated for 30s and 45s at 2k rpm (2.5mg/mL solution). J-V curves and device parameters of corresponding devices are shown in Figure 7-21 and Table 7-4. When PDIH films were spin coated for a longer time (i.e.45s), the V_{oc}, J_{sc} were both found to increase compared to devices with PDIH deposited for a shorter time (i.e.30s), and the PCE is finally increased by 19% from 4.8% to 5.7%. We hypothesize that the longer spin coating time could be beneficial to remove the big aggregates on the film surface (shown in Figure 7-18) through centrifugal force.

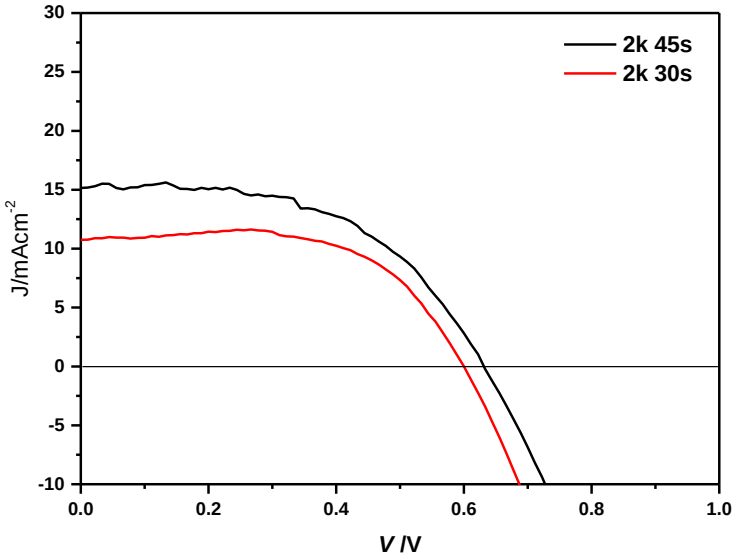

Figure 7-21 J-V curves of devices with PDIH deposited with different spin coating time. Devices are FTO/PDIH (30s or 45s, 2k rpm)/$CH_3NH_3PbI_{3-x}Cl_x$/spiro-OMeTAD/Au, and tested at 1 sun AM1.5 with a scan rate of 200 mV/s.

Table 7-4 device parameters of solar cells with PDIH films spin coated for different time.

Devices	PCE /%	V_{oc} / V	J_{sc} / mAcm^{-2}	FF /%
2k-45s	5.7 ± 0.60	0.60 ± 0.03	17.02 ± 1.30	0.55 ± 0.02
2k-30s	4.8 ± 0.20	0.58 ± 0.02	13.86 ± 0.38	0.60 ± 0.01

7.4 Conclusion and future work

In this chapter, the possibility of using PDIH as the electron-extracting layer in perovskite solar cells was investigated. Devices with PDIH layers were successfully fabricated, and the whole process was carried out at low temperatures (<200°C). PDIH films were prepared by spin coating, and the film morphology was modified by varying the solvent, concentration and additives in the solution. The best cells were obtained using a PDIH film deposited at 2k rpm for 30s from a 2.5mg/mL precursor solution; the film enhanced device parameters and reduced the hysteresis to some extent. The device performance was also monitored by varying the film annealing temperature. The aggregation state of PDIH film was found to change with the increase of the annealing temperature, and the film is more stable to solvent when annealed at higher temperature. The performance of PDIH devices can be further improved by prolonging the spin coating time from 30s to 45s and using ITO as conductive substrates.

In the future, more work needs to be done on PDIH film quality improvements. The aggregates on film surface remain an unsolved problem. However, using a different solvent that has a good interaction with PDIH will be useful to reduce the big aggregates on the film, and adjusting the additive ratio in the solution could also be an alternative approach to improve the solvent-material interaction. The study on annealing temperature can be extended to a wider range, and corresponding devices with optimal conditions need to be fabricated and analysed.

7.5 Acknowledgements

The author thanks Dr. Ralf Niemann for helping with the PDIH film thickness measurements.

7.6 References

1. Jeon NJ, Noh JH, Kim YC, Yang WS, Ryu S, Seok SI. Solvent engineering for high-performance inorganic–organic hybrid perovskite solar cells. *Nat Mater* 2014, **13**(9)**:** 897-903.

2. Son D-Y, Im J-H, Kim H-S, Park N-G. 11% Efficient Perovskite Solar Cell Based on ZnO Nanorods: An Effective Charge Collection System. *J Phys Chem C* 2014, **118**(30)**:** 16567-16573.

3. Wojciechowski K, Saliba M, Leijtens T, Abate A, Snaith HJ. Sub-150 [degree]C processed meso-superstructured perovskite solar cells with enhanced efficiency. *Energy Environ Sci* 2014, **7**(3)**:** 1142-1147.

4. Idigoras J, Todinova A, Sanchez-Valencia JR, Barranco A, Borras A, Anta JA. The interaction between hybrid organic-inorganic halide perovskite and selective contacts in perovskite solar cells: an infrared spectroscopy study. *Phys Chem Chem Phys* 2016, **18**(19)**:** 13583-13590.

5. Roose B, Pathak S, Steiner U. Doping of TiO2 for sensitized solar cells. *Chem Soc Rev* 2015, **44**(22)**:** 8326-8349.

6. Nishimoto N, Yamada Y, Ohnishi Y, Imawaka N, Yoshino K. Effect of temperature on the electrical properties of ITO in a TiO2/ITO film. *physica status solidi (a)* 2013, **210**(3)**:** 589-593.

7. Malinkiewicz O, Yella A, Lee YH, Espallargas GM, Graetzel M, Nazeeruddin MK*, et al.* Perovskite solar cells employing organic charge-transport layers. *Nat Photon* 2014, **8**(2)**:** 128-132.

8. Zhang H, xue l, han j, Fu YQ, Shen Y, Zhang Z-G*, et al.* New Generation Perovskite Solar Cells with Solution-Processed Amino-substituted Perylene Diimide Derivative as Electron-Transport Layer. *J Mater Chem A* 2016, **4**(22)**:** 8724-8733.

9. Xue Q, Hu Z, Liu J, Lin J, Sun C, Chen Z*, et al.* Highly efficient fullerene/perovskite planar heterojunction solar cells via cathode modification with an amino-functionalized polymer interlayer. *J Mater Chem A* 2014, **2**(46)**:** 19598-19603.

10. Seo J, Park S, Chan Kim Y, Jeon NJ, Noh JH, Yoon SC*, et al.* Benefits of very thin PCBM and LiF layers for solution-processed p-i-n perovskite solar cells. *Energy Environ Sci* 2014, **7**(8)**:** 2642-2646.

11. Zhang Z-G, Qi B, Jin Z, Chi D, Qi Z, Li Y*, et al.* Perylene diimides: a thickness-insensitive cathode interlayer for high performance polymer solar cells. *Energy Environ Sci* 2014, **7**(6)**:** 1966-1973.

12. Cai B, Xing Y, Yang Z, Zhang W-H, Qiu J. High performance hybrid solar cells sensitized by organolead halide perovskites. *Energy Environ Sci* 2013, **6**(5)**:** 1480-1485.

13. Tuntiwechapikul W, Taka T, Béthencourt M, Makonkawkeyoon L, Randall Lee T. The influence of pH on the G-quadruplex binding selectivity of perylene derivatives. *Bioorg Med Chem Lett* 2006, **16**(15)**:** 4120-4126.

14. Yongzhen W, Xudong Y, Han C, Kun Z, Chuanjiang Q, Jian L*, et al.* Highly compact TiO 2 layer for efficient hole-blocking in perovskite solar cells. *Applied Physics Express* 2014, **7**(5)**:** 052301.

15. Balakrishnan K, Datar A, Naddo T, Huang J, Oitker R, Yen M*, et al.* Effect of side-chain substituents on self-assembly of perylene diimide molecules: morphology control. *J Am Chem Soc* 2006, **128**(22)**:** 7390-7398.

16. Draper ER, Walsh JJ, McDonald TO, Zwijnenburg MA, Cameron PJ, Cowan AJ*, et al.* Air-stable photoconductive films formed from perylene bisimide gelators. *J Mater Chem C* 2014, **2**(28)**:** 5570-5575.

17. Zhang X, Lu Z, Ye L, Zhan C, Hou J, Zhang S*, et al.* A Potential Perylene Diimide Dimer-Based Acceptor Material for Highly Efficient Solution-Processed Non-Fullerene Organic Solar Cells with 4.03% Efficiency. *Adv Mater* 2013, **25**(40)**:** 5791-5797.

18. Jeng J-Y, Chen K-C, Chiang T-Y, Lin P-Y, Tsai T-D, Chang Y-C*, et al.* Nickel Oxide Electrode Interlayer in CH3NH3PbI3 Perovskite/PCBM Planar-Heterojunction Hybrid Solar Cells. *Adv Mater* 2014, **26**(24)**:** 4107-4113.

19. Shao Y, Xiao Z, Bi C, Yuan Y, Huang J. Origin and elimination of photocurrent hysteresis by fullerene passivation in CH3NH3PbI3 planar heterojunction solar cells. *Nat Commun* 2014, **5:** 5784.

20. Han Y, Meyer S, Dkhissi Y, Weber K, Pringle JM, Bach U*, et al.* Degradation observations of encapsulated planar CH3NH3PbI3 perovskite solar cells at high temperatures and humidity. *J Mater Chem A* 2015, **3**(15)**:** 8139-8147.

21. Jung M-C, Raga SR, Ono LK, Qi Y. Substantial improvement of perovskite solar cells stability by pinhole-free hole transport layer with doping engineering. *Sci Rep* 2015, **5:** 9863.

22. Hau SK, Yip H-L, Acton O, Baek NS, Ma H, Jen AKY. Interfacial modification to improve inverted polymer solar cells. *J Mater Chem* 2008, **18**(42)**:** 5113-5119.

23. Li ADQ, Wang W, Wang L-Q. Folding versus Self-Assembling. *Chemistry – A European Journal* 2003, **9**(19)**:** 4594-4601.

24. Wang W, Han JJ, Wang L-Q, Li L-S, Shaw WJ, Li ADQ. Dynamic π−π Stacked Molecular Assemblies Emit from Green to Red Colors. *Nano Lett* 2003, **3**(4)**:** 455-458.

Chapter 8 Conclusion and future work

8.1 Conclusion

In this project, procedures for making baseline perovskite solar cells were developed and small molecules such as perylene diimdes and benzoic acids were investigated as interlayers or charge transporting layers.

In the first part, research was carried out to study the n-i-p structure perovskite solar cells layer by layer. It was found that TEC15 and TEC7 glasses are more suitable to be used in high temperature required procedures to make solar cells than ITO glasses, and the performances of solar cells based on TEC15 and TEC7 are similar. Several different methods for making the hole blocking layer (TiO_2) were investigated, spray pyrolysis films were better than spin coated films as the perovskite precursor solution wet the surface more easily and a more uniform perovskite layer could be formed. In addition, the humidity of the environment, the pre-annealing procedure and the lead sources can all highly affect the quality of the perovskite film. The PCE characterisation of perovskite solar cells based on J-V scans at different scan rates and in different scan directions was also studied for both planar and mesoporous perovskite solar cells. It was observed that the hysteresis and the effects of scan rate on device performance are negligible in mesoporous solar cells. While in a planar device, the calculated efficiency is highly dependent on the scan rates. Optimisation of the baseline perovskite solar cells also included development of the device configuration, and a substrate with 6 pixels was used in the final devices.

In order to modify the properties of the compact TiO_2 layer in planar perovskite cell, perylene diimides (PDIs) with carboxyl functional groups (e.g. PDIH and PDIV) were used as interlayers deposited on top of TiO_2. PDIs have energy levels that match with that of other layers in the solar cell device and it has previously been shown that organic interlayers can reduce hysteresis and improve stability in perovskite solar cells. Cyclic voltammetry was used to estimate the energy levels of the two molecules. The HOMO/LUMO for PDIH and PDIV were measured to be -6.24eV/-4.00eV and -6.23eV/-3.98eV, respectively. Optical and thermal stability of the molecules were also

studied by UV-Vis and TGA measurements. The preparation method used to prepare the PDI layers strongly effect the performance of the solar cells. PDIH interlayers spin coated on TiO_2 increased the device stability (2k rpm deposited film as an example) and reduced the hysteresis. However, solar cells with PDIH films deposited at 1 krpm, 2 krpm and 3 krpm all showed decreased PCE. It was concluded that the spin coating method may be the best way to prepare PDIH interlayers as thicker multi-layers that were visible to the naked eye were formed. A dip coating method was then used to make PDIV and PDIH interlayers. The perovskite solar cells with PDIH interlayer showed higher PCE (10.5%) than the control (8.5%), and the PDIVs was observed decreased the PCE comparing with the control. The result of the stability test is consistent with previous research, showing lower degradation when PDIH was used in the device.

Benzoic acids with different terminal functional groups, 4-(aminomethyl) benzoic acid, 4-(methylamino) benzoic acid and 4-amino benzoic acid were also applied in planar perovskite solar to investigate their effect on the perovskite layer and the device efficiency. After the addition of NH_4OH, the solubility of the benzoic acid was improved and the corresponding solar cells with benzoic acids as interlayers showed enhanced PCE. From this study, it was the different benzoic acids interacted differently with the perovskite. Primary amino groups, which are 4-aminobenzoic acid and 4-(methylamino) benzoic acid displayed an enhancement of J_{sc} (18.51 $mAcm^{-2}$ *vs.* 15.77 $mAcm^{-2}$), while secondary amino (4-aminomethyl benzoic acid) showed negative impact on J_{sc} (15.48 $mAcm^{-2}$ *vs.* 15.77 $mAcm^{-2}$) in comparison with control devices. The recombination of charges in the devices was found to be different by impedance spectroscopy. It was observed that benzoic acids interlayers can increase the recombination resistance, and 4-methylamino benzoic acid shows the best performance among the three interlayers. However, in this study there was not a clear trend in all the parameters measured (e.g. V_{oc} and FF). These inconsistencies and some of the possible reasons for them are discussed in detail. It is assumed that changes in the ambient environment (e.g. temperature, humidity and the atmosphere) caused differences in the perovskite films which hid some of the changes introduced by the interlayers. In future any inconsistency can be reduced by controlling these parameters more strictly.

In the last part of this project, PDIH was used as a hole blocking layer to replace the compact TiO_2. By using this material, the perovskite solar cells were prepared at a lower temperature (below 150°C), and a PCE of 5.7% was obtained (deposited at 2 krpm for 30 s) in a PDIH perovskite device. In this work, the deposition of PDIH was carried out by spin coating a solution of PDIH and ammonium hydroxide (v/v=4:1) in methanol onto a FTO substrate, and the device performance was optimized by changing the concentration of precursor solutions, spin coating speed and film annealing temperature. It was also found that the annealing temperature of the PDIH films is critical to the type of PDIH film formed. By annealing the film at 50°C, 100°C, 150°C and 200°C it was found that films annealed at higher temperatures were more resistant to solvent washing. UV-Vis suggested that fewer aggregates were present in the films annealed at higher temperature.

8.2 Future work

1. Investigation of the surface properties of compact TiO_2layers

In the future, there are several parts of this project which can be continued. Firstly, an investigation of the pre-treatment of the compact TiO_2 can be carried out (e.g. solvent used, atmosphere used, the effect of acids or bases added to the solutions the TiO_2 is being treated with) . It has been reported that the functional groups naturally at the surface of the TiO_2 film (e.g. -OH) can influence chemisorption[1]. The age of the TiO_2 layer was found to make a large difference to the contact angle – possibly as organic contaminants adsorb on the surface when it is stored. A systematic study of how the titania affects interlayer adsorption, perovskite morphology, device performance and long-term stability should be carried out. The surface functionality of the TiO_2 could be studies by IR and titration experiments[2, 3]

2. Aggregation of the interlayer molecules.

The other interesting work that can be investigated is the aggregation state of the interlayer molecules. In chapter 7 PDIH was used as a blocking layer in a device.. PDIs and benzoic acid we used in this project can self-assemble and it has been found that the degree of aggregation of the PDIH changes device performance and how easily the PDIH can be removed by solvent washing. It has also been reported that the aggregation of PDIs influences their conductivity and optical properties[5]. Therefore, a study of the

interlayer to get more details about the aggregation states and its impacts on device would be very useful. In addition, the coverage of the interlayer molecules on the TiO_2 surface can be studied, which can be realized by desorption of the adsorbed molecules and get the amount of molecules through spectroscopy (e.g. UV-Vis)[4].

3. PDIH blocking layer optimization and alternative methods to deposit the perovskite layer.

In our study, replacing of TiO_2 compact layer with PDIH films meant that cells could be prepared below 200 °C (*vs*. 450 °C of TiO_2 based device). However, the PDIH was not as effective as a selective contact as the titania and lower efficiencies were obtained. This is possibly due to pinholes in the PDI layer which act as recombination pathways. Future work will look at the optimization of the PDIH film including the thickness, morphology and the annealing temperature in order to get a better quality hole blocking layer. In addition, the PDIH blocking layer was found to be partially removed by the solvent that was used for depositing the perovskite film on top. This could seriously affect the uniformity of the blocking layer and eventually cause a performance decrease in the solar cells. Instead of using a solution-processable method, vacuum evaporation can be used as an alternative way to deposit perovskite layers in order to avoid damage to PDIH film.

4. Study the charge recombination and collection at the interface

In chapter 6, light intensity dependent impedance spectroscopy revealed that molecular interlayers can significantly change the recombination resistance of the device, and the recombination resistance is highly affected by the terminal functional groups. It would be interesting to understand the charge separating behaviour at the interface by using various techniques. Techniques such as open circuit voltage decay (OCVD), temperature dependent impedance, intensity modulated photocurrent spectroscopy (IMVS) and intensity modulated photovoltage spectroscopy (IMPS) can be used to deeply understand the interface properties after depositing of molecular interlayers.

8.3 References

1. Meroni D, Lo Presti L, Di Liberto G, Ceotto M, Acres RG, Prince KC, *et al.* A Close Look at the Structure of the TiO2-APTES Interface in Hybrid

Nanomaterials and Its Degradation Pathway: An Experimental and Theoretical Study. *J Phys Chem C* 2017, **121**(1)**:** 430-440.

2. Bonelli B, Cozzolino M, Tesser R, Di Serio M, Piumetti M, Garrone E*, et al.* Study of the surface acidity of TiO2/SiO2 catalysts by means of FTIR measurements of CO and NH3 adsorption. *J Catal* 2007, **246**(2)**:** 293-300.

3. Busca G, Saussey H, Saur O, Lavalley JC, Lorenzelli V. FT-IR characterization of the surface acidity of different titanium dioxide anatase preparations. *Applied Catalysis* 1985, **14:** 245-260.

4. Qu Q, Geng H, Peng R, Cui Q, Gu X, Li F*, et al.* Chemically Binding Carboxylic Acids onto TiO2 Nanoparticles with Adjustable Coverage by Solvothermal Strategy. *Langmuir* 2010, **26**(12)**:** 9539-9546.

5. Kozma E, Grisci G, Mróz W, Catellani M, Eckstein-Andicsovà A, Pagano K*, et al.* Water-soluble aminoacid functionalized perylene diimides: The effect of aggregation on the optical properties in organic and aqueous media. *Dyes and Pigments* 2016, **125:** 201-209.